The viscosity of volcanic melts: From pure amorphous systems to nanoscale heterogeneities and their impact on magmatic processes

Doctoral Thesis

submitted to obtain the academic degree of Doctor of Natural Sciences

(Dr. rer. nat.)

of the Bayreuth Graduate School of Mathematical and Natural Sciences

(BayNAT)

of the University of Bayreuth

Pedro Antonio Valdivia Muñoz

from Santiago, Chile

Bayreuth, 2025

This doctoral thesis was prepared at the Bavarian Research Institute of Experimental

Geochemistry and Geophysics (BGI) at the University of Bayreuth from 10/2021 until 08/2025

and was supervised by Dr. Danilo Di Genova and Prof. Dr. Hans Keppler.

This is a full reprint of the thesis submitted to obtain the academic degree of Doctor of Natural

Sciences (Dr. rer. nat.) and approved by the Bayreuth Graduate School of Mathematical and

Natural Sciences (BayNAT) of the University of Bayreuth.

Form of the dissertation: cumulative thesis

Date of submission: 07.08.2025

Admission by the executive board: 13.08.2025

Date of defence: 17.10.2025

Acting director: Prof. Dr. Jürgen Senker

Doctoral committee:

Prof. Dr. Hans Keppler

(reviewer)

Prof. Dr. Fabio Arzilli

(reviewer)

PD Dr. Gerd Steinle-Neumann

(chairman)

Prof. Dr. Daniel Frost

2

Zusammenfassung

Die Viskosität vulkanischer Schmelzen ist eine grundlegende physikalische Eigenschaft, die die Dynamik des Magmaaufstiegs, der Entgasung und der Fragmentierung steuert. Ihre präzise Charakterisierung ist entscheidend für das Verständnis des Ausbruchsverhaltens und für die Entwicklung numerischer Modelle, die vulkanische Prozesse simulieren. Während theoretische und experimentelle Ansätze zur Messung der Viskosität gut etabliert sind, stellen vulkanische Schmelzen, insbesondere Wasser-reiche und eisenhaltige Zusammensetzungen wie Basalte und Andesite, erhebliche experimentelle Herausforderungen dar. Aktuelle Forschung hat gezeigt, dass nanoskalige chemische Heterogenitäten, die Nanokristallisation von Fe-Ti-Oxiden (d. h. Nanolithe), und ein experimentell bedingter Wasserverlust sowohl vor (d. h. während der Probenherstellung) als auch während der Viskositätsmessungen auftreten können. All dies kann die Messung der Schmelzviskosität stark beeinträchtigen. Diese nanoskaligen Effekte und Wasserverluste können zu systematischen Überschätzungen der Viskosität und wichtiger Parameter für deren numerische Modellierung führen, wie der Glasübergangstemperatur (Tg) und der Schmelzfragilität (m).

Diese Dissertation entwickelt einen kombinierten experimentellen und modellbasierten Ansatz, um die Bestimmung der Schmelzviskosität in Magmen zu verbessern, die anfällig für nanoskalige Strukturbildung (vor und nach der Viskositätsmessung) und Wasserverluste während der Messung der Viskosität sind. Der Ansatz kombiniert die Synthese von wasserfreien und wasserhaltigen Gläsern unter kontrollierten Redox-Temperaturbedingungen mit einem strengen Multi-Technik-Screening-Protokoll, einschließlich Raman-, Mössbauer- und Brillouin-Spektroskopie, Fourier-Transform-Infrarotspektroskopie (FTIR) und Electronen Mikrosonde (EMPA), um (nanoskalig) strukturell veränderte Proben vor und nach den Viskositätsmessungen auszuschließen. Diese

Messungen wurden mit Mikropenetrationsviskosimetrie im Hochviskositätsbereich, Differential Scanning Calorimetry (DSC), und konzentrischer Zylinderviskosimetrie im Niederviskositätsbereich durchgeführt. Bemerkenswert ist, dass die Modellierung der Schmelzviskosität ausschließlich auf nanolithfreien Daten basierte.

Im ersten Teil dieser Arbeit präsentieren wir ein neues Viskositätsmodell für wasserhaltigen Stromboli-Basalt. Unsere Ergebnisse zeigen, dass frühere Modelle die Schmelzviskosität unter präeruptiven Bedingungen um den Faktor 2,5–5,7 überschätzt haben. Dies impliziert deutlich schnellere Magmaaufstiegsraten als bisher angenommen, und steht in besserem Einklang mit Beobachtungsdaten der paroxysmalen Eruptionen von 2019.

Im zweiten Teil untersuchen wir die Effekte der Bildung von Fe-Ti-Nanolithen in andesitischen Schmelzen unter Verwendung zeitaufgelöster Viskosimetrie hochauflösender struktureller Charakterisierung mittels Transmissions-Elektronenmikroskopie (TEM), Small-Angle X-ray Scattering (SAXS), und Wide Angle Xray Scattering (WAXS). Wir zeigen, dass Nanolithe sich innerhalb von Sekunden oberhalb von Tg bilden und nanoskalige chemische Heterogenitäten verursachen. Diese umfassen kieselsäurereiche Schmelzdomänen und Aluminium-angereicherte Halos um die neu gebildeten Nanokristalle. Diese Veränderungen führen zu Viskositätserhöhungen um bis zu das 30-fache bei eruptiven Temperaturen, selbst wenn die Nanolithfraktionen unter 1 Vol.-% bleiben. Wichtig ist, dass diese Effekte nicht allein durch den Kristallgehalt oder Änderungen der Gesamtzusammensetzung erklärt werden können, was darauf hinweist, dass Nanolithinduzierte strukturelle Reorganisationen einen starken Einfluss auf die Schmelzrheologie während der frühen Stadien der Kristallisation ausüben.

Aufbauend auf diesen Erkenntnissen entwickelt der letzte Teil dieser Dissertation ein neues Viskositätsmodell für wasserhaltige andesitische Schmelzen, basierend auf Zusammensetzungen, die repräsentativ für den Sakurajima-Vulkan sind. Durch die Synthese

von Eisen-haltigen und Eisen-freien Analoga, hydratisiert auf verschiedene H₂O-Gehalte, und durch die Integration von Daten aus Viskosimetrie, DSC und Brillouin-Spektroskopie, quantifizieren wir die Rollen von Übergangsmetallen und flüchtigen Komponenten auf Tg und

m. Wir führen zwei neue empirische Gleichungen ein, die die Schmelzfragilität mit elastischen Eigenschaften verknüpfen, maßgeschneidert für eisenreiche und eisenfreie Zusammensetzungen. Das resultierende Modell sagt Viskositäten voraus, die bis zu 45-fach niedriger sind als frühere Schätzungen, und erklärt damit langjährige Diskrepanzen in präeruptiven Viskositäts-Vorhersagen für andesitische Systeme.

Insgesamt zeigt diese Dissertation, dass nanoskalige Kristallisation und chemische Heterogenität eine weitaus größere Rolle bei der Schmelzviskosität spielen als bisher erkannt. Durch die Kombination von nanoskaliger Bildgebung, Hochtemperatur-Experimenten und physikalisch fundierten Modellen liefert diese Arbeit einen neuen Maßstab für die präzise Charakterisierung der Schmelzrheologie und verbessert erheblich unsere Fähigkeit, Magmaaufstieg, Fragmentierung und Eruption in flüchtigkeitsreichen vulkanischen Systemen zu simulieren.

Summary

The viscosity of volcanic melts is a fundamental physical property governing the dynamics of magma ascent, degassing, and fragmentation. Its accurate characterization is essential for understanding eruptive behavior and for developing numerical models that simulate volcanic processes. While theoretical experimental approaches for measuring viscosity are well established, volcanic melts, especially volatile-rich and iron-bearing compositions such as basalts and andesites, present significant experimental challenges. Recent research has shown that nanoscale chemical heterogeneities, nano-crystallization of Fe-Ti oxides (i.e., nanolites), and syn-experimental water loss can occur before (i.e., during sample synthesis) or during viscosity measurements. All of these can severely compromise the measurement of melt viscosity. These nanoscale effects and water loss can lead to systematic overestimations of viscosity and key parameters for its numerical modelling, such as the glass transition temperature (T_g) and melt fragility (m).

This thesis develops a combined experimental and modelling framework to improve the determination of melt viscosity in magmas prone to nanoscale modifications and loss of water during the measurement of viscosity. The approach combines the synthesis of anhydrous and hydrous glasses under controlled redox and thermal conditions with a rigorous multitechnique screening protocol, including Raman, Mössbauer, Brillouin, and Fourier Transform Infrared (FTIR) spectroscopies, including Electron probe micro-analysis (EMPA) and Transmission electron microscopy (TEM), to identify (nanoscale) structurally altered samples before and after viscosity measurements. Viscosity measurements were performed using micropenetration viscometry and Differential Scanning Calorimetry (DSC) in the high-mid-viscosity regime, and concentric cylinder viscometry in the low-viscosity regime. Thus, the modelling of melt viscosity was based exclusively on nanolite-free data.

In the first part of this work (Chapter 4.1), we present a new viscosity model for hydrous Stromboli basalt. Our results show that previous models overestimate melt viscosity at pre-eruptive conditions by a factor of 2.5–5.7. This implies significantly faster magma ascent rates than previously thought, aligning better with observational constraints from the 2019 paroxysmal eruptions.

In the second part (Chapter 4.2), we investigate the effects of Fe-Ti nanolite formation in andesitic melts using time-resolved viscometry and high spatial resolution structural characterization using Transmission Electron Microscopy (TEM), Small-Angle X-ray Scattering (SAXS), and Wide Angle X-ray Scattering (WAXS). We show that nanolites form within seconds above T_g , triggering nanoscale chemical heterogeneity. These include silicarich melt domains and aluminum-enriched halos around the newly formed nanocrystals. These changes cause viscosity increases of up to 30-fold at eruptive temperatures, even at nanolite fractions remained below \sim 2 vol%. Importantly, these effects cannot be explained by crystal content or changes in bulk composition alone, indicating that nanolite-driven structural and chemical reorganization exerts a strong control on melt rheology during early stages of crystallization.

Building on these findings, the final part of the thesis (Chapter 4.3) develops a new viscosity model for hydrous andesitic melts based on compositions representative of Sakurajima volcano. By synthesizing Fe-bearing and Fe-free analogues hydrated to various H_2O contents, and integrating data from viscometry, DSC, and Brillouin spectroscopy, we quantify the roles of transition metals and volatiles on T_g and m. We introduce two new empirical equations linking melt fragility to elastic properties, tailored for Fe-bearing and Fe-free compositions. The resulting model predicts viscosities up to 45 times lower than previous estimates, resolving longstanding discrepancies in pre-eruptive viscosity predictions for andesitic systems.

Altogether, this thesis demonstrates that nanoscale crystallization and chemical heterogeneity play a far more significant role in melt viscosity than previously recognized. By combining nanoscale imaging, high-temperature experiments, and physically grounded models, this work provides a new benchmark for accurately characterizing melt rheology and significantly enhances our ability to simulate magma ascent, fragmentation, and eruption scenarios in volcanic systems.

Acknowledgments

I want to thank God...

Table of Contents

Zusammenfassung	3
Summary	6
Acknowledgments	9
Table of Contents	10
1. Introduction	12
1.1 Magma viscosity as a key to understanding volcanic processes	12
1.2 The influence of nanocrystals on magma viscosity	17
1.3 Limitations of existing viscosity models and the need for a new framework	20
2. Analytical techniques and methods	26
2.1 Synthesis of anhydrous starting materials	26
2.2 Synthesis of hydrous glasses	27
2.2.1 Piston cylinder apparatus	28
2.2.2 Internally heated pressure vessel (IHPV)	30
2.3 Electron probe micro-analysis	33
2.4 Raman spectroscopy	35
2.4 Mössbauer spectroscopy	38
2.5 Water content determination	39
2.5.1 Karl Fischer titration (KFT)	40
2.5.1 Fourier-transform infrared spectroscopy (FTIR)	41
2.6 Micropenetration viscometry	44

2.7 Concentric cylinder viscometry
2.8 Differential Scanning Calorimetry
2.8.1 Conventional DSC (C-DSC)
2.8.2 Flash DSC (F-DSC)51
2.9 Brillouin light scattering spectroscopy
2.10 Transmission electron microscopy
2.11 Small- and -wide angle X-ray scattering (SAXS and WAXS)
3. Synopsis
3.1 Are volcanic melts less viscous than we thought? The case of Stromboli basalt63
3.2. Nanoscale chemical heterogeneities control the viscosity of andesitic melts66
3.3. A viscosity model for hydrous andesitic magmas69
3.4. List of manuscripts and statement of authors' contribution
References
4. Manuscript of the thesis
4.1 Are volcanic melt less viscous than we thought? The case of Stromboli basalt88
4.2 Nanoscale chemical heterogeneities control the viscosity of andesitic magmas121
4.3 A viscosity model for hydrous andesitic magmas
List of publications

1. Introduction

1.1 Magma viscosity as a key to understanding volcanic processes

Magma is a three-phase system consisting of a multi-component silicate melt, suspended crystals, and a gas phase typically manifested as exsolved bubbles (Bowen, 1947). Among the physical properties of magma, viscosity is widely recognized as one of the most critical parameters controlling the rheological behavior of magma during ascent and eruption (Alidibirov and Dingwell, 1996; Cassidy et al., 2018; Gonnermann and Manga, 2013; Sparks, 2003). Magma viscosity regulates the transport of magma and its rheological response to decompression and deformation (Di Genova et al., 2017; Dingwell, 1996; Gonnermann, 2015; Koyaguchi and Mitani, 2005; Lautze and Houghton, 2007; Okumura et al., 2010; Papale, 1999; Vona et al., 2011; Webb and Dingwell, 1990; Zhang, 1999), ultimately modulating the eruptive style (Sparks, 2003).

Magma viscosity is primarily controlled by the temperature and composition of the liquid phase, but it is also significantly influenced by the volume fraction and shape of crystals and bubbles suspended within the melt (Friedman et al. 1963; Richet et al. 1996; Ishibashi and Sato 2007; Vetere et al. 2007; Vona et al. 2011; Gonnermann and Manga 2012; Robert et al. 2013; Sehlke et al. 2014; Chevrel et al. 2015; Campagnola et al. 2016; Di Genova et al. 2017a, 2018; Cassidy et al. 2018; Romano et al. 2020).

Numerous studies have quantified the temperature- and composition-dependent viscosity of aluminosilicate melts relevant to volcanology (Davì et al., 2009; Dingwell et al., 1996; Ishibashi and Sato, 2007; Lejeune and Richet, 1995; Liebske et al., 2003, 2005; Misiti et al., 2011; Richet et al., 1996; Stevenson et al., 1998; Vetere et al., 2007, 2008; Whittington et al., 2000, 2009). These studies demonstrate that silicate melt viscosity spans up to twelve orders of magnitude depending on temperature, chemical composition, and volatile content (Giordano

et al., 2009). Increasing temperature decreases viscosity by enhancing atomic mobility and, critically, by increasing the configurational entropy (S_{conf}) of the melt, which reflects the number of accessible structural arrangements (Adam and Gibbs, 1965). This increase in S_{conf} facilitates the cooperative rearrangement of structural units, which is the fundamental mechanism of viscous flow (Adam and Gibbs, 1965). In contrast, the presence of crystals increases viscosity, as the suspended solid phase impedes flow (Costa, 2005; Mueller et al., 2011b; Vona et al., 2011). Crystal shape also plays a critical role, as elongated or acciding crystals further increase viscosity due to stronger mechanical interactions, alignment, and interlocking within the melt (Mader et al., 2013).

The dependence of melt viscosity on chemical composition is fundamentally linked to the melt's structure, particularly the degree of polymerization of the anionic network and the distribution of Q^n species, where n indicates the number of bridging oxygens per tetrahedral unit (Mysen and Richet, 2005). This is controlled by the connectivity of tetrahedrally coordinated cations (T), such as Si, Al, Fe, and Ti, through shared oxygen atoms. When oxygen atoms are shared between two tetrahedra, termed as bridging oxygens, the melt becomes more polymerized and resistant to flow. The temperature dependence of viscosity is often non-Arrhenian, especially near the glass transition temperature (T_g) , a behavior quantified by the melt's fragility (Angell, 1995). At these lower temperatures (i.e., close to T_g), the decreasing S_{conf} exerts a dominant control on viscosity, as described by the Adam-Gibbs theory (Adam and Gibbs, 1965). At higher, superliquidus temperatures, while the energetic barriers associated with the dynamic breaking and reformation of T-O bonds contribute significantly to the activation energy for viscous flow, the process remains a cooperative rearrangement of structural units (Mysen and Richet, 2005; Webb and Dingwell, 1990). The strength of Si-O bonds, being among the highest in silicate melts, contributes significantly to the high viscosity of silica-rich melts like rhyolites (Di Genova et al., 2013). However, the presence of other

network formers (e.g., Al³⁺), whose Al-O bonds are generally weaker than Si-O bonds, and the influence of network-modifying cations (e.g., Na⁺, K⁺, Ca²⁺) and volatiles (e.g., H₂O), are also critical. These components introduce non-bridging oxygen atoms, disrupt network connectivity, and alter the energy landscape for cooperative motion, leading to melt depolymerization and a significant reduction in viscosity (Mysen and Richet, 2005; Whittington et al., 2000). This structural principle explains the strong rheological contrast between high-silica (e.g., rhyolitic) and low-silica (e.g., basaltic) melts, and underscores the critical role of water as a viscosity-reducing agent (Dingwell et al., 1996; Richet et al., 1996; Urbain et al., 1982).

The eruptive style of a volcano is primarily governed by the decompression and deformation rates, and by how efficiently the gas phase separates from the ascending melt (Cashman and Scheu, 2015; Cassidy et al., 2018; Degruyter et al., 2012; Gonnermann, 2015; Mueller et al., 2008). In this context, melt viscosity plays a central role in modulating the timescale over which a silicate melt can respond to deformation, as described by the Maxwell relaxation time:

$$\tau = \frac{\eta}{G_{\infty}} \tag{1}$$

where τ is the relaxation time, η is the dynamic viscosity of the melt, and G_{∞} is the instantaneous shear modulus of the melt, representing its purely elastic response at very short timescales (Webb and Dingwell, 1990). The Maxwell relaxation time defines the timescale required for a viscoelastic material to relax applied stress. Thus, when deformation occurs on timescales significantly shorter than τ , the melt responds elastically; if deformation timescales are longer, it allows for viscous flow. Therefore, high-viscosity melts exhibit longer relaxation times, impeding efficient gas segregation and escape (e.g., by hindering bubble coalescence and the formation of permeable pathways). This increases the potential for internal

overpressure buildup, as the melt becomes unable to dissipate stress through viscous flow and instead fails in a brittle manner, ultimately promoting explosive eruptions. In contrast, low-viscosity melts relax more rapidly, promoting efficient gas decoupling and favoring effusive behavior (Dingwell and Webb, 1990; Gonnermann, 2015; Koyaguchi and Mitani, 2005; Lautze and Houghton, 2007; Zhang, 1999).

This framework is directly connected to magma fragmentation, which marks the threshold at which magma transitions from a continuous liquid to a fragmented mixture of melt and gas, resulting in explosive volcanic activity (Cashman and Scheu, 2015; Cassidy et al., 2018; Gonnermann, 2015; Papale, 1999). Fragmentation is generally triggered by two key mechanisms: (1) the buildup of bubble overpressure due to hindered gas expansion in viscous melts (Kueppers et al., 2006; Mueller et al., 2008), and (2) the exceedance of a critical strain rate, beyond which the deformation timescale becomes shorter than the relaxation time of the melt (Dingwell, 1996; Okumura et al., 2010; Papale, 1999). In this case, the melt fails in a brittle manner, initiating fragmentation.

Therefore, changes in melt viscosity during volcanic eruptions can strongly influence the transition from effusive to explosive eruptive styles (Arzilli et al., 2019; Cashman and Scheu, 2015; La Spina et al., 2022). These changes are often driven by syn-eruptive processes that alter the physical and chemical properties of the magma during ascent. Rapid crystallization increases the crystal volume fraction, thereby increasing magma viscosity and hindering flow (Arzilli et al., 2019; Vona et al., 2011). Simultaneously, degassing and volatile loss, particularly of H₂O, lead to increased melt polymerization, further raising viscosity (Whittington et al., 2000), promoting further crystallization (Su et al., 2016). Vesiculation and bubble growth add complexity: While isolated bubbles can reduce density and potentially lower viscosity (Richet et al., 2000), high bubble fractions and bubble-crystal aggregates often increase the effective viscosity, especially when deformation is rapid (Mueller et al., 2008;

Okumura et al., 2010). Additionally, magma mixing, wall-rock assimilation, and conduit autobrecciation can introduce thermal and compositional disequilibrium, promoting crystallization or modifying melt structure, which further increases viscosity (Marshall et al., 2022). Even modest changes in viscosity (0.5–1 log units) can critically affect melt relaxation and gas retention, ultimately tipping the system toward fragmentation (Di Genova et al., 2017; Dingwell, 1996).

Previous work has shown that syn-eruptive variations in melt viscosity directly influence the explosivity and recurrence of eruptive events by regulating the rates at which overpressure is generated and released during magma ascent (Arzilli et al., 2019; Blundy and Cashman, 2001; Hammer et al., 1999). A key contributor to these changes is the rapid crystallization of micrometer-sized crystals (i.e., microlites). Numerous studies have demonstrated that syn-eruptive microlite crystallization significantly increases melt viscosity, reducing gas mobility and enhancing internal overpressure (Arzilli et al., 2019; Bamber et al., 2020; La Spina et al., 2016; Sable et al., 2006). As the crystal volume fraction approaches the maximum packing limit, the system becomes increasingly resistant to flow, favoring brittle failure and triggering the transition to explosive eruption (Cashman and Scheu, 2015; Cassidy et al., 2018; Gonnermann, 2015).

These interconnected processes underscore the highly dynamic nature of magma viscosity. It is not a static property, but one that evolves continuously in response to ongoing compositional, thermal, and textural changes occurring during magma ascent. The coupling between crystallization, degassing, and rheology plays a critical role in controlling eruption dynamics and transitions in eruptive style. Therefore, understanding how viscosity varies through space and time within volcanic systems is fundamental to accurately modelling magma transport and forecasting eruptive behavior.

1.2 The influence of nanocrystals on magma viscosity

While the effects of microlite crystallization on magma rheology are well recognized (Mader et al., 2013; Mueller et al., 2011a; Vona et al., 2011), a finer scale of complexity arises when crystallization occurs at the nanometric scale. Microlites, generally defined as crystals $<100 \,\mu\text{m}$, are ubiquitous in volcanic products and typically form in response to decompression-driven undercooling and volatile exsolution within the conduit (Andrews and Befus, 2020; Arzilli et al., 2019; Blundy and Cashman, 2001; Hurwitz and Navon, 1994; La Spina et al., 2016). Their impact on bulk viscosity depends strongly on their volume fraction (ϕ), shape, and spatial distribution (Mader et al., 2013; Mueller et al., 2011a; Vona et al., 2011). When ϕ approaches the maximum packing fraction, microlites can cause exponential increases in suspension viscosity (Mader et al., 2013).

Despite advances in modeling microlite-bearing suspensions, recent evidence reveals that nanocrystals or "nanolites" can dramatically affect magma viscosity even at volume fractions well below the packing limit. Unlike microlites, nanolites operate at the interface of crystallization and structural reorganization, and their rheological effects cannot be described by classical suspension models. Evidence from material science suggests that nanoparticle-rich suspensions exhibit nonlinear viscosity responses due to size-dependent surface and interparticle forces (Rudyak and Krasnolutskii, 2014; Sharma et al., 2016). In silicate melts, these principles translate into unexpectedly strong rheological impacts. Experimental work by Di Genova et al. (2020b) demonstrated that the formation of TiO_2 - and FeO-bearing nanocrystals can produce significant viscosity increases even at low ϕ compared to microlites (Fig. 1).

Nanolites are believed to nucleate during early stages of crystallization, under high nucleation and low growth conditions, as described by classical nucleation theory (Cormier, 2014). Nanolites are expected to be the product of that transient and incipient process that leads

to the formation of larger crystals (i.e., microlites). Therefore, their formation is promoted by magma undercooling during decompression, parallel to microlite formation but occurring on shorter timescales and smaller spatial scales (Arzilli et al., 2019; Blundy and Cashman, 2001; Hammer et al., 1999). However, studies focusing on understanding the relationship between magma undercooling and nanolite formation are still absent.

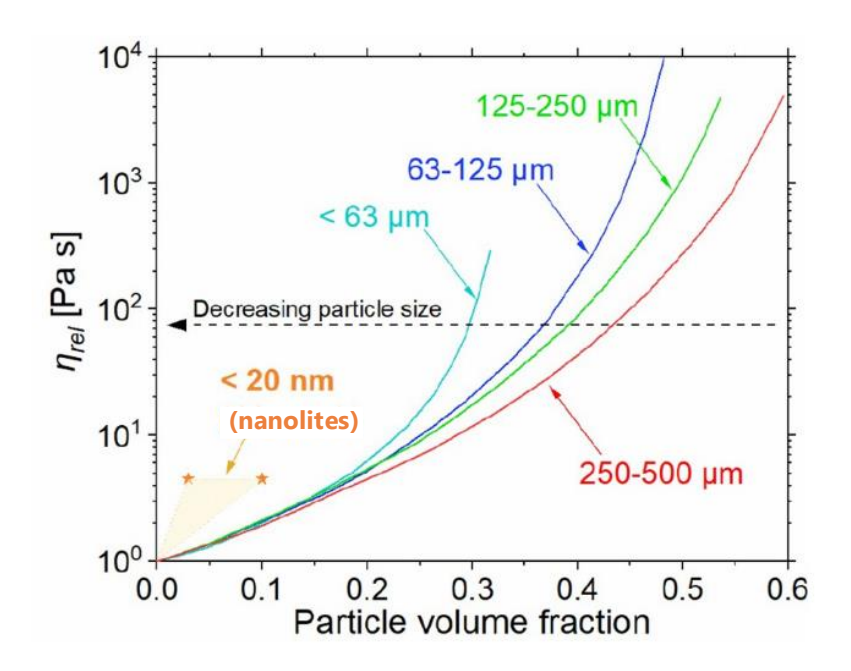


Figure 1. Dependence of the relative viscosity η_{rel} on the volume fraction of particles suspended in the carrying liquid phase. Modified after Di Genova et al. (2020b).

Recently, nanolites have been increasingly identified in volcanic products from explosive eruptions. They have been found in Shinmoedake volcano in Japan (Mujin et al., 2017; Mujin and Nakamura, 2020, 2014), Mt. Etna (Barone et al., 2016), and other volcanic systems (Knafelc et al., 2022; Thivet et al., 2023; Yoshida et al., 2023; Zellmer et al., 2016). These observations consistently associate nanolites with vesicles and quenched fragmentation textures, suggesting a potential role in bubble nucleation, strain localization, and fragmentation. However, the timing of nanolite formation and their contribution to explosivity remain under

debate (Cáceres et al., 2020; Di Genova et al., 2018, 2020a; Knafelc et al., 2022; Mujin et al., 2017; Mujin and Nakamura, 2014, 2020; Okumura et al., 2022).

Laboratory studies provide strong support for the role of nanolites in modulating viscosity. Experimental results show that even trace amounts of nano-crystallization can induce nonlinear increases in viscosity, likely due to coupled chemical and structural changes in the melt (Di Fiore et al., 2024; Di Genova et al., 2020a; Fanesi et al., 2025; Liebske et al., 2003; Okumura et al., 2022; Scarani et al., 2022; Valdivia et al., 2023, 2025). Two principal mechanisms have been proposed. First, at high viscosities near the glass transition temperature ($\eta \approx 10^8$ - 10^{13} Pa s), nanolites formation increases melt viscosity by the diffusion of iron and titanium within the initially homogenous melt to form Fe-Ti-rich nanolites. For instance, Okumura et al. (2022) proposed that the increase of the anhydrous viscosity due to magnetite nano-crystallization in andesitic magmas is well-explained by the complete depletion of iron in the melt phase. However, in this work, we show that this mechanism alone cannot explain the mechanism of viscosity increase within andesitic magmas.

The second mechanism operates at higher temperatures where melt viscosities are lower ($\eta \approx 10^{-3}$ - 10^{3} Pa s), where nanolites aggregate and entrap interstitial melt, increasing the effective solid volume (Bamber et al., 2025). This behavior has been observed during in situ heating experiments and in natural pyroclasts from the 122 CE Plinian eruption at Mt. Etna (Di Genova et al., 2020a). Similar melt entrapment effects were noted in dendritic microlite textures under water-saturated conditions (Arzilli et al., 2022), suggesting that this phenomenon may operate across multiple crystal size scales.

Together, these mechanisms reveal that nanolites increase viscosity through both physical and chemical reconfiguration, even at low crystal contents. Importantly, their effects go beyond what is predicted by current suspension models, which are typically calibrated on nanolite-free compositions. As nanolites are increasingly recognized in both experimental and

natural samples, their inclusion in future rheological models is critical for improving our understanding of magmatic processes and eruption dynamics.

1.3 Limitations of existing viscosity models and the need for a new framework

Several studies spanning a wide range of melt compositions, including basaltic (Bouhifd et al., 2004; Di Genova et al., 2020b; Scarani et al., 2022; Valdivia et al., 2023), andesitic (Liebske et al., 2003; Okumura et al., 2022; Pereira et al., 2024; Richet et al., 1996; Vetere et al., 2006), tephri-phonolitic-foiditic (Fanesi et al., 2025; Kleest et al., 2020), and rhyolitic melts (Cáceres et al., 2024; Di Genova et al., 2017) have significantly improved our understanding of the compositional and temperature controls on silicate melt viscosity. These works have enabled the derivation of isochemical, temperature-dependent viscosity parametrizations by fitting experimental viscosity data. The two most popular parametrizations are the Vogel-Fulcher-Tammann (VFT) (Fulcher, 1925; Tammann and Hesse, 1926; Vogel, 1921) and the Mauro-Yue-Ellison-Gupta-Allan (MYEGA) (Mauro et al., 2009) equations. The VFT equation provides an empirical approach to capture the non-Arrhenian behavior of silicate melt viscosity as a function of temperature:

$$log_{10}\eta(T) = A_{VFT} + \frac{B_{VFT}}{T - C_{VFT}} \tag{2}$$

where A_{VFT} , B_{VFT} , and C_{VFT} are empirical fitting parameters unique to each melt composition. The parameter A_{VFT} represents the logarithm of viscosity at infinite temperature in Pa s, effectively describing the lower limit of viscosity (i.e., $\log \eta_{\infty}$). The B_{VFT} term is related to a pseudo-activation energy for viscous flow, reflecting the energy barrier that must be overcome

for structural rearrangement within the melt. The parameter C_{VFT} parameter is the temperature in K at which viscosity becomes infinite (Russell et al., 2022).

In contrast to the empirically based VFT formulation, the MYEGA equation provides a physically grounded alternative for describing the non-Arrhenian temperature dependence of silicate melt viscosity. Unlike VFT, which relies on empirical fitting constants without direct physical interpretation, MYEGA is derived from the temperature dependence of configurational entropy, which links the atomic-scale structure of glass-forming liquids to their macroscopic transport properties (Mauro et al., 2009). It is expressed as:

$$log_{10}\eta(T) = log_{10}\eta_{\infty} + (12 - log_{10}\eta_{\infty}) \frac{T_g}{T} exp\left[\left(\frac{m}{12 - log_{10}\eta_{\infty}} - 1\right)\left(\frac{T_g}{T} - 1\right)\right]$$
 (3)

where η_{∞} is the logarithmic viscosity at infinite temperature, T_g is the glass transition temperature, and m is the melt fragility (Eq. 4) defined as the slope of viscosity curve evaluated at T_g (Angell, 1995):

$$m = \frac{\partial log_{10}\eta}{\partial T_g/T}\bigg|_{T=T_g} \tag{4}$$

Melt fragility (m) is a key rheological parameter that, when combined with T_g , enables the MYEGA parametrization to describe viscosity variations across a broad temperature range (Langhammer et al., 2022; Mauro et al., 2009). It is particularly valuable from a practical point of view, as it enables the extrapolation of viscosity to eruptive conditions using two parameters (m and T_g) that can be derived experimentally, where direct measurements are challenging due to the rapid degassing and crystallization that volcanic melts experience during viscosity experiments.

Additionally, using extensive experimental datasets, several authors have developed general-purpose models that predict melt viscosity as a function of composition and water content across a broad temperature range (Giordano et al., 2008; Hui and Zhang, 2007; Langhammer et al., 2022). For example, the model by Giordano et al. (2008) was constructed using a data set of 1774 viscosity measurements, corresponding to anhydrous (N=932) and hydrous (N=842) compositions. In contrast, the Langhammer et al. (2022) model employed 3482 data points from 153 different compositions, encompassing virtually the entire chemical space of terrestrial magmas, as well as analogues of some extraterrestrial melts. Despite their broad applicability, these widely used models are primarily based on experimental datasets that assume the melts are homogeneous and free of crystals and bubbles. However, this assumption does not hold in many natural systems, particularly in anhydrous and hydrous iron-rich melts, where nanoscale heterogeneities and early-stage crystallization can significantly affect viscosity (Fanesi et al., 2025; Valdivia et al., 2025, 2023).

Recent work has demonstrated that during high-temperature experiments, Fe-Ti-rich nanolites can form rapidly and remain undetected by standard SEM-like techniques due to their extremely small size, typically less than 100 nm (Bondar et al., 2025; Di Genova et al., 2020a; Fanesi et al., 2025; Scarani et al., 2022; Valdivia et al., 2023, 2025). Moreover, synexperimental water loss further complicates viscosity determination. Previous studies have shown that structurally bound water can be progressively lost during high-temperature experiments, especially under prolonged heating or during multiple measurement cycles (Fanesi et al., 2025; Valdivia et al., 2023). This dehydration not only increases melt viscosity but also promotes nanolite formation by enhancing undercooling. This dual effect of dehydration and crystallization skews the measured viscosity-temperature relationship, leading to biased estimates of both viscosity and key rheological descriptors such as the glass transition temperature (T_g) and melt fragility (m). These effects are especially pronounced in Fe-rich

compositions where degassing and nanolite nucleation occur simultaneously, creating irreversible changes in melt structure. When such measurements are affected by nanoscale crystallization and water loss, the derived values of T_g and m become unreliable. As a result, any viscosity extrapolations based on these parameters are inherently flawed. This, in turn, undermines the accuracy of models used to simulate volcanic processes and diminishes the reliability of probabilistic forecasts of eruptive behavior.

To overcome these challenges, recent studies (Bondar et al., 2025; Di Genova et al., 2020a, 2023; Fanesi et al., 2025; Scarani et al., 2022; Valdivia et al., 2023, 2025) have adopted a multipronged approach integrating SEM-BSE imaging, FTIR, Raman, Mössbauer, and Brillouin spectroscopy to screen samples before and after viscosity measurements. This combination of techniques enables the detection and exclusion of nanolite-contaminated data, ensuring that viscosity calibrations are based exclusively on structurally pristine, nanolite-free glasses. Such rigorous screening has become essential for improving the reliability of viscosity models in volatile-rich, nanolite-prone systems, where even minor undetected crystallization can severely bias rheological interpretations. In this context, determining the T_g using differential scanning calorimetry (DSC) offers a key advantage, as it allows for rapid acquisition of thermo-rheological data without prolonged exposure to high temperatures, thereby minimizing the risk of syn-experimental nano-crystallization and degassing compared to conventional high-temperature viscometry.

Prior empirical models have inferred *m* using relationships with sound velocity data (Cassetta et al., 2021; Novikov et al., 2005; Novikov and Sokolov, 2004; Sokolov et al., 2007), the Raman Boson peak position (Cassetta et al., 2021), or with structural proxies such as the number of non-bridging oxygen atoms per tetrahedrally coordinated cation (NBO/T) (Giordano and Dingwell, 2003; Malfait and Sanchez-Valle, 2013). However, recent work (Fanesi et al., 2025; Valdivia et al., 2025, 2023) shows that the values derived from these correlations

(Cassetta et al., 2021; Malfait and Sanchez-Valle, 2013; Novikov et al., 2005; Novikov and Sokolov, 2004; Sokolov et al., 2007), as well as from global viscosity models (Giordano et al., 2008; Hui and Zhang, 2007; Langhammer et al., 2022), does not accurately predict the crystal-free viscosity of andesitic and basaltic compositions (Di Genova et al., 2017, 2020b; Scarani et al., 2022; Valdivia et al., 2023, 2025).

In response to these limitations, this thesis adopts a refined methodology for modelling volcanic melt viscosity that combines (1) rigorous screening using a suite of spectroscopic and imaging techniques to detect and exclude nanolite-bearing or structurally heterogeneous samples from viscosity measurements, and (2) viscosity calibration based exclusively on crystal-free data.

Within this framework, we present newly calibrated viscosity models for both basaltic and andesitic melts, grounded in a dataset filtered for nanolite contamination. Additionally, we introduce two new empirical equations that correlate melt fragility (*m*) with the elastic properties of glasses, as determined by Brillouin spectroscopy. These equations are developed separately for transition metal-rich and transition metal-free compositions, enhancing the accuracy of viscosity predictions across a broad range of natural magmatic systems.

Building on these models, we further explore the impact of nanolites on silicate melt rheology by integrating viscosity measurements with high-resolution nanoscale characterization techniques, including transmission electron microscopy (TEM), small-angle X-ray scattering (SAXS), and wide-angle X-ray scattering (WAXS). These complementary methods enable us to resolve the formation of nanocrystals and associated nanoscale chemical heterogeneities that develop during early crystallization stages. Our results reveal that even minimal nanolite formation can induce significant viscosity increases through structural reorganization and element redistribution, effects that cannot be accounted for by bulk composition or crystal volume alone. By capturing this previously unresolved processes, this

work establishes a new, physically grounded and experimentally validated framework for estimating magma viscosity, thereby improving the modeling of magma ascent, degassing, and fragmentation for magmas at volcanic systems that are volatile-rich and prone to nanocrystallization.

2. Analytical techniques and methods

2.1 Synthesis of anhydrous starting materials

The anhydrous starting materials employed in this study included both natural and synthetic glasses, formulated to replicate the compositions of Stromboli basalt (Italy) and Sakurajima andesite (Japan), respectively. Additionally, glasses with variable concentrations of transition metals were synthesized to broaden the compositional range of the materials examined.

For the analysis of the Stromboli basalt, ash- to lapilli-sized pyroclasts were selected from the low-porphyritic (LP) deposit produced during the July-August 2019 eruption of Stromboli volcano. A homogeneous, anhydrous, crystal- and bubble-free glass was first prepared by crushing and melting the natural samples in a platinum crucible at 1400 °C for four hours using a box furnace. The resulting glass was then crushed to a fine powder, thoroughly mixed, and subjected to a second melting under the same conditions to achieve chemical homogenization.

For the study of andesitic melts, synthetic glasses were prepared by mixing high-purity chemical reagents (SiO₂, TiO₂, Al₂O₃, Fe₂O₃, MnO, MgO, CaCO₃, Na₂CO₃, K₂CO₃ and P₂O₅) according to their target compositions determined through molar mass calculations. The powdered reagents were combined in an agate mortar with ethanol and manually ground for approximately 45 minutes. After mixing, the material was dried under infrared light and then heated overnight at 900 °C in an alumina crucible to remove CO₂ from the carbonate phases. The decarbonated mixture was subsequently transferred to a platinum crucible and melted at 1400 °C for 24 hours. The melt was rapidly quenched in water to prevent crystallization. The quenched material was crushed into a powder using a stainless-steel percussion mortar,

manually homogenized, and then subjected to a second melting at 1400 °C for four hours, followed by rapid quenching to obtain a homogeneous glass.

In both the natural and synthetic systems, portions of the final glasses were ground into powders and separated into two grain size fractions by sieving, targeting particles smaller than $100 \mu m$, and between 100 and $250 \mu m$. These two size fractions were then mixed in equal weight proportions to minimize porosity during the subsequent high-temperature and high-pressure synthesis of water-bearing glasses.

2.2 Synthesis of hydrous glasses

At atmospheric pressure, the solubility of water in silicate melts is extremely limited, resulting in rapid degassing and the generation of bubbles rather than the formation of homogeneous hydrous glasses (Botcharnikov et al., 2015; Dixon et al., 1995; Lesne et al., 2011; Moore et al., 1998; Stabile et al., 2018; Vetere et al., 2010). To overcome this limitation and to ensure that water is fully incorporated into the silicate network, experiments must be conducted under high-pressure conditions. In this study, both a piston-cylinder apparatus and an internally heated pressure vessel (IHPV) were used to reproduce the pressure-temperature conditions under which magmas naturally retain volatiles prior to eruption.

The anhydrous glass powders used for hydrous synthesis were previously processed and sieved into two grain-size fractions, which were combined in equal proportions to optimize packing (Section 2.1). To hydrate the samples, distilled water was added incrementally to the dry powder, and the mixture was loaded into Pt or Au₈₀Pd₂₀ capsules of 4.6 mm inner diameter, 5.0 mm outer diameter, and 10-20 mm length. The Au₈₀Pd₂₀ alloy was preferred over Pt for iron-bearing compositions for its to minimize iron loss during high-temperature experiments (Pichavant et al., 2013). After sealing by arc welding, the capsules were weighed and then

heated overnight at 150 °C to test for leakage. Capsules that maintained their mass were selected for subsequent high-pressure synthesis.

2.2.1 Piston cylinder apparatus

The end-loaded piston-cylinder apparatus is a well-established technique for conducting high-pressure and high-temperature experiments that replicate conditions in the Earth's lower crust and upper mantle, reaching temperatures up to ~2000 °C and pressures up to ~5 GPa (Boyd and England, 1960). The apparatus consists of a stacked configuration composed of three main components: a lower bridge, a pressure vessel, and a top plate (Fig. 2). The pressure vessel, often referred to as the "bomb", is made of concentric steel cylinders that surround a tungsten carbide (WC) core with a central cavity. The sample assembly is inserted into this cavity, and pressure is applied uniaxially via a WC piston driven by hydraulic oil. At the same time, the bomb is compressed by a much larger force (the "end load") in order to increase its yield strength.

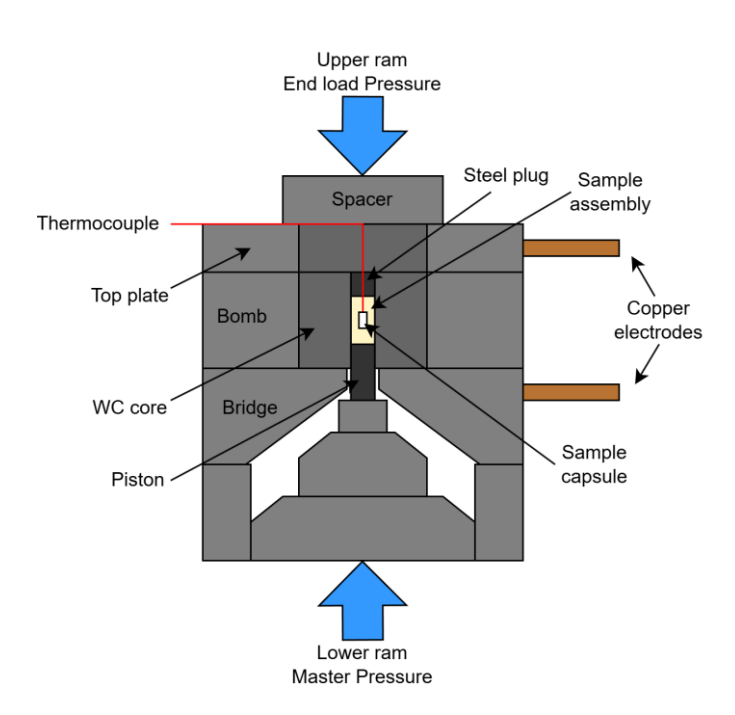


Figure 2. Schematic diagram of the end-loaded set-up used for piston cylinder experiments. Details of sample assembly in Fig. 3.

Pressure is generated hydraulically via a master ram, which transmits uniaxial force through a WC piston. The nominal pressure (P) is calculated from the force (F) and the cross-sectional area (A) of the piston according to:

$$P = \frac{F}{A} \tag{5}$$

In this study, we used two assembly sizes: ½" and ¾". For these configurations, pressure values were corrected using fixed friction coefficients of 18% and 20%, respectively, to account for force losses due to internal sliding and deformation within the assembly. These corrections were derived from prior calibrations using the same assembly design.

The high-pressure cell assembly (Fig. 3) consisted of concentric layers of talc, Pyrex, and alumina (Al₂O₃), designed to efficiently transmit pressure while minimizing thermal gradients (Johannes et al., 1971). The graphite heater, shown as cylindrical in Fig. 3, actually had a conical inner shape tapering toward both ends to increase resistance and ensure a uniform temperature around the sample. Temperature was monitored using a Type S thermocouple (Pt-Pt₉₀Rh₁₀) placed in contact with the capsule. Heating was achieved by passing current through copper electrodes connected to the graphite heater via steel contact plates (Fig. 2).

Experiments were conducted at the Bayerisches Geoinstitut in Bayreuth (BGI), in Germany, using pressures of 0.5-1.5 GPa and temperatures between 950 and 1150 °C for 12 to 24 hours, depending on the melt composition and desired water content. These conditions were selected to ensure complete hydration of the melt while preventing degassing or crystallization, based on published solubility models (Behrens et al., 2009; Botcharnikov et al., 2015, 2007). The redox conditions were controlled intrinsically by the use of graphite and other assembly materials, maintaining oxygen fugacity slightly below the NNO buffer (f_{0_2} < NNO).

At the end of each run, power was shut off to quench the melt rapidly at an estimated rate of ~100 K s⁻1, while pressure was maintained using an automated controller to avoid degassingor vesiculation during cooling. After vitrification, the sample was decompressed slowly to ambient pressure to minimize fracturing. Capsules were then sectioned and inspected for bubbles, nanolites, or crystals prior to further analysis.

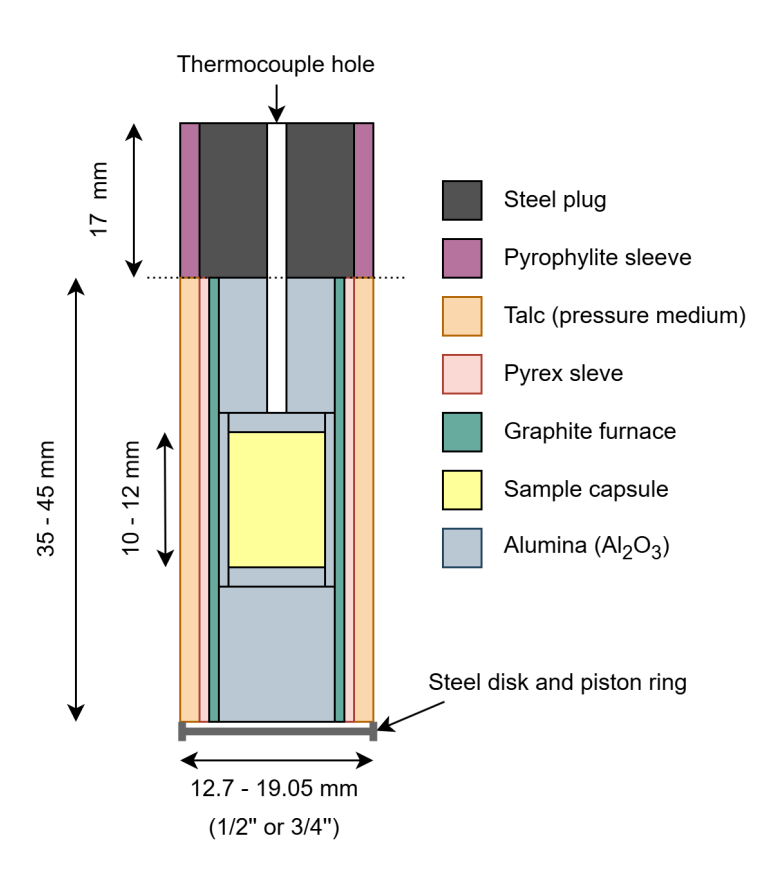


Figure 3. Schematic diagram of the piston cylinder assembly used in this study. Dimensions corresponding to $\frac{1}{2}$ " and $\frac{3}{4}$ " assembly sizes, respectively.

2.2.2 Internally heated pressure vessel (IHPV)

The internally heated pressure vessel (IHPV) is a gas-medium apparatus designed to simulate the shallow crustal storage conditions of magmas under volatile-saturated environments. It is particularly well suited for synthesizing hydrous silicate melts at low to moderate pressures (≤ 0.5 GPa) and provides excellent control over temperature, pressure, and

oxygen fugacity (Holloway et al., 1992). In contrast to solid-media systems, pressure in the IHPV is applied isostatically by compressed argon gas, which ensures hydrostatic conditions around the sample.

Andesitic hydrous glasses were synthesized using the internally heated pressure vessel (IHPV) apparatus at the Bayerisches Geoinstitut in Bayreuth (BGI) in Germany (Fig. 4). This vessel was manufactured by Harwood Inc. (Walpole, Massachusetts, USA) and is rated to a maximum pressure of 150,000 psi (> 1 GPa). The pressure chamber is made from two concentric steel shells and cooled by cooling water from the outside during the experiments. The autoclave is fitted with an internal, two-zone resistive furnace made of Mo wire that allows precise temperature control with an accuracy better than ±2 °C.

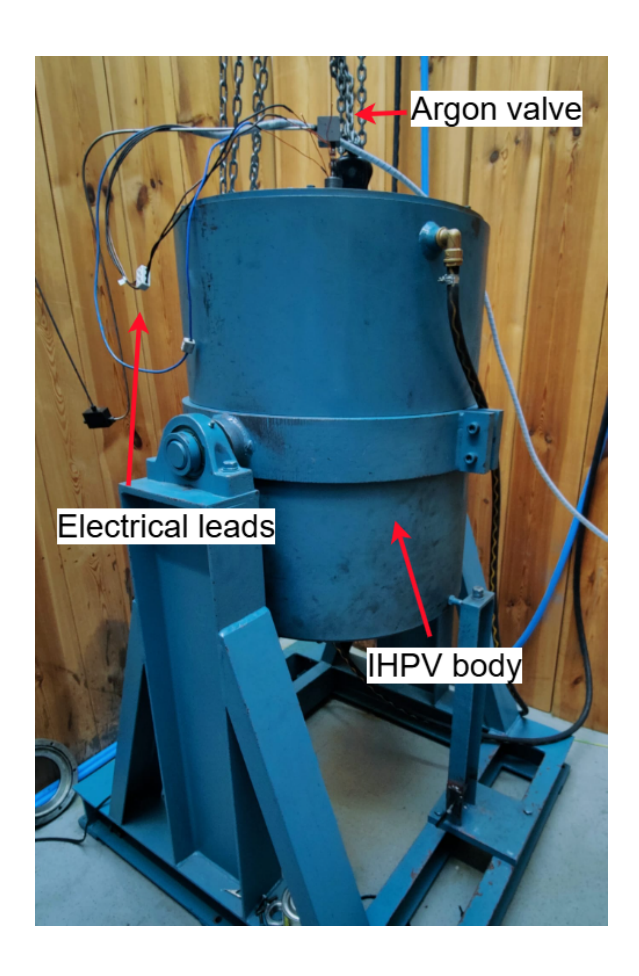


Figure 4. Photography of the internally heated pressure vessel (IHPV) apparatus used at the Bayerisches Geoinstitut (BGI) in Bayreuth, Germany.

The sample capsule is suspended vertically in the hot zone, hanging from a platinum wire as illustrated in Fig 5. Temperatures are monitored using two Type S thermocouples (Pt-Pt₉₀Rh₁₀) placed adjacent to the capsule, and pressure is generated by a membrane compressor connected to an argon tank.

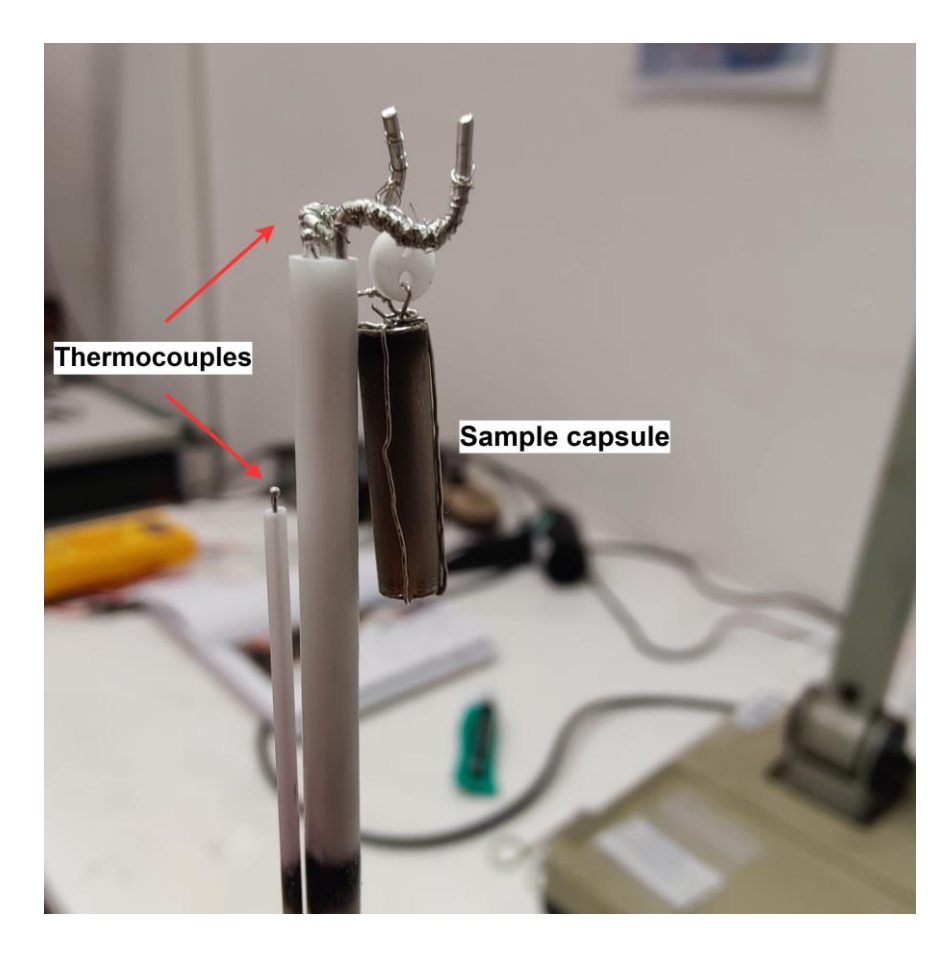


Figure 5. Experimental setup showing an Au₈₀Pd₂₀ sample capsule (right), suspended by a platinum wire, adjacent to two Type S thermocouples (left).

In this study, samples were either stacked or loaded individually, and synthesis was performed at 3 to 5 kbar and 1250 °C for 24 hours under relatively oxidizing conditions (f_{O_2} = NNO +2.6 ± 0.5), as determined by Schuessler et al. (2008). Rapid quenching was achieved by electrically melting the platinum suspension wire, causing the capsule to drop into a cooler zone of the pressure vessel and achieving a cooling rate of approximately 150 K s⁻¹ at isobaric pressure.

2.3 Electron probe micro-analysis

The major element compositions of the synthesized glasses were determined using Electron Probe Micro-Analysis (EPMA) with a JEOL JXA-8200 electron microprobe at the Bayerisches Geoinstitut (BGI) in Germany (Fig. 6a). EPMA is a type of Scanning Electron Microscope (SEM) optimized for chemical microanalysis via characteristic X-ray emission, providing higher precision and accuracy than standard SEM equipped with Energy Dispersive Spectrometry (SEM-EDS). Unlike SEM-EDS, which collects a broad range of X-ray energies simultaneously, EPMA uses multiple Wavelength Dispersive Spectrometers (WDS) to detect X-rays with high spectral resolution, allowing for the precise quantification of major and minor elements (Rinaldi and Llovet, 2015).

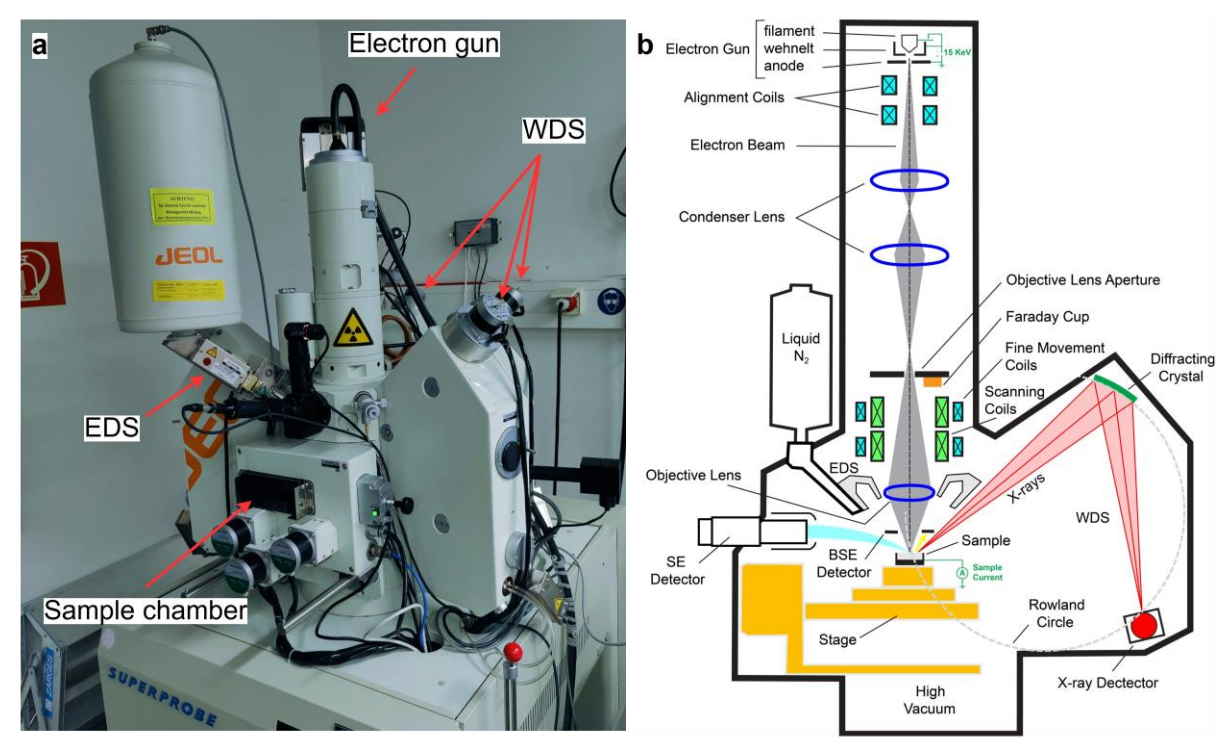


Figure 6. (a) Electron Probe Microanalyzer (EPMA) instrument showing three of the five wavelength-dispersive spectrometers (WDS) mounted on the system. (b) Schematic diagram illustrating the internal configuration of an EPMA, including the electron gun, sample stage, diffracting crystal, and X-ray detector arranged along the Rowland circle geometry (adapted from UCLA.edu).

The analytical advantage of EPMA lies in its ability to resolve overlapping peaks and to detect minor and trace elements with high precision. This is achieved by diffracting X-rays through specialized crystals that isolate specific wavelengths based on Bragg's law:

$$n\lambda = 2d\sin\theta \tag{6}$$

Here, n is the diffraction order, λ is the X-ray wavelength, d is the lattice spacing of the crystal, and θ is the diffraction angle. The geometry of the system is governed by the Rowland circle (Fig. 6b), an arrangement in which the sample (X-ray source), the curved diffracting crystal, and the detector are all positioned on the circumference of a fixed circle. This setup ensures constructive interference at specific angles, thereby focusing only X-rays of the target wavelength onto the detector (Burany, 2003).

Due to the physical constraints of diffraction geometry, no single crystal can span the entire X-ray wavelength range required for multi-element analysis. For this reason, the JEOL JXA-8200 is equipped with five WDS channels, each fitted with crystals of varying interplanar spacing, such as LiF (2d = 4.026 Å), PET (2d = 8.742 Å), and TAP (2d = 25.9 Å), to enable simultaneous detection of multiple elements.

Prior to analysis, glass samples were embedded in epoxy, polished to optical smoothness, and coated with a thin carbon layer to ensure conductivity. Analyses were performed at 15 kV accelerating voltage and 5 nA beam current, using a 10 µm defocused beam to mitigate alkali migration and beam damage. Each element was measured for 20 seconds, and between 10 and 30 analytical points were acquired per sample to assess chemical homogeneity. To reduce potential elemental loss during analysis, sodium and potassium were measured first, following best practices outlined by Hughes et al., (2019).

Calibration was achieved using synthetic mineral standards including wollastonite (Si, Ca), periclase (Mg), hematite (Fe), spinel (Al), orthoclase (K), albite (Na), manganese titanate (Mn, Ti), and apatite (P). Prior to data acquisition, each sample area was inspected under backscattered electron (BSE) imaging mode to confirm the absence of microlites, vesicles, or other heterogeneities.

2.4 Raman spectroscopy

Raman spectroscopy was employed in this study to confirm the amorphous nature of synthesized glasses, and to corroborate the presence of dissolved water in the silicate network. Raman spectroscopy probes the vibrational structure of silicate networks by measuring the inelastic scattering of monochromatic light. When photons from the laser interact with the sample, the majority are scattered elastically (Rayleigh scattering; Fig. 7a), meaning they retain their original energy and wavelength. A small fraction of photons, however, are scattered inelastically, exchanging energy with the vibrational modes of the material ($v_{vibration}$). In Stokes scattering, the photon loses energy to the sample, resulting in scattered light at lower frequency (Fig. 7b). In anti-Stokes scattering, the photon gains energy from vibrationally excited states in the sample, resulting in scattered light at higher frequency (Fig. 7c). The Raman shift (v_{Raman}) is defined as:

$$v_{Raman} = v_0 \pm v_{vibration} \tag{7}$$

where the v_0 is the frequency of the incident laser and $v_{vibration}$ corresponds to molecular vibrational frequencies.

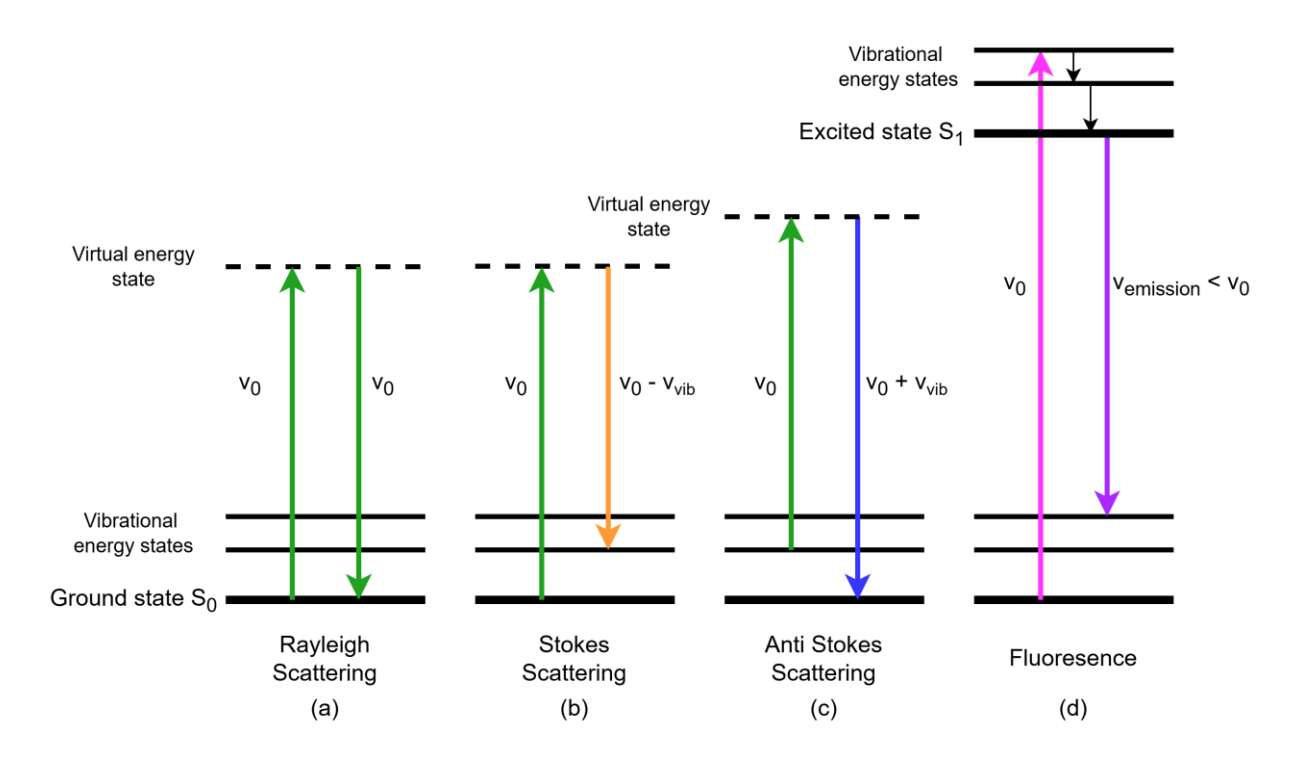


Figure 7. Schematic representation of (a) Rayleigh scattering (elastic), (b) Stokes scattering (inelastic), (c) Stokes scattering (inelastic), and (d) Fluorescence effect.

The intensity of Raman scattering (I_R) is inversely proportional to the fourth power of the laser wavelength as shown in Eq. 8:

$$I_R \propto \frac{1}{\lambda^4}$$
 (8)

This means that shorter-wavelength lasers are more efficient at generating Raman signals. However, they also tend to enhance fluorescence, an unwanted background emission that can obscure the relatively weak Raman signal (Fig. 7d). In natural and experimental volcanic glasses, which often contain Fe-bearing species and other fluorescence-inducing components (e.g., Mn), laser wavelength selection is critical. The 532 nm laser provides an optimal balance: it generates a strong Raman signal while maintaining moderate fluorescence levels, making it particularly suitable for analyzing volcanic silicate glasses (Bondar et al., 2025; González-García et al., 2020).

Room temperature Raman spectra were acquired using a WITec alpha300R confocal Raman imaging microscope at the Institute of Non-Metallic Materials, TU Clausthal, Germany (Fig. 8). Measurements were performed with a 100× objective, using a 532 nm laser operating at a power of 10 mW. Spectra were acquired using an integration time of 10 s and an accumulation count of 5. Spectral ranges included the 10-1300 cm⁻¹ region, covering the silicate network vibrational modes (bending and stretching of the Si-O bond), and the 2700-4000 cm⁻¹ region, where the O-H stretching vibrations related to water incorporation are observed.

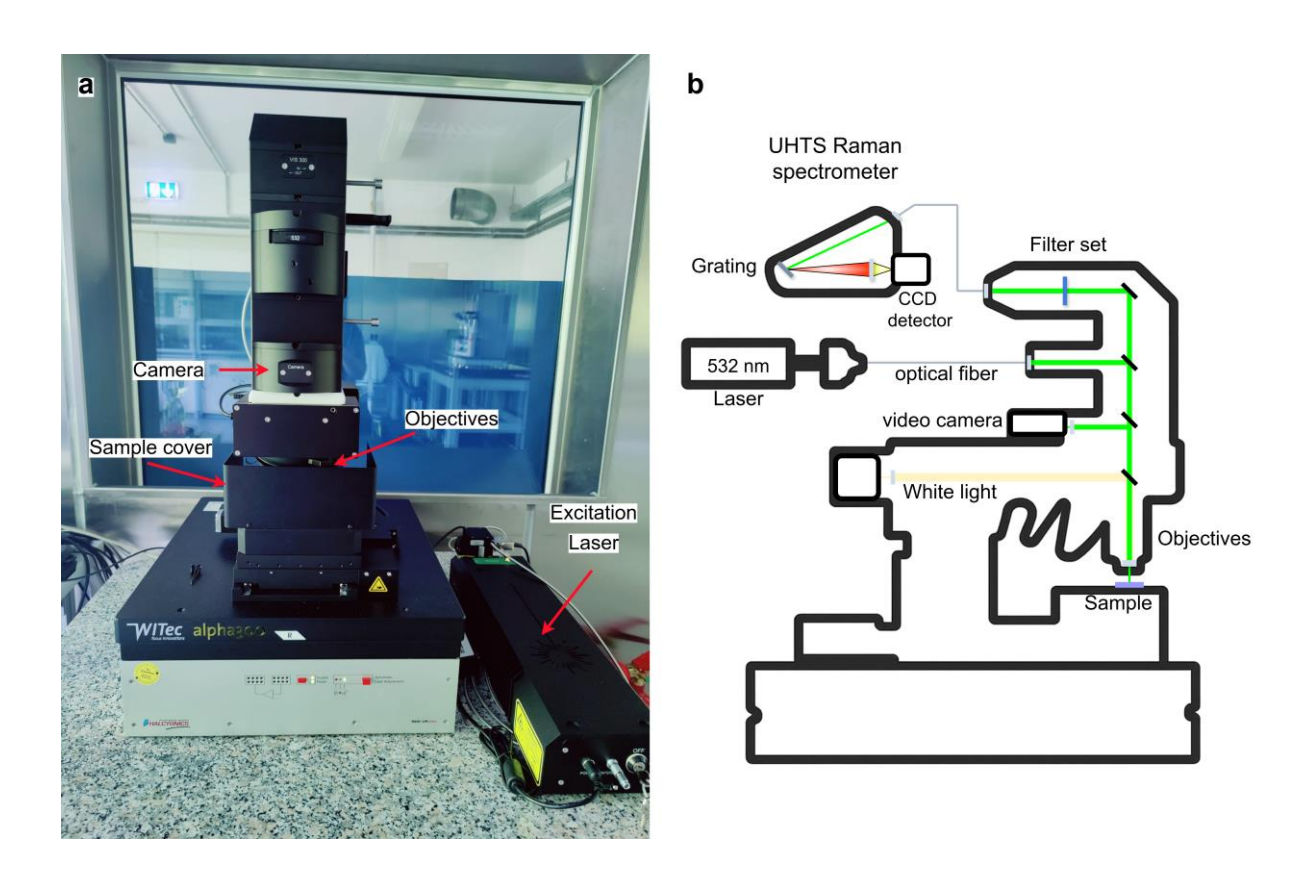


Figure 8. Configuration of the confocal Raman spectroscopy system used in this study. (a) Photograph of the WITec alpha300R confocal Raman imaging microscope, equipped with a 532 nm laser. (b) Schematic diagram of the optical pathway of the system, illustrating the laser excitation source, beam routing through the objective lenses, sample interaction, and collection of the Raman signal through the filter set, diffraction grating, and CCD detector.

Additionally, high-temperature Raman spectra were acquired using a Renishaw InVia Qontor Raman spectrometer with a heating plate at the CEMHTI, Orleans (France). Spectra

were collected using a 20× NA 0.35 objective in the ranges between 150-2000 cm⁻¹. Acquisition parameters included an integration time of 60 seconds, and a laser power of 20 mW.

2.4 Mössbauer spectroscopy

Mössbauer spectroscopy was employed to determine the oxidation state of Fe $(Fe^{3+}/Fe^{2+} \text{ ratio})$ in the samples, both before and after experimental treatments. The technique is based on the recoil-free emission and absorption of gamma (γ) radiation by ⁵⁷Fe nuclei in a solid matrix known as the Mössbauer effect (Mössbauer, 1958). This method provides detailed information on the chemical, structural, and magnetic environment of Fe atoms, and is widely used to resolve oxidation state, spin state, and coordination geometry.

A typical Mössbauer spectrometer consists of a γ -ray source, sample holder (absorber), and detector (Fig. 9). By moving the source relative to the sample at controlled velocities, the energy of the emitted monochromatic γ -rays is modulated via the Doppler effect. The spectrum, recorded as count rate versus source velocity (mm s⁻¹), exhibits characteristic absorption features (dips) at velocities corresponding to resonant energy levels of the Fe nuclei. These features arise from hyperfine interactions between the nucleus and its electronic and magnetic environment, specifically the isomer shift (sensitive to electron density and oxidation state), quadrupole splitting (related to electric field gradient and site symmetry), and, if present, magnetic hyperfine splitting (due to internal or external magnetic fields).

Measurements were conducted at the Bayerisches Geoinstitut (BGI), University of Bayreuth, Germany. Glass samples of approximately 4 mm diameter and 500-600 μm thickness were analyzed at room temperature (293 K) using a constant acceleration Mössbauer spectrometer equipped with a high specific activity ⁵⁷Co point source (370 MBq) embedded in a 12 μm thick Rh matrix (Fig. 9). The velocity scale was calibrated against a 25 μm thick α-Fe

foil, and data were collected over a velocity range of ± 5 mm s⁻¹, with acquisition times of 2-3 days per sample.

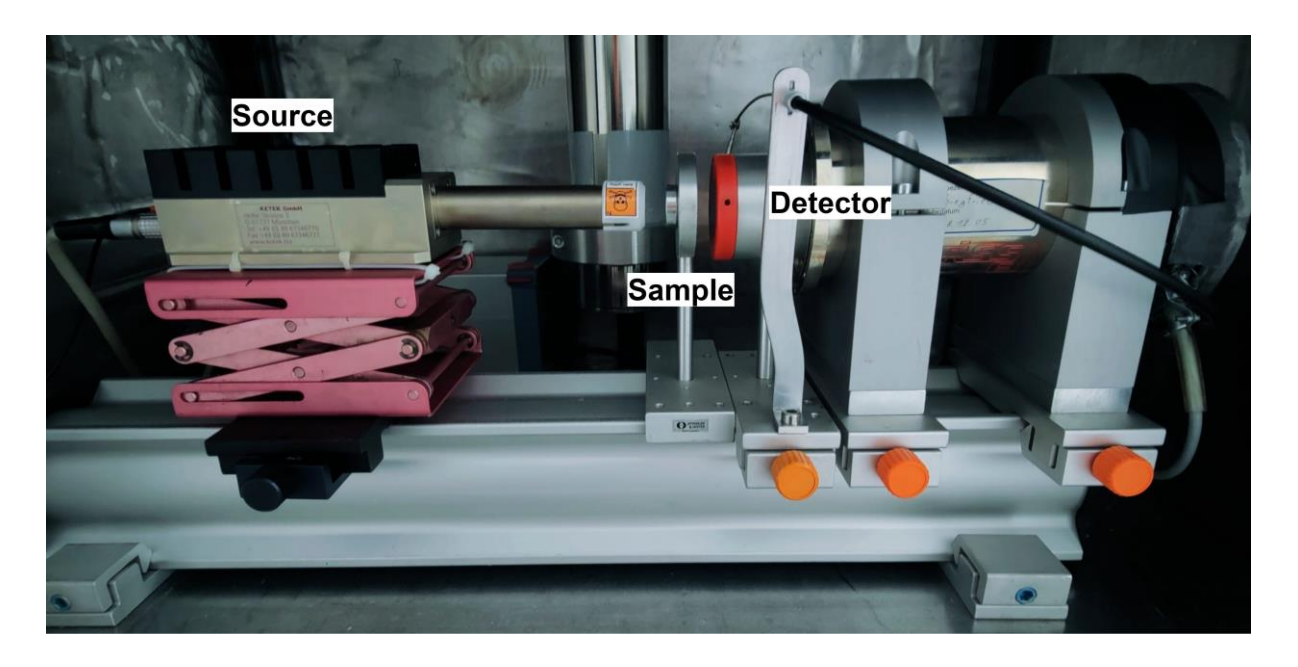


Figure 9. Setup of the Mössbauer spectrometer used in this study. Photograph of the constant acceleration Mössbauer spectrometer, showing the 57 Co γ -ray source, sample holder, and detector in transmission geometry.

The collected Mössbauer spectra were fitted using the full transmission integral method implemented in the MossA software (Prescher et al., 2012). Spectra were deconvoluted into Lorentzian doublets corresponding to Fe²⁺ and Fe³⁺ environments. The Fe³⁺/Fe²⁺ ratio was calculated from the relative area of the fitted components, with corrections applied for potential effects related to line shape, sample thickness, and recoil-free fraction.

2.5 Water content determination

The accurate determination of the water content in the synthesized glasses is essential, as dissolved H₂O significantly affects melt structure and physical properties such as viscosity. Thus, precise water quantification is particularly important for developing viscosity models

capable of accurately predicting melt behavior across a wide range of water concentrations. In this study, water content was measured using two complementary techniques: Karl Fischer titration (KFT), providing absolute H₂O concentrations, and Fourier-transform infrared spectroscopy (FTIR), offering additional insight into water speciation within the glass network.

2.5.1 Karl Fischer titration (KFT)

Karl Fischer Titration (KFT) was used to determine the absolute water content of selected glass samples. KFT is a coulometric technique based on the quantitative reaction of water with iodine (Eq. 9):

$$I_2 + SO_2 + H_2O \leftrightarrow 2HI + SO_3 \tag{9}$$

Iodine is generated electrolytically at the anode according to Eq. 10:

$$2I^- \leftrightarrow I_2 + 2e^- \tag{10}$$

Because one mole of iodine reacts stoichiometrically with one mole of water, the water content can be directly calculated from the charge required for electrolysis, with 1 mg of H_2O corresponding to 10.71 coulombs.

Glass samples (~20 mg) were finely crushed and heated in an induction coil at a rate of 100 °C min⁻¹ (Fig. 10), following the method of Behrens et al. (1996). Water released during heating was measured using a Mitsubishi CA-05 coulometer with pyridine-free reagents (Aquamicron AS and Aquamicron CS). After sample loading, the titration was started following a 2-minute purge to remove surface-adsorbed water, and continued until the sample

reached 1300 °C. This method provides absolute H_2O content with an analytical uncertainty of ± 0.1 wt%.

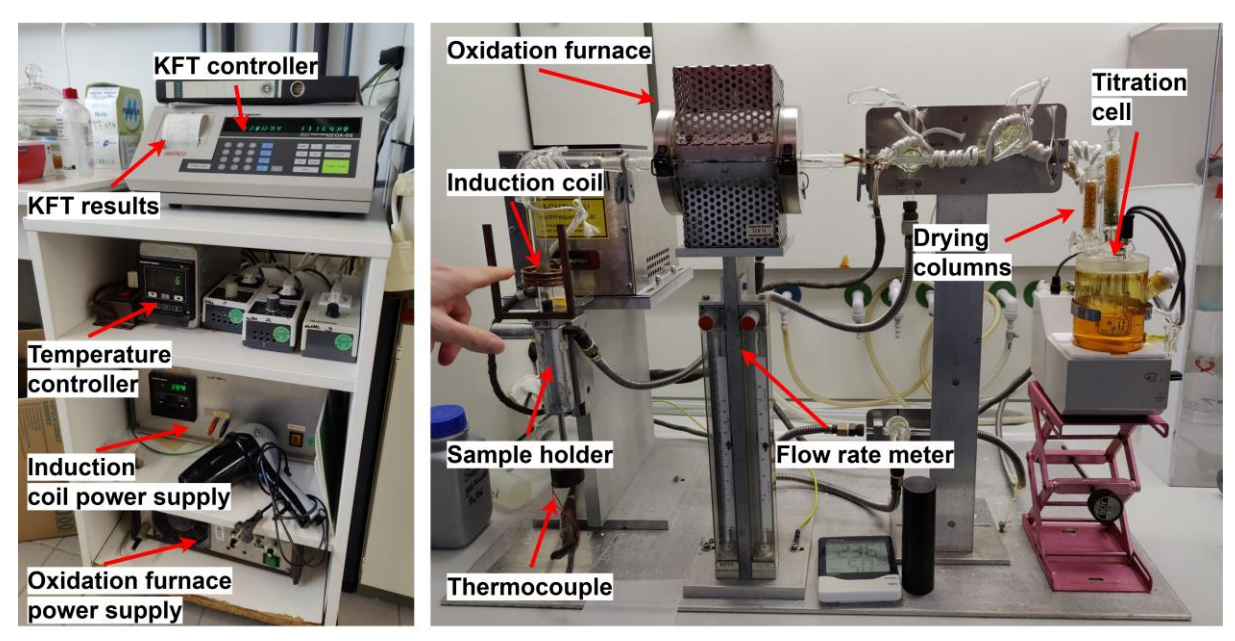


Figure 10. Setup of the Karl Fischer titration (KFT) system used in this study. The system consists of (left) the KFT controller, temperature and power supply units, and (right) the sample heating line including an oxidation furnace, induction coil with sample holder, thermocouple, flow rate meter, drying columns, and coulometric titration cell.

2.5.1 Fourier-transform infrared spectroscopy (FTIR)

In this study, Fourier-transform infrared spectroscopy (FTIR) was used to determine the water content of the synthesized glasses, both before and after experiments. Specifically, it was employed to quantify both molecular water (H₂O_{mol}) and hydroxyl groups (OH⁻) based on their characteristic absorption vibrational bands.

FTIR is a vibrational spectroscopic technique that records high-resolution infrared absorption spectra over a broad spectral range. The method operates by passing an infrared light beam through an interferometer, where it is split into two beams by a beam splitter (Fig. 11). One beam reflects off a fixed mirror, while the other reflects off a moving mirror. The beams are recombined, creating a modulated beam, which is then directed through the sample. As the light passes through the sample, a portion is absorbed at specific wavelengths

corresponding to the vibrational energies of molecular bonds. The transmitted light is detected and the interferogram (light intensity as function of time or mirror position) is mathematically converted into a spectrum of light intensity as function of frequency or wavenumber by a Fourier transformation. The absorbance spectrum A(v) is then calculated by comparing the light intensity measured with the sample (I) to the light intensity (I₀) measured in a so-called background spectrum without sample in the beam path according to $A(v) = log I_0/I$.

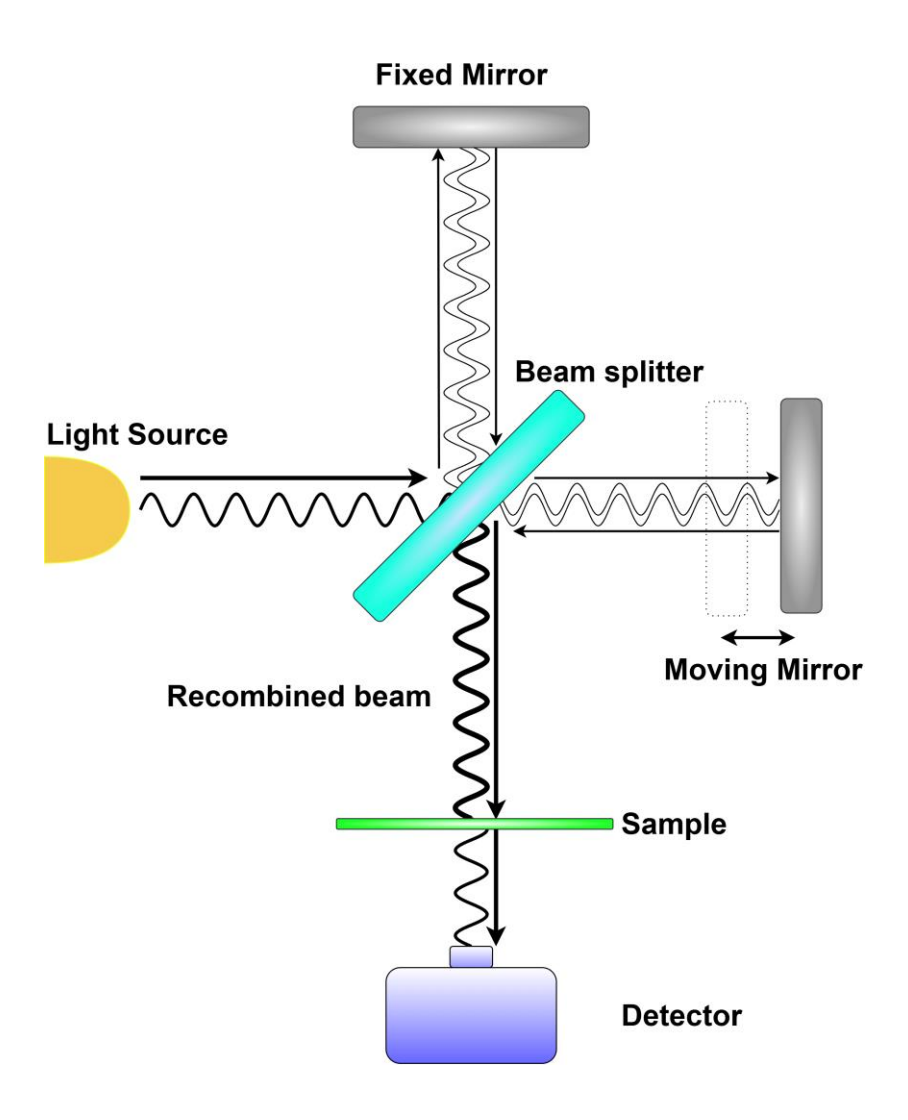


Figure 11. Schematic diagram of a typical FTIR system. The infrared beam is split into two beams using a beam splitter. After reflection from a fixed mirror and a moving mirror, the beams are recombined and directed through the sample. The resulting interferogram is converted into an absorption spectrum using a Fourier transform.

In silicate glasses, water is incorporated in two forms: hydroxyl groups (OH⁻), producing a characteristic absorption band near ~4500 cm⁻¹, and molecular water (H₂O_{mol}), producing a characteristic band near ~5200 cm⁻¹. The intensity of these bands is proportional to the concentration of water species ($C_{(H_2O,OH)}$), as described by the Beer–Lambert law (Ohlhorst et al., 2001):

$$C_{(H_2O,OH)} = \frac{1802 \cdot A_{(H_2O,OH)}}{d \cdot \varepsilon_{(H_2O,OH)} \cdot \rho}$$
 (11)

where C is the concentration in wt%, $A_{(H_2O,OH)}$ is the integrated absorbance (the area of the corresponding water absorption band), d is the sample thickness, ε is the molar absorption coefficient, and ρ is the density of the glass.

FTIR analyses were conducted at the Bayerisches Geoinstitut (University of Bayreuth, Germany), using a Bruker IFS 120 high-resolution spectrometer coupled to a Bruker IR microscope (Fig. 12). The system was used with a tungsten light source, a Ge-coated CaF₂ beam splitter and a liquid N₂-cooled narrow-band MCT detector. Measurements were performed at room temperature on doubly polished glass sections of approximately 200-600 μm thickness. Spectra were collected in transmission mode over the range of 1000-6000 cm⁻¹, with a spot size of 100 μm and using 200 scans at a spectral resolution of 4 cm⁻¹. For each sample, at least three spectra were recorded at different positions to assess homogeneity.

Water concentrations were calculated using Eq. 11, with baseline correction performed using the two Gaussian (GG) method, and molar absorption coefficients from Ohlhorst et al. (2001) were used for quantification. This approach enables accurate determination of water content across a wide range of compositions and is well suited for the silica-rich compositions of the glasses used in this study.

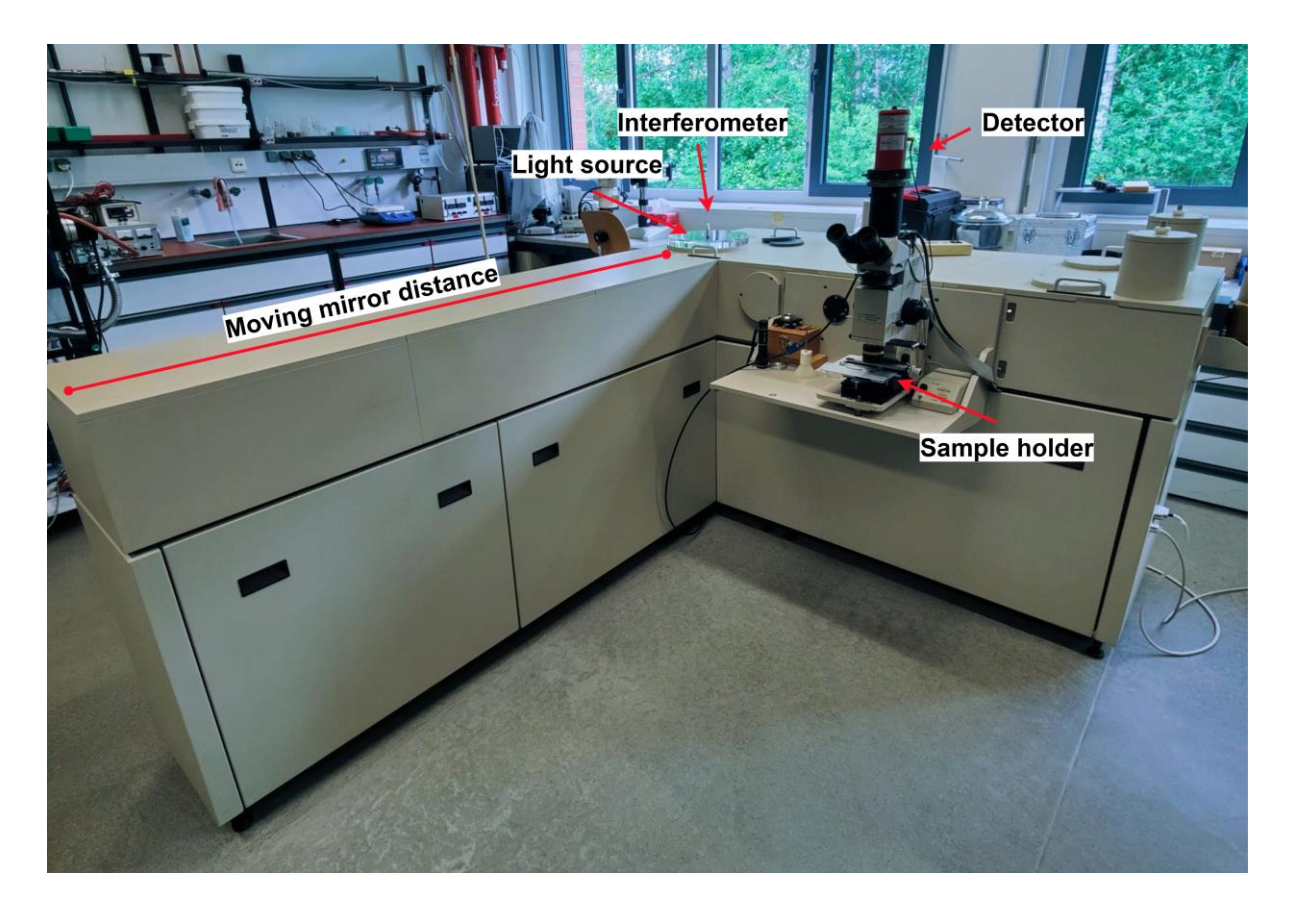


Figure 12. FTIR system used in this study. Photograph of the Bruker IFS 120 high-resolution spectrometer coupled with a Bruker IR microscope.

2.6 Micropenetration viscometry

Micropenetration (MP) viscometry was employed to measure the viscosity of the synthesized melts in the high-viscosity regime interval, near and above the glass transition temperature (T_g , where viscosity is 10^{12} Pa s). The method involves monitoring the indentation rate of a sapphire sphere (radius r = 0.75 mm) as it penetrates the sample surface under a constant gravitational load during isothermal holding (Fig. 13). The entire setup is enclosed in a high-temperature vertical furnace, which allows stable temperature control and minimizes thermal gradients during the measurement. The system includes a SiO₂ tube that is continuously flushed with argon (Ar) to maintain an inert atmosphere and prevent oxidation. Temperature was regulated using an S-type thermocouple (Pt-Pt₉₀Rh₁₀) positioned

approximately 1.5 mm from the sample surface, with an estimated uncertainty of ± 2 °C due to thermocouple accuracy and placement (Behrens et al., 2018).

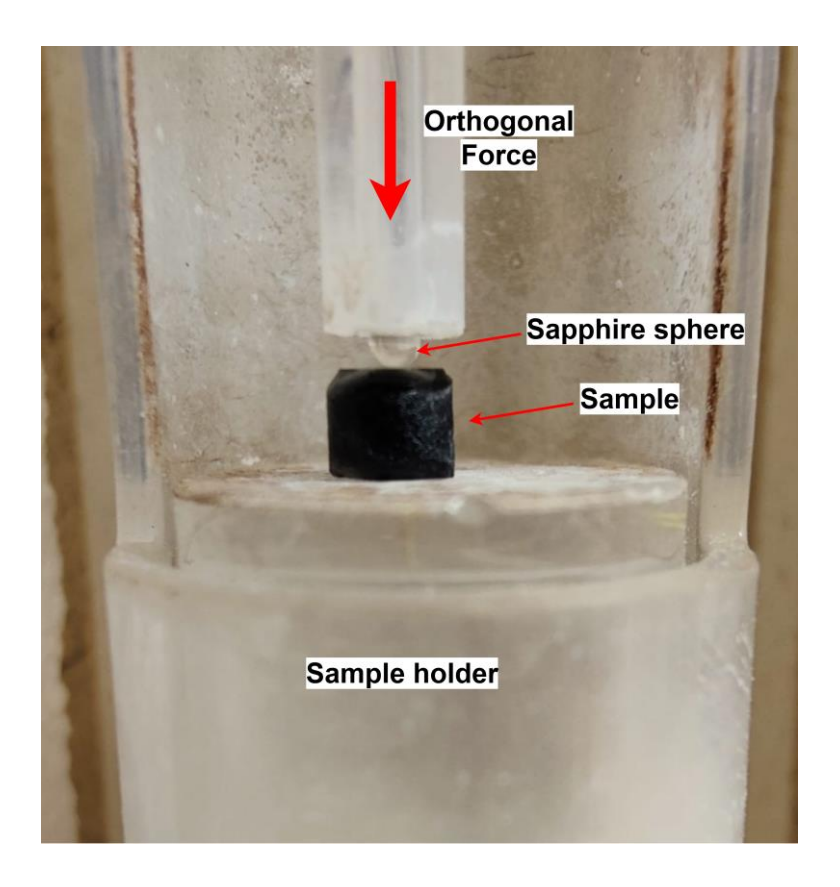


Figure 13. Close-up view of the micropenetration (MP) viscometry setup used in this study. The image shows the sapphire sphere positioned on the sample, indented under a controlled orthogonal force (the thermocouple is placed behind the rod). The entire setup is enclosed in a high-temperature furnace for controlled isothermal viscosity measurements.

The viscosity was calculated from the indentation data using the analytical solution of Douglas et al. (1965), which describes the viscous resistance to the penetration of a sphere into a viscous medium:

$$\eta = \frac{3F}{16\sqrt{2rL}\frac{dl}{dt}}\tag{12}$$

where η is the Newtonian viscosity (Pa s), F is the applied force (N), t is the time (s), r is the radius of the sphere (m), L is the cumulative indentation depth (m), and $\frac{dl}{dt}$ is the indentation within a measurement interval. The instrument was calibrated using standard glass DGG-1, reproducing certified viscosity data (Meerlender, 1974) within ± 0.1 log units.

2.7 Concentric cylinder viscometry

Concentric cylinder (CC) viscometry was employed to determine the viscosity of the synthesized melts in the low-viscosity regime, at superliquidus temperatures. In this method, viscosity is calculated from the torque required to rotate a spindle at controlled angular velocity within a molten sample. The sample is contained between a stationary crucible (fixed cylinder) and a rotating spindle (inner cylinder), generating a well-defined shear flow (Fig. 14).

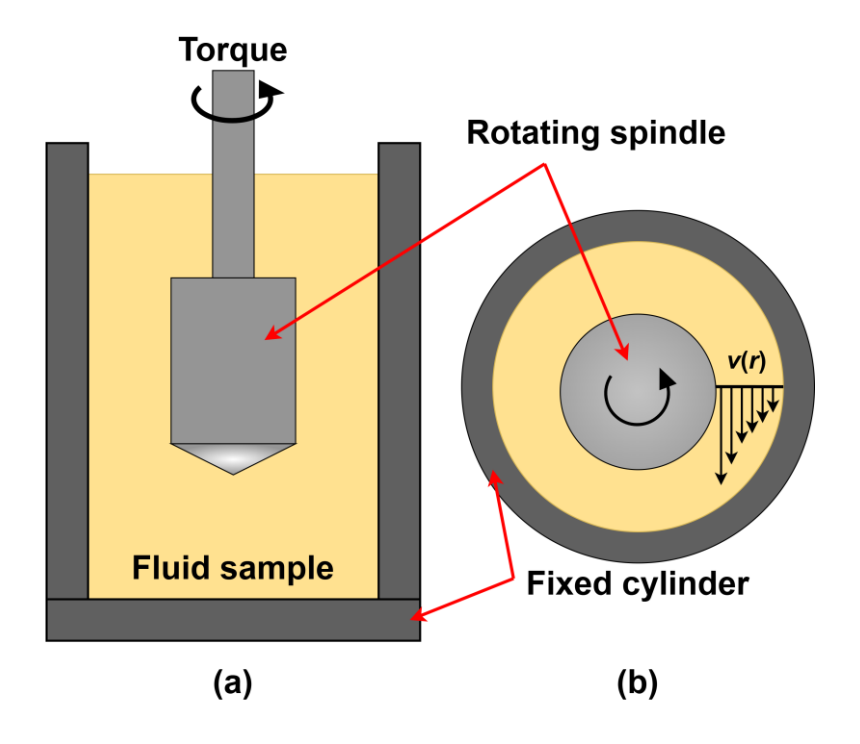


Figure 14. Schematic representation of the concentric cylinder (CC) viscometry setup used in this study. (a) Cross-sectional view: The fluid sample is sheared between a rotating spindle and a fixed outer cylinder. The torque required to rotate the spindle is used to calculate viscosity. (b) Top view: Velocity profile $\nu(r)$ develops across the gap between the rotating and fixed cylinders, allowing determination of the shear rate and corresponding viscosity.

CC measurements were conducted using two complementary setups: a Rheotronic II Rotational Viscometer (Theta Instruments) at the Experimental Volcanology and Petrology Laboratory (EVPLab), Roma Tre University (Italy), and a Haake RV20 viscometer at the Institute of Non-Metallic Materials, TU Clausthal (Germany).

At EVPLab (Rome), the Rheotronic II viscometer was equipped with an Anton Paar Rheolab QC head (maximum torque capacity: 75 mN m), coupled to a high-temperature furnace for stable thermal control (Fig. 15). The CC geometry consisted of a $Pt_{80}Rh_{20}$ crucible (62 mm height, 32 mm inner diameter) and a $Pt_{80}Rh_{20}$ spindle (3.2 mm diameter, 42 mm length). The glass samples were first homogenized by stirring at 1435 °C for 5 hours at a constant shear rate ($\dot{\gamma} = 10 \text{ s}^{-1}$), under ambient pressure in air. Following homogenization, viscosity measurements were performed during stepwise cooling, using 25–50 °C intervals, with each temperature step held isothermally (~45 min) to ensure thermal and rheological equilibrium. Temperature control was achieved using a factory-calibrated S-type thermocouple with an accuracy of ± 2 °C. The system was calibrated using NIST standard glass 717a, reproducing certified viscosities within a deviation of $\pm 0.03 \log_{10}$ units.

In addition, complementary measurements were performed at the Institute of Non-Metallic Materials, TU Clausthal (Germany). The system was calibrated with standard glass DGG-1 (Deubener et al., 2009), achieving viscosity accuracy of $\pm 0.02 \log_{10}$ units over a shear rate range of 0.1 to 96 s⁻¹. Glass samples were melted in a platinum crucible and stirred under controlled conditions to ensure thermo-chemical homogenization. Viscosity measurements were carried out during stepwise cooling, with each temperature step held isothermally until thermal and rheological equilibrium was reached. Temperature control was maintained using a factory-calibrated S-type thermocouple (accuracy ± 2 °C).

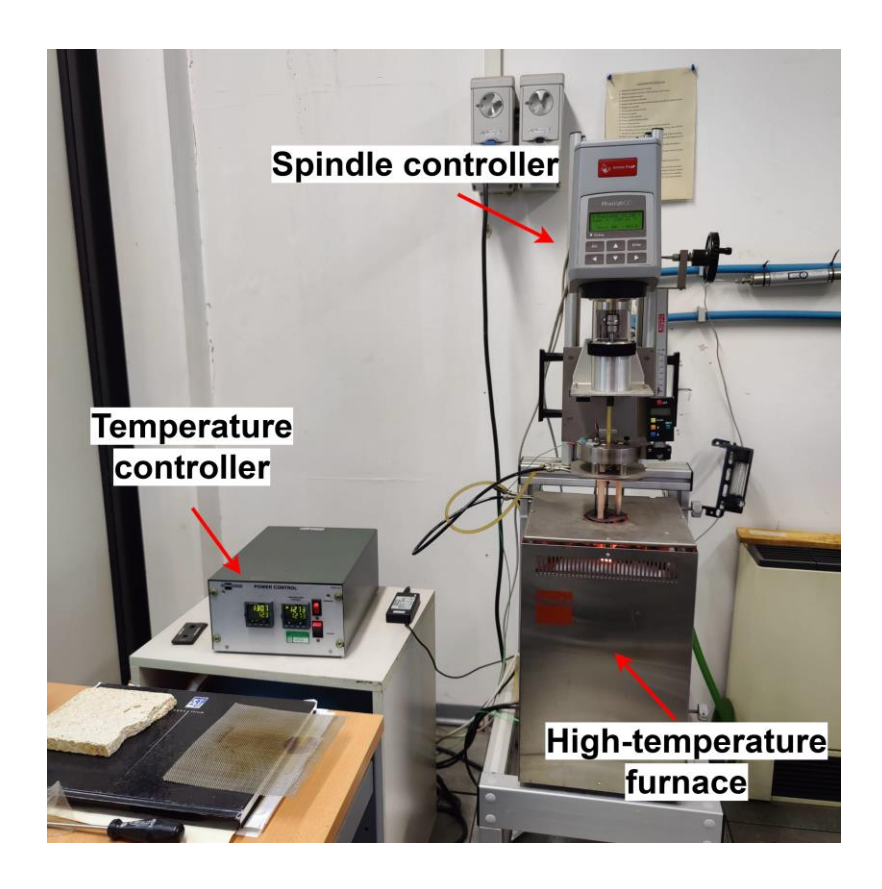


Figure 15. Photograph of the Rheotronic II rotational viscometer (EVPLab, Roma Tre University) used in this study. The system consists of an Anton Paar Rheolab QC spindle controller, a high-temperature furnace, and a temperature controller. Viscosity is calculated from the torque required to rotate the spindle within the molten sample under controlled thermal conditions.

2.8 Differential Scanning Calorimetry

Accurate determination of viscosity across a wide temperature range is essential for modeling the rheological behavior of volcanic melts, particularly in systems prone to nanocrystallization, volatile loss, or structural relaxation effects. Differential scanning calorimetry (DSC) was used in this study as a complementary method to direct viscometry, to derive viscosity near and above the glass transition temperature (T_g). DSC measures the difference in heat flow between a sample and a reference as they undergo a programmed temperature profile. Thermal events such as glass transition, crystallization, and melting produce characteristic

deviations in heat flow, from which characteristic temperatures (e.g., T_{onset} and T_{peak} ; Fig. 16) can be extracted and correlated to viscosity following Eq. 13:

$$log_{10}\eta(T_{onset,peak}) = K_{onset,peak} - log_{10}(q_h)$$
(13)

where $K_{onset} = 11.20 \pm 0.15$ and $K_{peak} = 9.84 \pm 0.20$ (Di Genova et al., 2020b; Fanesi et al., 2025; Stabile et al., 2021). It is important to mention that when the heating rate $q_h = 10$ °C min⁻¹, $\eta(T_{onset}) \approx 10^{12}$ Pa s, and therefore, $T_{onset} \approx T_g$. This approach enables viscosity determination without the prolonged dwell times required in conventional viscometry, reducing the risk of nano-crystallization and volatile loss (Valdivia et al., 2023). In this study, both Conventional DSC (C-DSC) and Flash DSC (F-DSC) were employed to fully characterize viscosity behavior.

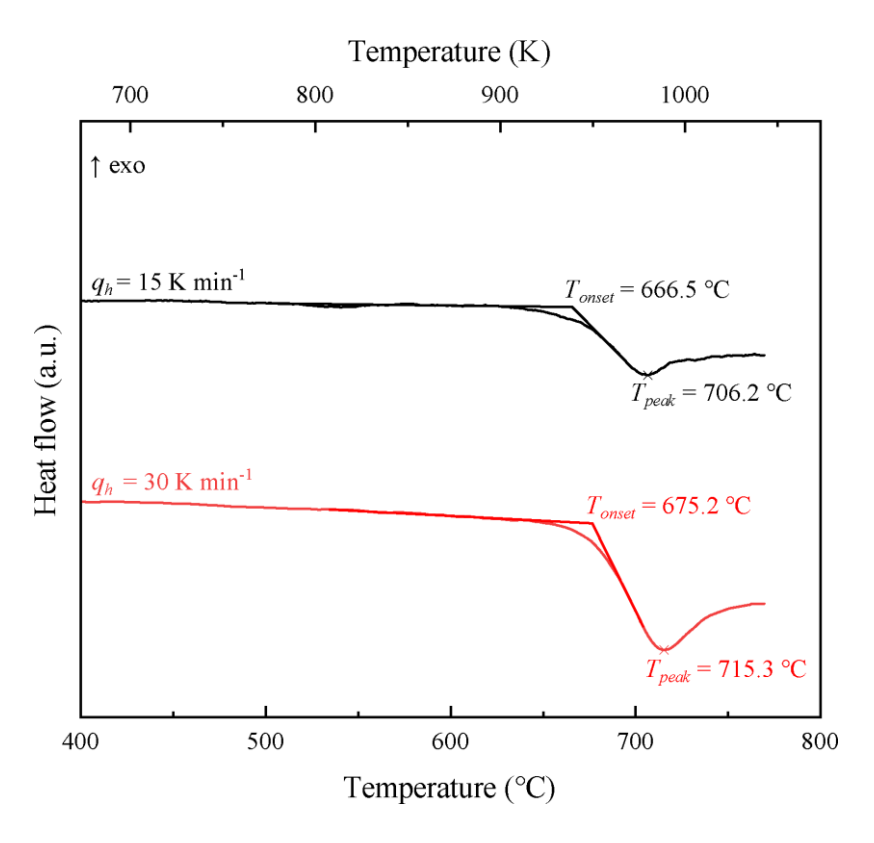


Figure 16. Representative C-DSC curves showing heat flow as a function of temperature for anhydrous Stromboli glasses. The red and black traces correspond to second heating runs conducted at 30 and 15 K min⁻¹, respectively, using the rate-matching method expressed in Eq. 13). Extracted from Valdivia et al. (2023).

2.8.1 Conventional DSC (C-DSC)

C-DSC measurements were conducted at the Institute of Non-Metallic Materials, TU Clausthal (Germany), using two apparatuses: A Netzsch 404 F3 Pegasus (Fig. 17) and 404 cell DSC instruments. Approximately 15 ± 5 mg of glass was loaded into a Pt₈₀Rh₂₀ crucible under constant nitrogen flow (20 ml min⁻¹). Heating rates of 10 and 20 °C min⁻¹ were applied. To erase thermal history, each sample was initially heated slightly above T_{peak} and cooled to 100 °C with controlled cooling rate (q_c). The viscosity-relevant measurement was then performed during the second heating cycle (upscan) using the rate-matching method ($q_h = q_c$). T_{onset} and T_{peak} were extracted from this second upscan and inserted into Eq. 13 to derive viscosity. This method minimizes kinetic artifacts and enables reproducible viscosity determination near T_g .

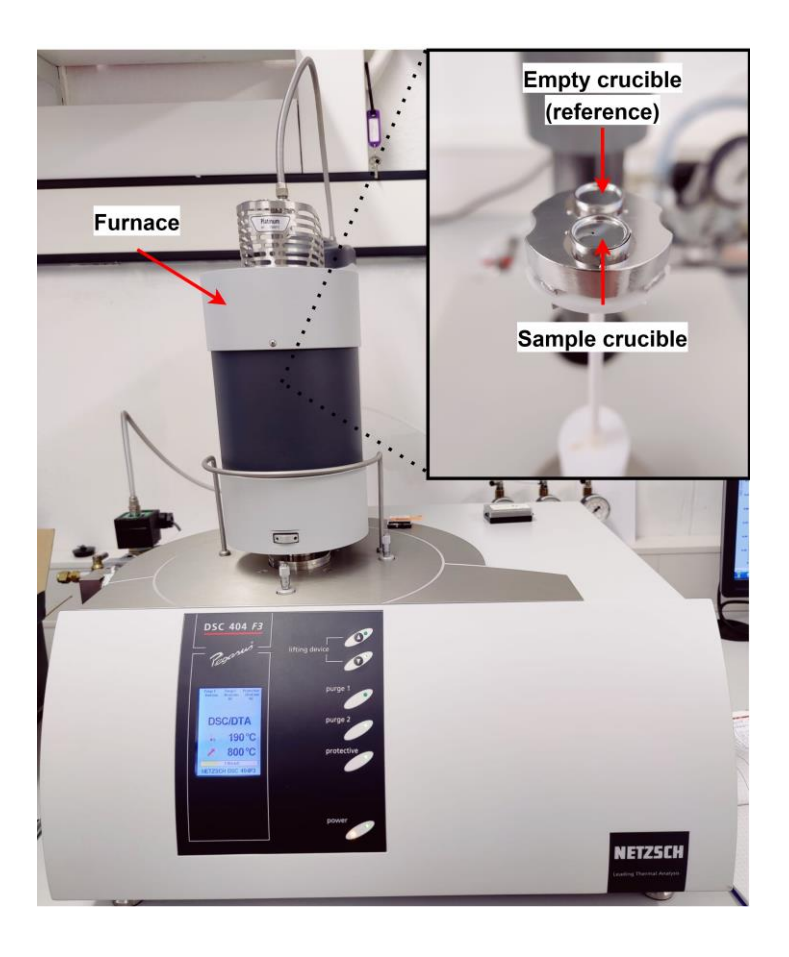


Figure 17. Conventional differential scanning calorimetry (C-DSC) setup used in this study (Netzsch 404 F3 Pegasus, TU Clausthal). The image shows the main furnace unit and an inset of the sample holder assembly with an empty reference crucible and a sample crucible used for heat flow measurements.

2.8.2 Flash DSC (F-DSC)

Flash DSC (F-DSC) is an advanced calorimetric technique designed to overcome limitations of conventional DSC. By operating at ultra-fast heating and cooling rates, F-DSC allows the glass transition and related viscosity behavior to be probed on timescales where kinetic effects are strongly suppressed. This capability is especially valuable for hydrous, Ferich volcanic glasses, where structural changes can occur rapidly even during moderate heating in C-DSC.

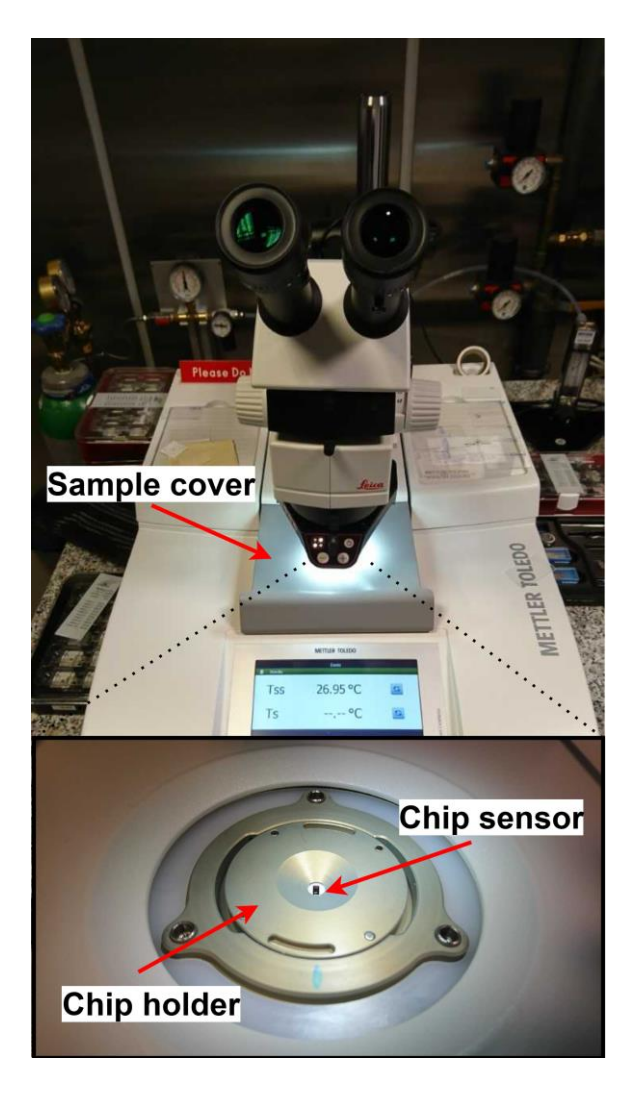


Figure 18. Flash differential scanning calorimetry (F-DSC) setup used in this study (Mettler Toledo Flash DSC 2+). The image shows the sample cover and microscope, with an inset of the chip sensor and chip holder used for ultra-fast heat flow measurements.

In this study, F-DSC measurements were conducted at the Institute of Non-Metallic Materials, TU Clausthal (Germany) using a Mettler Toledo Flash DSC 2+ equipped with UFH 1 sensors (Fig. 18). Approximately 50 ng of glass powder was placed on the chip sensor under an argon flow of 40 ml min⁻¹. Ultra-fast heating and cooling rates of 1000 °C s⁻¹ (60000 °C min⁻¹) were applied, enabling accurate tracking of T_{onset} and T_{peak} with minimal time for structural relaxation or crystallization. The rate-matching approach ($q_h = q_c$) was used consistently with C-DSC, and viscosity was calculated from Eq. (13). The extremely high scan rates of F-DSC expand the measurable viscosity window towards lower viscosities ($\sim 10^6$ - 10^8 Pa s), complementing the high-viscosity data from C-DSC and micropenetration.

2.9 Brillouin light scattering spectroscopy

Brillouin light scattering (BLS) spectroscopy was employed in this study to determine the high-frequency elastic properties of both anhydrous and hydrous glasses, specifically the ratio between bulk and shear moduli (K/G).

Brillouin light scattering is based on the inelastic scattering of monochromatic laser light by thermally excited acoustic phonons in the sample. When incident photons interact with these phonons, they undergo a small energy shift, producing Stokes and anti-Stokes Brillouin doublets (Fig. 19). The magnitude of this frequency shift ($\Delta\omega$) is directly related to the sound velocity of the material. Longitudinal (v_p) and shear (v_s) sound velocities can be derived from the measured $\Delta\omega$ using the following relation:

$$v_{p,s} = \frac{\Delta\omega\lambda}{2n\sin(\theta/2)}\tag{14}$$

where λ is the laser wavelength, n is the refractive index of the sample, and θ is the angle between the incident and scattered beams (Sinogeikin et al., 2006; Whitfield et al., 1976).

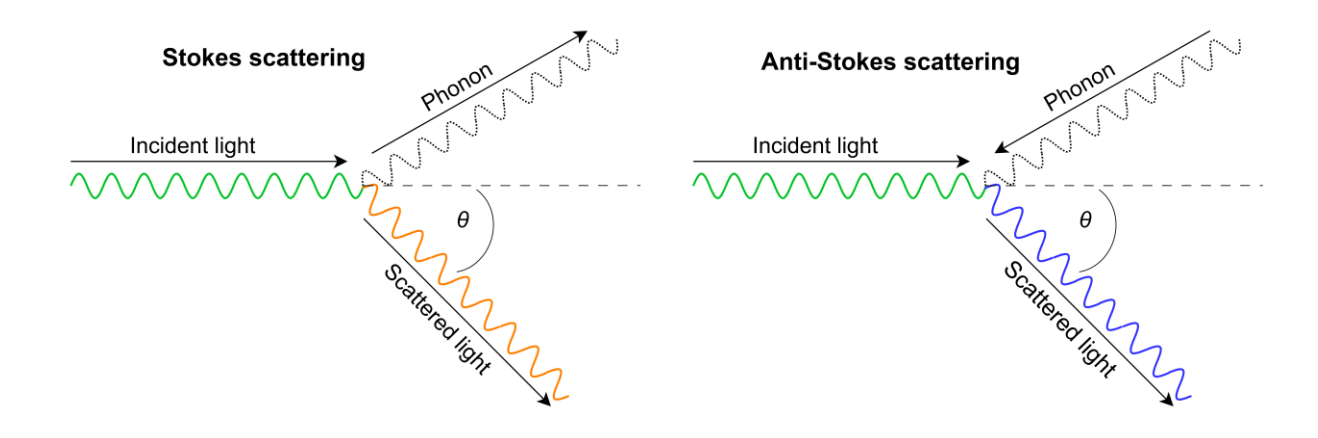


Figure 19. Schematic of Brillouin light scattering. Stokes and anti-Stokes components arise from inelastic scattering of incident light by acoustic phonons, with the frequency shift depending on the phonon energy and scattering angle (θ) .

BLS measurements were performed at the Bayerisches Geoinstitut (University of Bayreuth, Germany). Glass plates with a plane-parallel geometry and a thickness of approximately 50 μ m were measured using a solid-state Nd:YVO4 laser source (532 nm wavelength, 50 mW power). The Brillouin frequency shift was determined with a six-pass Fabry-Perot interferometer (Whitfield et al., 1976) coupled to a single-pixel photon counter detector. A symmetric forward scattering configuration (Whitfield et al., 1976) with a scattering angle of $\theta = 79.8^{\circ}$, was employed, with the angle accuracy verified through calibration against a reference silica glass. In this geometry, the refractive index of the sample does not need to be known. Thus, assuming the refractive index of air is 1, the equation for the symmetric platelet geometry can be written as:

$$v_{p,s} = \frac{\Delta\omega\lambda}{2\sin(\theta/2)}\tag{14a}$$

Eight spectra were collected for each sample at varying rotation angles ranging from -180° to $+180^{\circ}$ to account for uncertainties resulting from possible deviations from the symmetric platelet scattering geometry. The complete optical and mechanical setup is shown in Figure 20. Finally, the K/G factor was determined by Eq. 15:

$$\frac{K}{G} = \left(\frac{v_p}{v_s}\right)^2 - \frac{4}{3} \tag{15}$$

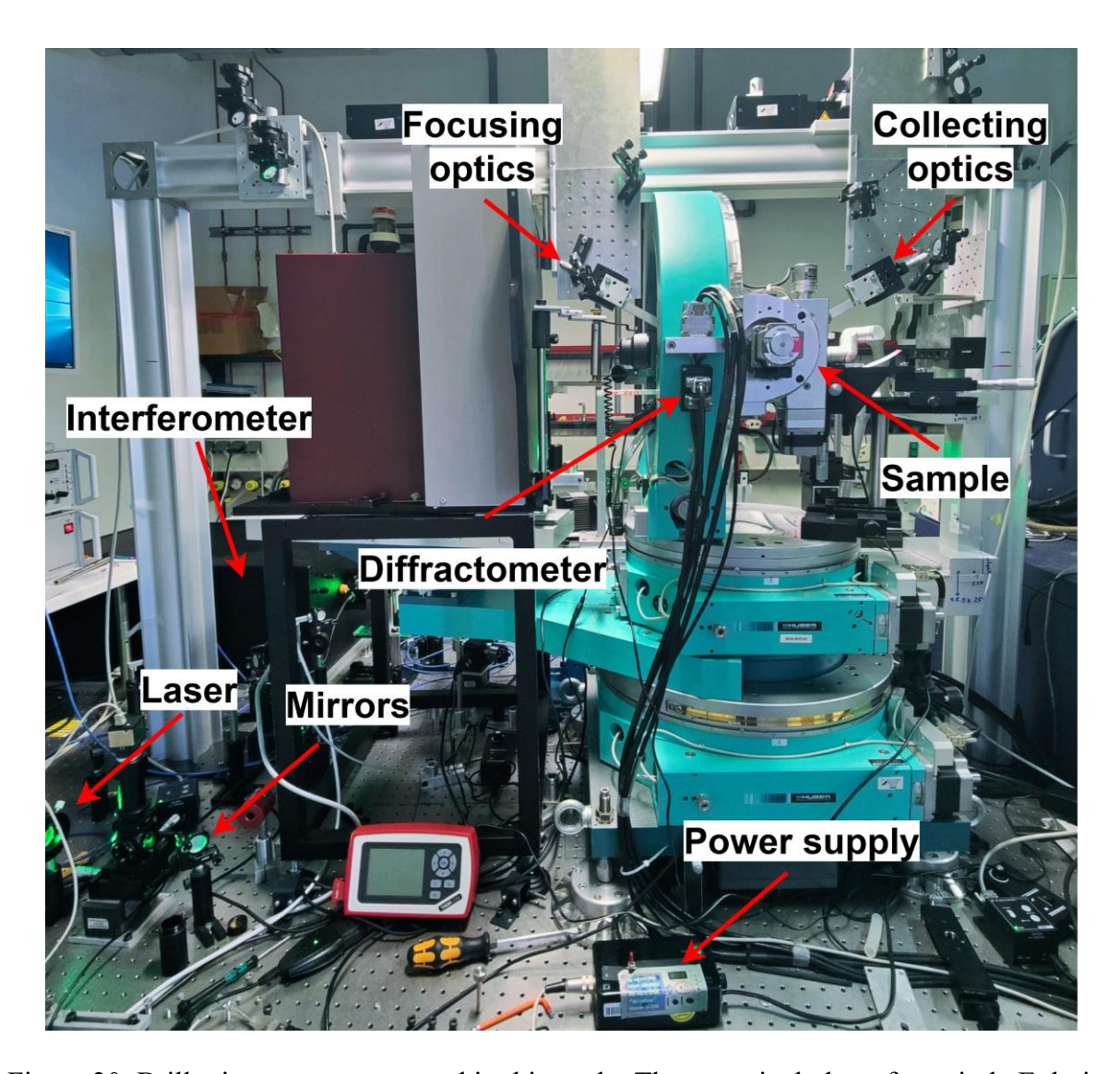


Figure 20. Brillouin spectrometer used in this study. The setup includes a four-circle Eulerian cradle diffractometer (Huber) for precise sample orientation, with laser focusing and collecting optics aligned for phonon velocity measurements.

2.10 Transmission electron microscopy

Transmission electron microscopy (TEM) was employed to investigate nano-structural features and crystallization processes in the andesitic glass samples, with a focus on characterizing nanocrystals in both post-experimental samples and the pristine starting glasses. TEM provides several analytical modes to investigate internal sample structure at high spatial resolution; in this study, we used conventional imaging, selected area electron diffraction (SAED), and scanning transmission electron microscopy (STEM) coupled with energy-dispersive X-ray spectroscopy (EDS). As TEM requires electron-transparent sections (typically <100 nm thick), cross-sectional lamellae were prepared using a focused ion beam (FIB) system. Room-temperature analyses were carried out at the Bayerisches Geoinstitut (University of Bayreuth, Germany) using a FEI Titan G2 80–200 S/TEM operated at 200 kV (Fig. 21a), while lamella preparation was conducted with a SCIOS Dual Beam FIB-SEM system (FEI Company; Fig. 21b).

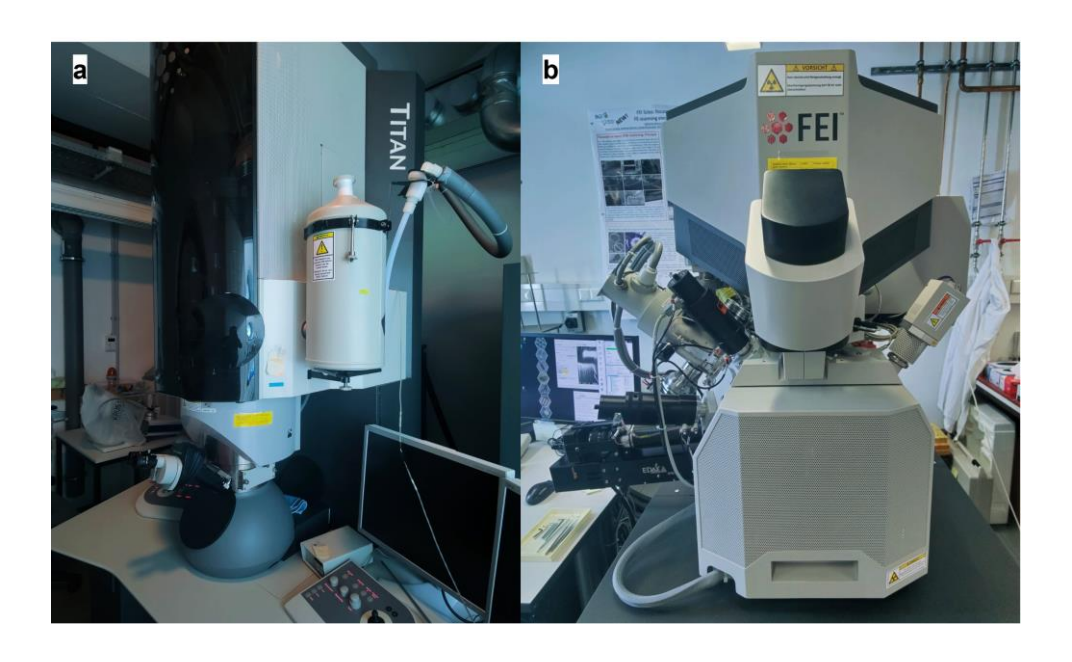


Figure 21. Instruments used for TEM sample preparation and analysis. (a) FEI Titan G2 80–200 S/TEM used for high-resolution transmission electron microscopy and STEM imaging in this study. (b) Focused Ion Beam (FIB) instrument used for site-specific preparation of electron-transparent lamellae.

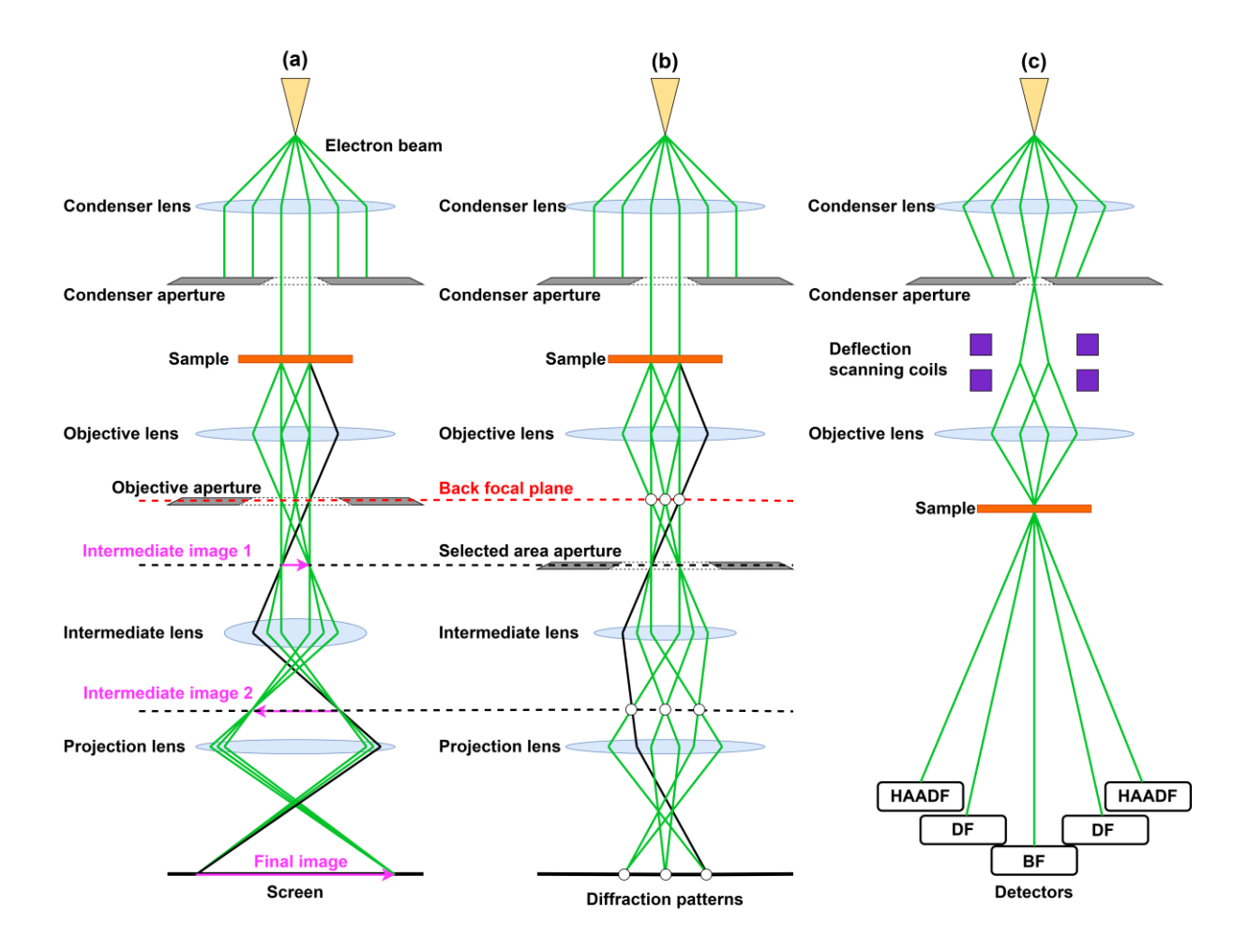


Figure 22. Transmission electron microscopy (TEM) modes used in this study. (a) Imaging mode forms real-space images using a broad electron beam. Pink arrows show the image orientation. (b) Diffraction mode projects the back focal plane to obtain selected area electron diffraction (SAED) patterns. (c) Scanning TEM (STEM) mode uses a focused probe scanned across the sample, with signals collected by BF, DF, and HAADF detectors.

FIB preparation involved identifying regions of interest within the samples previously used for micropenetration experiments, coating the surface with a protective Pt layer, and sequentially milling two trenches to isolate the lamella. Final thinning to a thickness between 24(2) and 50(2) nm was performed using progressively lower Ga⁺ ion beam currents. The lamellae were lifted out with a micromanipulator and mounted onto TEM grids for analysis.

In TEM imaging mode (Fig. 22a), contrast results from differences in sample thickness, density, and diffraction behavior, allowing direct visualization of nanocrystal morphology within the glass matrix. In diffraction mode (Fig. 22b), the objective lens is adjusted to project

the back focal plane onto the detector, producing selected area electron diffraction (SAED) patterns that reveal the crystallographic structure and orientation of specific phases. In STEM mode (Fig. 22c), the electron beam is focused into a sub-nanometer probe that scans across the sample, while transmitted and scattered signals are recorded by detectors placed at various angles. High-angle annular dark-field (HAADF) imaging provided compositional contrast based on atomic number (Z-contrast), and EDS spectra were collected using a Bruker QUANTAX system with four silicon drift detectors. Elemental maps were acquired using a probe current below 0.05 nA, a dwell time of 16 s per pixel, and total acquisition times between 12 and 30 minutes. Quantitative EDS analysis included corrections for atomic number and absorption, with drift correction activated throughout. HAADF images were segmented using ilastik (v1.4.0) to extract nanocrystal size, nanolite number density, and spatial distribution.

In situ heating TEM experiments were carried out at CNRS CEMHTI (Orléans, France) using a JEOL ARM200F operated at 80 kV, equipped with a cold field emission gun, dual spherical aberration correctors, a Gatan Imaging Filter (GIF), and a OneView camera. The pristine andesitic glass was crushed, suspended in ethanol, and a droplet of the suspension was deposited onto MEMS heating grids compatible with a Protochips Fusion double-tilt holder. Plasma cleaning was avoided to preserve the redox state of iron. The sample was first annealed at 200 °C for 1 h to remove volatile contaminants, then heated manually at 1 °C s ⁻¹ to temperatures between 200 °C and 750 °C, with isothermal dwells of 30–60 s to observe nanocrystal nucleation and growth. Manual drift correction was applied during acquisition, and image sequences were post-processed using DigitalMicrograph GMS.3. High-resolution TEM images were analyzed via fast Fourier transforms (FFT) to identify nanocrystalline phases, and complementary EDS maps were acquired at 200 kV using a 1 Å probe with ~11-minute acquisition times. The combination of imaging, diffraction, and analytical STEM techniques

allowed a comprehensive reconstruction of nanoscale crystallization pathways and spatial heterogeneity in the experimental andesitic glasses.

2.11 Small- and -wide angle X-ray scattering (SAXS and WAXS)

Small-angle and wide-angle X-ray scattering (SAXS and WAXS) measurements were carried out at the ID02 beamline of the European Synchrotron Radiation Facility (ESRF) (Narayanan et al., 2022) in Grenoble, France. This facility provides a highly intense and well-collimated monochromatic X-ray beam optimized for structural characterization at multiple length scales. SAXS experiments were performed in a pinhole geometry with a sample-to-detector distance of 6 meters, enabling access to a broad range of scattering vectors (q), from 0.01 nm^{-1} to 2.5 nm^{-1} . The scattering vector is defined as

$$q = |q| = \frac{4\pi \sin(\theta)}{\lambda},\tag{16}$$

where $\lambda = 1$ Å is the X-ray wavelength and θ is the scattering angle. A guard slit placed immediately before the sample (0.45 mm vertical × 0.5 mm horizontal) was used to minimize parasitic scattering around the direct beam. Data reduction was conducted using the PyFAI software package, which applies the beamline-specific geometry for accurate azimuthal integration of the 2D scattering patterns.

SAXS is particularly sensitive to electron density fluctuations at the nanometer scale and is therefore well-suited to probing the size, shape, and spatial organization of nanoscale structures such as clusters or nanoparticles, which has been successfully validated and applied in previous studies (Longo et al., 2022; Maurizio et al., 2003). For data analysis, the scattering intensity I(q) was modeled assuming spherical particles and incorporating both interparticle

interactions and size distributions, in agreement with TEM observations suggesting possible particle contact. The total intensity was described using the decoupling approximation (Förster et al., 2005; Jeffries et al., 2021; Jensen et al., 2006; Longo et al., 2022):

$$I(q) = \Delta(\rho)^2 S(q) P(q) + bck + \frac{K_{Porod}}{q^4}$$
(17)

where $\Delta(\rho)^2$ is the difference of electronic density between the nanoparticles and the surroundings, bck is the background constant, P(q) is the contribution given by a poly-disperse system of not-interacting homogeneous spheres,

$$P(q) = \int_{q}^{\infty} D(\bar{R}, r) F(r, q, \bar{R})^{2} r^{6} dr$$
(18)

F(q,r) is the form factor of a sphere of radius r given by Eq. 19

$$F(q,r) = \frac{\sin(qr) - qr\cos(qr)}{qr^3},\tag{19}$$

and $D(r, \bar{R})$ is the Weibull size distribution of particle sizes defined as:

$$D(r,\bar{R}) = \left(\frac{r}{\bar{R}}\right)^{(b-1)} \exp\left(\frac{r}{\bar{R}}\right)^{b},\tag{20}$$

where \bar{R} is the average radius of the nanoparticle and b is the shape parameter. When needed, a bimodal distribution was implemented by summing up two Weibull functions centered at different radii (R_1 and R_2). Interparticle correlations were modeled using a hard-sphere

structure factor S(q), which accounts for excluded-volume interactions in concentrated systems. This factor was computed analytically using the Percus-Yevick approximation, which is suitable for short-range repulsive systems. The structure factor is expressed as:

$$S(q, R_{HS}) = [1 + 24\eta_{HS} f(R_{HS}, q)]^{-1}$$
(21)

where η_{HS} is the volume fraction and R_{HS} is the effective hard-sphere radius. The function f(x) (with $x = qR_{HS}$) is expressed analytically and involves coefficients α , β , and γ , which are dependent on η_{HS} . These terms capture the interference effects arising from short-range ordering between neighboring particles. f(x) is expressed as

$$f(x) = \frac{\alpha(-x\cos x + \sin x)}{x^3} + \frac{\beta(-x^2\cos x + 2x\sin x + 2\cos x - 2)}{x^4} + \gamma[-x^4\cos x + 4x^3\sin x + 12x^2\cos x - 24x\sin x - 24\cos x + 24]}{x^6}$$
(22)

with,

$$\alpha = \frac{(1+2\eta_{HS})^2}{(1-\eta_{HS})^4},\tag{23}$$

$$\beta = \frac{-6\eta_{HS} \left(1 + \frac{\eta_{HS}}{2}\right)^2}{(1 - \eta_{HS})^4} \tag{24}$$

$$\gamma = \frac{\eta_{HS} \,\alpha}{2} \tag{25}$$

To account for the finite separation between particles, the effective interaction radius R_{HS} was assumed to scale with the actual nanoparticle radius via the relation $R_{HS} = 2Rkc$ (Jeffries et al., 2021; Jensen et al., 2006; Longo et al., 2022), where kc is a constant term ≥ 1 . This factor enables the model to account for systems in which nanoparticles are not fully in contact but are still close enough to influence each other. Additionally, to accurately describe the SAXS signal at low q a Porod behavior K_{porod}/q^4 was included. This component captures the characteristic decrease in scattering intensity at high q and is associated with sharp interfaces between particles and matrix.

The Porod function is instrumental in understanding the surface roughness and the specific surface area of the particles in the sample. It assumes an ideal, smooth interface, leading to a clean power law, but deviations from this behavior can reveal information about surface fractal dimensions and the nature of the interface.

Finally, we calculated d-spacings (d) for the crystalline phases from WAXS experiments using Eq. 26 (Gumede et al., 2018),

$$d = \frac{2\pi}{q_{peak}},\tag{26}$$

with q_{peak} corresponding to the WAXS peaks.

3. Synopsis

This synopsis summarizes the main results of three manuscripts presented in Chapter 4 that have been published or will be submitted to peer-reviewed journals.

In Chapter 4.1, a revised viscosity model for hydrous Stromboli basalt is developed. By systematically excluding artifacts caused by nano-crystallization and water loss, the study shows that previous models overestimated melt viscosity by factors of 2.5–5.7, leading to revised interpretations of magma ascent rates and eruption dynamics at Stromboli volcano.

In Chapter 4.2, the role of nanolite formation in andesitic melts is investigated. Experimental results demonstrate that the development of nanoscale chemical heterogeneities around Fe-Ti nanolites significantly increases melt viscosity at low crystallinity. These findings highlight the critical influence of early-stage nanolite crystallization on magma rheology.

In Chapter 4.3, a new viscosity model for hydrous andesitic melts is presented. By combining viscometry, calorimetry, and Brillouin spectroscopy on well-characterized Febearing and Fe-free melts, the model accurately captures the effects of water, temperature, and transition metal content on viscosity. The results resolve key discrepancies in previous predictions and provides an improved framework for modelling magmatic processes at andesitic volcanoes.

3.1 Are volcanic melts less viscous than we thought? The case of Stromboli basalt

Melt viscosity governs the transport and eruption dynamics of magma, and its accurate determination is essential for modelling volcanic processes. For basaltic systems like Stromboli, viscosity has traditionally been estimated through experimental techniques such as micropenetration viscometry, concentric cylinder, and falling-sphere methods (Giordano et al., 2009; Misiti et al., 2009). However, recent work has shown that these approaches, especially when applied to hydrous melts, can be affected by water loss and the formation of Fe-Ti nanocrystals during heating (Scarani et al., 2022). Even in the absence of microlites, detectable by Scanning Electron Microscopy (SEM), these nanoscale phases can alter melt composition and structure, artificially increasing viscosity and leading to systematic overestimations that propagate into magma ascent models.

To tackle this challenge, we synthesized a series of anhydrous and hydrous glasses (up to 4.7 wt% H₂O) from natural pyroclasts of the 2019 Stromboli eruption. The goal was to determine melt viscosity across a realistic range of pre-eruptive water contents while isolating the effects of nano-crystallization. Glasses were produced using piston cylinder and IHPV techniques under controlled redox and thermal conditions. Raman spectroscopy was employed to detect nanolite formation, with particular attention to the broad Fe-Ti oxide band around 690 cm⁻¹ (Di Genova et al., 2020b), while Fourier Transform Infrared Spectroscopy (FTIR) was used to quantify water content and monitor structural changes. This combined approach enabled the identification of even subtle crystallization or water loss not evident through SEM imaging. Only those samples that remained structurally pristine before and after measurements were selected for model calibration.

Viscosity was measured using both conventional and flash Differential Scanning Calorimetry (DSC), as well as micropenetration viscometry at sub-liquidus conditions. Glass transition temperatures (T_g) were derived from DSC, while the melt fragility index (m) was

determined independently through Brillouin spectroscopy and configurational heat capacity estimates. T_g was observed to decrease systematically with increasing water content, from 667 °C in the anhydrous glass to 400 °C in the sample with 4.7 wt% H₂O. Interestingly, melt fragility remained constant at $m = 40.7 \pm 0.7$. This invariance was supported by a stable K/G ratio observed in Brillouin spectroscopy experiments, along with consistent configurational heat capacity ($\Delta C_p(T_g)$) at T_g values across different water contents. These results contradict earlier models (Giordano et al., 2008; Langhammer et al., 2022) that suggested decreasing melt fragility with hydration, likely an artefact driven by nanolite formation during viscosity measurements or even glass synthesis.

Using only nanolite-free data, we developed a new viscosity model for Stromboli basalt (Fig. 22) based on the MYEGA equation (Mauro et al., 2009).

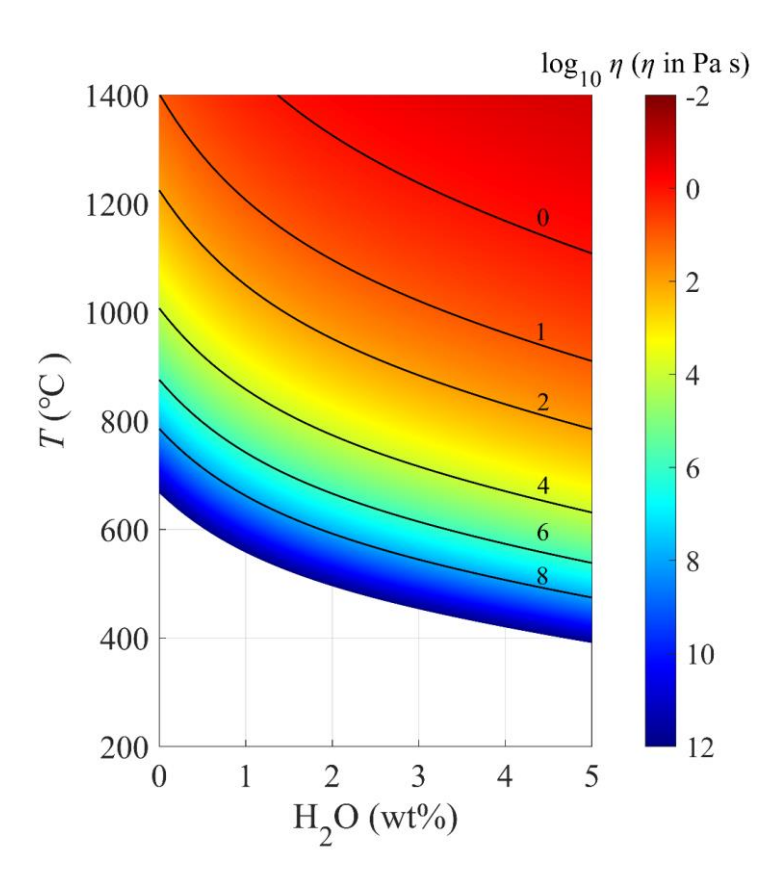


Figure 22. Viscosity of Stromboli basalt as a function of water content (wt%) and temperature (°C). Figure from Valdivia et al. (2023).

When applied to conditions relevant to the plumbing system of Stromboli volcano (1150 °C and 3.67 wt% H₂O), our model predicts viscosities that are approximately 2.5 to 5.7 times lower than those from earlier formulations. Under typical conduit conditions, this translates into magma ascent velocities exceeding 40 m s⁻¹, in agreement with observational constraints from the 2019 paroxysms, during which thermal and acoustic signals were detected only seconds after the onset of ground deformation (Ripepe et al., 2021).

In conclusion, this study presents a revised viscosity model for Stromboli basalt that more accurately captures the rheological behavior of volatile-rich melts. By systematically filtering out experimental artefacts related to nano-crystallization and water loss, the model provides more realistic input for magma ascent simulations and strengthens our ability to assess eruption dynamics in basaltic systems like Stromboli.

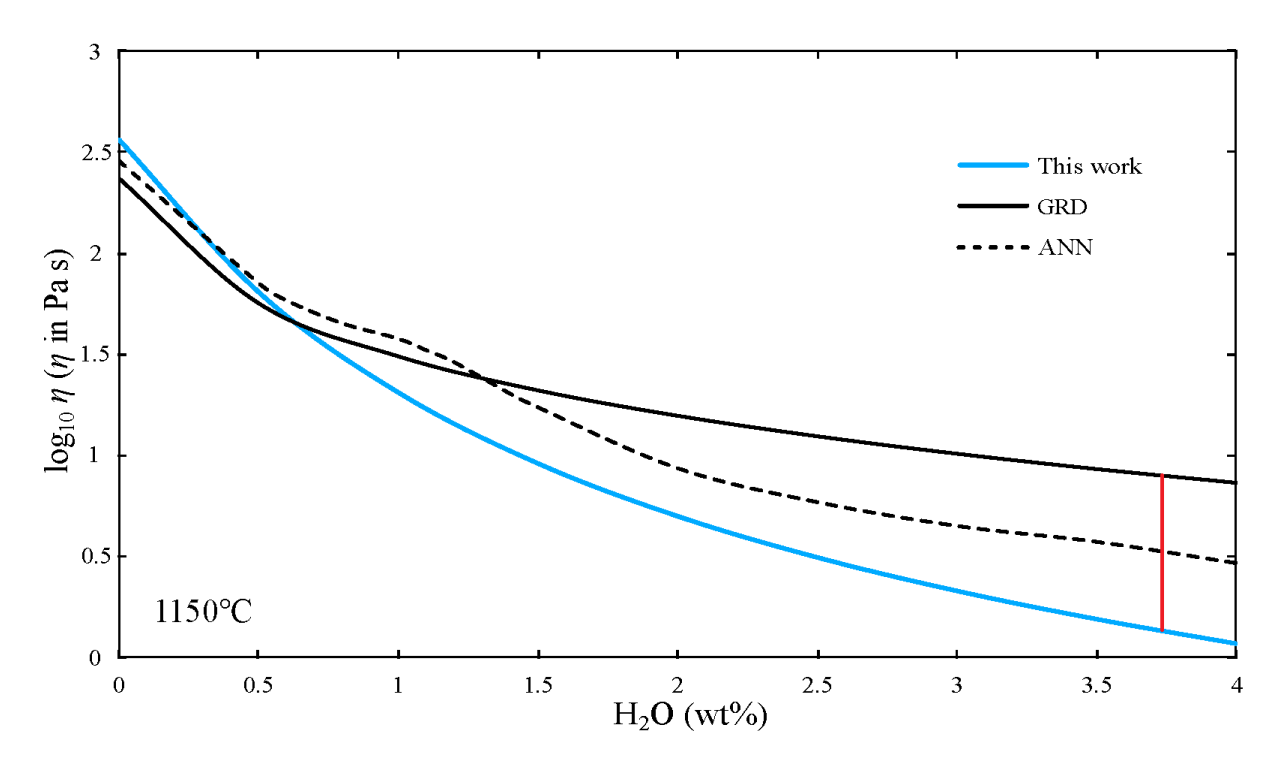


Figure 23. Comparison of predicted viscosity as a function of water content at the pre-eruptive temperature (T = 1150°C). The vertical red line marks the pre-eruptive water content of Stromboli basalt (Andronico et al., 2021; Giordano et al., 2009; La Spina et al., 2015). Modified from Valdivia et al. (2023).

3.2. Nanoscale chemical heterogeneities control the viscosity of andesitic melts

The viscosity of magmatic melts plays a central role in controlling eruptive style and magma transport. In intermediate compositions, such as andesite, small changes in viscosity can affect the conditions under which fragmentation occurs. Previous studies have shown that Fe-Ti oxide nanolites can increase melt viscosity (Valdivia et al., 2023). However, the physical and chemical processes linking nanolite formation to changes in viscosity are not fully understood. In this study, we present experimental evidence that nanolite formation induces nanoscale chemical heterogeneity in andesitic melts, which in turn leads to substantial increases in viscosity. By systematically comparing the viscosity of nanolite-free and nanolite-bearing samples, we establish a robust reference framework to assess how crystallization of nanolites influences melt viscosity.

We synthesized five andesitic glasses with controlled variations in transition metal content and iron oxidation. The reference sample, AND100 (Fe³⁺/Fe_{total} = 0.64), is based on the composition of Sakurajima andesite. To assess the chemical effects of Fe-Ti extraction associated with nanolite formation, we produced two additional compositions: AND65 and AND0, containing 35% and 100% less transition metals (Fe, Ti and Mn), respectively. In addition, two redox-modified samples (AND100red and AND100ox) were derived from AND100 and synthesized under different oxygen fugacity, with Fe³⁺/Fe_{total} ratios of 0.27 and 0.71, respectively.

Viscosity was derived using conventional and flash differential scanning calorimetry (C-DSC and F-DSC, respectively), and measured using micropenetration and concentric cylinder viscometry. Viscosity-temperature relationships were fitted using the MYEGA model, calibrated exclusively from nanolite-free samples. These measurements were essential to build a crystal-free viscosity reference that could be used as a reliable baseline to isolate the effects of nanolite formation. Our results show that reducing the total transition metal content leads to

substantial increases in melt viscosity: AND65 is approximately five times more viscous than the reference composition AND100, and AND0 is up to 30 times more viscous at eruptive temperatures relevant for Sakurajima volcano (~900-1050 °C). On the other hand, increasing the Fe³⁺/Fe_{total} ratio from 0.27 (AND100red) to 0.71 (AND100ox) also resulted in a twofold increase in viscosity.

High-temperature in situ experiments (Fig. 24) revealed that titanomagnetite nanolites nucleate within seconds above the glass transition temperature. This process begins with the segregation of Fe-rich amorphous domains, followed by rapid crystallization of nanoscale titanomagnetite. Raman spectroscopy (Fig. 24a), and electron diffraction in TEM mode (Fig. 24b), confirmed the progressive ordering of these nanocrystals with increasing temperature.

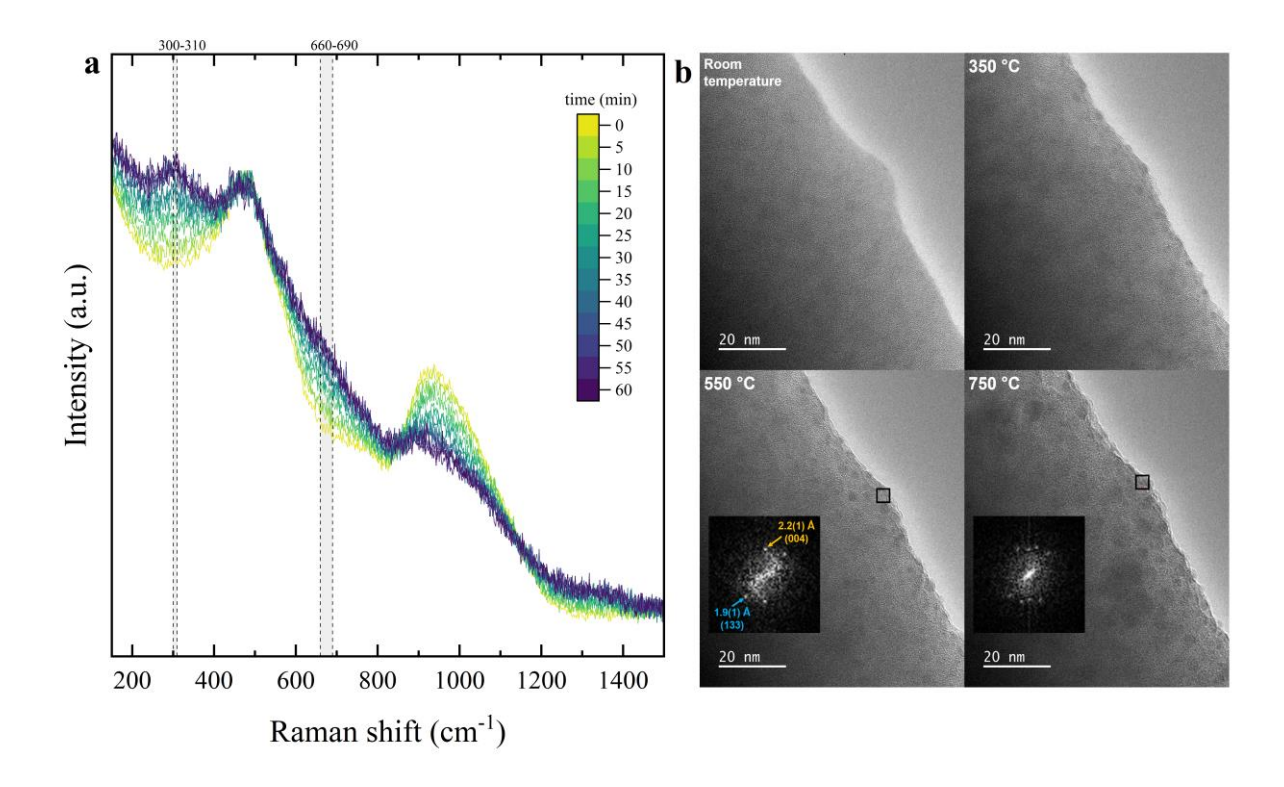


Figure 24. In situ high-temperature results. (a) Raman spectra of AND100 at 723 °C showing titanomagnetite crystallization above Tg (654 °C). Curves represent 5 min intervals; shaded areas mark key titanomagnetite peaks. (b) In situ TEM images showing AND100 evolving from homogeneous glass to nano-crystallized material (350–750 °C). FFTs and STEM-EDS identify magnetite-like crystals. Temperatures are qualitative values due to electron beam effects. Figure from Valdivia et al. (2025).

Isothermal viscosity measurements conducted during micropenetration experiments showed a continuous increase in viscosity over time at controlled temperatures, even though nanolite volume fractions remained below ~2 vol%. For example, at 660 °C, the viscosity of AND100 increased by nearly one order of magnitude over a 20-minute hold. Similar trends were observed at 723 and 808 °C, with viscosity exceeding model predictions based on Fe-Ti depletion alone (Fig. 25). These results suggest that the viscosity increase observed in nanolite-bearing samples cannot be explained by crystallization-induced chemical variations.

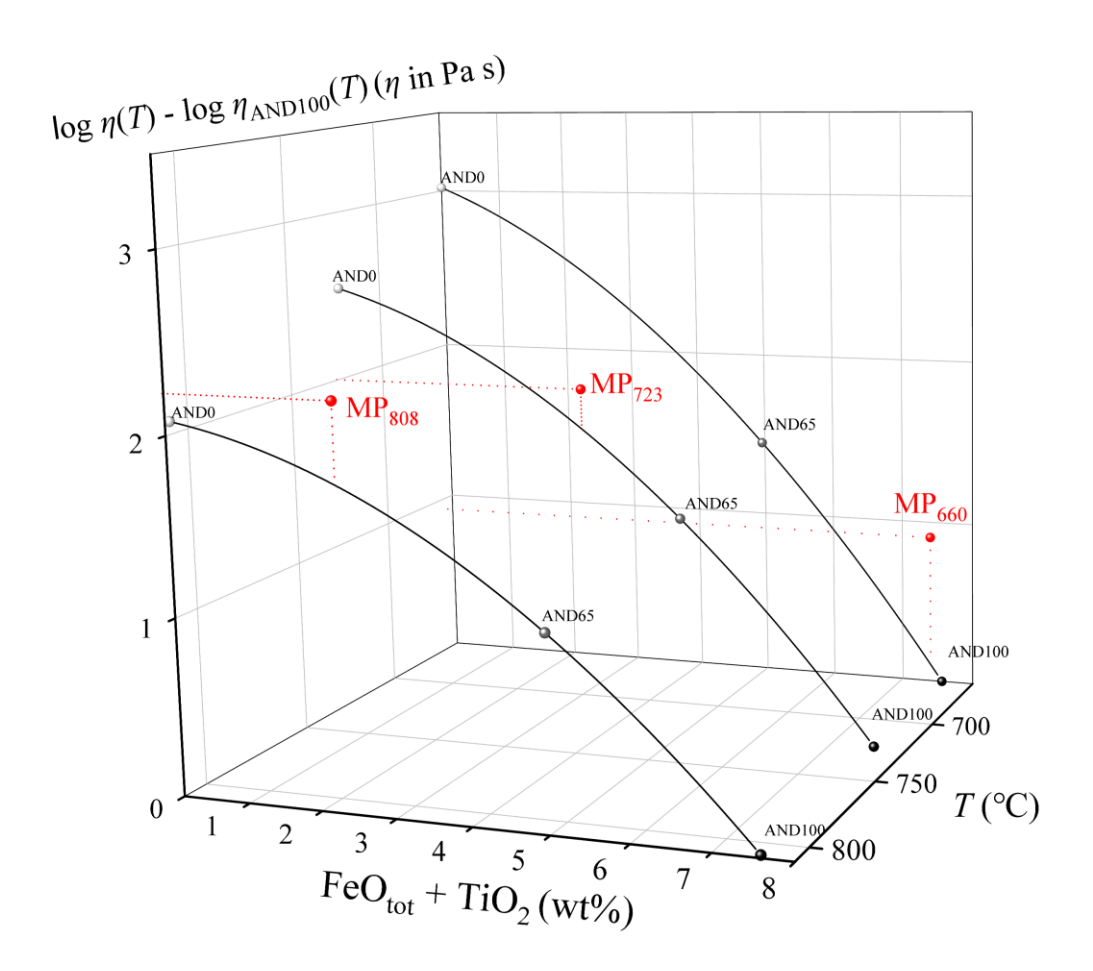


Figure 25. Normalized andesite viscosity as a function of temperature and FeO_{tot}+ TiO₂ content (wt%, STEM-EDS-derived residual composition). Viscosity is normalized to the AND100 melt. The MP sub-index represents the temperature (°C) of micropenetration measurement. The black curves correspond to the viscosity as a function of FeO_{tot} + TiO₂ content (wt%) at 660, 723 and 808 °C respectively. Figure from Valdivia et al. (2025).

STEM-EDS analyses revealed that nanolites are consistently surrounded by Al-rich shells, while the surrounding matrix becomes increasingly enriched in SiO₂, reaching concentrations of up to ~70 wt%. This value exceeds both the starting composition and that of the most polymerized, Fe-free melt (AND0), confirming the development of nanoscale chemical heterogeneity during nanolite formation. These chemically distinct domains (i.e., Ferich nanocrystals, Al-rich halos, and a highly polymerized SiO₂-rich matrix), introduce strong contrasts in local melt structure and flow behavior, significantly enhancing viscosity even at very low crystallinity.

These effects are most pronounced during early stages of crystallization (e.g., MP₆₆₀ in Fig. 25), where element redistribution is maximized and crystal content remains low. At higher temperatures, such as 808 °C, SAXS and WAXS analyses revealed nanolite growth and the onset of particle interactions. Additionally, co-crystallization of pyroxene was also detected, suggesting the emergence of a more complex crystalline assemblage, consistent with textures observed in natural samples from andesitic eruptions.

In conclusion, our results demonstrate that nanolite formation in andesitic melts leads to rapid and substantial increases in viscosity through the development of nanoscale chemical heterogeneity. These effects cannot be explained solely by changes in melt composition or crystal content alone. Instead, they result from dynamic melt reorganization, driven by element redistribution and structural segregation around growing nanolites. This process likely influences eruptive transitions in intermediate magmas, where even limited crystallization can significantly alter flow dynamics and promote fragmentation.

3.3. A viscosity model for hydrous andesitic magmas

Andesitic magmas are characterized by their high viscosity and volatile content.

Because viscosity governs the efficiency of degassing and the transition between effusive and

explosive behavior, accurately describing the rheology of hydrous andesitic melts is critical for modelling magma ascent and fragmentation. However, widely used models fail to reproduce the viscosity of hydrous andesitic melts, particularly in Fe-bearing systems where nanocrystallization and water loss often occur during measurements. In this study, we present a new viscosity model calibrated for variable transition metal content, using a combination of viscometry, calorimetry, and Brillouin spectroscopy, with a specific focus on the andesitic magma of Sakurajima volcano (Japan).

We investigated two compositional endmembers: AND100, a Fe-Ti-Mn-bearing andesite representative of Sakurajima, and AND0, an otherwise identical composition from which all transition metals were removed. Each composition was hydrated to water contents between 0.6 and 5.6 wt%. The amorphous and nanolite-free nature of the starting materials was confirmed using SEM and Raman spectroscopy, while the iron speciation was measured using Mössbauer spectroscopy. Water contents were determined with both KFT and FTIR techniques. Post-experiment Raman, Mössbauer, and FTIR analyses were performed to assess possible structural or compositional changes during viscosity measurements.

Viscosity was determined using micropenetration (MP), conventional (C-DSC), and flash (F-DSC) differential scanning calorimetry. Glass transition temperatures (T_g) were derived from C-DSC. Our results indicate that T_g decreases systematically with increasing water content in both systems, but the reduction is more pronounced in AND0, indicating a stronger depolymerizing effect of water in the absence of transition metals.

To model the viscosity of these systems, we used the MYEGA equation, with T_g and the melt fragility (m) as primary inputs. However, previously established relationships between sound velocity (K/G) and m (e.g., Cassetta et al., 2021) did not accurately reflect the behavior of our melts. We therefore established two new empirical relationships linking the melt fragility to K/G, tailored specifically for Fe-bearing and Fe-free compositions (Fig. 26). These were

derived from a well-characterized set of anhydrous endmembers, capturing the compositional dependence of elastic properties on melt structure.

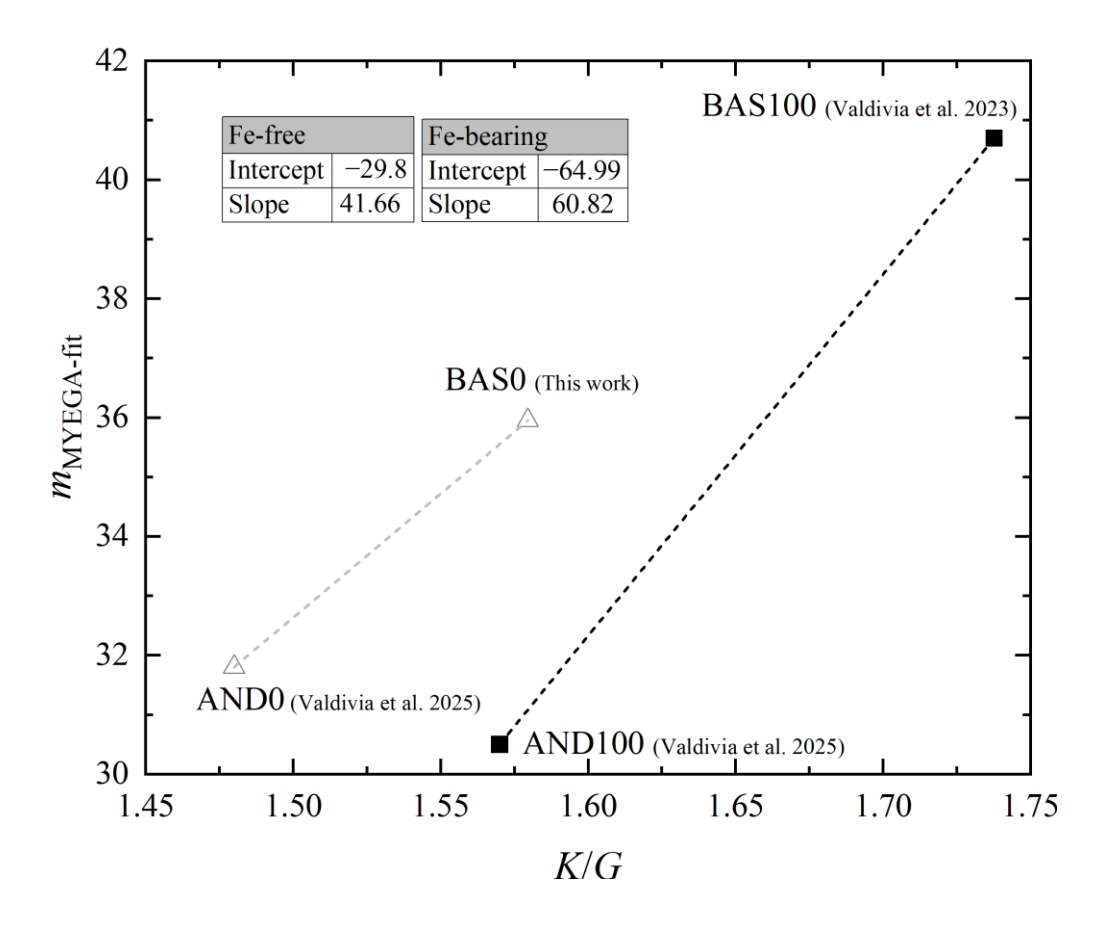


Figure 26. Viscosity-derived melt fragility ($m_{\text{MYEGA-fit}}$) as a function of K/G ratio. White open triangles are Fe-free samples and black filled squares are Fe-bearing compositions. Dashed lines represent the linear regressions.

We first modeled the viscosity of the two end-member compositions, AND100 and AND0, as functions of water content and temperature (Fig. 27). We then extended this approach by deriving a generalized viscosity model based on mathematical relationships linking relative composition, glass transition temperature (T_g), and melt fragility (m). Contrary to earlier models (e.g., Giordano et al., 2008), which predicts a decrease in melt fragility with hydration, we observed a linear increase in fragility with water content in both compositional series. We validated the model using an intermediate composition, AND65 (4.2 wt% H_2O), and successfully reproduced both T_g and viscosity within 0.03 log units.

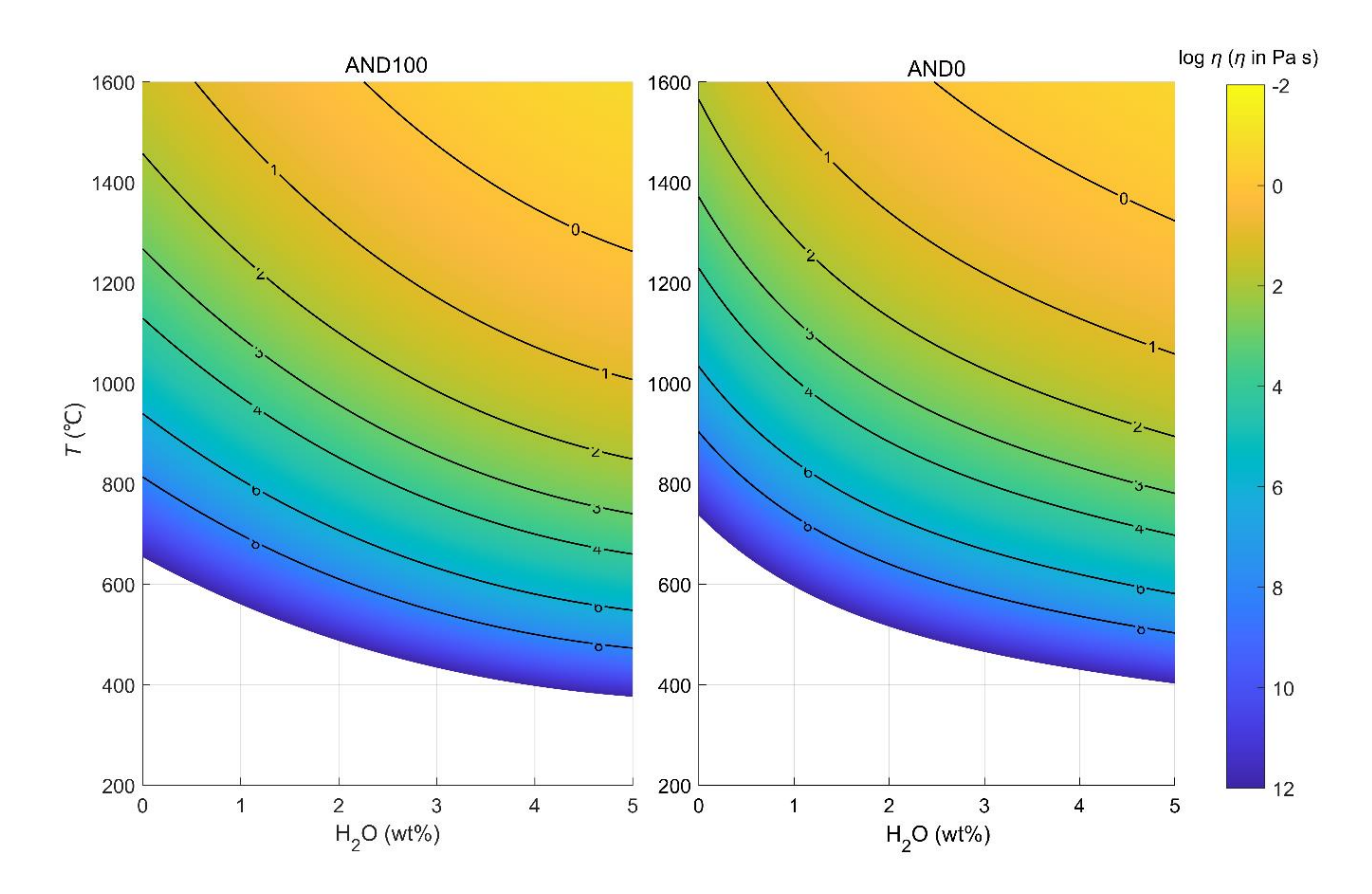


Figure 27. Viscosity of AND100 and AND0 as a function of water content (wt%) and temperature (°C).

Finally, we applied the model to calculate viscosities under pre-eruptive conditions relevant for Sakurajima andesite (1030 °C, 3 wt% H₂O). Our model predicts a viscosity that is 45 times lower than estimates from previous models. Similar reductions were obtained for other andesitic volcanoes, confirming that previous approaches have systematically overestimated the viscosity of hydrous andesitic melts.

In conclusion, we present a new viscosity model for hydrous andesitic melts that accounts for the combined influence of water content, temperature, and transition metal concentration. The viscosity model integrates new Brillouin-derived relationships for fragility and provides significantly improved accuracy for estimating pre-eruptive viscosity, offering a

robust framework for modelling magma ascent and fragmentation in volatile-rich andesitic systems.

3.4. List of manuscripts and statement of authors' contribution

[1] **Valdivia, P.,** Zandonà, A., Kurnosov, A., Ballaran, T.B., Deubener, J., Di Genova, D.. Are volcanic melts less viscous than we thought? The case of Stromboli basalt. *Contrib. Mineral. Petrol.* 178, 45 (2023). https://doi.org/10.1007/s00410-023-02024-w

Pedro Valdivia (**P.V.**) synthesized the starting materials, processed the experimental data, performed the analyses, derived the viscosity model, constructed the figures and tables, and drafted the original manuscript. **P.V.** and Danilo Di Genova (D.D.G.) conducted viscometry, calorimetry, Raman spectroscopy, and water content analyses. **P.V.**, Alexander Kurnosov (A.K.), and Tiziana Boffa Ballaran (T.B.B.) performed the Brillouin experiments. Joachim Deubener (J.D.) facilitated access to experimental laboratories. All co-authors reviewed and contributed to the final version of the manuscript.

[2] **Valdivia**, **P**., Zandonà, A., Löschmann, J., Bondar, D., Genevois, C., Canizarès, A., Allix, M., Miyajima, N., Kurnosov, A., Ballaran, T.B., Fiore, F. Di, Vona, A., Romano, C., Deubener, J., Bamber, E.C., Longo, A., Di Genova, D. Nanoscale chemical heterogeneities control the viscosity of andesitic magmas. *Commun. Earth Environ.* 6, 455 (2025). https://doi.org/10.1038/s43247-025-02424-9

Pedro Valdivia (P.V.) synthesized the starting materials, processed the experimental data, performed the data analyses, derived the viscosity models, conducted Mössbauer experiments, constructed the figures and tables, and drafted the original manuscript. **P.V.**, Alessio Zandonà (A.Z.), and Danilo Di Genova (D.D.G.) conceptualized the original idea. A.Z. and Cécile Genevois carried out the in situ high-temperature TEM experiments. Dmitry Bondar and Aurélien Canizarès performed the high-temperature Raman measurements. **P.V.**, Jessica

Löschmann and D.D.G. conducted micropenetration, room-temperature Raman, and calorimetry analyses. **P.V.** and Nobuyoshi Miyajima executed the room-temperature TEM. **P.V.** and Fabrizio Di Fiore carried out concentric cylinder measurements. **P.V.**, Alexander Kurnosov and Tiziana Boffa Ballaran performed the Brillouin analyses. Joachim Deubener, Claudia Romano, Alessandro Vona, and Mathieu Allix facilitated laboratory access and instrument availability. **P.V.**, A.Z., Emily C. Bamber and D.D.G. revised the manuscript following peer review. D.D.G. and Alessandro Longo processed SAXS/WAXS data. All coauthors provided feedback and contributed to the final version of the manuscript.

[3] **Valdivia, P.**, Löschmann, J., Zandonà A., Bondar, D., Kurnosov, A., Deubener, J., Di Genova, D. A viscosity model for hydrous andesitic magmas. To be submitted to *Earth Planet*. *Sci. Lett*.

Pedro Valdivia (**P.V.**) processed the experimental data, performed the Raman analyses, derived the viscosity models, conducted Mössbauer and Karl Fischer titration (KFT) measurements, and constructed the figures and tables, and drafted the original manuscript. **P.V.** and Dmitry Bondar (D.B.) synthesized the starting materials and conducted FTIR measurements. **P.V.** and Danilo Di Genova (D.D.G.) conceptualized the original idea. **P.V.** and Jessica Löschmann (J.L.) conducted micropenetration and calorimetry experiments. **P.V.** and Alexander Kurnosov (A.K.) performed the Brillouin analyses. **P.V.**, Alessio Zandonà (A.Z.), and D.D.G. revised the manuscript following peer review. All co-authors provided feedback and contributed to the final version of the manuscript.

References

- Adam, G., Gibbs, J.H., 1965. On the temperature dependence of cooperative relaxation properties in glass-forming liquids. J. Chem. Phys. 43, 139–146. https://doi.org/10.1063/1.1696442
- Alidibirov, M., Dingwell, D.B., 1996. Magma fragmentation by rapid decompression. Nature 380, 146–148. https://doi.org/10.1038/380146a0
- Andrews, B., Befus, K.S., 2020. Supersaturation Nucleation and Growth of Plagioclase: a numerical model of decompression-induced crystallization. Contrib. Mineral. Petrol. 175. https://doi.org/10.1007/s00410-020-1660-9
- Andronico, D., Del Bello, E., D'Oriano, C., Landi, P., Pardini, F., Scarlato, P., de' Michieli Vitturi, M., Taddeucci, J., Cristaldi, A., Ciancitto, F., Pennacchia, F., Ricci, T., Valentini, F., 2021. Uncovering the eruptive patterns of the 2019 double paroxysm eruption crisis of Stromboli volcano. Nat. Commun. 12, 1–14. https://doi.org/10.1038/s41467-021-24420-1
- Angell, C.A., 1995. Formation of Glasses from Liquids and Biopolymers. Science (80-.). 267, 1924–1935. https://doi.org/10.1126/science.267.5206.1924
- Arzilli, F., La Spina, G., Burton, M.R., Polacci, M., Le Gall, N., Hartley, M.E., Di Genova, D., Cai, B., Vo, N.T., Bamber, E.C., Nonni, S., Atwood, R., Llewellin, E.W., Brooker, R.A., Mader, H.M., Lee, P.D.D., 2019. Magma fragmentation in highly explosive basaltic eruptions induced by rapid crystallization. Nat. Geosci. 12, 1023–1028. https://doi.org/10.1038/s41561-019-0468-6
- Arzilli, F., Polacci, M., La Spina, G., Le Gall, N., Llewellin, E.W., Brooker, R.A., Torres-Orozco, R., Di Genova, D., Neave, D.A., Hartley, M.E., Mader, H.M., Giordano, D., Atwood, R., Lee, P.D., Heidelbach, F., Burton, M.R., 2022. Dendritic crystallization in hydrous basaltic magmas controls magma mobility within the Earth's crust. Nat. Commun. 13. https://doi.org/10.1038/s41467-022-30890-8
- Baker, D.R., 1996. Granitic melt viscosities: Empirical and configurational entropy models for their calculation. Am. Mineral. 81, 126–134. https://doi.org/10.2138/am-1996-1-216
- Bamber, E.C., Arzilli, F., Polacci, M., Hartley, M.E., Fellowes, J., Di Genova, D., Chavarría, D., Saballos, J.A., Burton, M., 2020. Pre- and syn-eruptive conditions of a basaltic Plinian eruption at Masaya Volcano, Nicaragua: The Masaya Triple Layer (2.1 ka). J. Volcanol. Geotherm. Res. 392, 106761. https://doi.org/10.1016/j.jvolgeores.2019.106761
- Barone, G., Mazzoleni, P., Corsaro, R.A., Costagliola, P., Di Benedetto, F., Ciliberto, E., Gimeno, D., Bongiorno, C., Spinella, C., 2016. Nanoscale surface modification of Mt. Etna volcanic ashes. Geochim. Cosmochim. Acta 174, 70–84. https://doi.org/10.1016/j.gca.2015.11.011
- Behrens, H., Bauer, U., Reinsch, S., Kiefer, P., Müller, R., Deubener, J., 2018. Structural relaxation mechanisms in hydrous sodium borosilicate glasses. J. Non. Cryst. Solids 497, 30–39. https://doi.org/10.1016/j.jnoncrysol.2018.05.025
- Behrens, H., Misiti, V., Freda, C., Vetere, F., Botcharnikov, R.E., Scarlato, P., 2009.

- Solubility of H₂O and CO₂ in ultrapotassic melts at 1200 and 1250 °C and pressure from 50 to 500 MPa. Am. Mineral. 94, 105–120. https://doi.org/10.2138/am.2009.2796
- Behrens, H., Romano, C., Nowak, M., Holtz, F., Dingwell, D.B., 1996. Near-infrared spectroscopic determination of water species in glasses of the system MAISi3O8 (M = Li, Na, K): an interlaboratory study. Chem. Geol. 128, 41–63. https://doi.org/10.1016/0009-2541(95)00162-X
- Blundy, J.D., Cashman, K. V., 2001. Ascent-driven crystallisation of dacite magmas at Mount St Helens, 1980-1986. Contrib. Mineral. Petrol. 140, 631–650. https://doi.org/10.1007/s004100000219
- Bondar, D., Canizarès, A., Bilardello, D., Valdivia, P., Zandonà, A., Romano, C., Allix, M., Di Genova, D., 2025. Nanolite crystallization in volcanic Glasses: Insights from high-temperature Raman spectroscopy and low-temperature rock-magnetic analysis. Geochemistry, Geophys. Geosystems 26. https://doi.org/10.1029/2024GC011846
- Botcharnikov, R.E., Holtz, F., Behrens, H., 2015. Solubility and fluid-melt partitioning of H₂O and Cl in andesitic magmas as a function of pressure between 50 and 500 MPa. Chem. Geol. 418, 117–131. https://doi.org/10.1016/j.chemgeo.2015.07.019
- Botcharnikov, R.E., Holtz, F., Behrens, H., 2007. The effect of CO₂ on the solubility of H₂O-Cl fluids in andesitic melt. Eur. J. Mineral. 19, 671–680. https://doi.org/10.1127/0935-1221/2007/0019-1752
- Bouhifd, M.A., Richet, P., Besson, P., Roskosz, M., Ingrin, J., 2004. Redox state, microstructure and viscosity of a partially crystallized basalt melt. Earth Planet. Sci. Lett. 218, 31–44. https://doi.org/10.1016/S0012-821X(03)00641-1
- Bowen, N.L., 1947. Magmas. Bull. Geol. Soc. Am. 58, 263–280. https://doi.org/https://doi.org/10.1130/0016-7606(1947)58[263:M]2.0.CO;2
- Boyd, F.R., England, J.L., 1960. Apparatus for phase-equilibrium measurements at pressures up to 50 kilobars and temperatures up to 1750°C. J. Geophys. Res. 65, 741–748. https://doi.org/https://doi.org/10.1029/JZ065i002p00741
- Burany, S., 2003. Scanning Electron Microscopy and X-Ray Microanalysis . J. Goldstein, D. Newbury, D. Joy, C, Lyman, P. Echlin, E. Lifshin, L. Sawyer, and J. Michael. Kluwer Academic, Plenum Publishers, New York; 2003, 688 pages. ISBN 0-306-47292-9. Microsc. Microanal. 9, 484–484. https://doi.org/10.1017/S1431927603030617
- Cáceres, F., Hess, K.U., Eitel, M., Döblinger, M., McCartney, K.N., Colombier, M., Gilder, S.A., Scheu, B., Kaliwoda, M., Dingwell, D.B., 2024. Oxide nanolitisation-induced melt iron extraction causes viscosity jumps and enhanced explosivity in silicic magma. Nat. Commun. 15. https://doi.org/10.1038/s41467-024-44850-x
- Cáceres, F., Wadsworth, F.B., Scheu, B., Colombier, M., Madonna, C., Cimarelli, C., Hess, K.U., Kaliwoda, M., Ruthensteiner, B., Dingwell, D.B., 2020. Can nanolites enhance eruption explosivity? Geology 48, 997–1001. https://doi.org/10.1130/G47317.1
- Campagnola, S., Vona, A., Romano, C., Giordano, G., 2016. Crystallization kinetics and rheology of leucite-bearing tephriphonolite magmas from the Colli Albani volcano (Italy). Chem. Geol. 424, 12–29. https://doi.org/10.1016/j.chemgeo.2016.01.012
- Cashman, K. V., Scheu, B., 2015. Chapter 25 Magmatic Fragmentation, in: Sigurdsson, H. (Ed.), The Encyclopedia of Volcanoes (Second Edition). Academic Press, Amsterdam,

- pp. 459–471. https://doi.org/https://doi.org/10.1016/B978-0-12-385938-9.00025-0
- Cassetta, M., Di Genova, D., Zanatta, M., Ballaran, T.B., Kurnosov, A., Giarola, M., Mariotto, G., Boffa Ballaran, T., 2021. Estimating the viscosity of volcanic melts from the vibrational properties of their parental glasses. Sci. Rep. 11, 1–14. https://doi.org/10.1038/s41598-021-92407-5
- Cassidy, M., Manga, M., Cashman, K., Bachmann, O., 2018. Controls on explosive-effusive volcanic eruption styles. Nat. Commun. 9, 2839. https://doi.org/10.1038/s41467-018-05293-3
- Chevrel, M.O., Cimarelli, C., DeBiasi, L., Hanson, J.B., Lavallée, Y., Arzilli, F., Dingwell, D.B., 2015. Viscosity measurements of crystallizing andesite from Tungurahua volcano (Ecuador). Geochemistry, Geophys. Geosystems 16, 870–889. https://doi.org/10.1002/2014GC005661
- Cormier, L., 2014. Nucleation in glasses New experimental findings and recent theories. Procedia Mater. Sci. 7, 60–71. https://doi.org/10.1016/j.mspro.2014.10.009
- Costa, A., 2005. Viscosity of high crystal content melts: Dependence on solid fraction. Geophys. Res. Lett. 32, 1–5. https://doi.org/10.1029/2005GL024303
- Davì, M., Behrens, H., Vetere, F., De Rosa, R., 2009. The viscosity of latitic melts from Lipari (Aeolian Islands, Italy): Inference on mixing—mingling processes in magmas. Chem. Geol. 259, 89–97. https://doi.org/10.1016/j.chemgeo.2008.10.009
- Degruyter, W., Bachmann, O., Burgisser, A., Manga, M., 2012. The effects of outgassing on the transition between effusive and explosive silicic eruptions. Earth Planet. Sci. Lett. 349–350, 161–170. https://doi.org/10.1016/j.epsl.2012.06.056
- Deubener, J., Bornhöft, H., Reinsch, S., Müller, R., Lumeau, J., Glebova, L.N., Glebov, L.B., 2009. Viscosity, relaxation and elastic properties of photo-thermo-refractive glass. J. Non. Cryst. Solids 355, 126–131. https://doi.org/10.1016/j.jnoncrysol.2008.10.002
- Di Fiore, F., Vona, A., Di Genova, D., Pontesilli, A., Calabrò, L., Mollo, S., Taddeucci, J., Romano, C., Scarlato, P., 2024. Magma titanium and iron contents dictate crystallization timescales and rheological behaviour in basaltic volcanic systems. Commun. Earth Environ. 5. https://doi.org/10.1038/s43247-024-01452-1
- Di Genova, D., Bondar, D., Zandonà, A., Valdivia, P., Al-Mukadam, R., Fei, H., Withers, A.C., Boffa Ballaran, T., Kurnosov, A., McCammon, C., Deubener, J., Katsura, T., 2023. Viscosity of anhydrous and hydrous peridotite melts. Chem. Geol. 625. https://doi.org/10.1016/j.chemgeo.2023.121440
- Di Genova, D., Brooker, R.A., Mader, H.M., Drewitt, J.W.E.E., Longo, A., Deubener, J., Neuville, D.R., Fanara, S., Shebanova, O., Anzellini, S., Arzilli, F., Bamber, E.C., Hennet, L., La Spina, G., Miyajima, N., 2020a. In situ observation of nanolite growth in volcanic melt: A driving force for explosive eruptions. Sci. Adv. 6. https://doi.org/10.1126/sciadv.abb0413
- Di Genova, D., Caracciolo, A., Kolzenburg, S., 2018. Measuring the degree of "nanotilization" of volcanic glasses: Understanding syn-eruptive processes recorded in melt inclusions. Lithos 318–319, 209–218. https://doi.org/10.1016/j.lithos.2018.08.011
- Di Genova, D., Kolzenburg, S., Wiesmaier, S., Dallanave, E., Neuville, D.R., Hess, K.U., Dingwell, D.B., 2017. A compositional tipping point governing the mobilization and

- eruption style of rhyolitic magma. Nature 552, 235–238. https://doi.org/10.1038/nature24488
- Di Genova, D., Romano, C., Hess, K.U., Vona, A., Poe, B.T., Giordano, D., Dingwell, D.B., Behrens, H., 2013. The rheology of peralkaline rhyolites from Pantelleria Island. J. Volcanol. Geotherm. Res. 249, 201–216. https://doi.org/10.1016/j.jvolgeores.2012.10.017
- Di Genova, D., Zandona, A., Deubener, J., 2020b. Unravelling the effect of nanoheterogeneity on the viscosity of silicate melts: Implications for glass manufacturing and volcanic eruptions. J. Non. Cryst. Solids 545, 120248. https://doi.org/10.1016/j.jnoncrysol.2020.120248
- Dingwell, D.B., 1996. Volcanic dilemma flow or blow? Science (80-.). 273, 1054–1055. https://doi.org/10.1126/science.273.5278.1054
- Dingwell, D.B., Romano, C., Hess, K.U., 1996. The effect of water on the viscosity of a haplogranitic melt under P-T-X conditions relevant to silicic volcanism. Contrib. Mineral. Petrol. 124, 19–28. https://doi.org/10.1007/s004100050170
- Dingwell, D.B., Webb, S.L., 1990. Relaxation in silicate melts. Eur. J. Mineral. 2, 427–451. https://doi.org/10.1127/ejm/2/4/0427
- Dixon, J.E., Stolper, E.M., Holloway, J.R., 1995. An experimental study of water and carbon dioxide solubilities in mid-ocean ridge basaltic liquids. part I: Calibration and solubility models. J. Petrol. 36, 1607–1631. https://doi.org/10.1093/oxfordjournals.petrology.a037267
- Douglas, R.W., Armstrong, W.L., Edward, J., Hall, D., 1965. A penetration viscometer. Glas. Technol. 6, 52–55.
- Fanesi, E., Di Genova, D., Valdivia, P., Bondar, D., Dominijanni, S., Abeykoon, S., Giuliani, G., Kurnosov, A., Giordano, G., Cassetta, M., Vona, A., Romano, C., Arzilli, F., 2025.
 A review of the differential scanning calorimetry shift–factor approach: Application to Colli Albani melt viscosity and implications for mafic Plinian eruptions. J. Volcanol. Geotherm. Res. 461, 108276. https://doi.org/10.1016/j.jvolgeores.2025.108276
- Förster, S., Timmann, A., Konrad, M., Schellbach, C., Meyer, A., Funari, S.S., Mulvaney, P., Knott, R., 2005. Scattering curves of ordered mesoscopic materials. J. Phys. Chem. B 109, 1347–1360. https://doi.org/10.1021/jp0467494
- Friedman, I., Long, W., Smith, R.L., 1963. Viscosity and water content of rhyolite glass. J. Geophys. Res. 68, 6523–6535. https://doi.org/10.1029/jz068i024p06523
- Fulcher, G.S., 1925. Analysis of recent measurements of the viscosity of glasses. J. Am. Ceram. Soc. 75, 1043–1055. https://doi.org/10.1111/j.1151-2916.1992.tb05536.x
- Giordano, D., Ardia, P., Romano, C., Dingwell, D.B., Di Muro, A., Schmidt, M.W., Mangiacapra, A., Hess, K.U., 2009. The rheological evolution of alkaline Vesuvius magmas and comparison with alkaline series from the Phlegrean Fields, Etna, Stromboli and Teide. Geochim. Cosmochim. Acta 73, 6613–6630. https://doi.org/10.1016/j.gca.2009.07.033
- Giordano, D., Dingwell, D.B., 2003. The kinetic fragility of natural silicate melts. J. Phys. Condens. Matter 15, S945–S954. https://doi.org/10.1088/0953-8984/15/11/318

- Giordano, D., Russell, J.K., Dingwell, D.B., 2008. Viscosity of magmatic liquids: A model. Earth Planet. Sci. Lett. 271, 123–134. https://doi.org/10.1016/j.epsl.2008.03.038
- Gonnermann, H.M., 2015. Magma Fragmentation. Annu. Rev. Earth Planet. Sci. 43, 431–458. https://doi.org/10.1146/annurev-earth-060614-105206
- Gonnermann, H.M., Manga, M., 2013. Dynamics of magma ascent in the volcanic conduit, in: Fagents, S.A., Gregg, T.K.P., Lopes, R.M.C.E. (Eds.), Modeling Volcanic Processes. Cambridge University Press, pp. 55–84. https://doi.org/10.1017/CBO9781139021562.004
- Gonnermann, H.M., Manga, M., 2012. Chapter 4: Dynamics of magma ascent in the volcanic conduit. Model. Volcan. Process. Phys. Math. Volcanism 55–84.
- González-García, D., Giordano, D., Russell, J.K., Dingwell, D.B., 2020. A Raman spectroscopic tool to estimate chemical composition of natural volcanic glasses. Chem. Geol. 556, 119819. https://doi.org/10.1016/j.chemgeo.2020.119819
- Gumede, T.P., Luyt, A.S., Pérez-Camargo, R.A., Tercjak, A., Müller, A.J., 2018. Morphology, nucleation, and isothermal crystallization kinetics of Poly(Butylene Succinate) mixed with a polycarbonate/MWCNT masterbatch. Polymers (Basel). 10, 1–22. https://doi.org/10.3390/polym10040424
- Hammer, J.E., Cashman, K. V., Hoblitt, R.P., Newman, S., 1999. Degassing and microlite crystallization during pre-climactic events of the 1991 eruption of Mt. Pinatubo, Philippines. Bull. Volcanol. 60, 355–380. https://doi.org/10.1007/s004450050238
- Holloway, J.R., Dixon, J.E., Pawley, A.R., 1992. An internally heated, rapid-quench, high-pressure vessel. Am. Mineral. 77, 643–646.
- Hughes, E.C., Buse, B., Kearns, S.L., Blundy, J.D., Kilgour, G., Mader, H.M., 2019. Low analytical totals in EPMA of hydrous silicate glass due to sub-surface charging: Obtaining accurate volatiles by difference. Chem. Geol. 505, 48–56. https://doi.org/10.1016/j.chemgeo.2018.11.015
- Hui, H., Zhang, Y., 2007. Toward a general viscosity equation for natural anhydrous and hydrous silicate melts. Geochim. Cosmochim. Acta 71, 403–416. https://doi.org/10.1016/j.gca.2006.09.003
- Hummel, W., Arndt, J., 1985. Variation of viscosity with temperature and composition in the plagioclase system. Contrib. Mineral. Petrol. 90, 83–92. https://doi.org/10.1007/BF00373044
- Hurwitz, S., Navon, O., 1994. Bubble nucleation in rhyolitic melts: Experiments at high pressure, temperature, and water content. Earth Planet. Sci. Lett. 122, 267–280. https://doi.org/10.1016/0012-821X(94)90001-9
- Ishibashi, H., Sato, H., 2007. Viscosity measurements of subliquidus magmas: Alkali olivine basalt from the Higashi-Matsuura district, Southwest Japan. J. Volcanol. Geotherm. Res. 160, 223–238. https://doi.org/10.1016/j.jvolgeores.2006.10.001
- Jeffries, C.M., Ilavsky, J., Martel, A., Hinrichs, S., Meyer, A., Pedersen, J.S., Sokolova, A. V., Svergun, D.I., 2021. Small-angle X-ray and neutron scattering. Nat. Rev. Methods Prim. 1, 70. https://doi.org/10.1038/s43586-021-00064-9
- Jensen, H., Pedersen, J.H., Jørgensen, J.E., Pedersen, J.S., Joensen, K.D., Iversen, S.B.,

- Søgaard, E.G., 2006. Determination of size distributions in nanosized powders by TEM, XRD, and SAXS. J. Exp. Nanosci. 1, 355–373. https://doi.org/10.1080/17458080600752482
- Johannes, W., Bell, P.M., Mao, H.K., Boettcher, A.L., Chipman, D.W., Hays, J.F., Newton, R.C., Seifert, F., 1971. An interlaboratory comparison of piston-cylinder pressure calibration using the albite-breakdown reaction. Contrib. Mineral. Petrol. 32, 24–38. https://doi.org/10.1007/BF00372231
- Kleest, C., Webb, S.L., Fanara, S., 2020. Rheology of melts from the colli albani volcanic district (Italy): a case study. Contrib. Mineral. Petrol. 175, 82. https://doi.org/10.1007/s00410-020-01720-1
- Knafelc, J., Bryan, S.E., Jones, M.W.M., Gust, D., Mallmann, G., Cathey, H.E., Berry, A.J., Ferré, E.C., Howard, D.L., 2022. Havre 2012 pink pumice is evidence of a short-lived, deep-sea, magnetite nanolite-driven explosive eruption. Commun. Earth Environ. 3, 1–11. https://doi.org/10.1038/s43247-022-00355-3
- Koyaguchi, T., Mitani, N.K., 2005. A theoretical model for fragmentation of viscous bubbly magmas in shock tubes. J. Geophys. Res. 110, B10202. https://doi.org/10.1029/2004JB003513
- Kueppers, U., Scheu, B., Spieler, O., Dingwell, D.B., 2006. Fragmentation efficiency of explosive volcanic eruptions: A study of experimentally generated pyroclasts. J. Volcanol. Geotherm. Res. 153, 125–135. https://doi.org/10.1016/j.jvolgeores.2005.08.006
- La Spina, G., Arzilli, F., Burton, M.R., Polacci, M., Clarke, A.B., 2022. Role of volatiles in highly explosive basaltic eruptions. Commun. Earth Environ. 3, 156. https://doi.org/10.1038/s43247-022-00479-6
- La Spina, G., Burton, M., De'Michieli Vitturi, M., 2015. Temperature evolution during magma ascent in basaltic effusive eruptions: A numerical application to Stromboli volcano. Earth Planet. Sci. Lett. 426, 89–100. https://doi.org/10.1016/j.epsl.2015.06.015
- La Spina, G., Burton, M., De'Michieli Vitturi, M., Arzilli, F., 2016. Role of syn-eruptive plagioclase disequilibrium crystallization in basaltic magma ascent dynamics. Nat. Commun. 7. https://doi.org/10.1038/ncomms13402
- Langhammer, D., Di Genova, D., Steinle-Neumann, G., Steinle-Neumann, G., Steinle-Neumann, G., Steinle-Neumann, G., 2022. Modeling viscosity of volcanic melts with artificial neural networks. Geochemistry, Geophys. Geosystems 23, 24. https://doi.org/10.1029/2022GC010673
- Lautze, N.C., Houghton, B.F., 2007. Linking variable explosion style and magma textures during 2002 at Stromboli volcano, Italy. Bull. Volcanol. 69, 445–460. https://doi.org/10.1007/s00445-006-0086-1
- Lejeune, A.M., Richet, P., 1995. Rheology of crystal-bearing silicate melts: an experimental study at high viscosities. J. Geophys. Res. 100, 4215–4229. https://doi.org/10.1029/94JB02985
- Lesne, P., Scaillet, B., Pichavant, M., Iacono-Marziano, G., Beny, J.-M., 2011. The H₂O solubility of alkali basaltic melts: an experimental study. Contrib. Mineral. Petrol. 162, 133–151. https://doi.org/10.1007/s00410-010-0588-x

- Liebske, C., Behrens, H., Holtz, F., Lange, R.A., 2003. The influence of pressure and composition on the viscosity of andesitic melts. Geochim. Cosmochim. Acta 67, 473–485. https://doi.org/10.1016/S0016-7037(02)01139-0
- Liebske, C., Schmickler, B., Terasaki, H., Poe, B.T., Suzuki, A., Funakoshi, K. ichi, Ando, R., Rubie, D.C., 2005. Viscosity of peridotite liquid up to 13 GPa: Implications for magma ocean viscosities. Earth Planet. Sci. Lett. 240, 589–604. https://doi.org/10.1016/j.epsl.2005.10.004
- Longo, A., Giannici, F., Casaletto, M.P., Rovezzi, M., Sahle, C.J., Glatzel, P., Joly, Y., Martorana, A., 2022. Dynamic role of gold d-orbitals during CO oxidation under aerobic conditions. ACS Catal. 12, 3615–3627. https://doi.org/10.1021/acscatal.1c05739
- Mader, H.M., Llewellin, E.W., Mueller, S., 2013. The rheology of two-phase magmas: A review and analysis. J. Volcanol. Geotherm. Res. 257, 135–158. https://doi.org/10.1016/j.jvolgeores.2013.02.014
- Malfait, W.J., Sanchez-Valle, C., 2013. Effect of water and network connectivity on glass elasticity and melt fragility. Chem. Geol. 346, 72–80. https://doi.org/10.1016/j.chemgeo.2012.04.034
- Marshall, A.A., Manga, M., Brand, B.D., Andrews, B.J., 2022. Autobrecciation and fusing of mafic magma preceding explosive eruptions. Geology 50, 1177–1181. https://doi.org/10.1130/G50180.1
- Maurizio, C., Longo, A., Martorana, A., Cattaruzza, E., D'Acapito, F., Gonella, F., De Julian, C., Mattei, G., Mazzoldi, P., Padovani, S., Boeseckef, P., 2003. Grazing-incidence small-angle X-ray scattering and X-ray diffraction from magnetic clusters obtained by Co + Ni sequential ion implantation in silica. J. Appl. Crystallogr. 36, 732–735. https://doi.org/10.1107/S0021889803006137
- Mauro, J.C., Yue, Y., Ellison, A.J., Gupta, P.K., Allan, D.C., 2009. Viscosity of glass-forming liquids. Proc. Natl. Acad. Sci. U. S. A. 106, 19780–4. https://doi.org/10.1073/pnas.0911705106
- Meerlender, G., 1974. VISKOSITAETS-TEMPERATUR-VERHALTEN DES STANDARDGLASES I DER DGG. Glas. Ber 47, 1–3.
- Misiti, V., Vetere, F., Freda, C., Scarlato, P., Behrens, H., Mangiacapra, A., Dingwell, D.B., 2011. A general viscosity model of Campi Flegrei (Italy) melts. Chem. Geol. 290, 50–59. https://doi.org/10.1016/j.chemgeo.2011.08.010
- Misiti, V., Vetere, F., Mangiacapra, A., Behrens, H., Cavallo, A., Scarlato, P., Dingwell, D.B., 2009. Viscosity of high-K basalt from the 5th April 2003 Stromboli paroxysmal explosion. Chem. Geol. 260, 278–285. https://doi.org/10.1016/j.chemgeo.2008.12.023
- Moore, G., Vennemann, T., Carmichael, I.S.E., 1998. An empirical model for the solubility of H₂O in magmas to 3 kilobars. Am. Mineral. 83, 36–42. https://doi.org/10.2138/am-1998-1-203
- Mössbauer, R.L., 1958. Kernresonanzfluoreszenz von Gammastrahlung in Ir191. Zeitschrift für Phys. 151, 124–143. https://doi.org/10.1007/BF01344210
- Mueller, S., Llewellin, E.W., Mader, H.M., 2011a. The effect of particle shape on suspension viscosity and implications for magmatic flows. Geophys. Res. Lett. 38, 1–5. https://doi.org/10.1029/2011GL047167

- Mueller, S., Scheu, B., Kueppers, U., Spieler, O., Richard, D., Dingwell, D.B., 2011b. The porosity of pyroclasts as an indicator of volcanic explosivity. J. Volcanol. Geotherm. Res. 203, 168–174. https://doi.org/10.1016/j.jvolgeores.2011.04.006
- Mueller, S., Scheu, B., Spieler, O., Dingwell, D.B., 2008. Permeability control on magma fragmentation. Geology 36, 399–402. https://doi.org/10.1130/G24605A.1
- Mujin, M., Nakamura, M., 2020. Late-stage groundmass differentiation as a record of magma stagnation, fragmentation, and rewelding. Bull. Volcanol. 82, 48. https://doi.org/10.1007/s00445-020-01389-1
- Mujin, M., Nakamura, M., 2014. A nanolite record of eruption style transition. Geology 42, 611–614. https://doi.org/10.1130/G35553.1
- Mujin, M., Nakamura, M., Miyake, A., 2017. Eruption style and crystal size distributions: Crystallization of groundmass nanolites in the 2011 Shinmoedake eruption. Am. Mineral. 102, 2367–2380. https://doi.org/10.2138/am-2017-6052CCBYNCND
- Mysen, B.O., Richet, P., 2005. Silicate glasses and melts-property and structure. Dev. Geochemistry 10, 111–112.
- Narayanan, T., Sztucki, M., Zinn, T., Kieffer, J., Homs-Puron, A., Gorini, J., Van Vaerenbergh, P., Boesecke, P., 2022. Performance of the time-resolved ultra-small-angle X-ray scattering beamline with the Extremely Brilliant Source. J. Appl. Crystallogr. 55, 98–111. https://doi.org/10.1107/S1600576721012693
- Novikov, V.N., Ding, Y., Sokolov, A.P., 2005. Correlation of fragility of supercooled liquids with elastic properties of glasses. Phys. Rev. E Stat. Nonlinear, Soft Matter Phys. 71, 1–12. https://doi.org/10.1103/PhysRevE.71.061501
- Novikov, V.N., Sokolov, A.P., 2004. Poisson's ratio and the fragility of glass-forming liquids. Nature 431, 961–963. https://doi.org/10.1038/nature02947
- Ohlhorst, S., Behrens, H., Holtz, F., 2001. Compositional dependence of molar absorptivities of near-infrared OH-and H₂O bands in rhyolitic to basaltic glasses. Chem. Geol. 174, 5–20. https://doi.org/10.1016/S0009-2541(00)00303-X
- Okumura, S., Nakamura, M., Nakano, T., Uesugi, K., Tsuchiyama, A., 2010. Shear deformation experiments on vesicular rhyolite: Implications for brittle fracturing, degassing, and compaction of magmas in volcanic conduits. J. Geophys. Res. Solid Earth 115, 1–10. https://doi.org/10.1029/2009JB006904
- Okumura, S., Uesugi, K., Goto, A., Sakamaki, T., Matsumoto, K., Takeuchi, A., Miyake, A., 2022. Rheology of nanocrystal-bearing andesite magma and its roles in explosive volcanism. Commun. Earth Environ. 3, 241. https://doi.org/10.1038/s43247-022-00573-9
- Papale, P., 1999. Strain-induced magma fragmentation in explosive eruptions. Nature 397, 425–428. https://doi.org/10.1038/17109
- Pereira, L., Linard, Y., Wadsworth, F.B., Vasseur, J., Hess, K.U., Moretti, R., Dingwell, D.B., Neuville, D.R., 2024. The rheological response of magma to nanolitisation. J. Volcanol. Geotherm. Res. 448, 108039. https://doi.org/10.1016/j.jvolgeores.2024.108039
- Pichavant, M., Di Carlo, I., Rotolo, S.G., Scaillet, B., Burgisser, A., Le Gall, N., Martel, C.,

- 2013. Generation of CO₂-rich melts during basalt magma ascent and degassing. Contrib. Mineral. Petrol. 166, 545–561. https://doi.org/10.1007/s00410-013-0890-5
- Prescher, C., McCammon, C., Dubrovinsky, L., 2012. MossA: a program for analyzing energy-domain Mössbauer spectra from conventional and synchrotron sources. J. Appl. Crystallogr. 45, 329–331. https://doi.org/10.1107/S0021889812004979
- Richet, P., Lejeune, A.M.M., Holtz, F., Roux, J., 1996. Water and the viscosity of andesite melts. Chem. Geol. 128, 185–197. https://doi.org/10.1016/0009-2541(95)00172-7
- Richet, P., Whittington, A., Holtz, F., Behrens, H., Ohlhorst, S., Wilke, M., 2000. Water and the density of silicate glasses. Contrib. Mineral. Petrol. 138, 337–347. https://doi.org/10.1007/s004100050567
- Rinaldi, R., Llovet, X., 2015. Electron Probe Microanalysis: A Review of the Past, Present, and Future. Microsc. Microanal. 21, 1053–1069. https://doi.org/10.1017/S1431927615000409
- Ripepe, M., Lacanna, G., Pistolesi, M., Silengo, M.C., Aiuppa, A., Laiolo, M., Massimetti,
 F., Innocenti, L., Della Schiava, M., Bitetto, M., La Monica, F.P., Nishimura, T., Rosi,
 M., Mangione, D., Ricciardi, A., Genco, R., Coppola, D., Marchetti, E., Delle Donne,
 D., 2021. Ground deformation reveals the scale-invariant conduit dynamics driving
 explosive basaltic eruptions. Nat. Commun. 12. https://doi.org/10.1038/s41467-021-21722-2
- Robert, G., Whittington, A.G., Stechern, A., Behrens, H., 2013. The effect of water on the viscosity of a synthetic calc-alkaline basaltic andesite. Chem. Geol. 346, 135–148. https://doi.org/10.1016/j.chemgeo.2012.10.004
- Romano, C., Vona, A., Campagnola, S., Giordano, G., Arienzo, I., Isaia, R., 2020. Modelling and physico-chemical constraints to the 4.5 ka Agnano-Monte Spina Plinian eruption (Campi Flegrei, Italy). Chem. Geol. 532, 119301. https://doi.org/10.1016/j.chemgeo.2019.119301
- Rudyak, V.Y., Krasnolutskii, S.L., 2014. Dependence of the viscosity of nanofluids on nanoparticle size and material. Phys. Lett. Sect. A Gen. At. Solid State Phys. 378, 1845–1849. https://doi.org/10.1016/j.physleta.2014.04.060
- Russell, J.K., Hess, K.-U., Dingwell, D.B., 2022. Models for Viscosity of Geological Melts. Rev. Mineral. Geochemistry 87, 841–885. https://doi.org/10.2138/rmg.2022.87.18
- Sable, J.E., Houghton, B.F., Del Carlo, P., Coltelli, M., 2006. Changing conditions of magma ascent and fragmentation during the Etna 122 BC basaltic Plinian eruption: Evidence from clast microtextures. J. Volcanol. Geotherm. Res. 158, 333–354. https://doi.org/10.1016/j.jvolgeores.2006.07.006
- Scarani, A., Zandonà, A., Di Fiore, F., Valdivia, P., Putra, R., Miyajima, N., Bornhöft, H., Vona, A., Deubener, J., Romano, C., Di Genova, D., Zandona, A., 2022. A chemical threshold controls nanocrystallization and degassing behaviour in basalt magmas. Commun. Earth Environ. 3, 284. https://doi.org/10.1038/s43247-022-00615-2
- Schuessler, J.A., Botcharnikov, R.E., Behrens, H., Misiti, V., Freda, C., 2008. Amorphous materials: Properties, structure, and durability: Oxidation state of iron in hydrous phonotephritic melts. Am. Mineral. 93, 1493–1504. https://doi.org/10.2138/am.2008.2795
- Sehlke, A., Whittington, A.G., Robert, B., Harris, A., Gurioli, L., Médard, E., 2014.

- Pahoehoe to áá transition of Hawaiian lavas: An experimental study. Bull. Volcanol. 76. https://doi.org/10.1007/s00445-014-0876-9
- Sharma, A.K., Tiwari, A.K., Dixit, A.R., 2016. Rheological behaviour of nanofluids: A review. Renew. Sustain. Energy Rev. 53, 779–791. https://doi.org/10.1016/j.rser.2015.09.033
- Shaw, H.R., 1972. Viscosities of magmatic silicate liquids; an empirical method of prediction. Am. J. Sci. 272, 870–893. https://doi.org/10.2475/ajs.272.9.870
- Sinogeikin, S., Bass, J., Prakapenka, V., Lakshtanov, D., Shen, G., Sanchez-Valle, C., Rivers, M., 2006. Brillouin spectrometer interfaced with synchrotron radiation for simultaneous x-ray density and acoustic velocity measurements. Rev. Sci. Instrum. 77, 103905. https://doi.org/10.1063/1.2360884
- Sokolov, A.P., Novikov, V.N., Kisliuk, A., 2007. Fragility and mechanical moduli: Do they really correlate? Philos. Mag. 87, 613–621. https://doi.org/10.1080/14786430600880769
- Sparks, R.S.J., 2003. Dynamics of magma degassing. Geol. Soc. London, Spec. Publ. 213, 5—22. https://doi.org/10.1144/GSL.SP.2003.213.01.02
- Sparks, R.S.J., 1978. The dynamics of bubble formation and growth in magmas: A review and analysis. J. Volcanol. Geotherm. Res. 3, 1–37. https://doi.org/10.1016/0377-0273(78)90002-1
- Stabile, P., Radica, F., Bello, M., Behrens, H., Carroll, M.R., Paris, E., Giuli, G., 2018. H₂O solubility in pantelleritic melts: Pressure and alkali effects. Neues Jahrb. fur Mineral. Abhandlungen 195, 1–9. https://doi.org/10.1127/njma/2017/0060
- Stabile, P., Sicola, S., Giuli, G., Paris, E., Carroll, M.R., Deubener, J., Di Genova, D., 2021. The effect of iron and alkali on the nanocrystal-free viscosity of volcanic melts: A combined Raman spectroscopy and DSC study. Chem. Geol. 559, 119991. https://doi.org/10.1016/j.chemgeo.2020.119991
- Stevenson, R.J., Bagdassarov, N.S., Dingwell, D.B., Romano, C., 1998. The influence of trace amounts of water on the viscosity of rhyolites. Bull. Volcanol. 60, 89–97. https://doi.org/10.1007/s004450050218
- Su, Y., Huber, C., Bachmann, O., Zajacz, Z., Wright, H., Vazquez, J., 2016. The role of crystallization-driven exsolution on the sulfur mass balance in volcanic arc magmas. J. Geophys. Res. Solid Earth 121, 5624–5640. https://doi.org/10.1002/2016JB013184
- Tammann, G., Hesse, W., 1926. Die Abhängigkeit der Viskosität von der Temperatur bei unterkühlten Flüssigkeiten'. Allg. Chemie 156, 245–257.
- Thivet, S., Pereira, L., Menguy, N., Médard, É., Verdurme, P., Berthod, C., Troadec, D., Hess, K.U., Dingwell, D.B., Komorowski, J.C., 2023. Metastable liquid immiscibility in the 2018–2021 Fani Maoré lavas as a mechanism for volcanic nanolite formation. Commun. Earth Environ. 4. https://doi.org/10.1038/s43247-023-01158-w
- Urbain, G., Bottinga, Y., Richet, P., 1982. Viscosity of liquid silica, silicates and aluminosilicates. Geochim. Cosmochim. Acta 46, 1061–1072. https://doi.org/10.1016/0016-7037(82)90059-X
- Valdivia, P., Zandonà, A., Kurnosov, A., Ballaran, T.B., Deubener, J., Di Genova, D., 2023. Are volcanic melts less viscous than we thought? The case of Stromboli basalt. Contrib.

- Mineral. Petrol. 178, 45. https://doi.org/10.1007/s00410-023-02024-w
- Valdivia, P., Zandonà, A., Löschmann, J., Bondar, D., Genevois, C., Canizarès, A., Allix, M., Miyajima, N., Kurnosov, A., Ballaran, T.B., Di Fiore, F., Vona, A., Romano, C., Deubener, J., Bamber, E.C., Longo, A., Di Genova, D., 2025. Nanoscale chemical heterogeneities control the viscosity of andesitic magmas. Commun. Earth Environ. 6, 455. https://doi.org/10.1038/s43247-025-02424-9
- Vetere, F., Behrens, H., Holtz, F., Neuville, D.R., 2006. Viscosity of andesitic melts—new experimental data and a revised calculation model. Chem. Geol. 228, 233–245. https://doi.org/10.1016/j.chemgeo.2005.10.009
- Vetere, F., Behrens, H., Holtz, F., Vilardo, G., Ventura, G., 2010. Viscosity of crystal-bearing melts and its implication for magma ascent. J. Mineral. Petrol. Sci. 105, 151–163. https://doi.org/10.2465/jmps.090402
- Vetere, F., Behrens, H., Misiti, V., Ventura, G., Holtz, F., De Rosa, R., Deubener, J., 2007. The viscosity of shoshonitic melts (Vulcanello Peninsula, Aeolian Islands, Italy): Insight on the magma ascent in dikes. Chem. Geol. 245, 89–102. https://doi.org/10.1016/j.chemgeo.2007.08.002
- Vetere, F., Behrens, H., Schuessler, J.A., Holtz, F., Misiti, V., Borchers, L., 2008. Viscosity of andesite melts and its implication for magma mixing prior to Unzen 1991-1995 eruption. J. Volcanol. Geotherm. Res. 175, 208–217. https://doi.org/10.1016/j.jvolgeores.2008.03.028
- Vogel, H., 1921. Das Temperaturabhängigkeitsgesetz der Viskosität von Flüssigkeiten. Phys. Zeitschrift 22, 645–646.
- Vona, A., Romano, C., Dingwell, D.B., Giordano, D., 2011. The rheology of crystal-bearing basaltic magmas from Stromboli and Etna. Geochim. Cosmochim. Acta 75, 3214–3236. https://doi.org/10.1016/j.gca.2011.03.031
- Webb, S.L., Dingwell, D.B., 1990. Non-Newtonian rheology of igneous melts at high stresses and strain rates: experimental results for rhyolite, andesite, basalt, and nephelinite. J. Geophys. Res. 95, 15695–15701. https://doi.org/10.1029/jb095ib10p15695
- Whitfield, C.H., Brody, E.M., Bassett, W., 1976. Elastic moduli of NaCl by Brillouin scattering at high pressure in a diamond anvil cell. Rev. Sci. Instrum. 47, 942–947.
- Whittington, A., Richet, P., Holtz, F., 2000. Water and the viscosity of depolymerized aluminosilicate melts. Geochim. Cosmochim. Acta 64, 3725–3736. https://doi.org/10.1016/S0016-7037(00)00448-8
- Whittington, A.G., Hellwig, B.M., Behrens, H., Joachim, B., Stechern, A., Vetere, F., 2009. The viscosity of hydrous dacitic liquids: Implications for the rheology of evolving silicic magmas. Bull. Volcanol. 71, 185–199. https://doi.org/10.1007/s00445-008-0217-y
- Yoshida, K., Miyake, A., Okumura, S.H., Ishibashi, H., Okumura, S., Okamoto, A., Niwa, Y., Kimura, M., Sato, T., Tamura, Y., Ono, S., 2023. Oxidation-induced nanolite crystallization triggered the 2021 eruption of Fukutoku-Oka-no-Ba, Japan. Sci. Rep. 13, 7117. https://doi.org/10.1038/s41598-023-34301-w
- Zellmer, G.F., Sakamoto, N., Hwang, S.L., Matsuda, N., Iizuka, Y., Moebis, A., Yurimoto, H., 2016. Inferring the effects of compositional boundary layers on crystal nucleation, growth textures, and mineral chemistry in natural volcanic tephras through submicron-

resolution imaging. Front. Earth Sci. 4, 1–7. https://doi.org/10.3389/feart.2016.00088

Zhang, Y., 1999. A criterion for the fragmentation of bubbly magma based on brittle failure theory. Nature 402, 648–650. https://doi.org/10.1038/45210

4. Manuscript of the thesis

4.1 Are volcanic melt less viscous than we thought? The case of Stromboli basalt

Pedro Valdivia^{1*}, Alessio Zandonà², Alexander Kurnosov¹, Tiziana Boffa Ballaran¹, Joachim

Deubener³, Danilo Di Genova⁴

¹Bayerisches Geoinstitut, University of Bayreuth, Universitätsstraße 30, 95440, Bayreuth,

Germany

²Department of Glass and Ceramics, Institute of Materials Science, Friedrich-Alexander

University of Erlangen-Nuremberg, Martensstrasse 5, Erlangen, Germany

³Institute of Non-Metallic Materials, Clausthal University of Technology, Zehntnerstraße 2a,

D-38678 Clausthal-Zellerfeld, Germany

⁴Institute of Environmental Geology and Geoengineering, CNR, via Salaria km 29.300,

00015 Monterotondo, Rome, Italy

*Corresponding author: pedro.valdivia-munoz@uni-bayreuth.de

Status: Published

Contrib. Mineral. Petrol. 178, 45. https://doi.org/10.1007/s00410-023-02024-w

88

ORIGINAL PAPER



Are volcanic melts less viscous than we thought? The case of Stromboli basalt

Pedro Valdivia¹ · Alessio Zandonà² · Alexander Kurnosov¹ · Tiziana Boffa Ballaran¹ · Joachim Deubener³ · Danilo Di Genova⁴

Received: 15 February 2023 / Accepted: 12 June 2023 © The Author(s) 2023

Abstract

Melt viscosity is one of the most critical physical properties controlling magma transport dynamics and eruptive style. Although viscosity measurements are widely used to study and model the flow behavior of magmas, recent research has revealed that nanocrystallization of Fe–Ti-oxides can compromise the reliability of viscosity data. This phenomenon can occur during laboratory measurements around the glass transition temperature (T_g) and lead to the depletion of iron and titanium in the residual melt phase, with a significant increase in viscosity. Accurate viscosity measurements play a crucial role in determining the reliability of empirical models for magma viscosity, which are used to evaluate eruptive scenarios in hazardous areas. Here, we quantify the reliability of empirical models by elaborating a new viscosity model of Stromboli basalt that relies exclusively on viscosity data obtained from nanocrystal-free samples. We show that empirical models so far used to estimate melt viscosity at eruptive conditions overestimate Stromboli viscosity by a factor ranging between 2 and 5. In the context of numerical modelling of magmatic processes at Stromboli volcano, we analyse and interpret this finding. Based on our findings, we draw the conclusion that Stromboli basalt is anticipated to ascend from the storage area to the vent at a faster rate than previously hypothesized.

 $\textbf{Keywords} \;\; Stromboli \cdot Viscosity \cdot Nanolite \cdot Differential \; scanning \; calorimetry \cdot Brillouin \; spectroscopy \cdot Raman \; spectroscopy$

Communicated by Dante Canil.

Published online: 26 June 2023

- Pedro Valdivia pedro.valdivia-munoz@uni-bayreuth.de
- Bayerisches Geoinstitut, University of Bayreuth, Universitätsstraße 30, 95440 Bayreuth, Germany
- Department of Glass and Ceramics, Institute of Materials Science, Friedrich-Alexander University of Erlangen-Nuremberg, Martensstrasse 5, Erlangen, Germany
- Institute of Non-Metallic Materials, Clausthal University of Technology, Zehntnerstraße 2a, 38678 Clausthal-Zellerfeld, Germany
- Institute of Environmental Geology and Geoengineering, CNR, Via Salaria Km 29.300, 00015 Monterotondo, Rome, Italy

Introduction

Volcanic eruptions feature among the most dangerous natural hazards on Earth (Wendee 2022), and can range in style from effusive lava-fed fountains to explosive eruptions that are capable to generate pyroclastic flows and destructive ashfalls (Gonnermann et al. 2017; La Spina et al. 2020). Eruptive style is mainly controlled by the decompression rate and by the ability of the gas phase to escape the magma (Mueller et al. 2008; Degruyter et al. 2012; Cashman and Scheu 2015; Gonnermann 2015; Cassidy et al. 2018), with viscosity modulating the decoupling between magma and gas phase and the overall transport mechanism (Webb and Dingwell 1990; Zhang 1999; Koyaguchi and Mitani 2005; Lautze and Houghton 2007; Vona et al. 2011; Gonnermann 2015; Di Genova et al. 2017b). Therefore, viscosity is arguably the most important physical property controlling magma dynamics and eruptive styles (Sparks 2003; Giordano et al. 2008). Magma viscosity strongly depends on the composition of the molten phase (including dissolved



volatile phases), temperature, bubble content and crystal cargo (Friedman et al. 1963; Richet et al. 1996; Ishibashi and Sato 2007; Vetere et al. 2007; Vona et al. 2011; Gonnermann and Manga 2012; Robert et al. 2013; Sehlke et al. 2014; Chevrel et al. 2015; Campagnola et al. 2016; Di Genova et al. 2017a, 2018; Cassidy et al. 2018; Romano et al. 2020). Previous experimental studies have extensively investigated the dependence of melt viscosity on composition and temperature (Hui and Zhang 2007; Giordano et al. 2008, 2009; Misiti et al. 2009, 2011). However, recent works have demonstrated that volcanic melts are prone to nanocrystallization and dehydration during viscosity measurements (Di Genova et al. 2017a, 2020b; Kleest et al. 2020; Okumura et al. 2022; Scarani et al. 2022). These effects may hinder the accurate determination of melt viscosity, directly affecting the reliability of the resulting models assessing magma transport (Scarani et al. 2022), and therefore preventing effective numerical modelling of magma dynamics upon decompression.

In this work, we investigated the viscosity of Stromboli basalt as a function of temperature and dissolved water content, developing a novel and accurate viscosity model based on the Mauro-Yue-Ellison-Gupta-Allan (MYEGA) parametrization (Mauro et al. 2009). Combining conventional and flash differential scanning calorimetry (C-DSC and F-DSC), viscometry, Raman and Brillouin spectroscopy, we demonstrate that the hydrous Stromboli melt is prone to nano-crystallization during viscosity measurements and that its viscosity is significantly lower than expected based on literature models (Hui and Zhang 2007; Giordano et al. 2008, 2009; Langhammer et al. 2022).

Stromboli is the northernmost volcanic island of the Aeolian archipelago in the Tyrrhenian Sea (Italy), formed by the subduction of the African plate under the Eurasian plate (Revil et al. 2011). It reaches an elevation of 924 m above sea level and constitutes the exposed portion of a substantial stratovolcano measuring approximately 2500 m in height (Bertagnini et al. 2003). Stromboli volcano is known for its persistent strombolian activity and its sporadic paroxysmal events (Métrich et al. 2009; Vona and Romano 2013; Andronico et al. 2021; Mattia et al. 2021), the latter being responsible for the most hazardous eruptions. This behaviour has been associated with a sudden rapid rise of the magma (Métrich et al. 2009; Misiti et al. 2009; Pichavant et al. 2013; Le Gall and Pichavant 2016a; Andronico et al. 2021; Ripepe et al. 2021a, b), with ascent rates that can only be reliably estimated provided that a correct parametrization of magma viscosity is available. Due to the noticeably lower melt viscosity emerging from our experimental data with respect to previous studies, numerical models of magma ascent at Stromboli should therefore consider noticeably higher ascent rates, with implications for the outgassing dynamics upon decompression. Consequently, our findings are anticipated to improve numerical simulations, providing enhanced constraints on magma ascent time-scales and on the evolution of magma rheology resulting from decompression and degassing.

The current understanding of how the viscosity of volcanic melts is affected by the formation of nanocrystals

Various authors have recently focused their investigations on nanocrystallization processes occurring in volcanic melts, demonstrating that these processes may have a critical effect on rheology, namely an increase in the effective viscosity of magmas. Based on such literature, two parallel mechanisms can be identified to be responsible for this increase in viscosity.

The first mechanism dominates around the glass transition temperature, in the high viscosity interval (10^8 Pa s \lesssim $\eta \lesssim 10^{13} \text{ Pa s}$). Several studies that focused on a wide range of melt compositions, including basaltic (Bouhifd et al. 2004; Di Genova et al. 2020b; Scarani et al. 2022), andesitic (Richet et al. 1996; Liebske et al. 2003; Vetere et al. 2006; Okumura et al. 2022), tephri-phonolitic-foiditic (Kleest et al. 2020), and rhyolitic melts (Di Genova et al. 2017a) clarified that the increase in viscosity can be attributed to the diffusion of iron and titanium within the initially homogenous melt to form oxide (nano)crystals. For instance, Okumura et al. (2022) proposed that the increase of the anhydrous viscosity due to magnetite nanocrystallization in andesitic magmas is well-explained by the complete depletion of iron in the melt phase. Therefore, this process is crucially dependent on the (continuously evolving) composition of the melt phase. The gradual clustering of iron and titanium takes place, initially in an amorphous state, eventually resulting in the formation of Fe-Ti-enriched (nano)crystals (Scarani et al. 2022).

The second mechanism operates in the undercooled melt at high temperatures, where the low viscosity (10^{-3} Pa s) $\lesssim \eta \lesssim 10^3$ Pa s) of the melt is thought to promote nanolite aggregation and melt entrapment within these aggregates (Di Genova et al. 2020a). Although nanolites may be present in very low volume fractions (typically far less than 10 vol%, i.e., at fractions deemed to be uninfluential in the case of microlite suspensions; Mueller et al. 2011b; Vona et al. 2011), the melt entrapment within aggregates could result in an increased effective volume of the solid, which, in turn, increases the overall viscosity of the magma. Nanolite aggregation was observed in the laboratory, examining in situ a Mt. Etna trachybasalt, and in the eruptive products of the Plinian eruption of Mt. Etna 122 CE (Di Genova et al. 2020a). Notably, this melt entrapment mechanism is not necessarily restricted to the nano-sized domain; in-situ



high-temperature 4D studies of crystal growth kinetics and textural evolution during crystallization of Mt. Etna trachybasaltic magma under water-saturated conditions showed a rapid dendritic crystallization that favoured the entrapment of melt between microlite branches (Arzilli et al. 2022).

Finally, the role of nanocrystallization reaches beyond the liquid and crystalline fractions of the magma, as nano-sized Fe-Ti nanolite oxides have been shown to promote heterogeneous bubble nucleation (Cáceres et al. 2020; Di Genova et al. 2020a) that might be crucial for the fragmentation of the magma (Knafelc et al. 2022; Yoshida et al. 2023).

Materials and methods

Synthesis of Stromboli glasses

The starting materials used in this work are ash-to-lapillisized pyroclasts corresponding to the low porphyritic (LP) deposit from the July-August 2019 eruption of Stromboli volcano, Italy. Firstly, a homogeneous anhydrous crystaland bubble-free glass was produced by crushing and melting the natural samples in a Pt crucible at 1400 °C for 4 h. The obtained glass was crushed to powder size and mixed before a second melting was performed at the same conditions for chemical homogenization. A fraction of the glass material was subjected to grinding, resulting in a powdered form, which was subsequently divided into two different grain sizes through the process of sieving. (i.e., < 100 µm and 100–250 µm diameter). Subsequently, the two powder sizes were mixed at a 1:1 weight ratio to minimize porosity during the high-temperature and -pressure synthesis of water-bearing glasses. The remaining glass was kept to perform viscosity measurements and Brillouin spectroscopy of the anhydrous sample. Water-bearing glasses, from 0.9 ± 0.03 to 4.7 ± 0.26 wt% H₂O, were synthesized using a piston-cylinder apparatus at the Bayerisches Geoinstitut in Bayreuth (University of Bayreuth, Germany), in addition to an internally heated pressure vessel (IHPV) equipment at the Institute of Mineralogy in Göttingen (University of Göttingen, Germany). For the piston-cylinder experiments, hydrous samples were prepared by adding distilled water stepwise to the dry powder in Au₈₀Pd₂₀ capsules (4.6 mm inner diameter; 10-12 mm length), which have been shown to minimize iron loss during the synthesis of starting materials (Pichavant et al. 2013). After welding the capsules, they were weighed and then left overnight in a furnace at 150 °C to check for possible water loss. The capsules that did not show weight loss after this treatment were used for the hydrous synthesis using a talc-pyrex-Al₂O₃ assembly at 1200 °C and 5-10 kbar at intrinsic reduced oxygen fugacity conditions $(f_{O_2} < \text{NNO} + 0)$, with a 24 h dwell to ensure water homogenization within the sample. Eventually, a rapid cooling process with a rate of approximately 100 K s⁻¹ was applied to the melt. This was achieved by deactivating the heating power and employing an automatic pressure controller to maintain the pressure within nominal levels throughout the cooling phase. Samples were slowly decompressed to ambient pressure to avoid fractures. Additionally, one extra anhydrous glass was synthesised at 1250 °C and 5 kbar to account for the effect of pressure in the synthesis of our glasses. For the IHPV experiments, dry glass powder and an appropriate amount of distilled water were loaded in Au₈₀Pd₂₀ capsules (3 mm inner diameter; 15 mm length). All samples were stacked together and the synthesis was run at 5 kbar and 1250 °C for 24 h at relatively oxidizing conditions $(f_{Q_2} = \text{NNO} + 3 \pm 1)$ as determined by Schuessler et al. (2008). Samples were rapidly quenched with a cooling rate of ~ 150 K s⁻¹ at isobaric pressure. Throughout the manuscript, all samples are renamed based on their measured water content in wt% (e.g., S_0 for the anhydrous material and S_3.36 for a sample with 3.36 ± 0.01 wt% H₂O).

Electron microprobe analyses

The major elemental composition (Si, Ti, Al, Fe_{tot}, Mn, Mg, Ca, Na, K, and P) was determined using a JEOL JXA-8200 electron microprobe at the Bayerisches Geoinstitut (University of Bayreuth, Germany) (Supplementary Table 1). The anhydrous and hydrous glasses were embedded in epoxy, polished, and carbon coated. Measurements were performed using 15 kV voltage, 5 nA current, and 20 s of counting time. A defocused 10 µm beam was used for all elements. Between 20 and 30 points per sample were measured to account for heterogeneities. Synthetic wollastonite (Ca, Si), periclase (Mg), hematite (Fe), spinel (Al), orthoclase (K), albite (Na), manganese titanate (Mn, Ti), and apatite (P) were used as calibration standards. Sodium and potassium were analysed first to prevent alkali migration effects (Hughes et al. 2019). The findings from this analysis, as presented in Supplementary Material Table 1, provided confirmation that the composition of our anhydrous glass closely corresponded, within the margin of uncertainty, to previous studies that investigated the melt viscosity of Stromboli basalt (Giordano et al. 2006; Misiti et al. 2009).

Water content determination

The water content of Stromboli glasses was measured using Fourier-transform infrared spectroscopy (FTIR) at the Bayerisches Geoinstitut (University of Bayreuth, Germany). We used a Bruker IFS 120 spectrometer connected to a Bruker IR microscope. Spectra were acquired using a tungsten light source with a Si-coated CaF₂ beam-splitter and a narrowband MCT (mercury; cadmium; telluride) detector. FTIR measurements were acquired between 1000 to 6000 cm⁻¹ on



Table 1 Glass transition (T_g) , water speciation, total water concentrations and K/G factors of Stromboli glasses

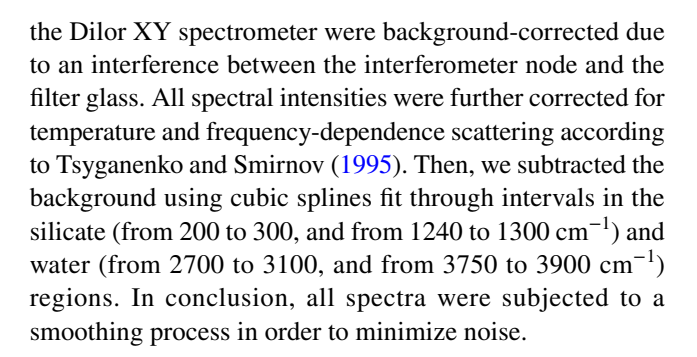
Sample	T_g (°C)	$C_{\mathrm{OH}}^{a} (\mathrm{wt\%})$	$C_{\rm H2O}^{a}$ (wt%)	$C_{\mathrm{OH}} + C_{\mathrm{H2O}} (\mathrm{wt\%})$	K/G ^b
S_0_atm	664.1	0.10 ± 0.01	_	0.10 ± 0.01	1.73 ± 0.02
S_0_5kbar	_	0.25 ± 0.01	_	0.25 ± 0.01	1.73 ± 0.02
S_0.91	562.3	0.70 ± 0.02	0.21 ± 0.03	0.91 ± 0.03	_
S_1.16	_	0.81 ± 0.02	0.35 ± 0.03	1.16 ± 0.03	1.73 ± 0.02
S_1.25	540.0	0.96 ± 0.01	0.29 ± 0.01	1.25 ± 0.01	_
S_1.97	497.3	1.40 ± 0.01	0.58 ± 0.01	1.97 ± 0.01	_
S_2.08	494.3*	1.54 ± 0.03	0.54 ± 0.01	2.08 ± 0.03	1.72 ± 0.02
S_2.87	455.5	1.78 ± 0.02	1.09 ± 0.04	2.87 ± 0.05	_
S_3.36	440.3*	2.14 ± 0.01	1.22 ± 0.01	3.36 ± 0.01	1.72 ± 0.02
S_4.01	416.8*	2.44 ± 0.02	1.57 ± 0.01	4.01 ± 0.02	1.73 ± 0.02
S_4.32	411.0	2.02 ± 0.15	2.30 ± 0.01	4.32 ± 0.15	1.75 ± 0.02
S_4.69	400.4*	2.77 ± 0.25	1.92 ± 0.07	4.69 ± 0.26	1.73 ± 0.02

^{*}Values derived from $T_{onset15}$ and $T_{onset30}$ linear regression

doubly polished samples (~0.2–0.3 mm thickness). The analysed spot was 100 µm in diameter with a spectral resolution of 4 cm⁻¹. For each spectrum, 200 scans were accumulated. All hydrous glasses were measured at least three times at different spots to account for possible heterogeneity. The total water content was derived using the peak areas of the OH^- and H_2O bands (~4500 cm⁻¹ and 5200 cm⁻¹, respectively), which correspond to the combination of the stretching and bending modes of OH⁻ groups and water molecules. To determine the peak area values, an appropriate baseline under the OH⁻ and H₂O bands was defined using the "two Gaussians" (GG) baseline and the "GGpar" integral molar absorption coefficients ($\varepsilon_{OH} = 0.62$; $\varepsilon_{H2O} = 0.71$) following Ohlhorst et al. 2001. This approach is more suitable than other methods (e.g., "straight line" (TT) baseline) for determining water concentration in basalts because the superimposition of bands resulting in a curved baseline is considered (Ohlhorst et al. 2001).

Raman spectroscopy

Stromboli glasses subjected to C-DSC, F-DSC and micropenetration were characterized before and after experimental measurements to account for potential modifications (i.e., crystallization and/or water loss). We used a confocal Raman imaging microscope at the Institute of Non-Metallic Materials, TU Clausthal (alpha300R, WITec GmbH), and a Dilor XY spectrometer at the Bayerisches Geoinstitut (Horiba Jobin Yvon Inc.). Spectra were acquired with a $100 \times \text{objective}$ in the ranges between $200-1300 \text{ cm}^{-1}$ for the silicate region and between $2700-4000 \text{ cm}^{-1}$ for the water region. The integration time was 7 s (3 accumulations, 13 mW laser power), and 30 s (2 accumulations, 2 mW laser power) for the Dilor XY spectrometer. Additionally, spectra acquired by



Micropenetration viscometry

We subjected polished plane-parallel glass chips (3 mm thick) to micropenetration viscometry measurements using a vertical dilatometer (Bähr VIS 404) at the Institute of Non-Metallic Materials, TU Clausthal. We measured the indentation rate of a sapphire sphere (r=0.75 mm) during isothermal dwells at temperatures controlled using an S-type thermocouple (Pt-PtRh) placed at ~2 mm from the sample surface. The temperature error is estimated to be ± 5 K considering the accuracy of the S-type thermocouple and its distance from the sample (Behrens et al. 2018). We followed standard procedures (Di Genova et al. 2014a, 2020b; Scarani et al. 2022) to achieve thermal equilibration of the sample at the target temperature. The indentation depth was measured as a function of time and the viscosity curve was determined according to Eq. 1 (Douglas et al. 1965):

$$\eta = \frac{9F}{32\sqrt{2r}\sqrt{L^3}}t\tag{1}$$

where η is the Newtonian viscosity (Pa s), F is the applied force (N), t is the time (s), r is the radius of the sphere (m) and L is the indentation depth (m). Viscosity measurements



 $[^]a$ FTIR results (Ohlhorst et. al 2001). Errors are given by the standard deviation ($\pm 1\sigma$) of our measurements

^bValues derived using Eq. 4

of the standard glass DGG-1 were used to calibrate the vertical dilatometer, reproducing the certified viscosity data (Meerlender 1974) with a deviation of ± 0.1 in log units. As the effect of a uniform (hydrostatic) pressure on the liquid viscosity of silicate melts is relatively small at around glass transition (0.1 log units per 100 MPa; Del Gaudio et al. 2007), micropenetration experiments at ambient pressure were used to model the dynamic behaviour of silicate melts under eruptive conditions.

Differential scanning calorimetry

Differential Scanning Calorimetry (DSC) measurements were performed at the Institute of Non-Metallic Materials (TU Clausthal) using two apparatuses. We used 20 ± 5 mg of glass in a PtRh20 crucible under a constant N₂ 5.0 flow rate (20 ml min⁻¹) in a conventional differential scanning calorimeter (C-DSC, 404 F3 Pegasus, Netzsch), which allowed the measurement of the heat flow at a heating rate (q_h) between 5 and 30 K min⁻¹. Moreover, we used ~ 50 ng of glass for the analyses performed with a flash calorimeter (F-DSC, Flash DSC 2+, Mettler Toledo) equipped with UFH 1 sensors, under constant Ar 5.0 flow (40 ml min⁻¹), which allowed the measurement of the heat flow at a heating rate (q_h) between 100 and 30,000 K s⁻¹ (6,000 and 1,800,000 K min⁻¹). The C-DSC was calibrated using melting temperatures and enthalpy of fusion of reference materials (pure metals: In, Sn, Bi, Zn, Al, Ag, and Au). The F-DSC was calibrated using the melting temperature of aluminium (melting temperature 933.6 K) and indium (melting temperature 429.8 K).

For C-DSC measurements, we followed the methodology presented by Stabile et al. (2021). Namely, we initially erased the thermal history of the glass via a two-step thermal treatment: we heated the sample at a rate $q_h = 20 \text{ K min}^{-1}$ up to a few degrees above T_{peak} (the undershoot of the heat flow curve in the glass transition region, see Fig. 1) and subsequently cooled the melt to 100 °C at a rate $q_c = 10$, 15, 20, or 30 K min⁻¹. We then performed the actual C-DSC measurement using the rate-matching method, by performing an additional upscan (i.e., heating segment at q_h) at a rate matching that of the previous downscan (i.e., cooling at q_c), i.e., $q_h = q_c$. From the measured heat flow during the second upscan, we extracted the characteristic temperatures T_{onset} and T_{peak} as indicated in Fig. 1: T_{peak} corresponds to the above-mentioned undershoot of the heat flow curve, while T_{onset} represents the intercept between the tangent to the heat flow curve of the glass (i.e., before the fictive temperature) and the tangent to the inflection point during the glass transition. For the F-DSC measurements, we used the same procedure mentioned above, but at higher $q_{h,c}$ (Di Genova et al. 2020b; Al-Mukadam et al. 2021; Stabile et al. 2021; Scarani et al. 2022). Finally, viscosity was calculated from C- and

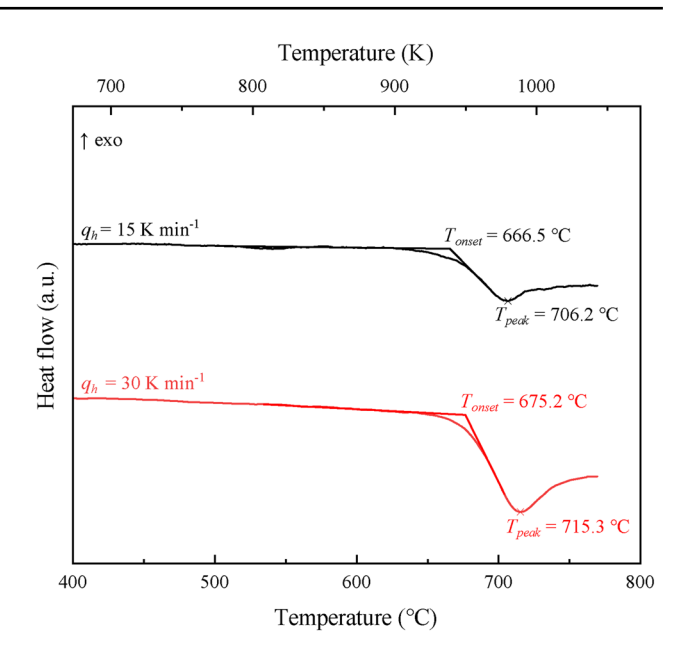


Fig. 1 Heat flow of anhydrous Stromboli glasses measured as a function of temperature using a conventional DSC. The red and black lines correspond to the second upscan during measurements performed at 30 and 15 K min⁻¹ using the rate-matching method (Di Genova et al. 2020b; Stabile et al. 2021), respectively

F-DSC data using the relationship between the matching heating rate (q_h) of the measurement and the shift factors K_{onset} and K_{peak} (Di Genova et al. 2020b; Stabile et al. 2021) expressed in Eq. 2:

$$log_{10}\eta(T_{onset,peak}) = K_{onset,peak} - log_{10}(q_h)$$
(2)

where $K_{onset} = 11.20 \pm 0.15$ and $K_{peak} = 9.84 \pm 0.20$ (Di Genova et al. 2020b; Stabile et al. 2021). Notably, when q_h is 10 K min^{-1} , $\eta(T_{onset}) \approx 10^{12} \text{ Pa}$ s, and therefore, $T_{onset} \approx T_g$

Brillouin spectroscopy

Brillouin spectroscopy (BLS) measurements were performed at the Bayerisches Geoinstitut in Bayreuth, Germany. Planeparallel polished glass samples of ~50 µm thickness were measured using a solid-state Nd: YVO₄ laser source with a wavelength of 532 nm, with a power at the source of 50 mW. The Brillouin frequency shift was quantified using a six-pass Fabry–Perot interferometer (Whitfield et al. 1976) combined with a single-pixel photon counter detector. The experiments were conducted using a symmetric forward scattering geometry (Whitfield et al. 1976; Cassetta et al. 2021) with a scattering angle of θ =79.8°. The scattering angle was calibrated using a silica reference glass. Frequency shifts ($\Delta \omega$) were converted to longitudinal (ν_p) and shear (ν_s) sound velocities using Eq. 3:



$$v = \frac{\Delta\omega\lambda}{2\sin(\theta/2)}\tag{3}$$

where λ is the laser wavelength and θ is the angle between the incident and scattered beams (Whitfield et al. 1976; Sinogeikin et al. 2006). We collected between 4 and 8 spectra for each sample at different rotation angles (from -180° to +180°) to account for uncertainties. Finally, we calculated the K/G ratio using the longitudinal (v_p) , and shear (v_s) acoustic velocities using Eq. 4:

$$\frac{K}{G} = \left(\frac{v_p}{v_s}\right)^2 - \frac{4}{3} \tag{4}$$

Viscosity modelling

The combination of C-DSC and Brillouin spectroscopy (BLS) enabled the parameterization of the melt viscosity of hydrous and anhydrous samples as a function of temperature $\eta(T)$, via the Mauro–Yue–Ellison–Gupta–Allan (MYEGA) equation (Eq. 5) (Mauro et al. 2009):

$$log_{10}\eta(T) = log_{10}\eta_{\infty} + \left(12 - log_{10}\eta_{\infty}\right)^{\frac{T_{s}}{T}} exp\left[\left(\frac{m}{12 - log_{10}\eta_{\infty}} - 1\right)\left(\frac{T_{s}}{T} - 1\right)\right]$$
(5)

where $log_{10}\eta_{\infty} = -2.93 \pm 0.3$ is the logarithmic viscosity at infinite temperature (Mauro et al. 2009; Langhammer et al. 2021), T_g is the glass transition temperature determined by C-DSC (T_{onset} at $q_{h,c} = 10$ K min⁻¹) and m is the melt fragility defined in Eq. 6 (Angell 1995) as the slope of viscosity curve evaluated at T_g :

$$m = \left. \frac{\partial log_{10}\eta}{\partial T_g/T} \right|_{T=T_g} \tag{6}$$

Simultaneously, the melt fragility parameter, m, can be obtained from BLS measurements using the empirical relationship introduced in Cassetta et al. (2021) (Eq. 7). This relationship has also been recently validated for peridotitic melts by Di Genova et al. (2023):

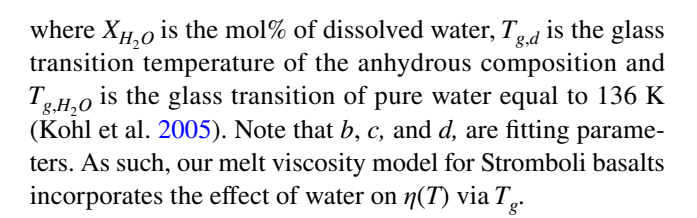
$$m = 43 \cdot \frac{K}{G} - 31 \tag{7}$$

To describe the dependence of T_g from total water content, we use the model proposed by Schneider et al. (1997), according to Langhammer et al. (2021) (Eq. 8):

$$\begin{split} T_g \left(x_{H_2 \mathrm{O}} \right) &= w_1 T_{g, H_2 \mathrm{O}} + w_2 T_{g, d} + c w_1 w_2 \left(T_{g, d} - T_{g, H_2 \mathrm{O}} \right) \\ &+ d w_1 w_2^{\ 2} \left(T_{g, d} - T_{g, H_2 \mathrm{O}} \right), \end{split}$$

with (8)

$$w_1 = \frac{x_{H_2O}}{b(100 - x_{H_2O}) + x_{H_2O}} \text{ and } w_2 = \frac{b(100 - x_{H_2O})}{b(100 - x_{H_2O}) + x_{H_2O}}, \tag{9}$$



Results

Scanning electron microscopy, Raman and FTIR analyses

Scanning electron microscopy imaging in backscattered electron (BSE) mode (Supplementary Material Fig. 1) and Raman spectra analysis (Fig. 2) were used to verify the pristine glass nature of the samples before and after viscosity and calorimetric measurements (Di Muro et al. 2009; Di Genova et al. 2016). Indeed, previous research (Di Genova et al. 2017a, b, 2020a, b; Giordano et al. 2021; Kleest and Webb 2022; Scarani et al. 2022) has demonstrated that BSE imaging alone cannot conclusively confirm the presence or absence of nanolites, since the spatial

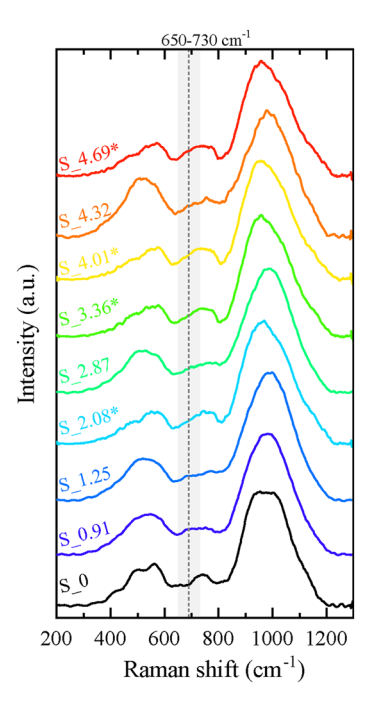


Fig. 2 Raman spectra of anhydrous and hydrous glasses before C-DSC and viscosity measurements. The spectral range (650–730 cm⁻¹) most prominently affected by the presence of Fe-Ti-oxides is shaded in gray, with a dashed line marking the usual maximum (~690 cm⁻¹) of the peak assigned to these phases (Di Genova et al. 2020b; Stabile et al. 2021). Samples labelled with asterisk were synthesized using IHPV, while the rest were synthesized under pistoncylinder experiments



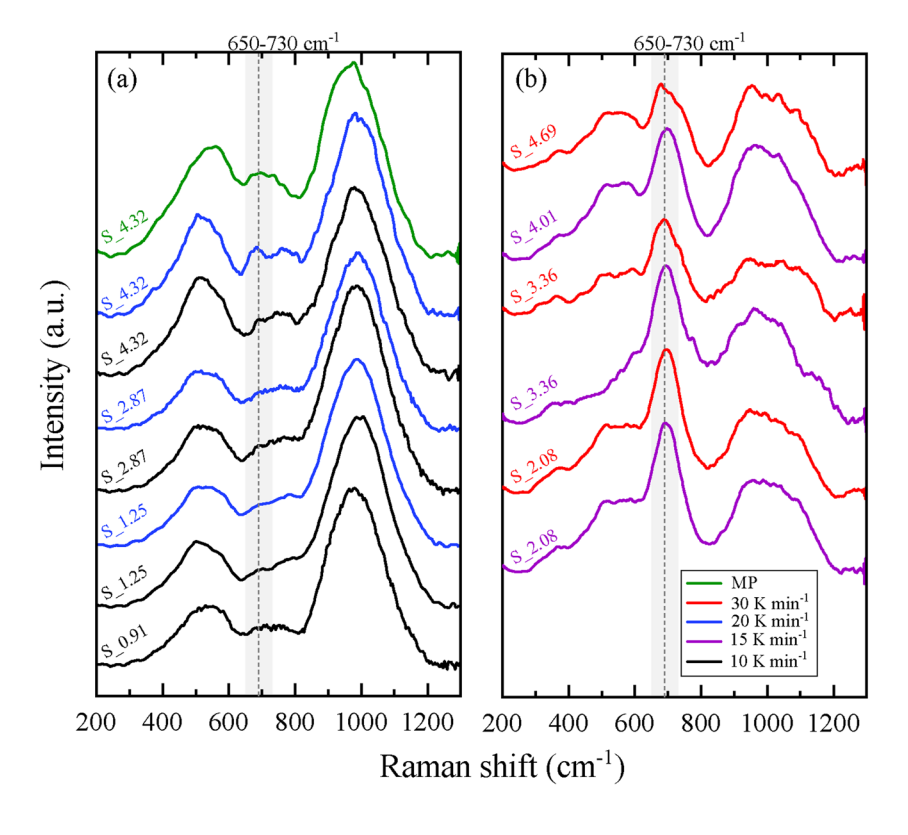
resolution of this technique is insufficient to identify objects exhibiting a size of only few tens of nanometers. Conversely, its combination with Raman spectroscopy represents a more reliable approach for detecting Fe-Ti nanolites, even when BSE images are unable to show crystals that are instead indisputably visible using transmission electron microscopy (Di Genova et al. 2017a, b, 2020a, b; Scarani et al. 2022).

In the case of our samples, BSE analyses (Supplementary Material Fig. 1) show no evidence of crystals or bubbles before and after viscosity experiments. As for Raman spectra (Fig. 2), they confirmed first-of-all the crystal-free amorphous nature of our initial anhydrous and hydrous samples (Di Muro et al. 2009; Di Genova et al. 2016). This confirmation arises from the absence of characteristic features in the 650–730 cm⁻¹ range, associated with the most prominent signal of Fe-Ti-oxides, which typically peaks around ~ 690 cm⁻¹ (Di Genova et al. 2020a, b). In contrast, and regardless of the fact that no nanolites were observed by BSE, Raman spectra acquired in the low-wavenumber range (<1300 cm⁻¹) post-DSC and post-micropenetration measurements (Fig. 3) evidence that samples with H₂O content greater than 1 wt% underwent a certain degree of crystallization of Fe-Ti-oxide nanolites during such high-temperature analyses. We identified two groups of nanolite-bearing glasses post-experiments: (i) samples showing a low-to-moderate degree of nanolitization (Fig. 3a), except for S_0.91 that did not experience nanolite crystallization, and (ii) samples that present a more prominent Raman feature peaking at ~690 cm⁻¹, suggesting a substantial compositional modification of the residual melt during C-DSC experiments (Fig. 3b). We observed that this difference is associated with the oxidation conditions of the starting materials. Samples synthesized using the relatively oxidizing IHPV method experienced the highest changes after DSC and viscosity measurements, compared to the ones synthesized by piston-cylinder experiments.

To account for possible loss of water during experiments, we acquired FTIR and Raman spectra of hydrous samples before and after DSC, as well as before and after micropenetration measurements (Fig. 4).

FTIR analyses show that the area of the molecular H_2O bands (5200 cm $^{-1}$) did not vary significantly after DSC measurements. However, for samples with the highest water content (S_3.36, S_4.32 and S_4.69), a new contribution at ~4300 cm $^{-1}$ was observed (Fig. 4a). This new feature might be related to the formation of free hydroxyl species: as recently suggested by Bondar et al. (2023), such OH groups could be associated to alkaline earth cations (e.g., Ca and Mg) rather than to tetrahedrally coordinated network formers (such as Al and Si), thereby playing a markedly different structural role. For the other samples characterized by a lower water content (<3 wt%), the area of the OH $^-$ bands did not show significant changes.

Fig. 3 Raman spectra of hydrous glasses after C-DSC analyses and micropenetration measurements (MP). The spectral range (650–730 cm⁻¹) most prominently affected by the presence of Fe-Ti-oxides is shaded in gray, with a dashed line marking the usual maximum ($\sim 690 \text{ cm}^{-1}$) of the peak assigned to these phases (Di Genova et al. 2020b; Stabile et al. 2021). The heating rate used during DSC measurements is reported in the legend. a Samples synthesized using piston-cylinder. Raman spectra show a low to moderate degree of nanolitization b Samples synthesized using IHPV. Raman spectra show a strong contribution in the 650-730 cm⁻¹ region associated with the crystallization of Fe-Ti-oxides





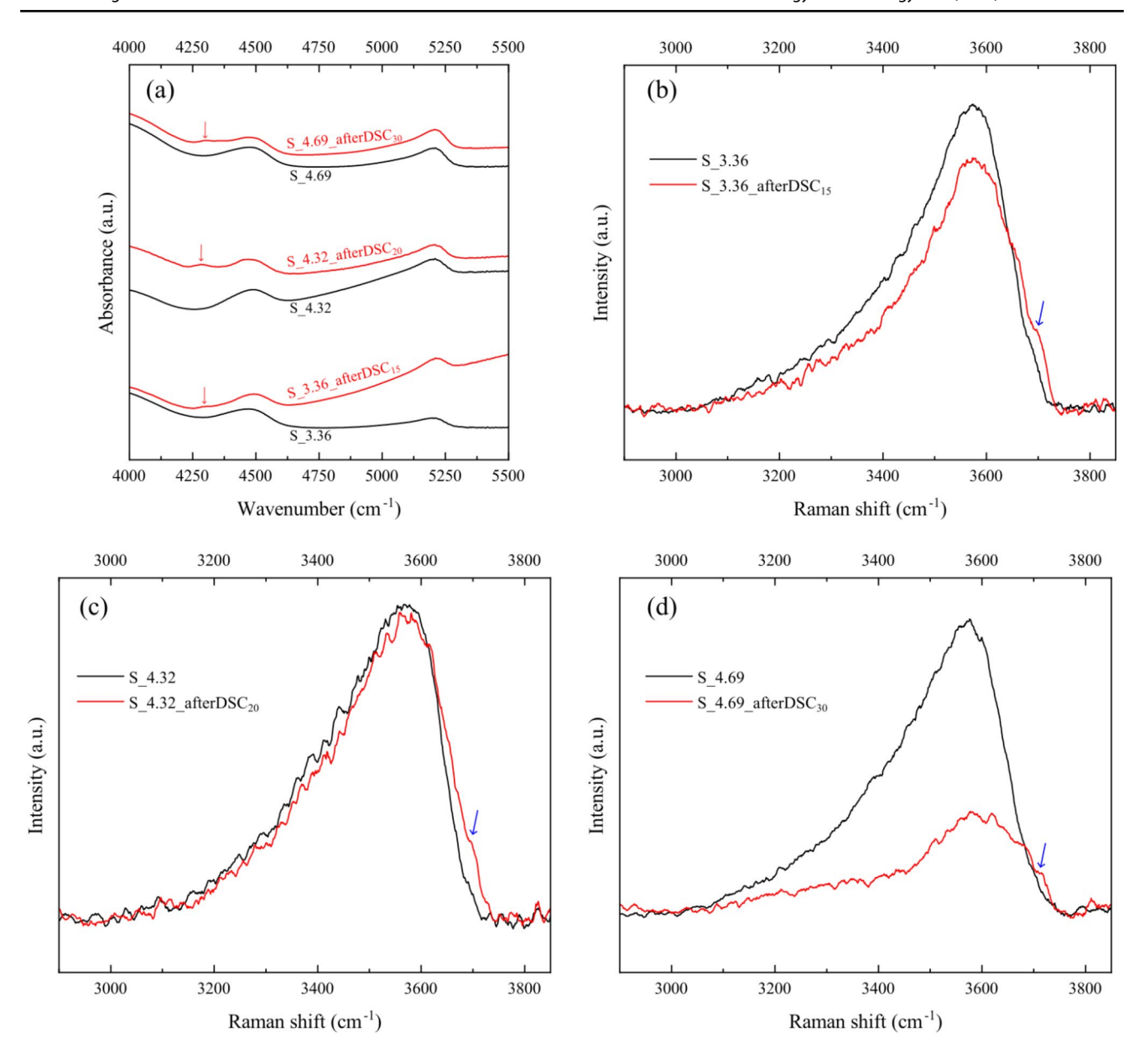


Fig. 4 a FTIR comparison of water spectral bands before and after C-DSC measurements. Red arrows show the formation of a new peak at ~4300 cm⁻¹ after C-DSC measurements that might be attributed to the apparition of free hydroxyl groups (Bondar et al. 2022). **b**, **c**, and

d correspond to the comparison of the Raman water region before and after C-DSC measurements. Blue arrows show the development of a shoulder at $\sim 3700~\text{cm}^{-1}$ associated to free OH species (Larre et al. 2020)

Concerning Raman data, we normalized the intensity of the water band area at high wavenumber (HW; 2700–4000 cm⁻¹) to the area of the silicate region at low wavenumber (LW; 200–1300 cm⁻¹) to check for possible water loss (Di Genova et al. 2017b). The comparison between the HW/LW ratio before and after DSC experiments showed a significant decrease for the sample with the highest water content (S_4.69). Nevertheless, the quantification of water content depletion was not performed using Raman spectroscopy due to previous studies indicating that this technique is not reliable for glasses that contain nanolites

(Di Genova et al. 2017b). Importantly, and for the same three samples mentioned (S_3.36, S_4.32 and S_4.69) above for FTIR analysis, we observed the development of a Raman shoulder at ~3700 cm⁻¹ (blue arrows in Fig. 4). This contribution was previously associated with the formation of free OH species, as suggested by Larre et al. (2020). Therefore, by combining FTIR and Raman spectra, we deduce that samples with a water content exceeding 3.3 wt% underwent both nanocrystallization and possibly the generation of free hydroxyls during the experiments. In general, regardless of the synthesis method employed, we observed more



pronounced structural modifications as the water content increased, particularly following DSC and micropenetration experiments.

Viscosity, fragility, and glass transition temperature of the anhydrous melt

C-DSC- and F-DSC-derived anhydrous melt viscosity are reported as a function of temperature in the Supplementary Material Table 2 and shown together with literature data in Fig. 5. To accurately characterize the anhydrous viscosity of Stromboli basalt, we used the MYEGA parametrization (Eq. 5), fixing $\log_{10}\eta_{\infty}$ = -2.93 (Mauro et al. 2009; Langhammer et al. 2021; Scarani et al. 2022), to fit our anhydrous C-DSC-derived viscosity (10.1 < log η < 11.98) together with micropenetration (7.8 < log η < 10.5) and concentric cylinder data (0.8 < $\log \eta$ < 1.9) from Scarani et al. (2022) to fully constrain the melt fragility index $(m = 40.7 \pm 0.7)$ and glass transition temperature ($T_{g} = 666.9 \pm 0.8$ °C). Our fragility estimates are slightly lower compared to the empirical viscosity model proposed by Giordano et al. (2009) for Stromboli composition (m = 42 and $T_g = 662.5$ °C), who nevertheless used a Vogel-Fulcher-Tammann (VFT) parameterization, $log_{10}\eta(T) = log_{10}\eta_{\infty} + \frac{B}{T-C}$, intrinsically involving a different viscosity at infinite temperature $(log_{10}\eta_{\infty} = -4.55)$ (Russell et al. 2003; Misiti et al. 2009;

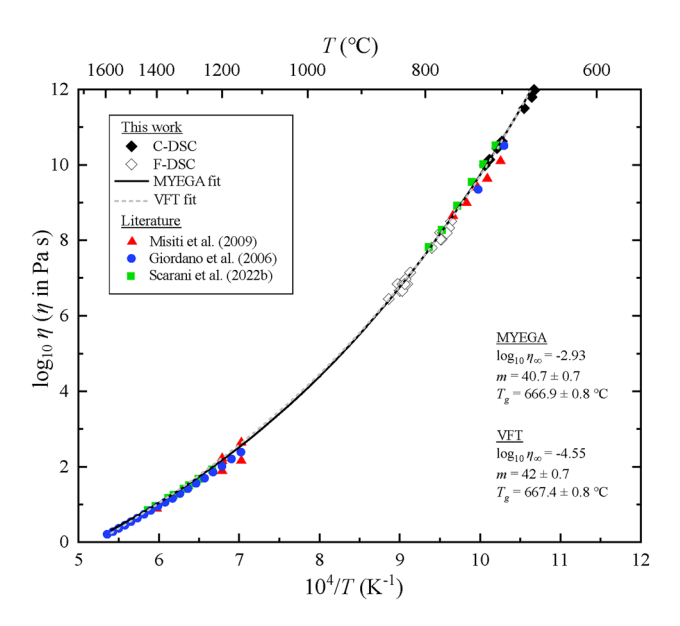


Fig. 5 Viscosity of anhydrous Stromboli melt as a function of temperature. The black line corresponds to the best fit of the data using the MYEGA equation (Eq. 5) combining our C-DSC data with micropenetration and concentric cylinder data from Scarani et al. (2022). The same data were also fit using the VFT formulation (dashed grey line, see text for details). F-DSC data were not used to constrain the MYEGA and VFT fits. For comparison purposes, we report viscosity data from Misiti et al. (2009) and Giordano et al. (2006) who examined the same composition

Langhammer et al. 2021). When we used the VFT parametrization and assuming $log_{10}\eta_{\infty}=-4.55$ to fit our dataset, we obtained $T_g=667.4\pm0.8$ °C and $m=42\pm0.7$, which is in excellent agreement with Giordano et al. (2009). Therefore, the viscosity formulation (MYEGA or VFT), and the resulting choice of $log_{10}\eta_{\infty}$, have a negligible effect on the estimations of m and T_g . Finally, we found that our anhydrous F-DSC-derived viscosity (6.4 < log < 8.5), which was not used to constrain our MYEGA parameterization, is in excellent agreement with our fit, suggesting that F-DSC-derived viscosity can be used to accurately derive viscosity of volcanic melts.

Viscosity, fragility, and glass transition temperature of the hydrous melt

The DSC-derived and measured hydrous viscosity are reported in Table 3 of the Supplementary Material and shown in Fig. 6. Raman spectroscopy results showed that almost all our hydrous glasses, except for S_0.91 and S_4.32 after F-DSC, crystallized Fe-Ti-oxide nanolites during viscosity measurements. On the other hand, we also observe that samples with water content higher than 3.3 wt% suffered occasional loss of total water content, with the parallel formation of free OH species during viscosity experiments. Previous studies (Stabile et al. 2021; Okumura et al. 2022; Scarani et al. 2022) have shown that the removal of Fe-Ti-oxides from volcanic melts during nanocrystallization

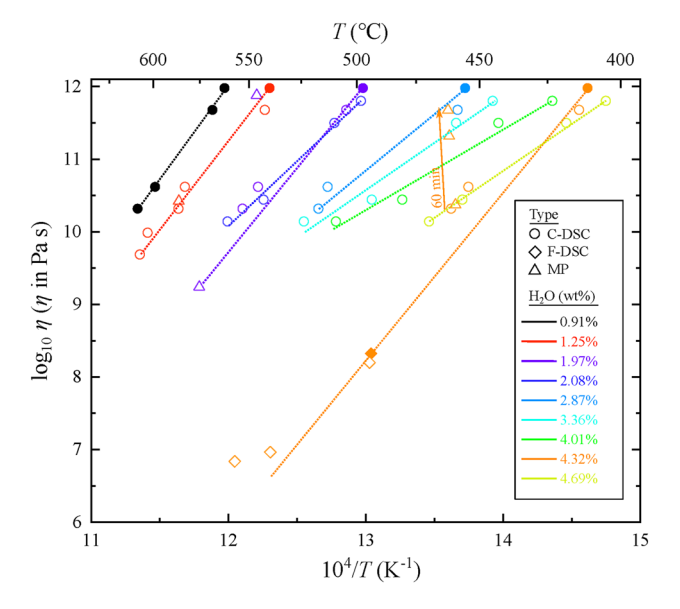


Fig. 6 Experimental viscosity of hydrous Stromboli melt. Water contents are labeled by color. Circles, diamonds, and triangles represent C-DSC, F-DSC, and MP measurements, respectively. Filled symbols correspond to nanolite-free measurements. Dashed lines are a guide for the eye. The arrow shows the increase in viscosity during MP measurements



induces a non-trivial increase in the viscosity of the residual melt. As such, we infer that our hydrous viscosity results do not represent the viscosity of the pure hydrous melt, which is expected to be lower, especially at high water contents. Nevertheless, measurements performed at the glass transition temperature T_o ($\eta = 10^{12}$ Pa s) were virtually unaffected by nanocrystallization, while the instability of the samples was more and more evident as the temperature increased. We remark that the timescale of nanocrystallization during C-DSC experiments seems to be in the order of seconds to a few minutes, occurring as soon as the temperature of the sample crosses T_{o} . We observe that considering these increasingly nanolite-bearing measurements as valid data points would misleadingly result in an apparent decrease of m, as inferred by the slopes of the dashed lines in Fig. 6. Conversely, when considering only nanolite-free measurements (i.e., S_0.91 and S_4.32 dashed lines in Fig. 6), we observe that the slope of the dashed lines does not exhibit a marked dependence on water content. The instability of hydrous samples during the measurements is reaffirmed by the data acquired by micropenetration. For example, when measuring sample S 4.32, we observed a time-dependent increase in viscosity from $10^{10.38}$ to $10^{11.67}$ Pa s in 60 min (orange arrow in Fig. 6) during the micropenetration measurement between 459 and 461 °C (i.e., ~ 50 °C above T_a), resulting in a viscosity almost two orders of magnitude greater than C-DSCderived estimations. Also, for sample S_1.97, we observed a considerable difference between micropenetration and C-DSC-derived viscosities, with $\eta = 10^{11.88}$ and $10^{10.62}$ Pa s (546 °C), respectively. We attribute the observed variation to the occurrence of nanocrystallization and water loss during micropenetration measurements, which are conducted for longer durations above T_g compared to DSC (differential scanning calorimetry) experiments.

The glass transition temperature (T_g) was either directly derived (T_{onset} at $q_{c,h} = 10 \text{ K min}^{-1}$, see methodology paragraphs for further details) or linearly extrapolated using the measured T_{onset} at $q_{c,h} = 15$ and 30 K min⁻¹ (Table 1). As expected (Giordano et al. 2008; Misiti et al. 2009; Bouhifd et al. 2013), T_g decreases with water content (Fig. 7), from 664.1 °C at anhydrous conditions to 400.4 °C when $H_2O = 4.69 \pm 0.26$ wt%. We used Eq. 8 and 9 to parameterize T_{ϱ} as a function of water content (dashed line in Fig. 7) using only the measured T_g data (i.e., T_{onset} at $q_{c,h} = 10 \text{ K min}^{-1}$) and we obtained the fit parameters b = 0.235, c = 1.234 and d = -1.47. Note that this model well-predicts our extrapolated T_g values (i.e., T_{onset} at $q_{c,h} = 15$ and 30 K min⁻¹) and it is in good agreement (Fig. 7) with T_{ϱ} values from Misiti et al. (2009), similarly calculated by the linear extrapolation of the two closest viscosity data points (i.e., around $\eta = 10^{12}$ Pa s). Additionally, we converted the polynomial relationship from mol% to wt% for Stromboli composition,

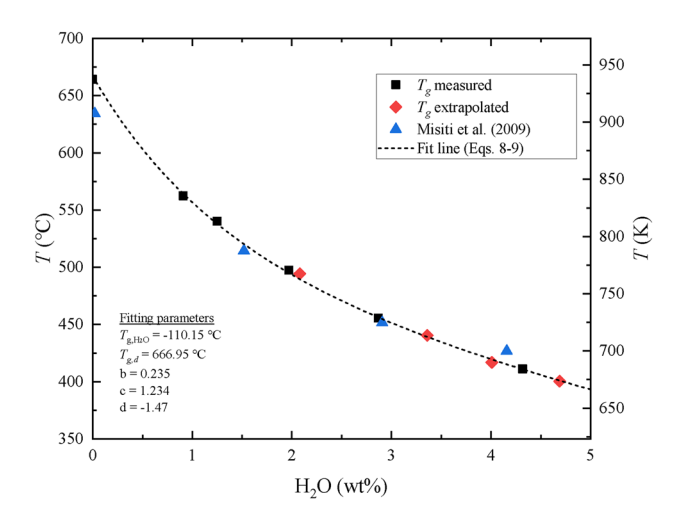


Fig. 7 Glass transition temperature (T_g) as a function of water content (wt%). The dashed line corresponds to the best fit solution using Eqs. 8 and 9 (Schneider et al. 1997). T_g measured corresponds to T_{onset} at $q_{c,h} = 10$ K min⁻¹, T_g extrapolated corresponds to values obtained from linear regression of T_{onset} at $q_{c,h} = 15$ and 30 K min⁻¹. Extrapolated T_g from the literature are also reported (Misiti et al. 2009)

to be able to calculate T_g for H_2O contents up to 10 wt% (see Supplementary Material Fig. 2).

Using Eq. 4 and Brillouin spectroscopy data (BLS), we calculated the K/G ratio for our anhydrous and hydrous samples (Table 1). We found that the K/G ratio is independent on the total water concentration between 0 and ~5 wt% $(K/G = 1.73 \pm 0.02)$ and that the effect of pressure is negligible when comparing samples synthesized up to 5 kbar. Additionally, our data are in good agreement with Cassetta et al. (2021) who calculated, using BLS data from the literature (Whittington et al. 2012), K/G = 1.74 and 1.68 for an anhydrous and hydrous ($H_2O = 3.02 \text{ wt\%}$) basalt, respectively. As such, based on the empirical relationship between K/G and m (Eq. 7) (Cassetta et al. 2021), we deduce here that, within the uncertainty, the fragility index (m) of the water-bearing melts equals m of the anhydrous melt $(m=40.7\pm0.7)$, which is reliably constrained by viscosity data over a large temperature interval (Fig. 5). We test this hypothesis in the discussion section using an independent set of data.

Discussion

The remarkable agreement between our anhydrous viscosity and literature data (Giordano et al. 2006; Misiti et al. 2009; Scarani et al. 2022), together with the virtual absence of Raman spectral features between 650 and 730 cm⁻¹, demonstrate that the anhydrous Stromboli melt is not prone to nanocrystallization during viscosity and DSC measurements. This agrees with the recent findings of Scarani et al. (2022)



who showed that the overall FeO_{tot} + TiO₂ content modulates the nanocrystallization of basaltic melts: the comparatively lower content in transition metal oxides of the Stromboli anhydrous composition results in a more stable melt with respect to, for instance, Mt. Etna trachybasalt. Moreover, the excellent agreement of our F-DSC-derived viscosity (6.4 < log η < 8.5) with the parameterization of anhydrous Stromboli basalt proposed by this work, as well as by previous studies (Giordano et al. 2008, 2009; Misiti et al. 2009; Scarani et al. 2022), demonstrates that the F-DSC approach represents a valuable tool for accessing unprecedented viscosity ranges, commonly restricted by melt crystallization and gas exsolution (Dingwell et al. 2004; Al-Mukadam et al. 2020; Langhammer et al. 2021; Di Genova et al. 2023).

In contrast, Raman spectra of hydrous glasses (Figs. 2 and 3) suggest that Stromboli hydrous melts with H_2O contents greater than 1 wt% are prone to Fe-Ti-oxide nanolite crystallization during viscosity and C-DSC measurements. Moreover, for samples with water content higher than 3.3 wt%, Raman and FTIR spectra suggest the formation of free hydroxyl (Fig. 4). These changes induce non-trivial chemical and structural modifications in the melt that are known to result in an overestimation of melt viscosity at temperatures above T_g (Di Genova et al. 2017a, b; Di Genova et al. 2020b; Liebske et al. 2003).

In general, Raman spectral signatures (Fig. 3) suggest an increasing degree of nanocrystallization as water content increases, which is in good agreement with previous studies (Davis et al. 1997). For instance, for low water content (S_{1.25}), micropenetration results show a relatively good agreement with C-DSC-derived viscosity data (Fig. 5), as supported by the comparison of Raman spectra acquired before and after the measurements that suggests moderate nanocrystallization (Figs. 2 and 3a). For higher water contents (e.g., S 2.08, S 3.36, S 4.01, S 4.32, and S 4.69), we observed stronger Raman intensity at ~650–730 cm⁻¹ (Fig. 3) and an evident time-dependent increase in viscosity during micropenetration measurements (Fig. 6). As such, the hydrous Stromboli basalt becomes more and more unstable during measurements as water content increases. Finally, the inspection of Raman spectra in Fig. 3 indicates that, for comparable water contents, a relatively more oxidized starting material (i.e., samples synthesised with IHPV apparatus) led to a higher degree of nanocrystallization during the experiments.

Since C-DSC measurements of T_g ($\eta=10^{12}$ Pa s) involve the lowest/shortest operatively achievable excursion to high temperatures, thereby minimizing the risk of nanocrystallization in the samples, we argue that our T_g values (Fig. 7) represent the most accurate starting point for a reliable description of the viscosity of the hydrous Stromboli melt. We therefore combined our T_g parameterization as a function of H_2O content (Fig. 7 and Table 1) with the estimated

and constant fragility index $m = 40.7 \pm 0.7$, entering them into the MYEGA parametrization (Eq. 5) to model the viscosity of Stromboli melt as a function of temperature and water content. We note that while our BLS results and the remarkable prediction of the F-DSC-derived hydrous viscosity (Fig. 9) support the hypothesis that m is not dependent on H₂O content and equals the value of the anhydrous melt $(m=40.7\pm0.7)$, the empirical viscosity model proposed by Giordano et al. (2009) for Stromboli composition predicts conversely that m should decrease significantly with increasing water content from 42 (anhydrous melt) to 36.5 ($H_2O = 5$ wt%). Keeping all other parameters unchanged, a lower m would necessarily return higher viscosity at temperatures above T_{σ} (e.g., at eruptive temperature); thus, disregarding for a moment the effects of nanocrystallization described above, it is important to ascertain whether or not melt fragility should depend on water concentration. To do so, we evaluate the relationship between m and water content for our Stromboli basalt within the framework of Adam and Gibbs (1965) theory that predicts a positive correlation between m and the configurational heat capacity (C_n^{conf}) of the melt (e.g., Bouhifd et al. 2013, 2006; Di Genova et al. 2014b; Robert et al., 2012; Smedskjaer et al. 2011). For glass-forming melts, C_n^{conf} at T_o can be expressed as follows:

$$C_p^{conf}(T_g) = C_{pl} - C_{pg}(T_g) \tag{10}$$

where C_{pl} is the heat capacity of the relaxed liquid, and $C_{pg}(T_g)$ is the heat capacity of the glass at T_g , which is extrapolated using the expression after Maier and Kelley (1932):

$$C_{pg}(T) = a + bT - cT^{-2} (11)$$

Using our DSC rate-matching data (i.e., second upscans), we derived C_p^{conf} of four samples with different water content following Bouhifd et al. (2013) (Supplementary Material Fig. 3). Our results show that C_p^{conf} does not vary significantly with water content, as $C_p^{conf}(T_g)$ dry is equal to 0.38 J g^{-1} K⁻¹, while it is equal to 0.37 J g^{-1} K⁻¹ at $2.87 \pm 0.05 \text{ H}_2\text{O}$ wt% (Supplementary Material Fig. 3). After conversion from mass to mol, $C_p^{conf}(T_g) \cong 23 \pm 1 \text{Jmol}^{-1} \text{K}^{-1}$ (under the assumption of 50% of the total iron as FeO); our values exhibit moreover very good agreement with the literature (Robert et al. 2014). We therefore conclude that the addition of water should not be expected to significantly change the melt fragility of Stromboli liquid, as suggested by (i) BLS data (Table 3), (ii) the low variation of the DSC-derived m when using only nanolite-free measurements (Fig. 6), and iii) the prediction of the F-DSC-derived hydrous viscosity (Fig. 9) using the anhydrous $m = 40.7 \pm 0.7$. Thus, the wellconstrained fragility of the anhydrous melt (Fig. 5) can be used to parameterize the melt viscosity as a function of



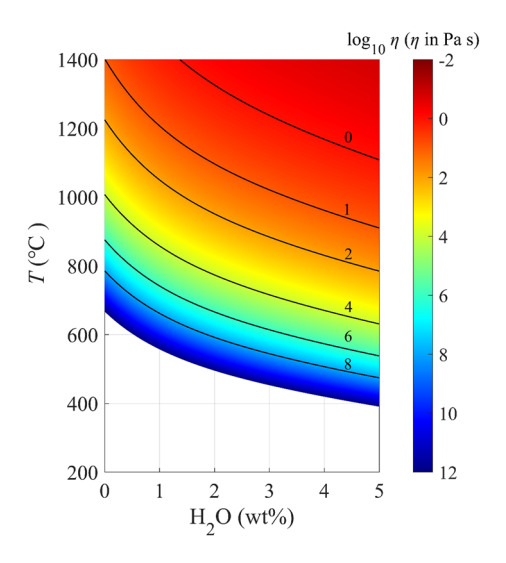


Fig. 8 Viscosity of Stromboli basalt as a function of water content (wt%) and temperature ($^{\circ}$ C)

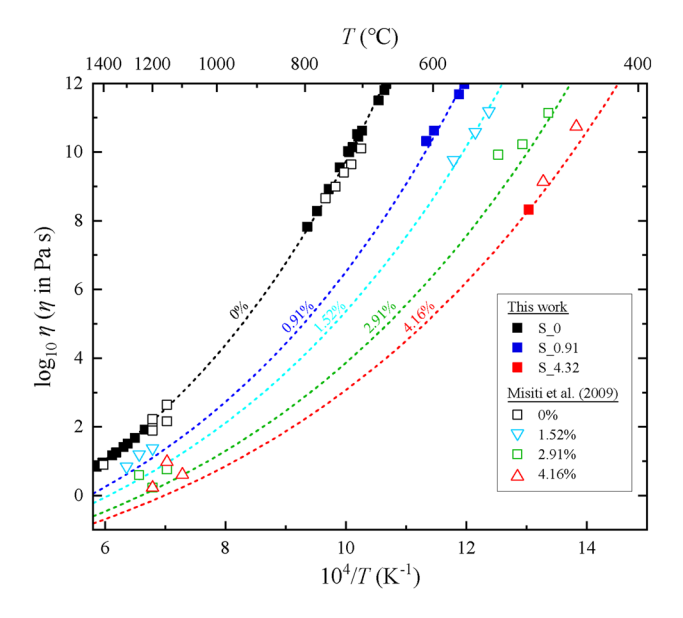


Fig. 9 Viscosity results of nanolite-free Stromboli samples and literature viscosity data from Misiti et al. (2009). Dashed lines represent the viscosity predictions of our model for 0, 0.91, 1.52, 2.91 and 4.16 $\rm H_2O~wt\%$

temperature and water content. This conclusion substantiates in a new viscosity model of Stromboli basalt as a function of temperature and water content $\eta(T, H_2O)$ (Fig. 8) based on the MYEGA parametrization (Eq. 5), where T_g is described according to Eq. 8 (Fig. 7 for fitting parameters) and m is fixed and equal to 40.7 ± 0.7 (Fig. 5). A viscosity calculator is provided in the Supplementary Material. We stress that our experimental data can also provide insight into the possible origin of the decrease in m with increasing water content in previous empirical models (e.g., Giordano et al. 2009,

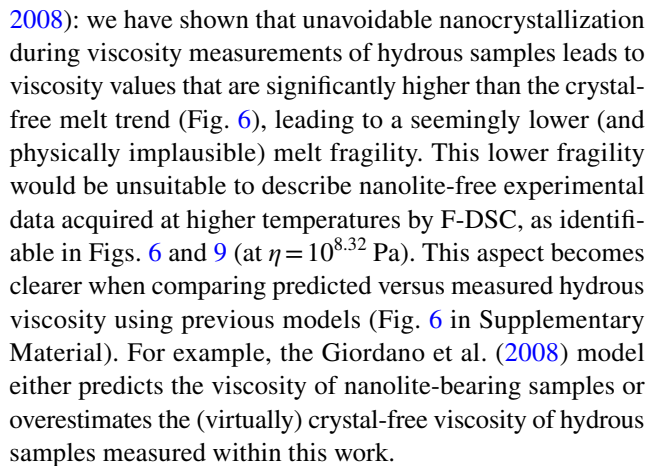


Figure 9 shows the comparison between our nanolite-free viscosity measurements, our model predictions, and the viscosity data reported by Misiti et al. (2009). The hydrous viscosity data obtained from melts that did not experience relevant nanocrystallization after either C-DSC (S_0.91, $10^{10.32} < < 10^{12}$ Pa s) or F-DSC (S_4.31, $\eta = 10^{8.32}$ Pa s) measurements are accurately predicted by our model. These data were not used to train our model, so its prediction capability is remarkable and demonstrates that the combination of T_g from C-DSC and m from BLS enables the accurate derivation of the anhydrous and hydrous viscosity (Cassetta et al. 2021).

Concerning the comparison with literature data from Misiti et al. (2009), we observed that, for a given water content, our model positively predicts the hydrous viscosity around 10¹² Pa s but then predicts lower viscosity with increasing temperature (Fig. 9). For example, at relatively low water content ($H_2O = 1.52 \text{ wt\%}$), we successfully predict viscosity data from Misiti et al. (2009) between 10^{11.18} Pa s (534.85 °C) and $10^{10.58}$ Pa s (549.85 °C) (Fig. 9); however, at 574.85 °C, our model predicts a viscosity of $\eta = 10^{9.56}$ Pa s, slightly lower than the $10^{9.76}$ Pa s reported by Misiti et al. (2009). At higher water content ($H_2O = 2.91 \text{ wt\%}$), Misiti et al. (2009) measured $\eta = 10^{11.1}$ Pa s (474.85 °C), while our prediction is $10^{10.94}$ Pa s. At 499.85 and 524.85 °C Misiti et al. (2009) measured respectively 10^{10.22} and 10^{9.92} Pa s, where our model predicts significantly lower viscosity values (10^{9.77} and 10^{8.77} Pa s, respectively). We also compared our model predictions with the high-temperature falling-sphere-derived viscosity reported by Misiti et al. (2009). In general, our model predicts significantly lower viscosity at high temperatures. For instance, at $H_2O = 1.52$ wt%, they reported viscosities of $10^{1.38}$, $10^{1.2}$ and $10^{0.84}$ Pa s at 1200, 1250 and 1300 °C respectively. For the same water content, our model predicts viscosities of $10^{0.70}$, $10^{0.47}$ and $10^{0.27}$ Pa s, respectively. At 2.91 H₂O wt%, our model successfully reproduced the $\eta = 10^{0.23}$ Pa s at 1200 °C reported by Misiti et al. (2009); however, their data subsequently display a physically paradoxical increase in viscosity with increasing temperature,



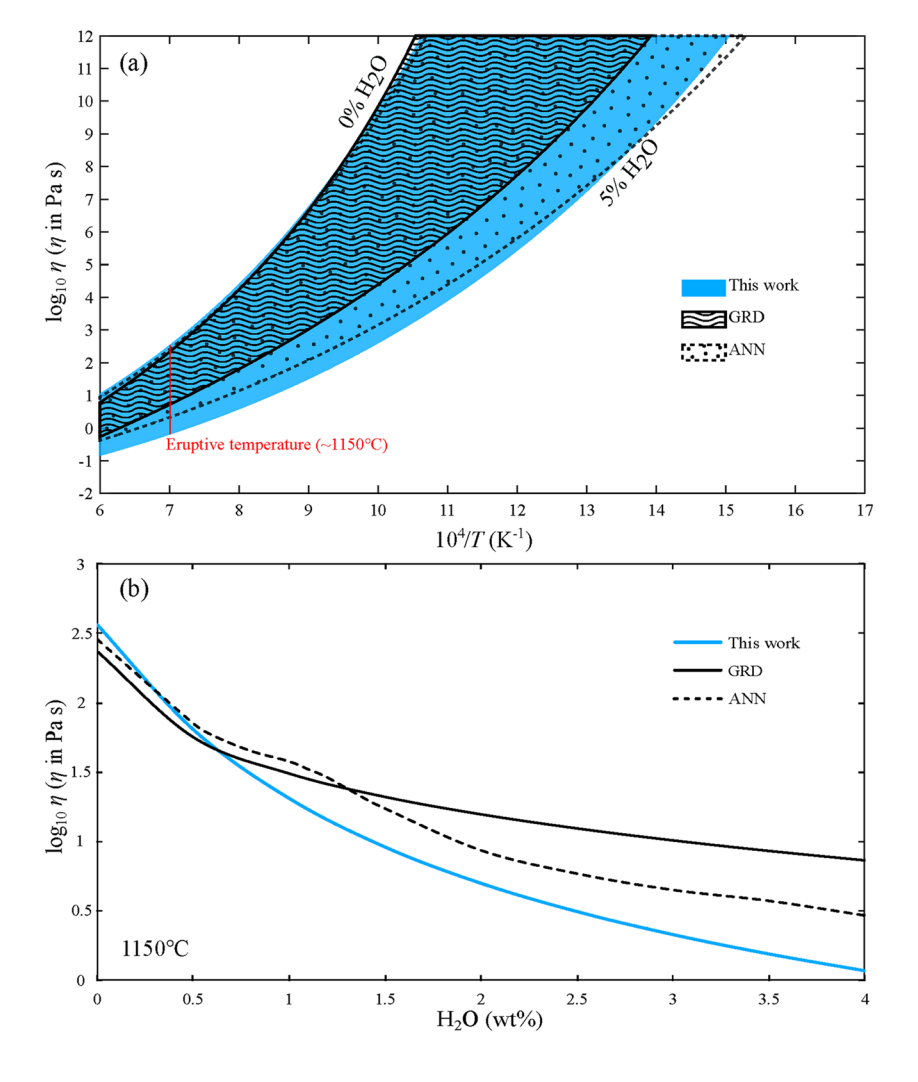
from $10^{0.23}$ Pa s (1200 °C) to $10^{0.6}$ Pa s (1250 °C). A similar behaviour is observed at 4.16 $\rm H_2O$ wt% in Misiti et al. (2009), where viscosity increased from $10^{0.61}$ to $10^{0.98}$ Pa s when temperature increased from 1100 to 1150 °C. As such, we conclude that falling-sphere measurements entail unavoidable experimental challenges that may seriously affect their reliability, whereas our experimental approach intrinsically circumvents such limitations.

Figure 10a shows the comparison between our model and two global viscosity models of volcanic melts (Giordano et al. 2008; Langhammer et al. 2022). We considered the Giordano et al. (2008) model (GRD) because it is the most used viscosity model in the literature, and the Langhammer et al. (2022) model (ANN), which is the most recent viscosity model and the first one based on artificial neural networks. We input the chemical composition of our Stromboli melt (Supplementary Material Table 1) and assumed a Fe³⁺/Fe²⁺ ratio of 0.5. In general, while the ANN performs more similarly to our parameterization than GRD, the two viscosity models predict excessively high viscosities with increasing temperature. This is also the case if we compare

our results with other viscosity models, such as the global model of Hui and Zhang (2007) and the Giordano et al. (2009), specifically targeted on Stromboli melt (Supplementary Material Fig. 4).

For the anhydrous melt (left border in Fig. 10a), our model shows similar behaviour in comparison to both GRD and ANN literature models. This result is consistent with the observation that the anhydrous Stromboli melt is not prone to nanocrystallization during viscosity measurements, preventing experimental artifacts whatever the methodology applied. Nevertheless, for water content higher than ~ 0.8 wt%, our model predicts lower viscosities (Fig. 10). For example, at pre-eruptive conditions of 1150 °C and 3.67 wt% H₂O (Giordano et al. 2009; La Spina et al. 2015; Andronico et al. 2021), our model predicts a viscosity of 10^{0.15} Pa s, in contrast to the 10^{0.91} and 10^{0.54} Pa s predicted by GRD and ANN respectively, i.e. 5.7-2.5 times lower than previous studies. We note that our model diverges from GRD when the water content increases above ~ 0.8 wt%. We argue that this behaviour is controlled by the ease of nanocrystallization of hydrous melts during viscosity measurements: for

Fig. 10 a Comparison of our model with two viscosity models for Stromboli basalt from 0 wt% (left border) to 5 wt% $\rm H_2O$ content (right border): Giordano et al. 2008 (GRD) and Langhammer et al. 2021 (ANN). The vertical red line marks the pre-eruptive temperature of Stromboli basalt ($\rm T$ = 1150 °C; Giordano et al. 2009; La Spina et al. 2015). **b** Comparison of predicted viscosity as a function of water content at the pre-eruptive temperature (T = 1150 °C)



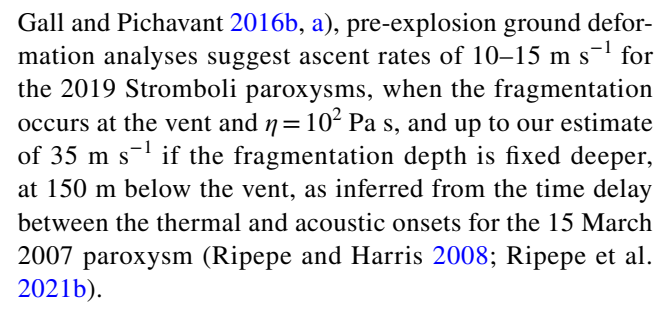


example, while the sample S_0.91 did not experience relevant crystallization during viscosity measurements (Fig. 3a and Fig. 6), we observed nanocrystallization when the water content is greater than 1.25 wt%, as suggested by Raman spectra (Fig. 3). Thus, we conclude that the excessively high viscosity predicted by the empirical models (Fig. 10) results from the (erroneously) assumed decrease in m with increasing water content, which we have shown to be related to the crystallization of nanolites and water loss during hydrous viscosity measurements. Parallelly, the ANN model predicts an unsteady decrease in viscosity between 0.5 and 1.5 H₂O wt% (Fig. 10b), which mirrors the respective dependence of m on H₂O (Supplementary Material Fig. 5). Because the ANN model does not make any conceptual assumptions concerning the dependence of melt fragility on water content (Langhammer et al. 2022), our study suggests that more high-quality hydrous viscosity data, combined with Brillouin spectroscopy and heat capacity data, are required to accurately constrain the variations of melt fragility with water concentrations, and thereby model the viscosity of hydrous volcanic melts by an artificial neural network approach.

Implications for Stromboli magma dynamics

Our observations suggest that the viscosity of Stromboli melt at pre-eruptive conditions is lower than identified so far (Giordano et al. 2009, 2008; Hui and Zhang 2007; Misiti et al. 2009). This aspect is critical when modelling the change in viscosity during magma ascent upon decompression, as we rely on viscosity models to define the rate of melt phase viscosity increase due to water exsolution. Such a rate is key in controlling the thermodynamic equilibrium or disequilibrium in magmas during ascent, and therefore, degassing and crystallization dynamics (Mangan and Sisson 2000; La Spina et al. 2016; Polacci et al. 2018; Arzilli et al. 2019; Kolzenburg et al. 2019). Notably, our model predicts a very large increase in melt viscosity upon water exsolution at a constant temperature of 1150 °C (Fig. 10), as we calculated $\eta = 10^{0.15}$ Pa s, at H₂O = 3.67 wt%, and $\eta = 10^{2.56}$ Pa s at anhydrous conditions, which difference is 9 times greater compared to GRD model predictions, respectively $\eta = 10^{0.91}$ and $10^{2.56}$ Pa s.

Considering a simple ascent rate model that neglects the shear-rate dependence of viscosity (Sparks et al. 2006; Kokandakar et al. 2018), and following Misiti et al. (2009), the ascent velocity of a bubble-free Stromboli basalt (T=1150 °C and $H_2O=3.67$ wt%) with a crystal content of 10 vol% through a 4 m wide dike is 41 m s⁻¹ using our viscosity model ~ 30% greater with respect to the previous estimation by Misiti et al. (2009). Although this result is significantly higher than estimates of 1.5–3 m s⁻¹ from bubble number density (BND) data of experimental samples and erupted materials (Pichavant et al. 2013; Le



In general, the lower melt viscosity revealed by our study promotes a more efficient decoupling between the magma and the gas phase (La Spina et al. 2017a; Valdivia et al. 2022), and decreases the minimum bubble diameter required for bubble segregation (Sparks 2003). This effect, in addition to the constant evolution of the permeable pathways in low-viscosity fluids, diminishes the accuracy of permeability-dependant estimations coming from pyroclastic vesicle textures (La Spina et al. 2017b). On the other hand, a lower magma viscosity produces higher estimations of ascent rates (Sparks et al. 2006; Kokandakar et al. 2018; La Spina et al. 2020), affecting the calculation of the Reynolds number, and increasing the likelihood of having a turbulent flow regime (Melnik and Sparks 2006).

Paroxysmal events at Stromboli volcano have been attributed to the rapid ascent of a low-porphyritic volatile-rich magma from a 7-10 km depth reservoir that interacts with a high-porphyritic crystal-rich and denser magma mush at shallower depths of 2-3 km (Andronico et al. 2021; Métrich et al. 2021; Ripepe et al. 2021b), being responsible for the most dangerous outcomes that occur unexpectedly (Bertagnini et al. 2003; Le Gall and Pichavant 2016a; Andronico et al. 2021; Mattia et al. 2021). Our results further support that the volatile-rich basalt rises rapidly and in a turbulent regime. Additionally, if we consider lower viscosity, the depth estimations for the onset of gas expansion used in ground deformation analyses should increase (Ripepe et al. 2021b), possibly matching the crystal-rich magma mush depth. If that is the case, as the volatile-rich gas-magma mix rises, the limited expansion of the gas phase, which is controlled by the interaction with a more viscous and denser crystal-rich magma, might generate enough overpressure to fragment the magma and produce a paroxysmal event. This effect would be also enhanced by the formation of nanolites during ascent as their presence reduce the required oversaturation for bubbles to form through heterogeneous nucleation at higher depths. Therefore, it is imperative to undertake further investigations to fully grasp the extensive implications arising from our viscosity predictions. This critical endeavour will not only enhance numerical modelling but also advance our comprehension of magma dynamics and outgassing processes in compositions akin to Stromboli basalt.



Conclusions

In this work, we measured the viscosity of anhydrous and hydrous Stromboli basalt. We accomplished full characterization of the Stromboli melt viscosity as a function of temperature and water content by combining conventional and flash differential scanning calorimetry with Raman, FTIR, and Brillouin spectroscopy. We showed that while the anhydrous Stromboli basalt is not prone to crystallization during viscosity measurements, the hydrous melt is prone to nanocrystallization of Fe-Ti-oxides when the water content is higher than 1 wt%.

As a consequence, the viscosity of Stromboli magma under eruptive conditions is 2 to 5 times lower than what previous empirical models predict. Our findings are crucial for advancing our understanding of the dynamics of Stromboli volcano. The observed reduction in pure melt viscosity can explain the rapid ascent of magma during paroxysmal events, which are often accompanied by shortlived geophysical signals.

Supplementary Information The online version contains supplementary material available at https://doi.org/10.1007/s00410-023-02024-w.

Acknowledgements PV and DDG acknowledge the funding by Deutsche Forschungsgemeinschaft (DFG) project DI 2751/2–1. DDG acknowledges the funding from the European Research Council (ERC) under the European Union's Horizon 2020 research and innovation programme (NANOVOLC, ERC Consolidator Grant–No. 101044772). AZ acknowledges the DFG for funding his research through the Walter Benjamin Program, project no. 448961237, ZA 1188/1-1 and ZA 1188/2-1. JD acknowledges DFG for financial support via the grant DE 598/33-1. We thank Alexander Rother and Raphael Njul for sample preparation at the Bayerisches Geoinstitut, Raschid Al-Mukadam and Sara Fanara for the support at TU Clausthal and the University of Goettingen, respectively.

Funding Open Access funding enabled and organized by Projekt DEAL.

Data availability The data used in this article can be accessed using the following link: https://zenodo.org/record/8070183.

Declarations

Conflict of interest All authors declare that they have no conflicts of interest.

Open Access This article is licensed under a Creative Commons Attribution 4.0 International License, which permits use, sharing, adaptation, distribution and reproduction in any medium or format, as long as you give appropriate credit to the original author(s) and the source, provide a link to the Creative Commons licence, and indicate if changes were made. The images or other third party material in this article are included in the article's Creative Commons licence, unless indicated otherwise in a credit line to the material. If material is not included in the article's Creative Commons licence and your intended use is not permitted by statutory regulation or exceeds the permitted use, you will need to obtain permission directly from the copyright holder. To view a copy of this licence, visit http://creativecommons.org/licenses/by/4.0/.

References

- Adam G, Gibbs JH (1965) On the temperature dependence of cooperative relaxation properties in glass-forming liquids. J Chem Phys 43:139–146. https://doi.org/10.1063/1.1696442
- Al-Mukadam R, Di Genova D, Bornhöft H, Deubener J (2020) High rate calorimetry derived viscosity of oxide melts prone to crystallization. J Non Cryst Solids 536:119992. https://doi.org/10.1016/j.jnoncrysol.2020.119992
- Al-Mukadam R, Zandona A, Deubener J (2021) Kinetic fragility of pure TeO2 glass. J Non Cryst Solids 554:1–6. https://doi.org/ 10.1016/j.jnoncrysol.2020.120595
- Andronico D, Del Bello E, D'Oriano C et al (2021) Uncovering the eruptive patterns of the 2019 double paroxysm eruption crisis of Stromboli volcano. Nat Commun 12:1–14. https://doi.org/10.1038/s41467-021-24420-1
- Angell CA (1995) Formation of Glasses from Liquids and Biopolymers. Science 267:1924–1935. https://doi.org/10.1126/science. 267.5206.1924
- Arzilli F, La Spina G, Burton M et al (2019) Magma fragmentation in highly explosive basaltic eruptions induced by rapid crystallization. Nat Geosci 12:1023–1028. https://doi.org/10.1038/s41561-019-0468-6
- Arzilli F, Polacci M, La Spina G et al (2022) Dendritic crystallization in hydrous basaltic magmas controls magma mobility within the Earth's crust. Nat Commun. https://doi.org/10.1038/s41467-022-30890-8
- Behrens H, Bauer U, Reinsch S et al (2018) Structural relaxation mechanisms in hydrous sodium borosilicate glasses. J Non Cryst Solids 497:30–39. https://doi.org/10.1016/j.jnoncrysol.2018.05.025
- Bertagnini A, Métrich N, Landi P, Rosi M (2003) Stromboli volcano (Aeolian Archipelago, Italy): An open window on the deep-feeding system of a steady state basaltic volcano. J Geophys Res Solid Earth. 108:22
- Bondar D, Zandona A, Withers AC et al (2022) Rapid-quenching of high-pressure depolymerized hydrous silicate (peridotitic) glasses. J Non Cryst Solids. https://doi.org/10.1016/j.jnoncrysol. 2021.121347
- Bondar D, Withers AC, Whittington AG et al (2023) Dissolution mechanisms of water in depolymerized silicate (peridotitic) glasses based on infrared spectroscopy. Geochim Cosmochim Acta 342:45–61. https://doi.org/10.1016/j.gca.2022.11.029
- Bouhifd MA, Richet P, Besson P et al (2004) Redox state, microstructure and viscosity of a partially crystallized basalt melt. Earth Planet Sci Lett 218:31–44. https://doi.org/10.1016/S0012-821X(03)00641-1
- Bouhifd MA, Whittington AG, Roux J, Richet P (2006) Effect of water on the heat capacity of polymerized aluminosilicate glasses and melts. Geochim Cosmochim Acta 70:711–722. https://doi.org/10.1016/j.gca.2005.09.012
- Bouhifd MA, Whittington AG, Withers AC, Richet P (2013) Heat capacities of hydrous silicate glasses and liquids. Chem Geol 346:125–134, https://doi.org/10.1016/j.chemgeo.2012.10.026
- Cáceres F, Wadsworth FB, Scheu B et al (2020) Can nanolites enhance eruption explosivity? Geology 48:997–1001. https://doi.org/10. 1130/G47317.1
- Campagnola S, Vona A, Romano C, Giordano G (2016) Crystallization kinetics and rheology of leucite-bearing tephriphonolite magmas from the Colli Albani volcano (Italy). Chem Geol 424:12–29. https://doi.org/10.1016/j.chemgeo.2016.01.012
- Cashman KV, Scheu B (2015) Magmatic Fragmentation. Elsevier Inc, Second Edi
- Cassetta M, Di Genova D, Zanatta M et al (2021) Estimating the viscosity of volcanic melts from the vibrational properties of



- their parental glasses. Sci Rep 11:1–14. https://doi.org/10.1038/s41598-021-92407-5
- Cassidy M, Manga M, Cashman KV, Bachmann O (2018) Controls on explosive-effusive volcanic eruption styles. Nat Commun 9:2839. https://doi.org/10.1038/s41467-018-05293-3
- Chevrel MO, Cimarelli C, DeBiasi L et al (2015) Viscosity measurements of crystallizing andesite from Tungurahua volcano (Ecuador). Geochemistry Geophys Geosystems 16:870–889. https://doi.org/10.1002/2014GC005661
- Davis MJ, Ihinger PD, Lasaga AC (1997) Influence of water on nucleation kinetics in silicate melt. J Non Cryst Solids 219:62–69. https://doi.org/10.1016/S0022-3093(97)00252-4
- Degruyter W, Bachmann O, Burgisser A, Manga M (2012) The effects of outgassing on the transition between effusive and explosive silicic eruptions. Earth Planet Sci Lett 349–350:161–170. https://doi.org/10.1016/j.epsl.2012.06.056
- Del Gaudio P, Behrens H, Deubener J (2007) Viscosity and glass transition temperature of hydrous float glass. J Non Cryst Solids 353:223–236. https://doi.org/10.1016/j.jnoncrysol.2006. 11.009
- Di Genova D, Romano C, Alletti M et al (2014a) The effect of CO2 and H2O on Etna and Fondo Riccio (Phlegrean Fields) liquid viscosity, glass transition temperature and heat capacity. Chem Geol 377:72–86. https://doi.org/10.1016/j.chemgeo.2014.04.001
- Di Genova D, Romano C, Giordano D, Alletti M (2014b) Heat capacity, configurational heat capacity and fragility of hydrous magmas. Geochim Cosmochim Acta 142:314–333. https://doi.org/10.1016/j.gca.2014.07.012
- Di Genova D, Hess KU, Chevrel MO, Dingwell DB (2016) Models for the estimation of Fe3+/Fetot. ratio in terrestrial and extra- terrestrial alkali- and iron-rich silicate glasses using Raman spectroscopy. Am Mineral 101:943–952
- Di Genova D, Kolzenburg S, Wiesmaier S et al (2017a) A compositional tipping point governing the mobilization and eruption style of rhyolitic magma. Nature 552:235–238. https://doi.org/10.1038/nature24488
- Di Genova D, Sicola S, Romano C et al (2017b) Effect of iron and nanolites on Raman spectra of volcanic glasses: A reassessment of existing strategies to estimate the water content. Chem Geol 475:76–86. https://doi.org/10.1016/j.chemgeo.2017.10.035
- Di Genova D, Caracciolo A, Kolzenburg S (2018) Measuring the degree of "nanotilization" of volcanic glasses: Understanding syn-eruptive processes recorded in melt inclusions. Lithos 318–319:209–218. https://doi.org/10.1016/j.lithos.2018.08.011
- Di Genova D, Brooker RA, Mader HM et al (2020a) In situ observation of nanolite growth in volcanic melt: A driving force for explosive eruptions. Sci Adv. https://doi.org/10.1126/sciadv.abb0413
- Di Genova D, Zandona A, Deubener J (2020b) Unravelling the effect of nano-heterogeneity on the viscosity of silicate melts: Implications for glass manufacturing and volcanic eruptions. J Non Cryst Solids 545:120248. https://doi.org/10.1016/j.jnoncrysol. 2020.120248
- Di Genova D, Bondar D, Zandonà A et al (2023) Viscosity of anhydrous and hydrous peridotite melts. Chem Geol. https://doi.org/10.1016/j.chemgeo.2023.121440
- Di Muro A, Métrich N, Mercier M et al (2009) Micro-Raman determination of iron redox state in dry natural glasses: Application to peralkaline rhyolites and basalts. Chem Geol 259:78–88. https://doi.org/10.1016/j.chemgeo.2008.08.013
- Dingwell DB, Courtial P, Giordano D, Nichols ARLRL (2004) Viscosity of peridotite liquid. Earth Planet Sci Lett 226:127–138. https://doi.org/10.1016/j.epsl.2004.07.017
- Douglas RW, Armstrong WL, Edward J, Hall D (1965) A penetration viscometer. Glas Technol 6:52–55

- Friedman I, Long W, Smith RL (1963) Viscosity and water content of rhyolite glass. J Geophys Res 68:6523–6535. https://doi.org/10.1029/jz068i024p06523
- Giordano D, Mangiacapra A, Potuzak M et al (2006) An expanded non-Arrhenian model for silicate melt viscosity: A treatment for metaluminous, peraluminous and peralkaline liquids. Chem Geol 229:42–56. https://doi.org/10.1016/j.chemgeo.2006.01.007
- Giordano D, Russell JK, Dingwell DB (2008) Viscosity of magmatic liquids: a model. Earth Planet Sci Lett 271:123–134. https://doi.org/10.1016/j.epsl.2008.03.038
- Giordano D, Ardia P, Romano C et al (2009) The rheological evolution of alkaline Vesuvius magmas and comparison with alkaline series from the Phlegrean Fields, Etna, Stromboli and Teide. Geochim Cosmochim Acta 73:6613–6630. https://doi.org/10.1016/j.gca.2009.07.033
- Giordano D, Vona A, Gonzalez-Garcia D et al (2021) Viscosity of Palmas-type magmas of the Paraná Magmatic Province (Rio Grande do Sul State, Brazil): Implications for high-temperature silicic volcanism. Chem Geol 560:119981. https://doi.org/10.1016/j.chemgeo.2020.119981
- Gonnermann HMHM (2015) Magma Fragmentation. Annu Rev Earth Planet Sci 43:431–458. https://doi.org/10.1146/annur ev-earth-060614-105206
- Gonnermann HM, Manga M (2012) Chapter 4: Dynamics of magma ascent in the volcanic conduit. Model Volcan Process Phys Math Volcanism. 55–84
- Gonnermann HM, Giachetti T, Fliedner C, et al (2017) Journal of Geophysical Research: Solid Earth. 1–24
- Hughes EC, Buse B, Kearns SL et al (2019) Low analytical totals in EPMA of hydrous silicate glass due to sub-surface charging: Obtaining accurate volatiles by difference. Chem Geol 505:48–56. https://doi.org/10.1016/j.chemgeo.2018.11.015
- Hui H, Zhang Y (2007) Toward a general viscosity equation for natural anhydrous and hydrous silicate melts. Geochim Cosmochim Acta 71:403–416. https://doi.org/10.1016/j.gca.2006.09.003
- Ishibashi H, Sato H (2007) Viscosity measurements of subliquidus magmas: Alkali olivine basalt from the Higashi-Matsuura district, Southwest Japan. J Volcanol Geotherm Res 160:223–238. https://doi.org/10.1016/j.jvolgeores.2006.10.001
- Kleest C, Webb SL (2022) Influence of Fe2+/Fetot on the viscosity of melts from the Colli Albani Volcanic District (Italy) – foidite to phonolite. J Volcanol Geotherm Res 431:107649. https://doi.org/ 10.1016/j.jvolgeores.2022.107649
- Kleest C, Webb SL, Fanara S (2020) Rheology of melts from the colli albani volcanic district (Italy): a case study. Contrib to Mineral Petrol. https://doi.org/10.1007/s00410-020-01720-1
- Knafelc J, Bryan SE, Jones MWM et al (2022) Havre 2012 pink pumice is evidence of a short-lived, deep-sea, magnetite nanolite-driven explosive eruption. Commun Earth Environ 3:1–11. https://doi.org/10.1038/s43247-022-00355-3
- Kohl I, Bachmann L, Mayer E et al (2005) Glass transition in hyperquenched water? Nature 435:E1–E1. https://doi.org/10.1038/ nature03707
- Kokandakar GJ, Ghodke SS, Rathna K et al (2018) Density, Viscosity and Velocity (Ascent Rate) of Alkaline Magmas. J Geol Soc India 91:135–146. https://doi.org/10.1007/s12594-018-0827-8
- Kolzenburg S, Giordano D, Di MA, Dingwell DB (2019) Equilibrium viscosity and disequilibrium rheology of a high magnesium basalt from piton de la fournaise volcano, la reunion, indian ocean, France. Ann Geophys 62:1–14. https://doi.org/10.4401/ag-7839
- Koyaguchi T, Mitani NK (2005) A theoretical model for fragmentation of viscous bubbly magmas in shock tubes. J Geophys Res 110:B10202. https://doi.org/10.1029/2004JB003513
- La Spina G, Burton M, De'Michieli Vitturi M, (2015) Temperature evolution during magma ascent in basaltic effusive eruptions: A



- numerical application to Stromboli volcano. Earth Planet Sci Lett 426:89-100. https://doi.org/10.1016/j.epsl.2015.06.015
- La Spina G, Burton M, De Michieli VM, Arzilli F (2016) Role of syn-eruptive plagioclase disequilibrium crystallization in basaltic magma ascent dynamics. Nat Commun. https://doi.org/10.1038/ ncomms13402
- La Spina G, Polacci M, Burton M, de' Michieli Vitturi M, (2017) Numerical investigation of permeability models for low viscosity magmas: Application to the 2007 Stromboli effusive eruption. Earth Planet Sci Lett 473:279–290. https://doi.org/10.1016/j.epsl.
- La Spina G, De Michieli VM, Clarke AB (2017) Transient numerical model of magma ascent dynamics: application to the explosive eruptions at the Soufrière Hills Volcano. J Volcanol Geotherm Res 336:118-139. https://doi.org/10.1016/j.jvolgeores.2017.02.
- La Spina G, Arzilli F, Llewellin EW et al (2020) Explosivity of basaltic lava fountains is controlled by magma rheology, ascent rate and outgassing. Earth Planet Sci Lett 553:116658. https://doi.org/10. 1016/j.epsl.2020.116658
- Langhammer D, Di Genova D, Steinle-Neumann G (2021) Modeling the Viscosity of Anhydrous and Hydrous Volcanic Melts. Geochemistry, Geophys Geosyst 22:1-26. https://doi.org/10.1029/ 2021GC009918
- Langhammer D, Di Genova D, Steinle-Neumann G (2022) Modeling Viscosity of Volcanic Melts With Artificial Neural Networks. Geochemistry, Geophys Geosyst 23:24. https://doi.org/10.1029/ 2022GC010673
- Larre C. Morizet Y. Bézos A et al (2020) Particular H2O dissolution mechanism in iron-rich melt: Application to martian basaltic melt genesis. J Raman Spectrosc 51:493-507. https://doi.org/ 10.1002/jrs.5787
- Lautze NC, Houghton BF (2007) Linking variable explosion style and magma textures during 2002 at Stromboli volcano, Italy. Bull Volcanol 69:445-460. https://doi.org/10.1007/ s00445-006-0086-1
- Le Gall N, Pichavant M (2016a) Experimental simulation of bubble nucleation and magma ascent in basaltic systems: implications for stromboli volcano. Am Mineral 101:1967-1985. https://doi. org/10.2138/am-2016-5639
- Le Gall N, Pichavant M (2016b) Homogeneous bubble nucleation in H 2 O- and H 2 O-CO 2 -bearing basaltic melts: Results of high temperature decompression experiments. J Volcanol Geotherm Res 327:604–621. https://doi.org/10.1016/j.jvolgeores.2016.10.
- Liebske C, Behrens H, Holtz F, Lange RA (2003) The influence of pressure and composition on the viscosity of andesitic melts. Geochim Cosmochim Acta 67:473-485. https://doi.org/10.1016/ S0016-7037(02)01139-0
- Maier CG, Kelley KK (1932) An equation for the representation of high temperature heat content data. J Am Chem Soc 54:3243-3246. https://doi.org/10.1021/ja01347a029
- Mangan MT, Sisson TW (2000) Delayed, disequilibrium degassing in rhyolite magma: Decompression experiments and implications for explosive volcanism. Earth Planet Sci Lett 183:441-455. https://doi.org/10.1016/S0012-821X(00)00299-5
- Mattia M, Di Lieto B, Ganci G et al (2021) The 2019 eruptive activity at stromboli volcano: A multidisciplinary approach to reveal hidden features of the "unexpected 3 july paroxysm. Remote Sens. https://doi.org/10.3390/rs13204064
- Mauro JC, Yue Y, Ellison AJ et al (2009) Viscosity of glass-forming liquids. Proc Natl Acad Sci U S A 106:19780-19784. https://doi. org/10.1073/pnas.0911705106
- Meerlender G (1974) Viskositäts-Temperaturverhalten des Standardglases I der DGG. Glas Ber 47:1-3

- Melnik O, Sparks RSJ (2006) Transient Models of Conduit Flows during Volcanic Eruptions. In: Mader HM (ed) Statistics in Volcanology. The Geological Society of London, UK
- Métrich N, Bertagnini A, Di Muro A (2009) Conditions of magma storage, degassing and ascent at Stromboli: New insights into the volcano plumbing system with inferences on the eruptive dynamics. J Petrol 51:603-626. https://doi.org/10.1093/petro logy/egp083
- Métrich N, Bertagnini A, Pistolesi M (2021) Paroxysms at Stromboli Volcano (Italy): Source, Genesis and Dynamics. Front Earth Sci 9:1-17. https://doi.org/10.3389/feart.2021.593339
- Misiti V, Vetere F, Mangiacapra A et al (2009) Viscosity of high-K basalt from the 5th April 2003 Stromboli paroxysmal explosion. Chem Geol 260:278-285. https://doi.org/10.1016/j.chemgeo. 2008.12.023
- Misiti V, Vetere F, Freda C et al (2011) A general viscosity model of Campi Flegrei (Italy) melts. Chem Geol 290:50–59. https://doi. org/10.1016/j.chemgeo.2011.08.010
- Mueller S, Scheu B, Spieler O, Dingwell DB (2008) Permeability control on magma fragmentation. Geology 36:399-402. https:// doi.org/10.1130/G24605A.1
- Mueller S, Scheu B, Kueppers U et al (2011) The porosity of pyroclasts as an indicator of volcanic explosivity. J Volcanol Geotherm Res 203:168–174. https://doi.org/10.1016/j.jvolgeores. 2011.04.006
- Ohlhorst S, Behrens H, Holtz F (2001) Compositional dependence of molar absorptivities of near-infrared OH-and H2O bands in rhyolitic to basaltic glasses. Chem Geol 174:5–20. https://doi. org/10.1016/S0009-2541(00)00303-X
- Okumura S, Uesugi K, Goto A et al (2022) Rheology of nanocrystal-bearing andesite magma and its roles in explosive volcanism. Commun Earth Environ 3:1-7. https://doi.org/10.1038/ s43247-022-00573-9
- Pichavant M, Di Carlo I, Rotolo SG et al (2013) Generation of CO2rich melts during basalt magma ascent and degassing. Contrib to Mineral Petrol 166:545-561. https://doi.org/10.1007/ s00410-013-0890-5
- Polacci M, Arzilli F, La Spina G et al (2018) Crystallisation in basaltic magmas revealed via in situ 4D synchrotron X-ray microtomography. Sci Rep 8:1-13. https://doi.org/10.1038/ s41598-018-26644-6
- Revil A, Finizola A, Ricci T et al (2011) Hydrogeology of Stromboli volcano, Aeolian Islands (Italy) from the interpretation of resistivity tomograms, self-potential, soil temperature and soil CO2 concentration measurements. Geophys J Int 186:1078-1094. https://doi.org/10.1111/j.1365-246X.2011.05112.x
- Richet P, Lejeune AMM, Holtz F, Roux J (1996) Water and the viscosity of andesite melts. Chem Geol 128:185-197. https://doi.org/ 10.1016/0009-2541(95)00172-7
- Ripepe M, Harris AJL (2008) Dynamics of the 5 April 2003 explosive paroxysm observed at Stromboli by a near-vent thermal, seismic and infrasonic array. Geophys Res Lett 35:1-6. https://doi.org/ 10.1029/2007GL032533
- Ripepe M, Delle Donne D, Legrand D et al (2021a) Magma pressure discharge induces very long period seismicity. Sci Rep 11:1–12. https://doi.org/10.1038/s41598-021-99513-4
- Ripepe M, Lacanna G, Pistolesi M et al (2021b) Ground deformation reveals the scale-invariant conduit dynamics driving explosive basaltic eruptions. Nat Commun. https://doi.org/10.1038/ s41467-021-21722-2
- Robert G, Whittington AG, Stechern A, Behrens H (2013) The effect of water on the viscosity of a synthetic calc-alkaline basaltic andesite. Chem Geol 346:135–148. https://doi.org/10.1016/j. chemgeo.2012.10.004



- Robert G, Whittington AG, Stechern A, Behrens H (2014) Heat capacity of hydrous basaltic glasses and liquids. J Non Cryst Solids 390:19-30. https://doi.org/10.1016/j.jnoncrysol.2014.02.011
- Romano C, Vona A, Campagnola S et al (2020) Modelling and physicochemical constraints to the 45 ka Agnano-Monte Spina Plinian eruption (Campi Flegrei, Italy). Chem Geol 532:119301. https:// doi.org/10.1016/j.chemgeo.2019.119301
- Russell JK, Giordano D, Dingwell DB (2003) High-temperature limits on viscosity of non-Arrhenian silicate melts. Am Mineral 88:1390-1394. https://doi.org/10.2138/am-2003-8-924
- Scarani A, Zandonà A, Di Fiore F et al (2022) A chemical threshold controls nanocrystallization and degassing behaviour in basalt magmas. Commun Earth Environ 3:284. https://doi.org/10.1038/ s43247-022-00615-2
- Schneider HA, Rieger J, Penzel E (1997) The glass transition temperature of random copolymers: 2. extension of the gordon - taylor equation for asymmetric Tg vs composition curves. Polymer (guildf) 38:1323–1337. https://doi.org/10.1016/S0032-3861(96) 00652-0
- Schuessler JA, Botcharnikov RE, Behrens H et al (2008) Amorphous Materials: Properties, structure, and Durability: Oxidation state of iron in hydrous phono-tephritic melts. Am Mineral 93:1493-1504. https://doi.org/10.2138/am.2008.2795
- Sehlke A, Whittington AG, Robert B et al (2014) Pahoehoe to áá transition of Hawaiian lavas: An experimental study. Bull Volcanol. https://doi.org/10.1007/s00445-014-0876-9
- Sinogeikin S, Bass J, Prakapenka V et al (2006) Brillouin spectrometer interfaced with synchrotron radiation for simultaneous x-ray density and acoustic velocity measurements. Rev Sci Instrum. Doi 10:2360884
- Smedskjaer MM, Mauro JC, Youngman RE et al (2011) Topological principles of borosilicate glass chemistry. J Phys Chem B 115:12930-12946. https://doi.org/10.1021/jp208796b
- Sparks RSJ (2003) Dynamics of magma degassing. Geol Soc Spec Publ 213:5-22. https://doi.org/10.1144/GSL.SP.2003.213.01.02
- Sparks RSJ, Baker L, Brown RJ et al (2006) Dynamical constraints on kimberlite volcanism. J Volcanol Geotherm Res 155:18-48. https://doi.org/10.1016/j.jvolgeores.2006.02.010
- Stabile P, Sicola S, Giuli G et al (2021) The effect of iron and alkali on the nanocrystal-free viscosity of volcanic melts: A combined Raman spectroscopy and DSC study. Chem Geol 559:119991. https://doi.org/10.1016/j.chemgeo.2020.119991
- Tsyganenko AA, Smirnov KS (1995) Vibrational spectroscopy of molecules and macromolecules on surfaces. Vib Spectrosc 9:308-309. https://doi.org/10.1016/0924-2031(95)90061-6
- Valdivia P, Marshall AA, Brand BD et al (2022) Mafic explosive volcanism at Llaima Volcano: 3D x-ray microtomography

- reconstruction of pyroclasts to constrain shallow conduit processes. Bull Volcanol 84:2. https://doi.org/10.1007/ s00445-021-01514-8
- Vetere F, Behrens H, Holtz F, Neuville DR (2006) Viscosity of andesitic melts - new experimental data and a revised calculation model. Chem Geol 228:233–245. https://doi.org/10.1016/j. chemgeo.2005.10.009
- Vetere F, Behrens H, Misiti V et al (2007) The viscosity of shoshonitic melts (Vulcanello Peninsula, Aeolian Islands, Italy): Insight on the magma ascent in dikes. Chem Geol 245:89–102. https://doi. org/10.1016/j.chemgeo.2007.08.002
- Vona A, Romano C (2013) The effects of undercooling and deformation rates on the crystallization kinetics of Stromboli and Etna basalts. Contrib to Mineral Petrol 166:491-509. https://doi.org/ 10.1007/s00410-013-0887-0
- Vona A, Romano C, Dingwell DB, Giordano D (2011) The rheology of crystal-bearing basaltic magmas from Stromboli and Etna. Geochim Cosmochim Acta 75:3214–3236. https://doi.org/10. 1016/j.gca.2011.03.031
- Webb SL, Dingwell DB (1990) Non-Newtonian Rheology of Igneous Melts at High Stresses and Strain Rates: Experimental Results for Rholite, Andesite, Basalt, and Nephelinite. J Geophys Res Earth Planets 95:15695-15701
- Wendee N (2022) Clear and Present Dangers: The Multiple Health Hazards of Volcanic Eruptions. Environ Health Perspect 130:1-9. https://doi.org/10.1289/EHP10541
- Whitfield CH, Brody EM, Bassett W (1976) Elastic moduli of NaCl by Brillouin scattering at high pressure in a diamond anvil cell. Rev Sci Instrum 47:942-947
- Whittington AG, Richet P, Polian A (2012) Water and the compressibility of silicate glasses: A Brillouin spectroscopic study. Am Mineral 97:455-467. https://doi.org/10.2138/am.2012.3891
- Yoshida K, Miyake A, Okumura SH et al (2023) Oxidation-induced nanolite crystallization triggered the 2021 eruption of Fukutoku-Oka-no-Ba. Japan Sci Rep 13:7117. https://doi.org/10.1038/ s41598-023-34301-w
- Zhang Y (1999) A criterion for the fragmentation of bubbly magma based on brittle failure theory. Nature 402:648-650. https://doi. org/10.1038/45210

Publisher's Note Springer Nature remains neutral with regard to jurisdictional claims in published maps and institutional affiliations.



Supplementary Material

Table 1. Chemical composition of Stromboli basalt

Oxide	S_0_atm ^a	STR^b
SiO_2	49.74 (0.77)	51.06 (0.39)
TiO_2	0.9 (0.08)	0.91 (0.10)
Al_2O_3	17.46 (0.04)	17.52 (0.28)
FeO_{tot}	7.58 (0.05)	7.58 (0.25)
MnO	0.14(0.1)	0.17 (0.07)
MgO	6.06 (0.14)	6.02 (0.20)
CaO	11.22 (0.10)	11.29 (0.29)
Na ₂ O	2.58 (0.24)	2.70 (0.19)
K_2O	2.04 (0.07)	2.12 (0.12)
P_2O5	0.53 (0.03)	0.64 (0.27)
Total	98.25	100
H ₂ O	0	0

^aThis work

Number in parenthesis Numbers in parenthesis indicate $\pm 1\sigma$.

^bScarani et al. (2022)

Table 2. Viscosity data of Stromboli anhydrous melt.

Type ^a	T (°C)	T(K)	$\log \eta \ (\eta \text{ in Pa s})$	Ref.
$C ext{-}DSC_{10 ext{-}10}$	664.2	937.3	12.0	*
$C ext{-}DSC_{10 ext{-}10}$	700.4	973.6	10.6	*
C-DSC ₁₀₋₁₀	721.0	994.2	10.0	*
C-DSC ₁₅₋₁₅	666.5	939.7	11.8	*
C-DSC ₁₅₋₁₅	706.2	979.4	10.4	*
C-DSC ₃₀₋₃₀	675.2	948.4	11.5	*
C-DSC ₃₀₋₃₀	715.3	988.5	10.1	*
F-DSC ₆₀₀₀₀₋₆₀₀₀₀	779.2	1052.4	8.2	*
F-DSC ₆₀₀₀₀₋₆₀₀₀₀	773.8	1046.9	8.2	*
F-DSC ₃₀₀₀₀₋₃₀₀₀₀	764.1	1037.2	8.5	*
F-DSC ₆₀₀₀₀₋₆₀₀₀₀	772.0	1045.1	8.2	*
F-DSC ₆₀₀₀₀₋₆₀₀₀₀	774.1	1047.2	8.2	*
F-DSC ₁₅₀₀₀₀₋₁₅₀₀₀₀	791.0	1064.2	7.8	*
F-DSC ₆₀₀₀₀₋₆₀₀₀₀	775.2	1048.4	8.2	*
F-DSC ₉₀₀₀₀₋₉₀₀₀₀	777.4	1050.5	8.0	*
F-DSC ₄₅₀₀₀₋₄₅₀₀₀	767.0	1040.2	8.3	*
F-DSC ₉₀₀₀₀₋₉₀₀₀₀	778.8	1052.0	8.0	*
F-DSC ₆₀₀₀₀₋₆₀₀₀₀	770.5	1043.6	8.2	*
F-DSC ₆₀₀₀₀₋₆₀₀₀₀	841.1	1114.3	6.8	*
F-DSC ₆₀₀₀₀₋₆₀₀₀₀	833.6	1106.8	6.8	*
F-DSC ₃₀₀₀₀₋₃₀₀₀₀	822.3	1095.4	7.1	*
F-DSC ₆₀₀₀₀₋₆₀₀₀₀	830.3	1103.5	6.8	*
F-DSC ₆₀₀₀₀₋₆₀₀₀₀	828.0	1101.2	6.8	*
F-DSC ₁₅₀₀₀₀₋₁₅₀₀₀₀	855.3	1128.4	6.4	*
F-DSC ₆₀₀₀₀₋₆₀₀₀₀	827.0	1100.1	6.8	*
F-DSC ₉₀₀₀₀₋₉₀₀₀₀	838.3	1111.4	6.7	*
F-DSC ₄₅₀₀₀₋₄₅₀₀₀	829.6	1102.8	7.0	*
F-DSC ₉₀₀₀₀₋₉₀₀₀₀	834.3	1107.5	6.7	*
F-DSC ₆₀₀₀₀₋₆₀₀₀₀	830.8	1104.0	6.8	*
MP	708.0	981.2	10.5	1
MP	723.0	996.2	10.0	1

MP	737.0	1010.2	9.6	1
MP	756.0	1029.2	8.9	1
MP	777.0	1050.2	8.3	1
MP	795.0	1068.2	7.8	1
CC	1227.0	1500.2	1.9	1
CC	1266.0	1539.2	1.7	1
CC	1295.0	1568.2	1.5	1
CC	1312.0	1585.2	1.4	1
CC	1343.0	1616.2	1.3	1
CC	1361.0	1634.2	1.2	1
CC	1405.0	1678.2	1.0	1
CC	1432.0	1705.2	0.8	1
FS	1149.9	1423.0	2.2	2
FS	1199.9	1473.0	1.9	2
FS	1199.9	1473.0	2.2	2
FS	1149.9	1423.0	2.6	2
FS	1199.9	1473.0	2.2	2
FS	1399.9	1673.0	0.9	2
MP	701.9	975.0	10.1	2
MP	717.9	991.0	9.6	2
MP	729.9	1003.0	9.4	2
MP	743.9	1017.0	9.0	2
MP	761.9	1035.0	8.7	2
CC	1593.9	1867.1	0.2	3
CC	1569.3	1842.5	0.3	3
CC	1544.7	1817.9	0.4	3
CC	1520.1	1793.3	0.5	3
CC	1495.5	1768.7	0.5	3
CC	1470.9	1744.1	0.6	3
CC	1446.3	1719.5	0.7	3
CC	1421.7	1694.9	0.8	3
CC	1397.1	1670.3	1.0	3
CC	1372.5	1645.7	1.1	3
CC	1347.8	1621.0	1.2	3
CC	1323.2	1596.4	1.3	3
CC	1298.6	1571.8	1.4	3
CC	1274.0	1547.2	1.6	3
CC	1249.4	1522.6	1.7	3
CC	1224.8	1498.0	1.9	3
CC	1200.2	1473.4	2.0	3
CC	1175.6	1448.8	2.2	3

CC	1151.0	1424.2	2.4	3
MP	729.5	1002.7	9.4	3
MP	697.9	971.1	10.5	3

^aType of measurement: C-DSC = conventional DSC; F-DSC = flash DSC; MP = micropenetration; CC = concentric cylinder; FS = falling sphere. C-DSC and F-DSC appendix values represent the cooling-heating rate in K min⁻¹. C-DSC- and F-DSC-derived viscosity was calculated using the K factor approach.

^{*}This work.

¹Scarani et al., 2022.

²Misiti et al., 2009

³Giordano et al., 2006

Table 3. Viscosity measurements of hydrous Stromboli melts.

Sample	H ₂ O (wt%) ^a	Type ^b	T (°C)	T (K)	log η (Pa s)
S_0.91	0.91 ± 0.03	$C ext{-}DSC_{10 ext{-}10}$	562.3	835.5	12.0
S_0.91	0.91 ± 0.03	$C ext{-}DSC_{10 ext{-}10}$	599.0	872.2	10.6
S_0.91	0.91 ± 0.03	$C ext{-}DSC_{20 ext{-}20}$	568.4	841.6	11.7
S_0.91	0.91 ± 0.03	$C ext{-}DSC_{20 ext{-}20}$	608.9	882.1	10.3
S_1.25	1.25 ± 0.01	$C ext{-}DSC_{10 ext{-}10}$	540.0	813.2	12.0
S_1.25	1.25 ± 0.01	$C ext{-}DSC_{10 ext{-}10}$	582.9	856.1	10.6
S_1.25	1.25 ± 0.01	$C ext{-}DSC_{10 ext{-}10}$	603.3	876.5	10.0
S_1.25	1.25 ± 0.01	$\text{C-DSC}_{20\text{-}20}$	542.2	815.4	11.7
S_1.25	1.25 ± 0.01	$\text{C-DSC}_{20\text{-}20}$	586.4	859.6	10.3
S_1.25	1.25 ± 0.01	$\text{C-DSC}_{20\text{-}20}$	607.6	880.8	9.7
S_1.25	1.25 ± 0.01	MP	586.0	859.2	10.4
S_1.97	1.97 ± 0.01	$\text{C-DSC}_{10\text{-}10}$	497.3	770.5	12.0
S_1.97	1.97 ± 0.01	$\text{C-DSC}_{10\text{-}10}$	545.5	818.7	10.6
S_1.97	1.97 ± 0.01	$\text{C-DSC}_{20\text{-}20}$	504.7	777.9	11.7
S_1.97	1.97 ± 0.01	$\text{C-DSC}_{20\text{-}20}$	553.2	826.4	10.3
S_1.97	1.97 ± 0.01	MP	546.2	819.3	11.9
S_1.97	1.97 ± 0.01	MP	576.3	849.5	9.3
S_2.08	2.08 ± 0.03	C-DSC ₁₅₋₁₅	498.2	771.4	11.8
S_2.08	2.08 ± 0.03	C-DSC ₁₅₋₁₅	542.8	816.0	10.4
S_2.08	2.08 ± 0.03	$C ext{-}DSC_{30 ext{-}30}$	509.9	783.1	11.5
S_2.08	2.08 ± 0.03	$C ext{-}DSC_{30 ext{-}30}$	560.7	833.9	10.1
S_2.87	2.87 ± 0.05	$\text{C-DSC}_{10\text{-}10}$	455.5	728.7	12.0
S_2.87	2.87 ± 0.03	$\text{C-DSC}_{10\text{-}10}$	512.9	786.1	10.6
S_2.87	2.87 ± 0.05	$C ext{-}DSC_{20 ext{-}20}$	458.5	731.7	11.7
S_2.87	2.87 ± 0.05	$C ext{-}DSC_{20 ext{-}20}$	517.1	790.3	10.3
S_3.36	3.36 ± 0.01	$C ext{-}DSC_{15 ext{-}15}$	445.0	718.2	11.8
S_3.36	3.36 ± 0.01	$C ext{-}DSC_{15 ext{-}15}$	493.6	766.8	10.4
S_3.36	3.36 ± 0.01	$C ext{-}DSC_{30 ext{-}30}$	459.0	732.2	11.5
S_3.36	3.36 ± 0.01	$C ext{-}DSC_{30 ext{-}30}$	523.7	796.9	10.1
S_4.01	4.01 ± 0.02	$C ext{-}DSC_{15 ext{-}15}$	423.3	696.5	11.8
S_4.01	4.01 ± 0.02	$C ext{-}DSC_{15 ext{-}15}$	480.7	753.9	10.4
S_4.01	4.01 ± 0.02	$C ext{-}DSC_{30 ext{-}30}$	442.9	716.1	11.5

$\begin{array}{cccccccccccccccccccccccccccccccccccc$						
$\begin{array}{cccccccccccccccccccccccccccccccccccc$	S_4.01	4.01 ± 0.02	C-DSC ₃₀₋₃₀	509.2	782.4	10.1
$\begin{array}{cccccccccccccccccccccccccccccccccccc$	S_4.32	4.32 ± 0.15	$C ext{-}DSC_{10 ext{-}10}$	411.1	684.3	12.0
$\begin{array}{cccccccccccccccccccccccccccccccccccc$	S_4.32	4.32 ± 0.15	$C ext{-}DSC_{10 ext{-}10}$	454.3	727.5	10.6
$\begin{array}{cccccccccccccccccccccccccccccccccccc$	S_4.32	4.32 ± 0.15	$C ext{-}DSC_{20 ext{-}20}$	414.0	687.2	11.7
$\begin{array}{cccccccccccccccccccccccccccccccccccc$	S_4.32	4.32 ± 0.15	$C ext{-}DSC_{20 ext{-}20}$	461.0	734.2	10.3
$\begin{array}{c ccccccccccccccccccccccccccccccccccc$	S_4.32	4.32 ± 0.15	F-DSC ₇₅₀₋₇₅₀	493.8	766.9	8.3
$\begin{array}{c ccccccccccccccccccccccccccccccccccc$	S_4.32	4.32 ± 0.15		539.6	812.7	7.0
$\begin{array}{cccccccccccccccccccccccccccccccccccc$	S_4.32	4.32 ± 0.15		494.5	767.7	8.2
$\begin{array}{cccccccccccccccccccccccccccccccccccc$	S_4.32	4.32 ± 0.15		557.0	830.2	6.8
$\begin{array}{cccccccccccccccccccccccccccccccccccc$	S_4.32	4.32 ± 0.15		459.0	732.2	10.4
$\begin{array}{cccccccccccccccccccccccccccccccccccc$	S_4.32	4.32 ± 0.15		461.0	734.2	11.3
$\begin{array}{cccccccccccccccccccccccccccccccccccc$	S_4.32	4.32 ± 0.15	MP	462.0	735.2	11.7
$\begin{array}{cccccccccccccccccccccccccccccccccccc$	S_4.69	4.69 ± 0.26	DSC ₁₅₋₁₅	404.9	678.1	11.8
$\begin{array}{cccccccccccccccccccccccccccccccccccc$	S_4.69	4.69 ± 0.26	DSC ₁₅₋₁₅	456.6	729.8	10.4
$\begin{array}{c ccccccccccccccccccccccccccccccccccc$	S_4.69	4.69 ± 0.26	DSC ₃₀₋₃₀	418.4	691.6	11.5
$\begin{array}{cccccccccccccccccccccccccccccccccccc$	S_4.69	4.69 ± 0.26	DSC ₃₀₋₃₀	469.8	743.0	10.1
$\begin{array}{cccccccccccccccccccccccccccccccccccc$	1	1.52	MP^b	534.9	808.0	11.2
$\begin{array}{cccccccccccccccccccccccccccccccccccc$	1	1.52	MP^b	549.9	823.0	10.6
$\begin{array}{cccccccccccccccccccccccccccccccccccc$	1	1.52	MP^b	574.9	848.0	9.8
$\begin{array}{cccccccccccccccccccccccccccccccccccc$	1	2.91	MP^b	474.9	748.0	11.1
$\begin{array}{cccccccccccccccccccccccccccccccccccc$	1	2.91	MP^b	499.9	773.0	10.2
$\begin{array}{cccccccccccccccccccccccccccccccccccc$	1	2.91	MP^b	524.9	798.0	9.9
$\begin{array}{cccccccccccccccccccccccccccccccccccc$	1	4.16	MP^b	449.9	723.0	10.7
$\begin{array}{cccccccccccccccccccccccccccccccccccc$	1	4.16	MP^b	479.9	753.0	9.1
1 1.52 FS^b 1299.9 1573.0 0.8 1 2.91 FS^b 1149.9 1423.0 0.8 1 2.91 FS^b 1199.9 1473.0 0.2 1 2.91 FS^b 1249.9 1523.0 0.6 1 4.16 FS^b 1099.9 1373.0 0.6 1 4.16 FS^b 1149.9 1423.0 1.0	1	1.52	FS^b	1199.9	1473.0	1.4
1 2.91 FSb 1149.9 1423.0 0.8 1 2.91 FSb 1199.9 1473.0 0.2 1 2.91 FSb 1249.9 1523.0 0.6 1 4.16 FSb 1099.9 1373.0 0.6 1 4.16 FSb 1149.9 1423.0 1.0	1	1.52	FS^b	1249.9	1523.0	1.2
1 2.91 FSb 1199.9 1473.0 0.2 1 2.91 FSb 1249.9 1523.0 0.6 1 4.16 FSb 1099.9 1373.0 0.6 1 4.16 FSb 1149.9 1423.0 1.0	1	1.52	FS^b	1299.9	1573.0	0.8
1 2.91 FS ^b 1249.9 1523.0 0.6 1 4.16 FS ^b 1099.9 1373.0 0.6 1 4.16 FS ^b 1149.9 1423.0 1.0	1	2.91	FS^b	1149.9	1423.0	0.8
1 4.16 FS ^b 1099.9 1373.0 0.6 1 4.16 FS ^b 1149.9 1423.0 1.0	1	2.91	FS^b	1199.9	1473.0	0.2
1 4.16 FS ^b 1149.9 1423.0 1.0	1	2.91	FS^b	1249.9	1523.0	0.6
	1	4.16	FS^b	1099.9	1373.0	0.6
1 4.16 FS ^b 1199.9 1473.0 0.2	1	4.16	FS^b	1149.9	1423.0	1.0
	1	4.16	FS ^b	1199.9	1473.0	0.2

 aH_2O (wt%) calculated using FTIR. Errors are given by the standard deviation ($\pm 1\sigma$) of our measurements.

^bType of measurement: C-DSC = conventional DSC; F-DSC = flash DSC; MP = micropenetration; CC = concentric cylinder; FS = falling sphere. C-DSC and F-DSC appendix values represent the cooling-heating rate in K min⁻¹. C-DSC- and F-DSC-derived viscosity was calculated using the K factor approach.

¹Misiti et al. (2009).

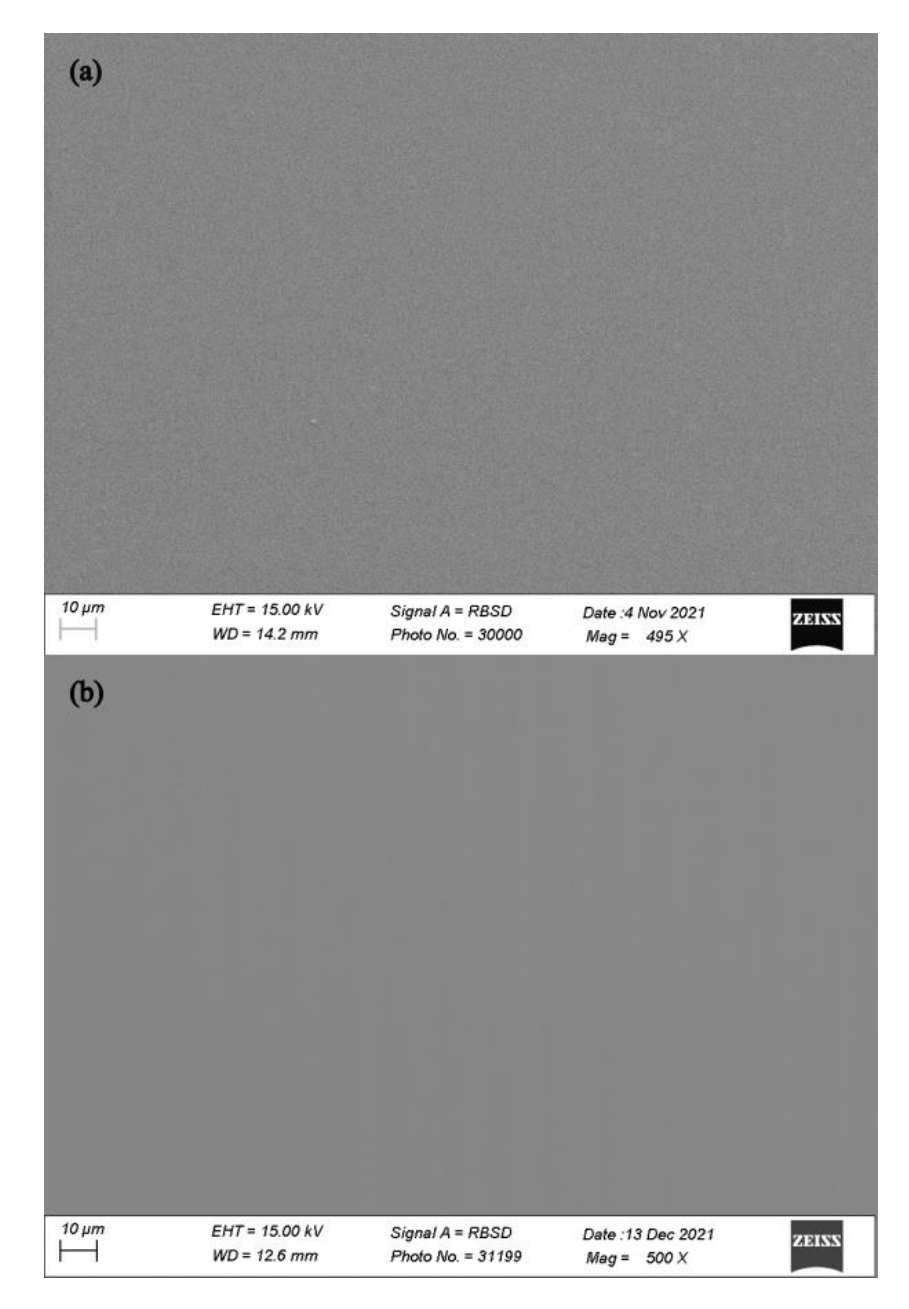


Fig. 1. Comparison of SEM/BSE images for sample $S_4.32$. (a) Starting material before measurements. (b) After C-DSC.

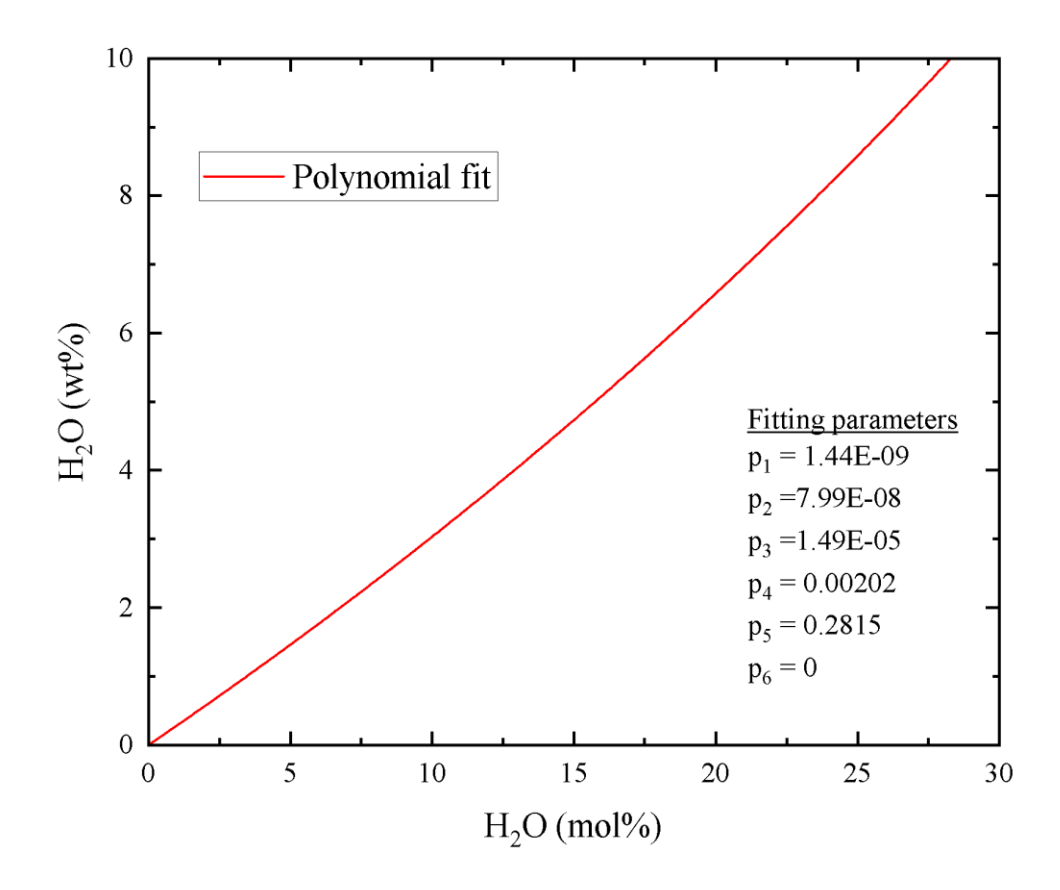


Fig. 2: polynomial relationship from mol% to wt% for Stromboli composition.

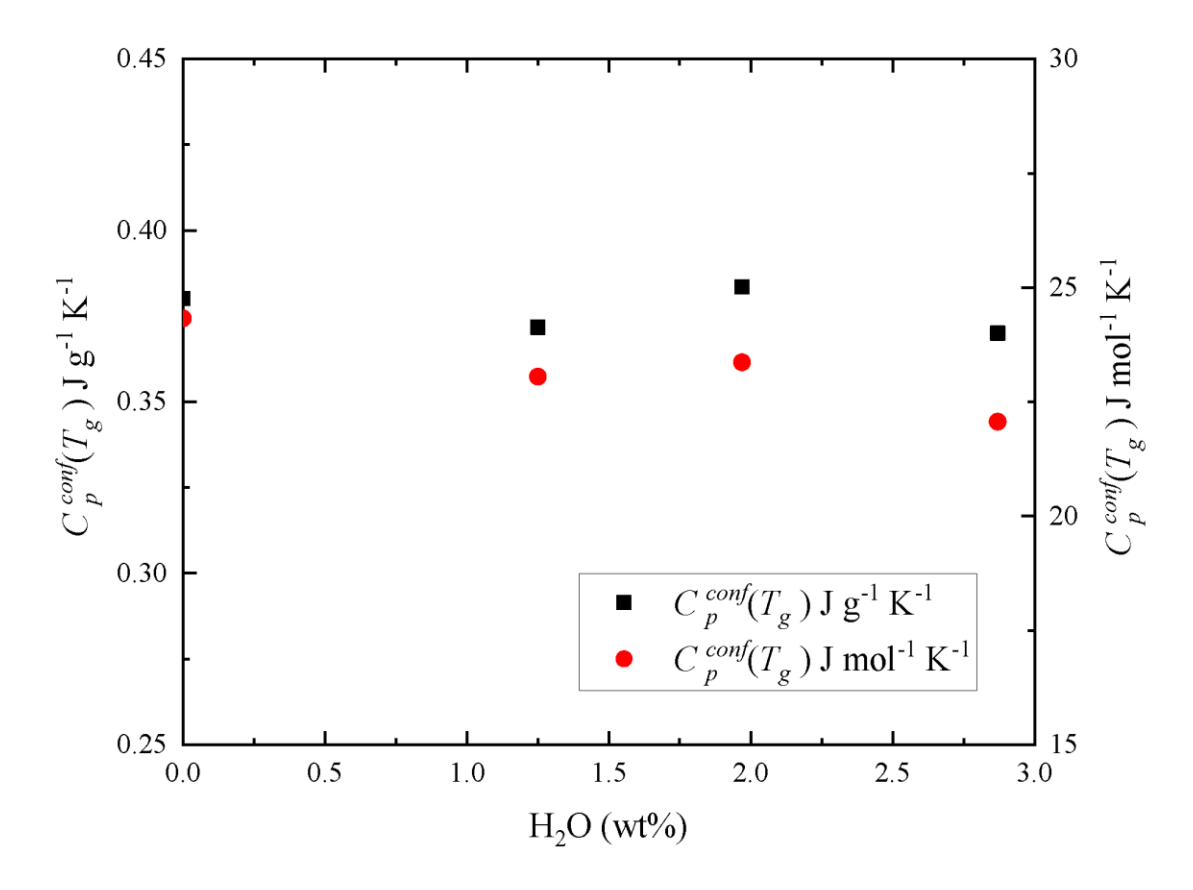


Fig. 3: $C_p^{conf}(T_g)$ as a function of H₂O wt%.

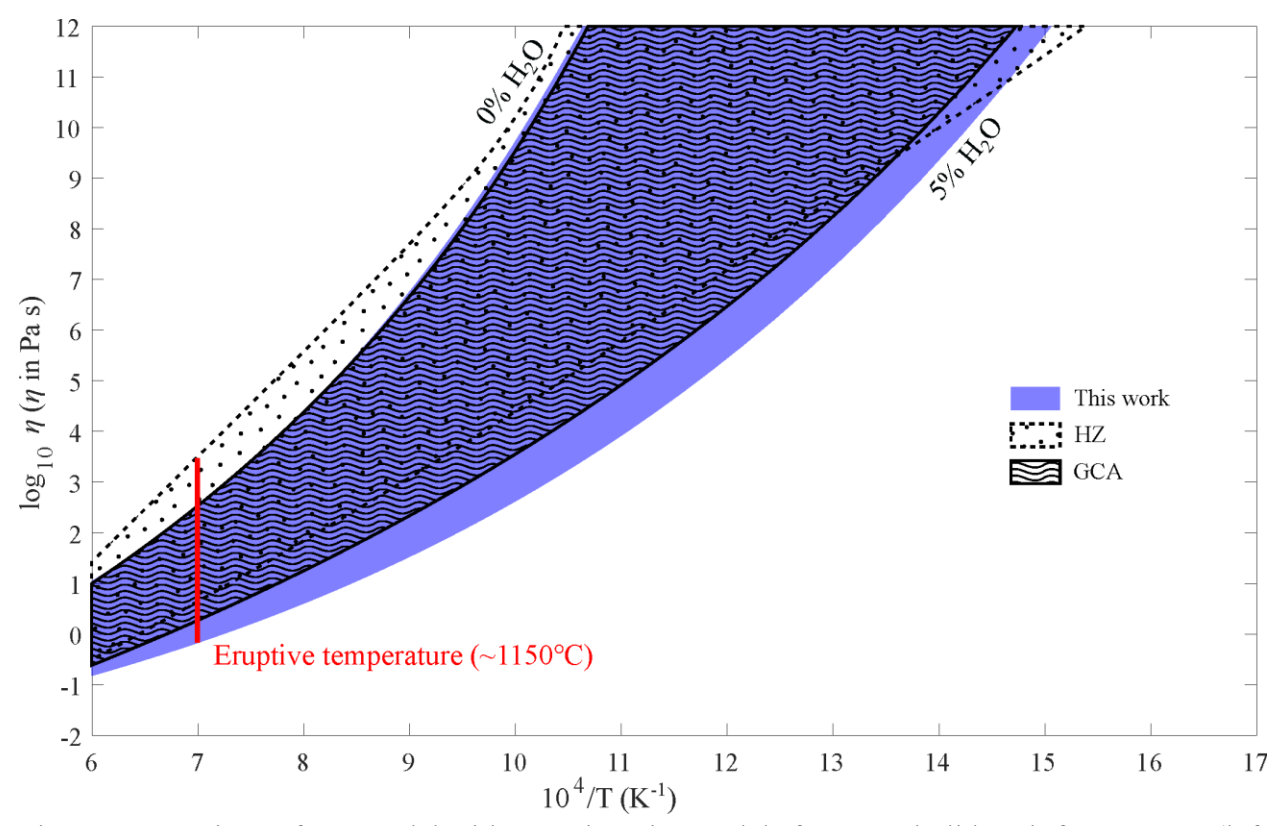


Fig. 4: Comparison of our model with two viscosity models for Stromboli basalt from 0 wt% (left border) to 5 wt% H_2O content (right border): Giordano et al. 2009 (GCA) and Hui and Zhang 2007 (HZ). The vertical red line corresponds to the pre-eruptive temperature of Stromboli basalt (T=1150°C; Giordano et al., 2009; La Spina et al., 2015).

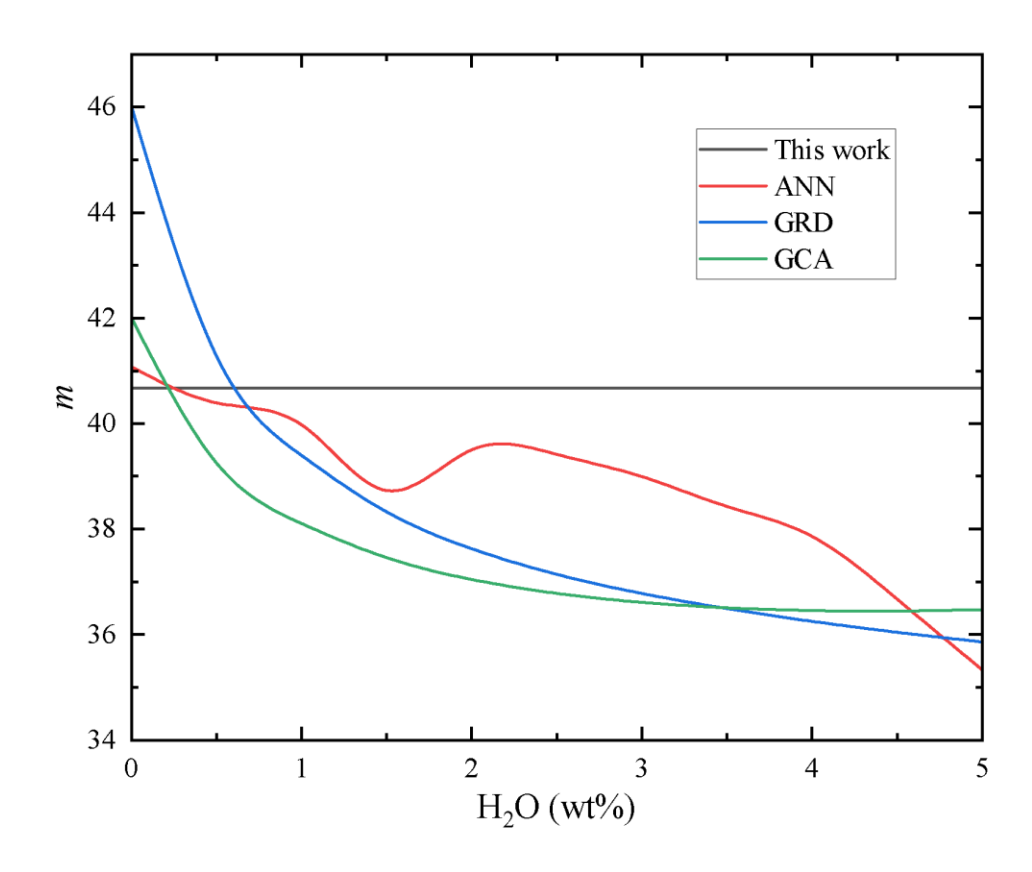


Fig. 5: m as a function of H₂O wt% for different viscosity models: ANN (Langhammer et al. 2022), GRD (Giordano et al. 2008), GCA (Giordano et al. 2009), and this work.

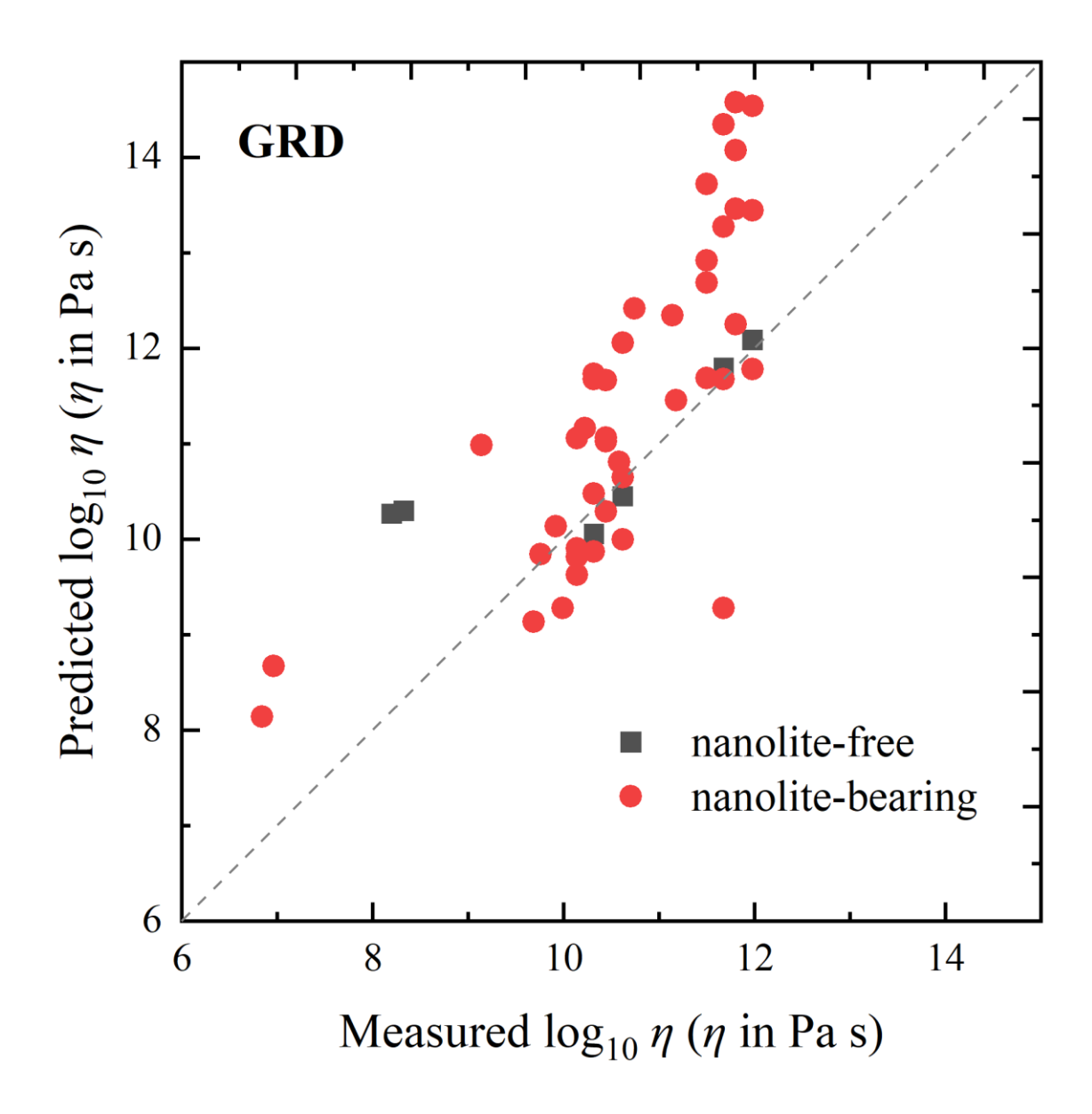


Fig. 6. Predicted vs Measured hydrous viscosity data of this work using the GRD (Giordano et al. 2008) viscosity model. Dashed line corresponds to a 1:1 line.

References

- Giordano D, Ardia P, Romano C, et al (2009) The rheological evolution of alkaline Vesuvius magmas and comparison with alkaline series from the Phlegrean Fields, Etna, Stromboli and Teide. Geochim Cosmochim Acta 73:6613–6630. https://doi.org/10.1016/j.gca.2009.07.033
- Giordano D, Mangiacapra A, Potuzak M, et al (2006) An expanded non-Arrhenian model for silicate melt viscosity: A treatment for metaluminous, peraluminous and peralkaline liquids. Chem Geol 229:42–56. https://doi.org/10.1016/j.chemgeo.2006.01.007
- Giordano D, Russell JK, Dingwell DB (2008) Viscosity of magmatic liquids: A model. Earth Planet Sci Lett 271:123–134. https://doi.org/10.1016/j.epsl.2008.03.038
- La Spina G, Burton M, De'Michieli Vitturi M (2015) Temperature evolution during magma ascent in basaltic effusive eruptions: A numerical application to Stromboli volcano. Earth Planet Sci Lett 426:89–100. https://doi.org/10.1016/j.epsl.2015.06.015
- Langhammer D, Di Genova D, Steinle-Neumann G (2022) Modeling Viscosity of Volcanic Melts With Artificial Neural Networks. Geochemistry, Geophys Geosystems 23:24. https://doi.org/10.1029/2022GC010673
- Misiti V, Vetere F, Mangiacapra A, et al (2009) Viscosity of high-K basalt from the 5th April 2003 Stromboli paroxysmal explosion. Chem Geol 260:278–285. https://doi.org/10.1016/j.chemgeo.2008.12.023
- Scarani A, Zandonà A, Di Fiore F, et al (2022) A chemical threshold controls nanocrystallization and degassing behaviour in basalt magmas. Commun Earth Environ 3:284. https://doi.org/10.1038/s43247-022-00615-2

4.2 Nanoscale chemical heterogeneities control the viscosity of andesitic magmas

Pedro Valdivia^{1,2}*, Alessio Zandonà³, Jessica Löschmann³, Dmitry Bondar^{1,2}, Cécile

Genevois⁴, Aurélien Canizarès⁴, Mathieu Allix⁴, Nobuyoshi Miyajima¹, Alexander Kurnosov¹,

Tiziana Boffa Ballaran¹, Fabrizio Di Fiore⁵, Alessandro Vona⁶, Claudia Romano⁶, Joachim

Deubener³, Emily C. Bamber^{2,7}, Alessandro Longo⁸, Danilo Di Genova²

¹Bayerisches Geoinstitut, University of Bayreuth, Universitätsstraße 30, 95447, Bayreuth,

Germany

²Institute of Science, Technology and Sustainability for Ceramics (ISSMC) of the National

Research Council (CNR), Via Granarolo 64, I-48018, Faenza, RA, Italy

³Institute of Non-Metallic Materials, Clausthal University of Technology, Zehntnerstraße 2a,

D-38678 Clausthal-Zellerfeld, Germany

⁴CNRS, CEMHTI UPR3079, Univ. Orléans, France.

⁵Istituto Nazionale di Geofisica e Vulcanologia, Sezione Roma 1, Via di Vigna Murata 605,

00143 Rome, Italy

⁶Dipartimento di Scienze, Università degli Studi Roma Tre, Largo San L. Murialdo 1, 00146

Rome, Italy

⁷Department of Earth Sciences, University of Turin, Via Valperga Caluso, 35, 10125 Turin,

⁸ESRF - The European Synchrotron, 38043 Cedex 9 Grenoble, France

*Corresponding author: pedro.valdivia-munoz@uni-bayreuth.de

Status: Published

Commun. Earth Environ. 6, 455. http://dx.doi.org/10.1038/s43247-025-02424-9

121

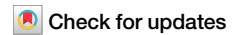
A Nature Portfolio journal



1

https://doi.org/10.1038/s43247-025-02424-9

Nanoscale chemical heterogeneities control the viscosity of andesitic magmas



Pedro Valdivia ^{1,2} ⊠, Alessio Zandonà ³, Jessica Löschmann³, Dmitry Bondar¹,², Cécile Genevois⁴, Aurélien Canizarès⁴, Mathieu Allix ⁴, Nobuyoshi Miyajima ¹, Alexander Kurnosov ¹, Tiziana Boffa Ballaran¹, Fabrizio Di Fiore ⁵, Alessandro Vona ⁶, Claudia Romano⁶, Joachim Deubener ³, Emily C. Bamber², Alessandro Longo ⁸ & Danilo Di Genova ²

Explosive volcanic eruptions, driven by magma fragmentation, pose significant geohazards due to their rapid energy release and widespread dispersal of pyroclasts. High magma viscosity promotes brittle fragmentation by limiting volatile escape and enhancing internal pressure buildup. Although recent studies have recognized that iron-titanium oxide nanocrystal formation increases melt viscosity, the mechanisms underlying this effect remain poorly constrained. Here we quantify the influence of nanocrystallization on magma viscosity by developing viscosity models that incorporate iron-titanium variations, calibrated against nanocrystal-free andesitic melts. Using time-resolved imaging, we show that nanocrystals form within seconds within synthetic andesitic melts. This process generates nanoscale chemical heterogeneities, including silica enrichment in the surrounding melt and aluminum-rich shells embedding the nanocrystals. These heterogeneities result in viscosity increases of up to 30-fold at eruptive temperatures. Our findings indicate that nanocrystallization modulates magma rheology during early crystallization, with direct implications for the dynamics of andesitic eruptions.

Explosive eruptions are recognized as one of the most hazardous natural phenomena on Earth¹, capable of injecting a large amount of gas and ash into the atmosphere, posing a threat to inhabited regions. These eruptions stem from magma fragmentation, the process by which a hot gas-pyroclast mixture is produced²-5. The triggers of magma fragmentation are twofold: bubble overpressure caused by limited bubble growth due to high viscosity⁰-7, and strain rates that exceed the relaxation time of the melt, which is controlled by its chemical composition²-8.9. Moreover, disequilibrium crystallization and degassing during magma ascent contribute to the enhanced explosivity of volcanic eruptions¹-0-13 by increasing melt viscosity¹-4,15, which hinders gas bubble expansion¹-16. Several studies¹-0,11,17,18 have shown that the syn-eruptive disequilibrium crystallization of microlites increases magma viscosity, generating overpressure that can lead to explosive eruptions³-5.

Previous authors^{19–23} have shown that the formation of Fe-Ti-oxide nanocrystals (nanolites) increases the viscosity of volcanic melts in

laboratory measurements. Given that nanolites are commonly found in volcanic products from explosive events²⁴⁻³², this supports the hypothesis that they influence magma ascent dynamics and eruptive style. Several mechanisms have been proposed: nanolite-induced chemical changes that increase magma viscosity^{19,33,34}, solid aggregation that hinders melt flow³⁵, and enhanced heterogeneous bubble nucleation that affects degassing³⁶. Recent work^{29,32,37} suggests that nanolites can serve as indicators of the physicochemical conditions of magma during transitions in eruptive style at andesitic volcanoes, also contributing to the rheological changes that promote more explosive behavior. However, despite accumulating evidence for their presence in explosive volcanic products, the extent and mechanisms of how nanolites influence magma rheology remain poorly constrained^{19,20,27,29,32,33,35-38}.

To the best of our knowledge, this study reports the first in situ, high-temperature imaging observation of nanolite formation in a synthetic andesitic melt. We leverage these observations to investigate the connection

¹Bayerisches Geoinstitut, University of Bayreuth, Universitätsstraße 30, 95447 Bayreuth, Germany. ²Institute of Science, Technology and Sustainability for Ceramics (ISSMC) of the National Research Council (CNR), Via Granarolo 64, I-48018 Faenza, RA, Italy. ³Institute of Non-Metallic Materials, Clausthal University of Technology, Zehntnerstraße 2a, D-38678 Clausthal-Zellerfeld, Germany. ⁴CNRS, CEMHTI UPR3079, Univ, Orléans, France. ⁵Istituto Nazionale di Geofisica e Vulcanologia, Sezione Roma 1, Via di Vigna Murata 605, 00143 Rome, Italy. ⁶Dipartimento di Scienze, Università degli Studi Roma Tre, Largo San L. Murialdo 1, 00146 Rome, Italy. ⁷Department of Earth Sciences, University of Turin, Via Valperga Caluso, 35, 10125 Turin, Italy. ⁸ESRF - The European Synchrotron, 38043 Grenoble, France. ⊠e-mail: pedro.valdivia-munoz@uni-bayreuth.de

between nanolite formation and the flow properties of various andesitic compositions. To establish a reliable basis for comparison, we develop chemical-dependent viscosity models using only viscosity data derived from samples free of nanolites. This approach is necessary because previous studies, including widely used viscosity models³⁹, tend to overestimate the viscosity of melts prone to nanocrystallization^{20,21,25,40}. Our results show that nanolite formation induces nanoscale chemical variations in the melt. These nanodomains increase melt viscosity and can significantly alter the physical properties of magma. This suggests that nanoscale chemical thresholds may influence magma properties and dynamics at early stages of crystallization.

Results and discussion

Preliminary in situ observations of nanolite formation during heating

We produced four anhydrous andesitic melts and one transition-metal-free analogue (Table 1). The sample AND100 (Fe³+/Fe_{tot} = 0.64) was designed to mirror the andesitic chemical composition of the magma erupted at Sakurajima volcano described in Okumura et al. 19. Samples AND100red (Fe³+/Fe_{tot} = 0.27) and AND100ox (Fe³+/Fe_{tot} = 0.71) represent isochemical analogues of AND100 with lower and higher Fe³+/Fe_{tot} respectively (Table 1). AND65 (Fe³+/Fe_{tot} = 0.74) and AND0 were produced based on the composition of AND100, from which 35% and 100% of the total transition metal content (FeO_{tot} TiO₂ and MnO) were removed. The amorphous nature of all samples was confirmed through a combination of scanning electron microscopy (SEM) imaging in backscattered electron (BSE) mode and Raman spectroscopy analysis; additional details can be found in the Supplementary Information (Supplementary Preliminary Characterization; Supplementary Fig. 1).

We initially explored the nanoscale textural response of the AND100 composition from a fundamental standpoint, performing in situ high-temperature measurements. High-temperature Raman results⁴¹ (Fig. 1a) reveal that the amorphous state of AND100 is considerably unstable against thermal treatments, leading to the formation of nano-sized titanomagnetite crystals already ~ 70 °C above the glass transition temperature (T_g), which was determined by conventional differential scanning calorimetry (C-DSC) (Table 1, Supplementary Table 2). This is evidenced by the appearance of vibrational features that can be assigned to Fe-Ti-oxides such as

titanomagnetite⁴⁰⁻⁴⁴, which become even more distinctive upon cooling the samples to room temperature (Supplementary Fig. 4b; Supplementary Postin situ Raman). To monitor the nanoscale changes associated with the nonstoichiometric precipitation of titanomagnetite, we also performed in situ nanoscale observation of nanolite formation in an andesitic composition using transmission electron microscopy (TEM) combined with a heating stage (Supplementary Movie). The experimental procedure, as previously optimized by Zandonà et al.⁴⁵, minimized possible artifacts arising from electron irradiation, which could be limited to a simple shift of thermally activated processes (i.e., phase separation and crystallization) to lower temperatures and a minor loss of alkalis during the heating in vacuum. During the heating experiment (Fig. 1b), we observed that the starting material, which appeared homogeneous within the experimental resolution, rapidly underwent amorphous phase separation⁴⁶, possibly due to liquidliquid immiscibility⁴⁷ or simply corresponding to a kinetically favored metastable stage of chemical clustering preceding non-isochemical crystal nucleation in the melt. This process led to the development of sub-rounded (<5 nm in diameter) higher-contrast domains that lacked crystalline order, as initially determined by local Fast Fourier transforms (FFTs) of the collected TEM images (Fig. 1b). Notably, these chemically differentiated nanodomains exhibited structural ordering into iron-rich nanosized crystals at higher temperatures (>550 °C), followed by gradual growth and accompanied by the development of aluminum-rich domains (Supplementary Fig. 5). Fast Fourier transforms (FFTs) of images acquired at this stage (Fig. 1b) are consistent with the formation of titanomagnetite^{48,49}. Energy-dispersive X-ray spectra (EDS) acquired before and after the in situ experiment (Supplementary Table 3) confirmed that the overall bulk composition remained almost constant after the experiment, except for an unavoidable loss of alkalis due to electron irradiation in a vacuum. The observed mechanism, i.e., amorphous phase separation, followed by the rapid formation and growth of nanocrystals within Fe-enriched domains, has previously been reported for other aluminosilicate glasses and melts^{21,50} and also mirrors those inferred from ex-situ observations on basaltic and basanitic melts^{21,51}. Therefore, they provide an accurate overview of the nanocrystallization processes that should be expected to occur in deeply supercooled melts and reheated glasses of andesitic composition.

Table 1 | Chemical analysis results^a (wt%) and parameters used for melt viscosity parameterization using the MYEGA equation (Eq. 5)

	AND400	AND400mad	AND400ev	ANDCE	ANIDO
	AND100	AND100red	AND100ox	AND65	AND0
SiO ₂	60.38 (0.36)	60.47 (0.40)	60.56 (0.35)	62.52 (0.19)	65.91 (0.34)
TiO ₂	0.79 (0.04)	0.80 (0.07)	0.81 (0.06)	0.56 (0.04)	0.04 (0.03)
Al ₂ O ₃	16.69 (0.18)	16.83 (0.22)	16.79 (0.19)	17.28 (0.22)	18.01 (0.11)
FeO _{tot}	6.77 (0.12)	6.87 (0.12)	6.76 (0.15)	4.40 (0.11)	0.04 (0.03)
MnO	0.17 (0.03)	0.18 (0.04)	0.18 (0.03)	0.11 (0.03)	0.01 (0.01)
MgO	3.00 (0.07)	2.94 (0.06)	2.95 (0.06)	3.02 (0.07)	3.21 (0.06)
CaO	6.62 (0.09)	6.51 (0.11)	6.49 (0.11)	6.76 (0.13)	7.26 (0.11)
Na ₂ O	3.50 (0.15)	3.46 (0.10)	3.40 (0.10)	3.49 (0.11)	3.82 (0.14)
K ₂ O	1.58 (0.07)	1.65 (0.07)	1.66 (0.06)	1.70 (0.05)	1.75 (0.06)
P ₂ O5	0.18 (0.05)	0.18 (0.05)	0.18 (0.05)	0.16 (0.05)	0.04 (0.03)
Fe ³⁺ /Fe _{tot} ^b	0.64 (0.03)	0.27 (0.03)	0.71 (0.03)	0.74 (0.03)	_
NBO/T°	0.34	0.31	0.34	0.27	0.16
K/G ^d	1.57 (0.02)	1.57 (0.02)	1.58 (0.02)	1.53 (0.02)	1.48 (0.02)
<i>T_g</i> ^e (°C)	654 (1)	645 (1)	662 (1)	696 (1)	737 (1)
m ^f	30.5 (1)	30.5 (1)	30.5 (1)	31 (0.6)	31.8 (0.2)

^aElectron microprobe average chemical composition (n = 10). Parentheses represent $\pm 1\sigma$.

^bFrom Mössbauer spectroscopy. Ratios were derived using MossA software⁹⁵. Numbers in parentheses represent ±1σ.

[°]NBO/T calculated after Prata et al. 107.

 $^{^{\}text{d}}\text{From Brillouin spectroscopy.}$ Numbers in parentheses represent $\pm 1\sigma.$

^eFrom C-DSC. Numbers in parentheses represent the experimental error.

^fFitted fragility using the Mauro-Yue-Ellison-Gupta-Allan (MYEGA) parametrization. Numbers in parentheses represent ±1σ.

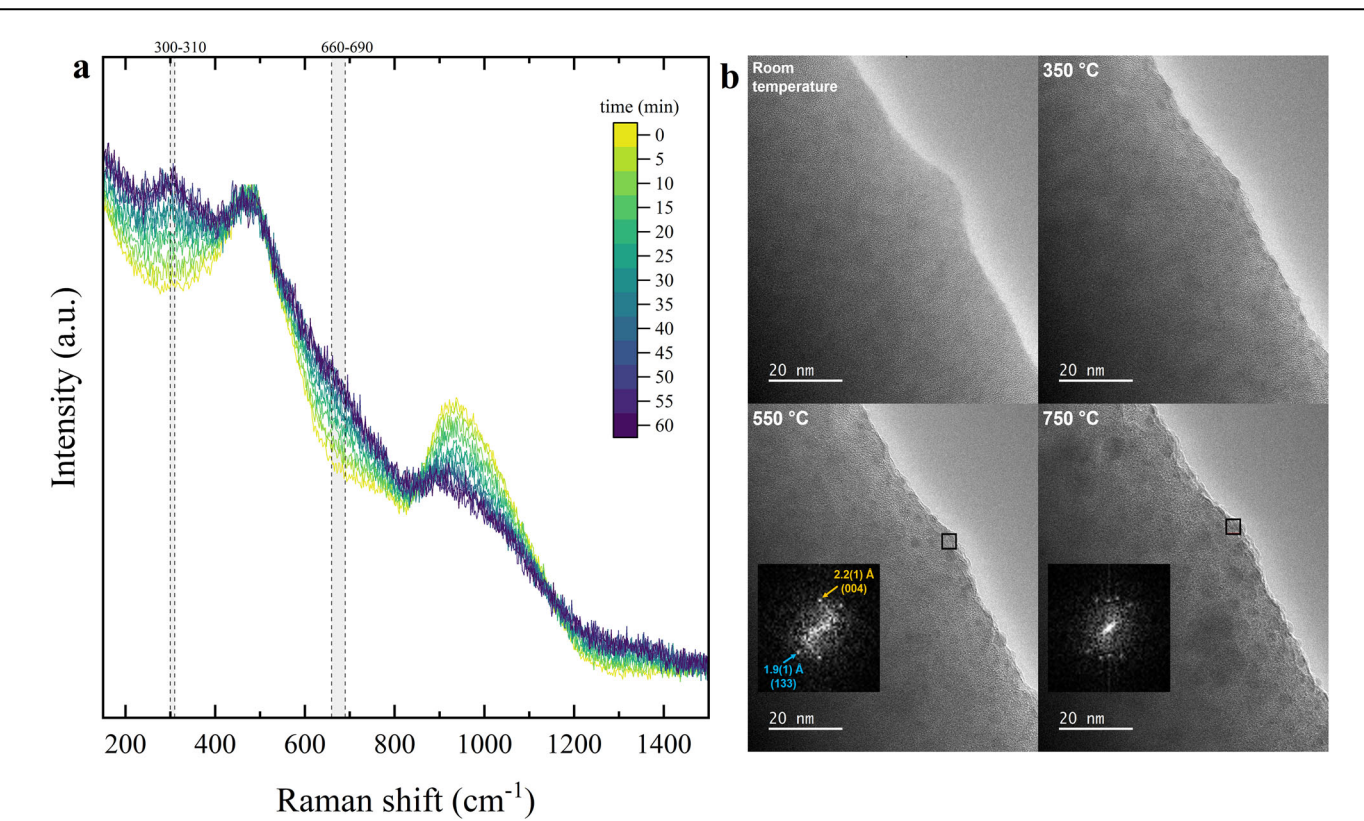


Fig. 1 | **In situ high-temperature results.** a Raman spectra evolution of sample AND100 at 723 °C revealing the formation of titanomagnetite crystals during an isothermal hold above T_g (654 °C; Table 1). Each colored curve represents 5 minutes. Shaded areas highlight the position of the most intense Raman features of titanomagnetite $^{40,42-44}$. **b** Images acquired during in situ heating TEM experiment (Supplementary Movie), detailing the nanoscale evolution of AND100 from a

homogeneous amorphous glass to a heterogeneous amorphous material (350 $^{\circ}$ C), and then a nano-crystallized glass (550 $^{\circ}$ C and 750 $^{\circ}$ C). FFTs (insets) and post-experiment STEM-EDS (Supplementary Fig. 5) confirm the formed crystals to be magnetite-like. Temperatures (Supplementary Fig. 6) are affected by electron irradiation and should be therefore considered only in qualitative terms.

The viscosity of homogeneous and crystal-free andesitic melts

High-temperature in situ measurements reveal the elevated reactivity of AND100 above its T_g (Fig. 1), highlighting the need for a meticulous experimental methodology to determine the melt viscosity^{20,21,52}. To this end, we employed direct viscometry techniques, including micropenetration and concentric cylinder viscometry (Supplementary Micropenetration; Supplementary Concentric Cylinder). We further expanded our dataset by incorporating indirect viscosity estimates obtained from conventional and flash differential scanning calorimetry (C-DSC and F-DSC, respectively; Supplementary C-DSC; Supplementary F-DSC). To monitor potential sample alteration during measurements, such as crystallization and/or iron oxidation, we conducted Raman and Mössbauer spectroscopy before and after each experiment (Supplementary Preliminary Characterization; Supplementary C-DSC; Supplementary F-DSC; Supplementary Micropenetration; Supplementary Concentric Cylinder).

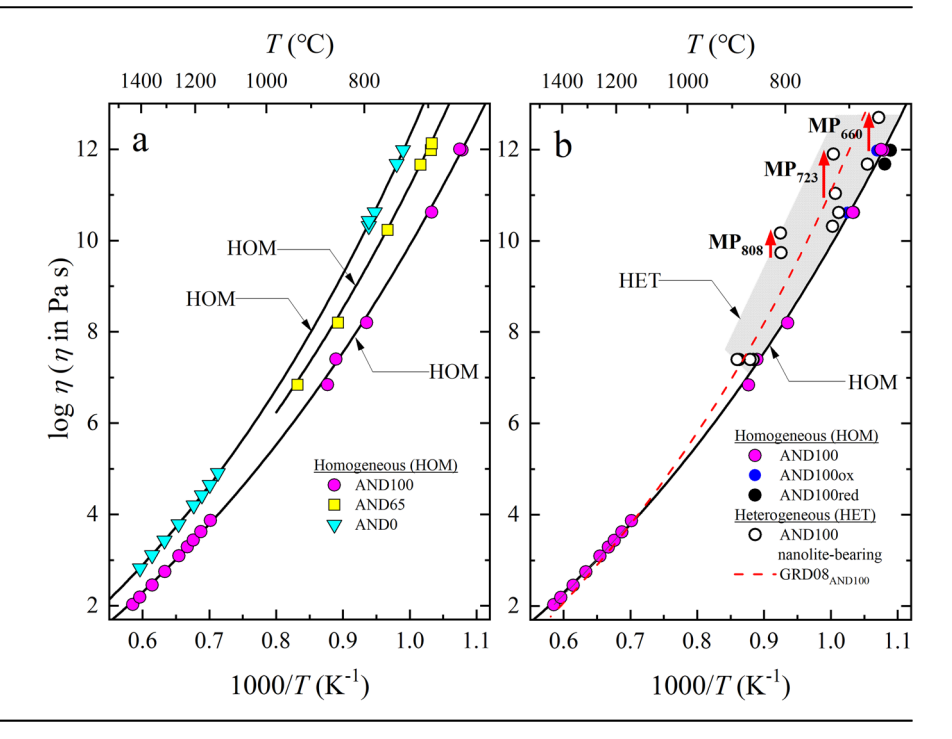
The accurate fitting of melt viscosity requires data from samples that preserved a homogeneous amorphous structure throughout all measurement stages. However, post-experiment Mössbauer and Raman results (Supplementary Preliminary Characterization; Supplementary C-DSC; Supplementary F-DSC; Supplementary Micropenetration; Supplementary Concentric Cylinder), as well as micropenetration (Fig. 2b) and post-micropenetration TEM results (Figs. 3, 4; Supplementary Figs. 11, 12 and 13), show that some viscosity measurements were affected by iron oxidation and titanomagnetite nanocrystallization during the experiments. Based on these observations, we exclusively used data from samples that remained nanolite-free after experiments to establish crystal-free viscosity parametrizations for our andesitic compositions (Supplementary Viscosity Parametrization). We accounted for iron oxidation by categorizing datasets according to the iron valence determined post-measurements. Combined with T_g values derived from C-DSC (Table 1; Supplementary C-DSC), we

applied the MYEGA parametrization (Eq. 5) using $\log_{10}\eta_{\infty} = -2.93^{53,54}$, to fit the melt fragility index (m). This allows us to characterize melt viscosity across a wide temperature range. Viscosity data from nanolite-free samples are shown as colored symbols in Fig. 2a, and the corresponding MYEGA fitting parameters are summarized in Table 1. To model andesite viscosity, we developed a calculator (provided as a Supplementary Data) applicable to compositions ranging from AND0 to AND100. This tool is based on the relationship between the transition metal content, glass transition temperature (T_g) , and fragility index (m) (Supplementary Viscosity Parametrization).

Our results (Fig. 2a) show that the viscosity of homogeneous andesitic melts increases with decreasing transition metal oxide content progressing from AND100 to AND65, and then AND0. A 35% reduction in transition metal oxides (FeO_{tot}, TiO₂ and MnO) from AND100 leads to an average viscosity increase of 0.7 ± 0.05 log₁₀ (approximately 5 times) at eruptive temperatures (900–1050 °C) relevant for Sakurajima volcano⁵⁵. Complete removal of transition metal oxides (i.e., AND0) increases viscosity by ~1.5 \pm 0.1 log₁₀ (~30 times) at 900 °C and by ~1.1 \pm 0.1 log₁₀ (~12 times) at 1050 °C. Moreover, within the same temperature range, increasing the iron oxidation in AND100 (from Fe³+/Fe_{tot} = 0.27 to 0.71) results in a viscosity increase of ~2 times (Supplementary Fig. 9), consistent with previous findings²^{22,56,57}.

It is important to note that these parametrizations apply specifically to homogeneous melts, free of nanolites or detectable nanoscale compositional heterogeneity in the amorphous state, as discussed further below. Our results indicate that the Giordano et al. ³⁹ model overestimates the viscosity of AND100 (GRD08_{AND100}, Fig. 2b) by up to a factor of 25 at 700 °C and a factor of 3 at 900 °C. This discrepancy is not observed for the AND0 composition (Supplementary Fig. 9). These findings are consistent with Valdivia et al. ²⁰, who reported similar behavior for basaltic melts, suggesting

Fig. 2 | Summary of viscosity results. a Colored symbols represent nanolite-free viscosity data for a homogeneous melt (HOM). Solid lines illustrate MYEGA parametrizations for AND100, AND65 and AND0 (Table 1). b Impact of heterogeneities and iron oxidation state on the viscosity of AND100 compositions. White symbols represent nanolitebearing viscosity data. The shaded grey region (heterogeneous melt, HET) represents the expected viscosity increase due to nanolite formation. Red arrows depict the isothermal rise in viscosity measured during micropenetration experiments at 660, 723 and 808 °C. The red dashed line shows the viscosity prediction for AND100 using the Giordano et al.39 model. Experimental errors are smaller than symbol sizes.



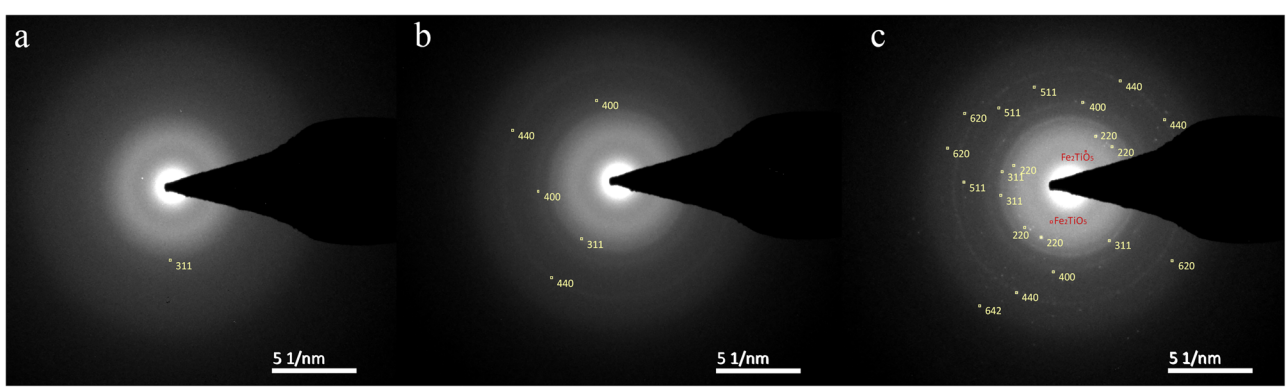


Fig. 3 | Post-micropenetration (TEM) diffraction patterns of AND100 samples. a MP_{660} . b MP_{723} . c MP_{808} . Yellow indices correspond to the assignment of electron diffraction rings to specific lattice planes in the structure of titanomagnetite based on the respective d-spacings. The red points are the identification of a single spot associated with pseudobrookite (Fe,TiO₅).

that the Giordano et al.³⁹ model may, for certain chemical domains, rely on viscosity data from melts containing nanoscale heterogeneities. Similarly, we observe deviations between our AND100 crystal-free parametrization and the nanolite-free viscosity data reported by Okumura et al.⁵⁸ (Supplementary Fig. 9), which also referenced the Giordano et al.³⁹ model.

Nanoscale characterization of nanolite-bearing andesitic melts

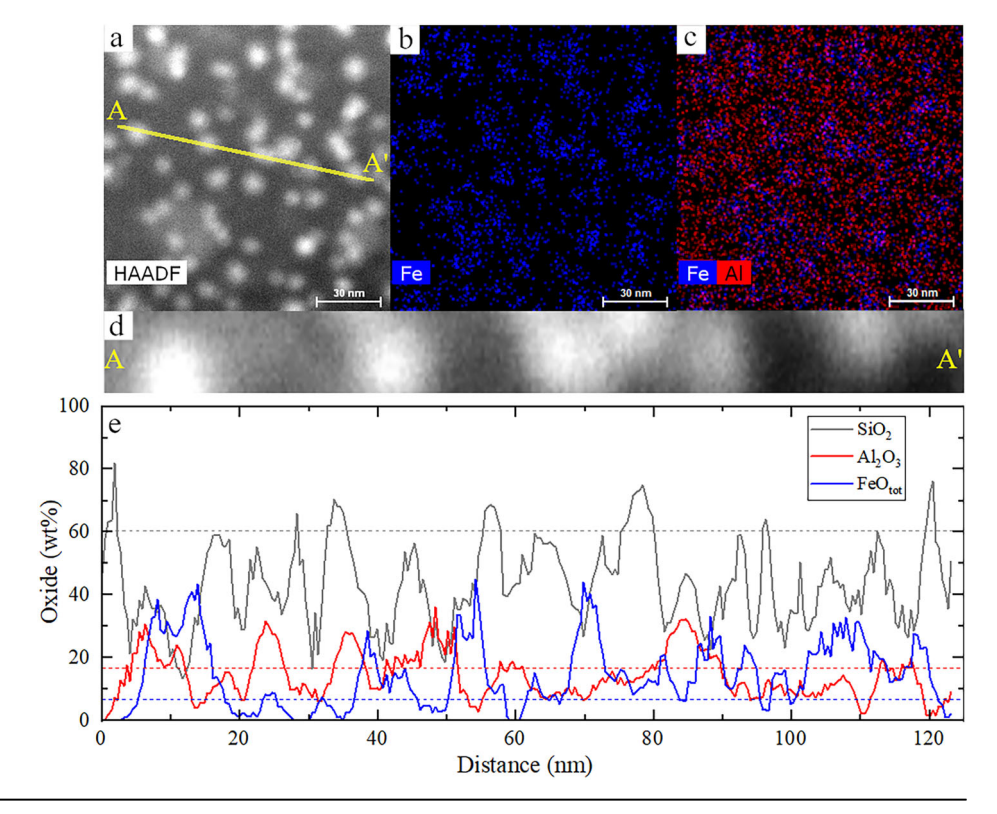
During micropenetration measurements on AND100 samples, we observed a time-dependent increase in viscosity at constant temperatures (Fig. 2b; Supplementary Micropenetration). Post-experiment analyses revealed that these changes were accompanied by nanocrystallization of titanomagnetite and iron oxidation. To investigate the mechanisms behind the viscosity increase, we conducted nanoscale characterization of the samples. We used room-temperature (S)TEM on FIB-prepared lamellas of known thickness (Table 2) to image the nanocrystals and obtain EDS chemical maps. To further assess nanoparticle size distribution and phase composition, we performed Small-Angle X-ray Scattering (SAXS) and Wide-Angle X-ray Scattering (WAXS) on 50 µm thick samples (see below).

Electron diffraction patterns (Fig. 3) and high-angle annular dark-field (HAADF) imaging (Fig. 4a), both acquired in TEM mode and STEM mode, respectively, confirmed the presence of nanocrystals. Selected area electron diffraction (SAED) patterns from post-micropenetration AND100 samples

are shown in Fig. 3. Most of the recorded d-spacings corresponds to the structure of titanomagnetite^{48,49,59}. The diffraction patterns evolved from diffuse circular halos in sample AND100_MP₆₆₀ to well-defined diffraction rings in AND100_MP723, and especially in AND100_MP808 (Fig. 3). Notably, AND100_MP₈₀₈ shows more pronounced diffraction features along the rings, indicating the presence of larger and more ordered nanocrystals. In particular, AND100_MP₆₆₀ displays one diffraction ring (d = 2.53(1)) Å) which matches the most intense reflection of titanomagnetite^{48,59}, corresponding to the (311) plane (Fig. 3a). In AND100_MP₇₂₃, two additional low-intensity rings appear, with *d*-spacings of 1.48(5) and 2.09(9) Å, assignable to the (440) and (400) planes, respectively 48,49,59 (Fig. 3b). These three diffraction rings become more pronounced in AND100_MP₈₀₈ and are accompanied by weaker ones assignable to the (220), (511), (620), and (642) planes⁴⁸ (Fig. 3c). Additionally, a single diffraction spot consistent with the (021) plane of pseudobrookite (Fe₂TiO₅, d-spacing = 4.3(1) Å) is uniquely observed in sample AND100 $_{\rm MP_{808}}$ (Fig. 3c) 60,61 .

Nanolites are recognizable in STEM-HAADF images (Fig. 4a) by their bright contrast, consistent with their higher density relative to the surrounding matrix. Elemental maps (Fig. 4b) show that these particles are Fe-rich, in agreement with previous analyses (Supplementary Fig. 5). Conversely, aluminum (Al) is preferentially concentrated around these

Fig. 4 | Nanoscale local variations in chemistry for AND100_MP₈₀₈. a STEM-HAADF image of the sample. The bright pixels represent the crystalline phase. b EDS elemental distribution map of Fe. c EDS elemental distribution map of Fe+Al showing a preferential distribution of Al around Fe-rich nanolites. d Magnification of A-A' EDS-line-scan. e EDS line profile (A-A') results, with SiO₂, Al₂O₃ and FeO_{tot} concentrations in wt%. Values on the x-axis represent the distance along the line profile (A-A'). Values on the y-axis represent the average composition of 7 neighboring pixels along the y-axis in d.



nanolites, creating Al-depleted zones between them. This distribution becomes especially evident when Fe and Al elemental maps are overlapped (Fig. 4c). To quantify local chemical variations, we extracted a representative STEM-EDS linescan across the sample (Fig. 4d). The resulting profile (Fig. 4e) confirmed the presence of Al-enriched halos surrounding Fe-rich nanolites. We also observed localized SiO₂ enrichment in the residual melt, corresponding to the darker region in the STEM-HAADF images (Fig. 4a).

From STEM-HAADF images (Supplementary STEM-HAADF) obtained from lamellas of known thickness, we determined the minimum nanolite radius, volume fraction, and nanolite number density (NND), accounting for possible nanolite overlap in the axis perpendicular to the plane of view. The average minimum nanolite radius increases from 1.4 ± 0.5 to 2.6 ± 0.8 nm as the temperature during viscosity measurements increases from 660 to 808 °C, with a progressive increase in nanolite content from 0.51 ± 0.1 to 2.45 ± 0.1 vol% (Table 2). This trend is consistent with Raman spectroscopy and electron diffraction results (Fig. 3; Supplementary Fig. 4) as well as high-temperature in situ experiments (Fig. 1; Supplementary Fig. 4), indicating that nanolite nucleation and growth become more pronounced as temperature increases above the glass transition.

To explore the temperature dependence of compositional heterogeneity, we quantified the average composition of four sub-regions: (1) the bulk image, (2) the nanolites, (3) the nanolites plus surrounding halos, and (4) the residual amorphous matrix (Fig. 5). Due to sample thickness (Table 2), compositions for nanolites and halos include a contribution from the surrounding amorphous matrix. The bulk STEM-EDS composition agrees well with the electron microprobe data for the AND100 starting material (Tables 1, 2), indicating minimal alkali migration during EDS analysis. Figure 5 illustrates the relative compositional differences of each sub-region normalized to the bulk composition (Table 2).

All three samples exhibit SiO_2 enrichment in the residual matrix, with average values near 70 wt% (Table 2), which is ca. 10 wt% higher than in the original AND100 composition and ca. 4 wt% higher than in the iron-free AND0 (Table 1). Conversely, Al_2O_3 and FeO_{tot} concentrations in the matrix decrease progressively as temperature increases from 660 to 808 °C. In parallel, FeO_{tot} concentrations increase within the nanolites, consistent with titanomagnetite growth observed in our in situ experiments (Fig. 1).

Notably, during the early stages of nanolite formation (660 °C), we observed that they coexist with a diffuse, high-contrast phase (Supplementary Postmicropenetration STEM-EDS) and show an initial Al_2O_3 enrichment (Fig. 5c), potentially reflecting a transient immiscibility between two aluminosilicate melts. At higher temperatures (808 °C), Al is expelled from the developing nanolites as more ordered titanomagnetite nanolites form (Fig. 5c). We infer that this process explains the observed Al accumulation around nanocrystals (Fig. 4; Supplementary Fig. 5) which is consistent with low mobility of Al in SiO₂-rich liquids 62.

This mechanism aligns with the titanomagnetite nanocrystallization pathway proposed for the 2018–2021 Fani Maoré lavas⁵¹, where nanolites formed from an Fe-rich immiscible melt⁶³. It is also consistent with well-established observations in glass-ceramic materials, where Al-enriched shells are observed to surround the TiO₂- and/or ZrO₂- bearing nanocrystals that serve as crystallization seeds during subsequent heating^{64,65}. Additionally, recent tracer diffusion experiments in TiO₂-containing albitic glass demonstrate that Al mobility in supercooled aluminosilicate melts is enhanced by the presence of transition metals⁶⁶, supporting a crystal nucleation mechanism involving the coupled diffusion of Al, Fe, and Ti.

To investigate nanoparticle distribution and crystallinity, we conducted SAXS and WAXS analyses. SAXS is sensitive to nanoscale electron density variations and provides information on particle size distributions, while WAXS captures scattering at larger angles, offering insights into longrange structural order and crystalline phases SAXS results (Fig. 6a) indicate the presence of a spherical phase with different density with respect to the matrix, and changes in the spherical particle size and distribution with temperature (SAXS parameters in Supplementary Table 4). The SAXS signal shifts from a peak at $\sim\!0.9~\rm nm^{-1}$ for the 660 °C sample to $\sim\!0.5~\rm nm^{-1}$ for the 723 °C sample. In the 808 °C sample, the scattering pattern changes markedly, showing at least two distinct contributions: one centered at $\sim\!0.5~\rm nm^{-1}$, as observed at 723 °C, and a second, broader feature emerging at lower q ($\sim\!0.1~\rm nm^{-1}$), indicating the presence of two separate phases.

SAXS fitting results show a decrease in the Porod parameter from 0.14×10^{-4} for the 660 °C sample to 0.24×10^{-6} for the 723 °C sample, indicating that the particles are relatively isolated, with limited aggregation and simple surface morphology. Due to the restricted q-range at low q

Table 2 | Post-micropenetration STEM-EDS^a (wt%), HAADF image analysis^b and SAXS/WAXS results for AND100 samples

	AND100_MP ₆₆₀	MP ₆₆₀			AND100_MP ₇₂₃	AP ₇₂₃			AND100_MP ₈₀₈	MP ₈₀₈		
	Bulk _{TEM}	Matrix _{TEM}	Nanolite _{TEM}	Nanolite+Halo _{TEM}	Bulk _{TEM}	Matrix _{TEM}	Nanolite _{TEM}	Nanolite+Halo _{TEM}	Bulk _{TEM}	Matrix _{TEM}	Nanolite _{TEM}	Nanolite+Halo _{TEM}
SiO ₂	61.8	(6) 0.2	55 (9)	60 (3)	62.7	71 (5)	53 (9)	(3)	60.4	70 (3)	44 (10)	58 (4)
TiO ₂	7.0	0.5 (1)	0.8 (1)	1 (1)	0.8	(6.0) 8.0	2.5 (6)	1.1 (0.5)	1:1	(6.0) 9.0	2.9 (2)	1.4 (0.5)
Al ₂ O ₃	17.5	16 (7)	21 (7)	20 (4)	17.4	16 (4.8)	18 (7)	18 (1.4)	16.7	14 (3.4)	16.1 (7)	18.5 (1.4)
FeO _{tot}	7.1	(9) 6:9	10.6 (6)	8 (2)	7.1	2.8 (1.6)	13 (6)	8.4 (2)	7.2	1.7 (1.7)	22 (5)	11 (2)
MgO	3.0	3.1 (5)	4.3 (6)	2.8 (1.5)	2.8	2 (1.4)	2.4 (2.7)	3.1 (0.9)	2.8	2.2 (1.9)	4 (3)	3.4 (1)
CaO	5.7	3.6 (2.7)	6.1 (3.5)	6.3 (2.3)	6.1	4.7 (1.9)	7.2 (4)	6.8 (4)	7.0	6.3 (2.1)	8 (4)	7.8 (1)
Na ₂ O	1.3	0.5 (1)	0.7 (1)	0.5 (0.5)	8.0	0.4 (0.6)	1.4 (3)	0.5 (0.4)	2.5	2 (1.6)	1 (1)	0.9 (0.8)
K ₂ O	2.3	0.9 (1)	0.8 (1)	0.6 (0.6)	2.0	(6.0) 8.0	1.3 (2)	(9.0) 6.0	2.3	1.7 (1.1)	0.8 (1)	1 (1)
P_2O_5	09:0	1.2 (2)	1.3 (2)	0.8 (1)	0.20	1 (0.6)	0.7 (2)	0.4 (0.6)	2.29	0.9 (1)	1 (0.9)	1 (1)
= u	-	40	23	20	1	22	40	9	1	13	37	8
radius _{TEM} ^b (nm)	1.39 (0.55)	1.39 (0.55) ROIs = 4002			2.44 (0.71)	2.44 (0.71) ROIs = 439			2.64 (0.82)	2.64 (0.82) ROIs = 656		
lamella thickness (nm)	50 (2)				50 (2)				24 (2)			
nanolite content (vol%)	0.51 (0.1)				1.7 (0.1)				2.45 (0.1)			
NND^c (nm $^{-3}$) $ imes$ 10^4	2.93				2.09				2.39			
radius _{sAXS} d (nm)	1.7 (0.02)				3.1 (0.01)				$R_1 = 14(1)$	$R_1 = 14 (1) R_2 = 3.8 (0.5)$		
size _{waxs} ^d (nm)	1				1				D _{pyroxene} =	19.2 (0.5) D _{titan}	$D_{\text{pyroxene}} = 19.2 (0.5) D_{\text{titanomagnetite}} = 6.7 (0.5)$	1.5)

 $^{\text{a}}$ Parentheses in STEM-EDS results represent $1\pm\sigma$. Bulk $_{\text{TEM}}$ measurements have an error margin of 2% of the measured value. ^bMore details in Supplementary STEM-HAADF.

°NND: nanolite number density. The amount of nanolites per volume.
⁴More details in Supplementary SAXS-WAXS. Parenthesis represents the fit error.
⁴More details in Supplementary Fig. 14. Parenthesis represents the fit error.

Fig. 5 | STEM-EDS local chemistry for each subregion. a Residual amorphous matrix. b Nanolites and the compositionally differentiated halo surrounding them. c Nanolite cores. Average values were normalized to the bulk composition of the sample (Bulk_{TEM} in Table 2). The data was obtained from the analysis of STEM-EDS maps (Supplementary Figs. 11, 12 and 13) performed on samples treated at 660 °C, 723 °C and 808 °C during viscosity measurements. Error bars correspond to $\pm 1\sigma$ (Table 2).

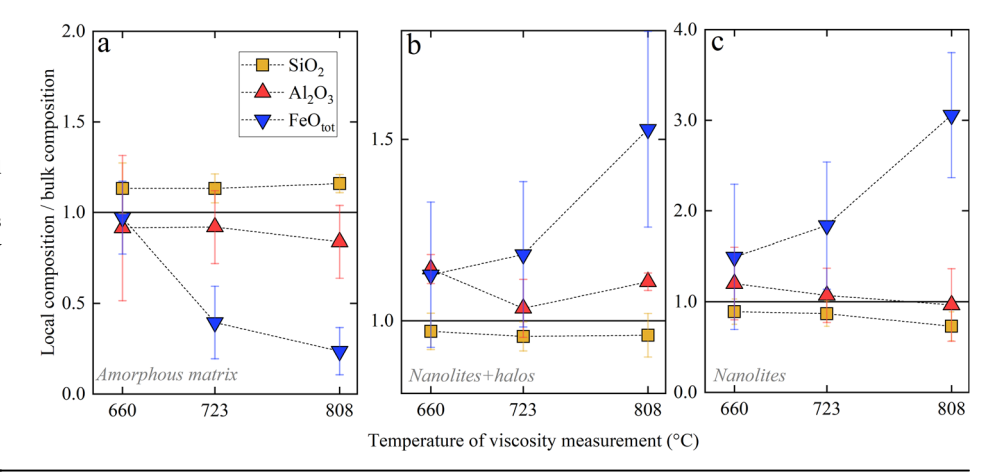
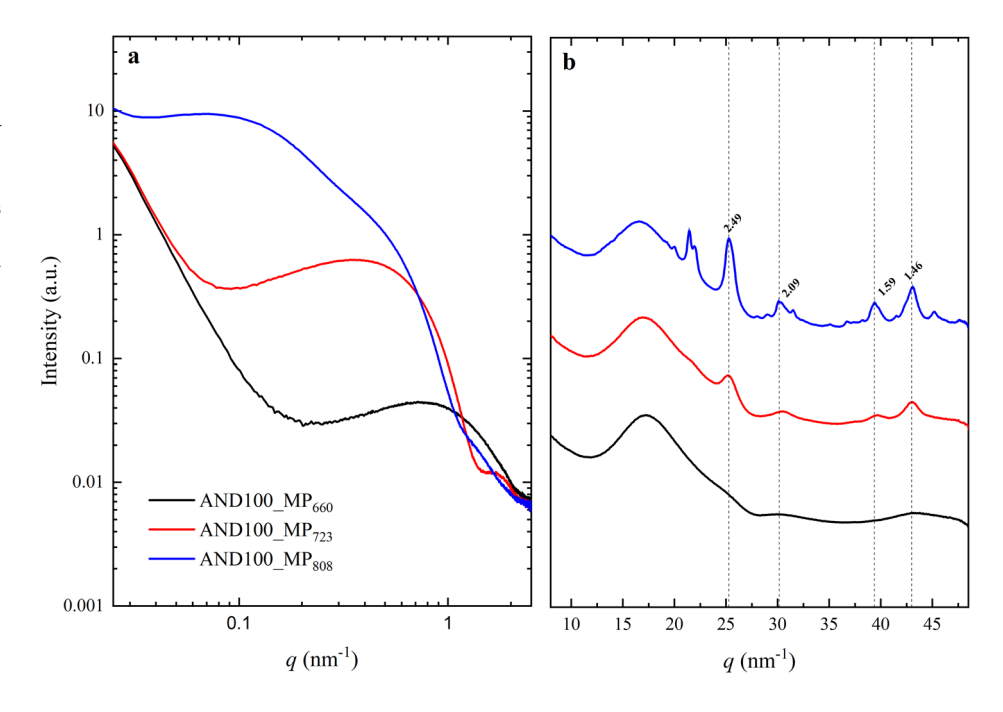


Fig. 6 | SAXS-WAXS analyses of postmicropenetration AND100 samples. a SAXS results. The fit SAXS parameters used for the modelling of particle size are reported in Supplementary Table 4. b WAXS results. The numbers above the peaks correspond to the calculated *d*-spacing (Å) using Eq. 18, where dashed lines correspond to peaks assignable to titanomagnetite^{40,42-44}. MP₆₆₀ was X-ray amorphous, while AND100_MP₇₂₃ exhibited diffraction peaks assignable to titanomagnetite and AND100_MP₈₀₈ contained titanomagnetite + pyroxene.



values, the Porod parameter estimated for the 808 °C sample (0.12) is not considered reliable. The extracted fractal dimension (fract = 3.75 ± 0.25 ; Supplementary Table 4) is consistent with spherical particle geometry. The structure factor (η_{HS} , Supplementary Table 4) is approximately 0.1 for the AND100_MP₆₆₀ and AND100_MP₇₂₃ samples, but decreases to ~0 for AND100_MP₈₀₈, indicating increased particle interaction and aggregation at higher temperature. Overall, the temperature-dependent shift of the SAXS signal toward lower q values suggests an increase in particle size, accompanied by more complex surface features and a higher degree of aggregation at elevated temperature.

SAXS modelling for AND100_MP₆₆₀ yields an average radius of amorphous nanoheterogeneities (see WAXS description below) of 1.7 ± 0.02 nm (Table 2). For AND100_MP₇₂₃, the average radius increases to 3.1 ± 0.1 nm, corresponding to nanocrystals as identified in WAXS. SAXS analysis of AND100_MP₈₀₈ reveals a dominant population with average radii of 3.8 ± 0.5 nm. These values are consistent with STEM-HAADF image analysis, which shows an increase in the average nanoheterogeneity radius from 1.4 ± 0.5 nm to 2.6 ± 0.8 nm (Table 2).

WAXS analysis provides complementary information on crystallinity and phase composition over larger volumes than those probed by TEM. The WAXS pattern of AND100_MP₆₆₀ (Fig. 6b) lacks sharp diffraction features,

indicating the absence of long-range order and the presence of nanoscale amorphous phase separation. This is consistent with SAXS data showing isolated particles with minimal aggregation and with the diffuse TEM diffraction patterns observed in Fig. 3a. For AND100_MP₇₂₃, WAXS patterns display distinct diffraction peaks corresponding to titanomagnetite^{48,49,59}, with *d*-spacings assignable to the (311), (400), (511), and (440) crystallographic planes. These observations match the TEM diffraction results for this sample, indicating the onset of crystalline phase formation.

The WAXS pattern for AND100_MP₈₀₈ reveals a more complex phase assemblage, including both titanomagnetite 48,49,59 and pyroxene 68 . Rietveld refinement shows that titanomagnetite crystals have an average crystal size of 6.7 ± 0.5 nm, while pyroxene crystals measure approximately 19.2 ± 0.5 nm (Table 2). These results are consistent with those reported by Mujin et al. 37 , who identified ferroaugite crystals measuring 20–30 nm and titanomagnetite particles ranging from 1 to 20 nm in pyroclasts from the 2011 Shinmoedake eruption.

Overall, the combined SAXS, WAXS, and TEM analyses provide a consistent and detailed picture of particle size evolution, phase composition, and crystallinity as a function of temperature at the nanoscale, demonstrating that our experimental results closely reflect natural magmatic processes.

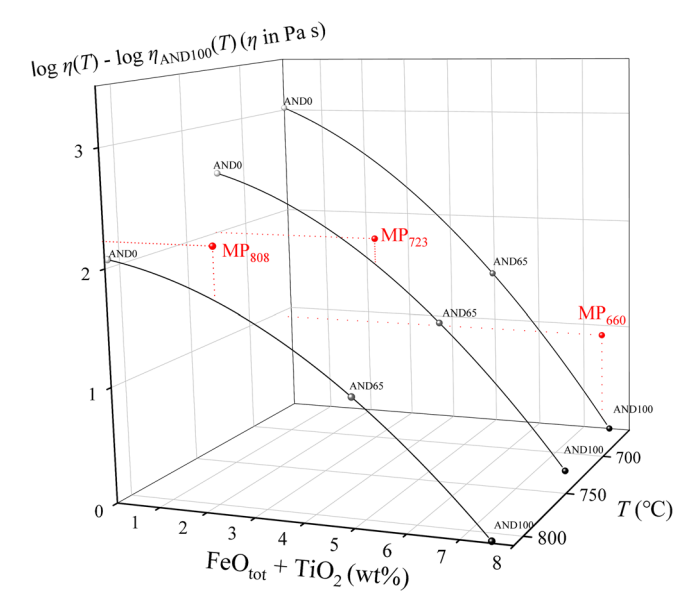


Fig. 7 | Nanolite-bearing viscosity of AND100 samples. Normalized viscosity as a function of temperature and FeO $_{\rm tot}$ + TiO $_2$ content (wt%) of their STEM-EDS-derived residual matrix composition (Fig. 5; Table 2). Viscosity is normalized to the AND100 melt (Table 1; Fig. 2). The MP sub-index represents the temperature (°C) of micropenetration measurement. The black curves correspond to the viscosity as a function of FeO $_{\rm tot}$ + TiO $_2$ content (wt%) at 660, 723 and 808 °C respectively. A viscosity calculator is provided as Supplementary Data.

The viscosity of nanolite-bearing andesitic melts

To elucidate the impact of nanocrystallization and iron oxidation on the viscosity of andesitic melts, we compare our viscosity micropenetration results for AND100 samples with the corresponding melt viscosity parametrizations (Fig. 2b). For AND100_MP₆₆₀, the initial viscosity measurement ($\eta = 10^{12}$ Pa s; Supplementary Table 2) closely matches the predicted melt viscosity of AND100 at 660 °C. However, a progressive increase in viscosity was observed under isothermal conditions, reaching a final value of $\eta = 10^{12.7}$ Pa s, accompanied by a slight increase in the iron oxidation state to $Fe^{3+}/Fe_{tot} = 0.7$. This final viscosity is approximately 8 times higher than the predicted value for AND100 ($Fe^{3+}/Fe_{tot} = 0.64$) at the same temperature. STEM-EDS data (Figs. 3 and 4; Table 2) show that less than 3 wt% of the total iron precipitated as nanocrystals in this sample. Thus, the presence of solid particles (<1 vol%; Table 2), as considered in classical particle suspension models⁶⁹, and the overall compositional variations^{34,58} (e.g., Fe-Ti removal in Fig. 7) of the surrounding amorphous phase are insufficient to account for the observed viscosity increase.

We propose that the rapid formation of a SiO_2 -enriched matrix, the segregation of Fe-rich immiscible domains, and subsequent crystallization of titanomagnetite, leads to the development of a complex and heterogeneous nanostructure (Fig. 4). This structural evolution likely explains the excess measured viscosity, as illustrated in Fig. 7.

Similar trends are observed at higher temperatures. For AND100_MP₇₂₃, the final viscosity ($\eta=10^{11.9}$ Pa s; Fe³⁺/Fe_{tot}=0.79) is nearly 5 times greater than the predicted viscosity of AND65 ($\eta=10^{11.18}$ Pa s) at 723 °C, even though the residual matrix retains approximately 40% of the initial FeO_{tot} content (Table 2). For AND100_MP₈₀₈, the final viscosity ($\eta=10^{10.17}$ Pa s; Fe³⁺/Fe_{tot}=0.83) slightly exceeds the predicted viscosity of AND0 at 808 °C ($\eta=10^{10}$; Fig. 2), despite the residual matrix still containing ~25% of the original FeO_{tot} (Fig. 5; Table 2).

It should be noted that complete precipitation of FeO_{tot} as crystalline phases is unlikely during the experiment, as the temperature-dependent solubility of FeO_{tot} in the metastable melt is not expected to approach zero, even under deep supercooling⁷⁰. Even in the comparatively evolved AND100_MP₈₀₈, the crystalline phase content (~2.45 vol%) is too low

to significantly affect melt viscosity through conventional suspension mechanisms⁶⁹.

Overall, our findings highlight the complex interplay of nanocrystallization, iron oxidation, and nanoscale phase separation in controlling the rheology of andesitic melts. While previous studies^{19,33} attributed the viscosity increase solely to iron depletion in the residual aluminosilicate matrix due to titanomagnetite nanocrystallization, our results suggest a more complex mechanism. We propose that the rapid segregation of nanoscale Fe-rich immiscible droplets initiates the formation of a relatively SiO₂-enriched matrix. Titanomagnetite nanocrystallization then occurs within these Fe-rich domains. As the nanocrystals grow and develop long-range order, aluminum is expelled from the crystal structure, forming Al-enriched shells around the nanolites.

Additionally, post-micropenetration Mössbauer spectroscopy (Supplementary Micropenetration; Supplementary Table 2) shows that the Fe³+/Fetot ratios of the AND100 samples exceed the stoichiometric requirement for titanomagnetite to consume all the iron in the melt. This indicates that in samples such as AND100_MP $_{723}$ and AND100_MP $_{808}$, which contain well-developed titanomagnetite nanolites, a significant portion of the remaining iron in the SiO2-enriched matrix likely exists as Fe³+. This oxidation state may enhance the polymerization of the residual melt structure by converting network-modifying cations into charge-compensating species and promoting Fe³+ as a network-forming component $^{57,71-73}$.

Notably, nanolite formation was observed under various oxygen fugacity conditions during our high-temperature experiments. This observation aligns with previous work 40,74, which shows that nanolites can form across a broad range of redox conditions relevant to both natural magmatic environments and experimental settings.

As discussed above, and accounting for Fe-Ti extraction due to nanocrystallization, we observe a consistent surplus in viscosity across all our nanolite-bearing samples, ranging from 2 to 6 times higher than the expected values for homogeneous melts (Fig. 7). Notably, nanoscale chemical heterogeneity has the greatest impact at low crystal fractions, as seen in MP $_{660}$ (Fig. 7), where the pronounced viscosity increase cannot be explained solely by Fe-Ti depletion, crystal suspension, or aggregation. Bulk Fe-Ti extraction appears to play a more significant role at low to moderate crystal fractions, such as in MP $_{723}$, where the initial melt viscosity is comparatively lower.

At higher nanolite contents, as in MP₈₀₈ (Fig. 7), SAXS data indicate the emergence of particle interaction, introducing an additional mechanism influencing viscosity during magmatic crystallization. This interaction likely arises from pervasive nanoscale heterogeneity driven by the concurrent diffusion and segregation of elements such as Al, Ti, and Fe (Figs. 4, 5; Table 2), in response to iron oxidation and titanomagnetite nanocrystallization⁷⁵. These processes lead to the formation of chemically distinct nanodomains in the initially homogeneous melt, including nano-sized crystals, Al-enriched shells, and highly SiO₂-enriched regions (up to ~70 wt%; Fig. 5; Table 2), significantly increasing the effective bulk viscosity (Fig. 2b).

The nanolite-bearing viscosity of AND100_MP $_{808}$ (Fig. 7) indicates that the viscosity of AND0, a homogeneous melt devoid of transition metals, only provides a lower bound for the viscosity of nanolite-bearing AND100 at temperatures above 808 °C. At these conditions, compositional fluctuations and particle interactions at the nanoscale become increasingly pronounced (Fig. 5).

These findings demonstrate that the physical properties of titanomagnetite-bearing silicate melts cannot be directly compared with those of homogeneous materials without a critical assessment of data reliability. We show that nanolite nucleation and growth result in chemically differentiated nanodomains that induce a complex and substantial increase in viscosity. For example, progressive titanomagnetite crystallization is accompanied by a systematic increase in DSC-derived characteristic temperatures (Supplementary C-DSC; Supplementary F-DSC). Despite the relatively low titanomagnetite content typically observed in natural melts, its effect on viscosity should not be underestimated.

Consistent with previous research^{28,35,36,76}, our findings suggest that the viscosity increase induced by nanocrystallization, and modulated by the formation of chemical heterogeneities at the nanoscale, may influence eruption dynamics. These results have important implications for understanding the behavior of andesitic magmas, which are characterized by diverse eruptive styles⁷⁷. Rapid magma ascent can generate high undercooling, promoting syn-eruptive crystallization within volcanic conduits¹⁰. This is known to enhance the coupling between gas and melt, potentially affecting the dynamics of magma ascent. Additionally, melt dehydration, oxidation, and thermal fluctuations during magma ascent may also lead to nanocrystallization in the shallow conduit^{29,30,32}.

Importantly, nanocrystallization not only increases magma viscosity, but it can also facilitate the formation of nucleation sites for gas bubbles^{36,78}, thereby hindering bubble connectivity and outgassing. We hypothesize that the formation of the documented heterogeneous texture composed of melt and (nano)crystalline phases may have a non-trivial impact on water exsolution. The development of nanoscale heterogeneities may locally elevate water concentration and induce supersaturation, as nanolites cannot accommodate volatiles, thereby "squeezing" water out of the surrounding melt. Additionally, this study also contributes to a better understanding of the evolving physical properties of andesitic domes and plugs, as they are known to be exposed to naturally occurring reheating processes⁷⁹.

Together, these effects could potentially act as a gateway for magma fragmentation¹³, explaining the explosivity of andesitic magmas⁸⁰. Supporting this, a recent study⁸¹ identified nanoscale Al-rich heterogeneities on the surfaces of natural andesitic ash particles, indicating that ash-forming fractures preferentially propagate through regions surrounding Fe-rich nanolites. This mechanism for fracture propagation is consistent with the formation of chemically differentiated nanodomains, as magma failure should propagate through the most viscous zones (i.e., the SiO₂-enriched matrix), resulting in Al-rich surfaces in the ash particles.

In summary, the formation of nanolites and associated chemical heterogeneity drives rheological changes in andesitic magma, influencing ascent dynamics and contributing to variations in eruptive style.

Conclusions

We present, to the best of our knowledge, the first in situ observation of nanolite formation in a synthetic andesitic melt and introduce viscosity models tailored to various andesitic compositions. Our observations show that iron oxidation and nanocrystallization readily occur above the glass transition temperature. This challenges conventional interpretations, as the observed viscosity increase due to titanomagnetite nanocrystallization cannot be explained solely by iron depletion in the residual amorphous matrix or by the presence of solid particles. Instead, we propose a more complex mechanism: rapid amorphous phase separation leads to the formation of nanoscale Fe-rich domains, inducing relative SiO₂ enrichment in the surrounding matrix. Titanomagnetite nanocrystallization then proceeds within these Fe-rich domains. As these titanomagnetite nuclei grow, aluminum is expelled from the crystalline nuclei, forming Al-enriched shells surrounding the nanolites. This sequence of events results in a viscosity increase of up to 30 times at eruptive temperatures. This increased magma viscosity, coupled with an inherently non-uniform mechanical response due to its nanoscale chemical heterogeneity, may significantly influence the rheological properties of the melt and, consequently, the eruption dynamics of andesitic volcanoes.

Materials and methods Synthesis of starting glasses

AND100, AND65 and AND0 were synthesized by mixing powder reagents (SiO_2 , TiO_2 , Al_2O_3 , Fe_2O_3 , MnO, MgO, $CaCO_3$, Na_2CO_3 , K_2CO_3 , and P_2O_5) according to their target compositions. The mass of each oxide and carbonate component was determined through molar mass calculations. All reagents were mixed using an agate mortar and ethanol. The mixture underwent manual grinding for ~45 min before being dried using an infrared light. Subsequently, the dry mixture was placed in an alumina

crucible and subjected to an overnight heat treatment at 900 °C to eliminate $\rm CO_2$ from the carbonate compounds. Following decarbonization, the material was transferred to a Pt crucible and melted for 24 h at 1400 °C. Afterwards, the melt was rapidly quenched in water to prevent crystallization. The resulting quenched glass was crushed to powder using a stainless-steel percussion mortar and then manually mixed before performing a second melting to achieve chemical homogenization. The second round of melting at 1400 °C lasted for 4 h, after which the crucible was swiftly immersed in water for rapid cooling. Subsequently, AND100red was produced by re-melting AND100 sample in a hanging $\rm Au_{80}Pd_{20}$ open capsule at 1275 °C and 1 atm for 24 h, using a gas mixing furnace with a gas mixture of 95% $\rm CO_2$ and 5% $\rm CO$. The resulting melt was rapidly quenched in water by melting the Pt wire.

Electron microprobe analyses (EMPA)

The major elemental composition (Si, Ti, Al, Fe_{tot}, Mn, Mg, Ca, Na, K, and P) of samples AND100, AND100ox, AND100red, AND65, and AND0 was determined using a JEOL JXA-8200 electron microprobe at the Bayerisches Geoinstitut (University of Bayreuth, Germany) (Table 1). Glasses were embedded in epoxy, polished, and carbon coated. Measurements were performed using 15 kV voltage, 5 nA current, and 20 s of counting time under a defocused 10 μ m beam. We collected 10 points per sample to account for heterogeneities. Synthetic wollastonite (Ca, Si), periclase (Mg), hematite (Fe), spinel (Al), orthoclase (K), albite (Na), manganese titanate (Mn, Ti), and apatite (P) were used as calibration standards. Sodium and potassium were analyzed first to mitigate alkali migration effects⁸².

Micropenetration viscometry

We conducted micropenetration (MP) viscometry measurements on plane-parallel and polished glass chips of 2-3 mm in thickness. These measurements were carried out utilizing a vertical dilatometer (Bähr VIS 404) at the Institute of Non-Metallic Materials, TU Clausthal (Germany). We measured the indentation rate of a sapphire sphere (r = 0.75 mm) during isothermal dwells at temperatures controlled using an S-type thermocouple (Pt-PtRh) placed at ~1.5 mm from the sample surface. The temperature error is estimated to be ± 2 °C considering the accuracy of the S-type thermocouple and its distance from the sample⁸³. We followed standard procedures^{20,21,40,84} to achieve thermal equilibration at the target temperature. The indentation depth was measured as a function of time and the viscosity curve was determined according to Eq. 1⁸⁵:

$$\eta = \frac{3F}{16\sqrt{2rL}\frac{dl}{dt}}\tag{1}$$

where η is the Newtonian viscosity (Pa s), F is the applied force (N), t is the time (s), r is the radius of the sphere (m), L is the cumulative indentation depth (m), and $\frac{dl}{dt}$ is the indentation within a measurement interval. The dilatometer was previously calibrated using a standard glass DGG-1, reproducing the certified viscosity data⁸⁶ with a deviation of \pm 0.1 in log units. Data points are reported in the text according to the scheme $SampleName_MP_{Temperature}$, with temperature representing the final experimental temperature expressed in °C, and the duration in minutes.

Concentric cylinder (CC) viscometry

High-temperature viscosity measurements were conducted using a Rheotronic II Rotational Viscometer (Theta Instruments) at the Experimental Volcanology and Petrology Laboratory (EVPLab, Roma Tre University, Italy). The experimental apparatus featured an Anton Paar Rheolab Qc viscometer head with a maximum torque capacity of 75 mN m⁸⁷. Temperature monitoring was carried out using a factory-calibrated S-type thermocouple, with a precision of ± 2 °C. The concentric cylinder was previously calibrated using a standard glass NIST 717a, reproducing the certified viscosity data with a deviation of \pm 0.03 in log units⁸⁸. To ensure thorough thermo-chemical homogenization, the glass materials were loaded into a Pt₈₀Rh₂₀ cylindric crucible (62 mm in height, and 32 mm inner

diameter) and stirred at $\dot{\gamma}=10~s^{-1}$ using a $Pt_{80}Rh_{20}$ spindle (3.2 and 42 mm in diameter and length, respectively) at 1435 °C at air oxygen fugacity and ambient pressure for 5 hours. Subsequently, the temperature was lowered by steps of 25–50 °C down to 1150 and 1130 °C for the samples AND100ox and AND0, respectively. The viscosity was measured at every step, holding the conditions constant until steady viscosity and temperature values had been achieved (~45 min). At the end of the experiments, the temperature was quickly raised to 1430 °C where a portion of the melt was rapidly quenched in water to determine the iron oxidation state of the high-temperature viscosity measurements.

Differential scanning calorimetry

Conventional differential scanning calorimetry (C-DSC) measurements were performed at the Institute of Non-Metallic Materials, TU Clausthal (Germany). Around 15 mg (\pm 5) of glass was placed in a Pt80Rh20 crucible under a constant N2 (5.0) flow rate of 20 ml min $^{-1}$. We used two conventional differential scanning calorimeters (C-DSC, 404 F3 Pegasus and 404 cell, Netzsch) to measure the heat flow at a heating rate (q_h) of 10 and 20 °C min $^{-1}$. Additionally, we used \sim 50 ng of glass to perform flash differential scanning calorimetry (F-DSC) analyses, using a Flash DSC 2+ (Mettler Toledo) equipped with UFH 1 sensors, under constant Ar 5.0 flow (40 ml min $^{-1}$).

The C-DSC was calibrated using melting temperatures and enthalpy of fusion of reference materials (pure metals: In, Sn, Bi, Zn, Al, Ag, and Au), and the F-DSC was calibrated using the melting temperature of aluminum (660.3 °C) and indium (156.6 °C). In our C-DSC measurements, we employed the methodology outlined by Stabile et al. 42. Initially, we erased the thermal history of the glass by subjecting the sample to a two-step thermal treatment. This involved a first upscan at a rate of $q_h = 20$ °C min⁻¹ until it reached a temperature slightly above T_{peak} , namely T_{max} . Subsequently, we cooled the melt to 100 °C at rates of $q_c = 10$ or 20 °C min⁻¹. The actual C-DSC measurements were then conducted using the rate-matching method, which entailed an additional upscan (matching heating segment) with a rate matching that of the preceding downscan (i.e., $q_h = q_c$). From the measured heat flow during the matching upscan, we extracted the characteristic temperatures T_{onset} and T_{peak} , both related to phase transitions or thermal events observed during the heating or cooling of a sample. For further details see the methodology presented in Valdivia et al.²⁰.

For F-DSC experiments, we followed the methodology described above employing a $q_h = q_c = 1000~{\rm ^{\circ}C~s^{-1}}$ (60000 ${\rm ^{\circ}C~min^{-1}}$). Subsequently, we conducted a series of measurements on the same sample, using the same chip, at 10000 ${\rm ^{\circ}C~s^{-1}}$ (600000 ${\rm ^{\circ}C~min^{-1}}$) to investigate the impact of nanocrystallization on the characteristic temperatures T_{onset} and T_{peak} due to consecutive thermal treatments.

Following the theoretical background discussed elsewhere $^{40,89-91}$, viscosity values were derived from C- and F-DSC data using the relationship between the matching heating rate (q_h) of the measurement and the shift factors K_{onset} and K_{peak} 40,42 expressed in Eq. 2:

$$log_{10}\eta(T_{onset,peak}) = K_{onset,peak} - log_{10}(q_h)$$
 (2)

where $K_{onset} = 11.20 \pm 0.15$ and $K_{peak} = 9.84 \pm 0.20^{40,42}$. It is important to mention that when q_h is 10 °C min⁻¹, $\eta(T_{onset}) \approx 10^{12}$ Pa s, and therefore, $T_{onset} \approx T_g$. The validation of the shift factor method (Eq. 2) for our compositions is discussed in the Supplementary Viscosity Parametrization.

Brillouin Spectroscopy

Brillouin spectroscopy (BLS) measurements were performed at the Bayerisches Geoinstitut (University of Bayreuth, Germany). Plane-parallel glass plates with a thickness of ~50 μ m were analysed using a solid-state Nd:YVO4 laser source operating at a wavelength of 532 nm and 50 mW power. The Brillouin frequency shift was quantified utilizing a six-pass Fabry–Perot interferometer⁹² coupled with a single-pixel photon counter detector. Measurements were conducted using a symmetric forward scattering configuration⁹² with a scattering angle of θ = 79.8°. The accuracy of

the scattering angle was established through calibration with a reference silica glass. Conversion of frequency shifts $(\Delta \omega)$ to longitudinal (ν_p) and shear (ν_e) sound velocities was carried out using Eq. 3:

$$v = \frac{\Delta\omega\lambda}{2\sin(\theta/2)}\tag{3}$$

where λ is the laser wavelength and θ is the angle between the incident and scattered beams ^{92,93}. We collected 8 spectra for each sample at different rotation angles (from -180° to $+180^{\circ}$) to factor for uncertainties. Finally, we calculated the K/G factor using the ratio between ν_p and ν_s (Eq. 4):

$$\frac{K}{G} = \left(\frac{v_p}{v_s}\right)^2 - \frac{4}{3} \tag{4}$$

Room- and high-temperature Raman spectroscopy

Glasses subjected to micropenetration, concentric cylinder viscometry, C-DSC and F-DSC were analysed before and after the measurements to account for potential modifications (i.e., crystallization and/or iron oxidation). For this, we used a confocal Raman imaging microscope at the Institute of Non-Metallic Materials, TU Clausthal (alpha300R, WITec GmbH), where spectra were acquired using a 100x objective in the ranges between 10 and 1300 cm⁻¹. Acquisition parameters included an integration time of 10 s, an accumulation count of 5, and a laser power of 10 mW. Spectra were smoothed to enhance the signal-to-noise ratio.

Additionally, we performed in situ high-temperature Raman analyses on the AND100 sample. We targeted the same temperatures and heating treatments as those used for micropenetration experiments. We used a Renishaw InVia Qontor Raman spectrometer at the CEMHTI, Orleans (France). Spectra were acquired using a 20x NA 0.35 objective in the ranges between 150 and 2000 cm⁻¹. Acquisition parameters included an integration time of 60 seconds, and a laser power of 20 mW.

Mössbauer spectroscopy

Mössbauer measurements were performed at the Bayerisches Geoinstitut (University of Bayreuth, Germany). Glass samples of ~4 mm diameter and ~600 μm thickness were measured before and after experiments at room temperature (293 K) using a constant acceleration Mössbauer spectrometer equipped with a high specific activity (370 MBq) 57 Co point source within a 12 μm thick Rh matrix. Calibration of the velocity scale was relative to a 25 μm thick α -Fe foil, and data were gathered within the range of \pm 5 mm s $^{-1}$, with acquisition durations of 2 to 3 days each. The recorded spectra were fitted with the full transmission integral using the MossA software 94 . Finally, the resulting Fe $^{3+}$ /Fe $^{2+}$ ratios were calculated using the relative area associated with each iron species.

Room- and high-temperature transmission electron microscopy (TEM) analyses

We performed room-temperature scanning TEM (STEM) analyses on the AND100 samples post-micropenetration experiments and in situ heating TEM observations on the AND100 starting glass. Room-temperature STEM explorations were performed at the Bayerisches Geoinstitut (University of Bayreuth, Germany) using a FEI Titan G2 80-200S/TEM. STEM imaging was acquired from lamellas made using a focused ion beam (FIB) with thicknesses ranging from 24(2) to 50(2) nm. These lamellas were extracted from the same samples that were used for micropenetration experiments, utilizing a SCIOS Dual Beam system from FEI Company. We used a Gallium ion beam with variable current, from 7.8 pA to 300 nA depending on the precision requirements. Analytical scanning transmission electron microscopy (STEM) micrographs were collected at 200 kV using an energy-dispersive X-ray spectrometer (EDS) system consisting of four silicon drift detectors (Bruker, QUANTAX EDS). The EDS maps were acquired with a dwell time of 16 s using a sub-nanometer-sized electron beam with less than 0.05 nA probe current at 200 kV-acceleration voltage.

To accumulate statistically relevant characteristic X-ray counts in a quantitative EDS map, the total acquisition time was 12-30 minutes. During the acquisition, an image drift correction function was always activated to prevent drift in the profile. To get quantitative compositions of the samples, we corrected the Z-number and absorption effects on the evaluations of the EDS spectrum^{95,96}. Geometrical analyses of STEM-HAADF images were subjected to pixel segmentation and classification using the ilastik software, version 1.4.0⁹⁷. To identify nanocrystalline phases in the silicate glasses, TEM-SAED patterns were collected after exploration in conventional TEM mode.

In situ heating experiments were performed at the CNRS CEMHTI in Orléans (France) using a JEOL ARM200F (JEOL Ltd.) Cold FEG microscope operating at 80 kV, mounting a double spherical aberration corrector, a Gatan Imaging Filter (GIF, Gatan Ltd.) and a OneView camera. The experimental procedure was optimized in a previous work⁴⁵ to minimize artifacts and sample damage due to highly energetic electron irradiation. The AND100 glass was crushed and ground in an agate mortar, adding ethanol to obtain a diluted suspension; one drop of the liquid was then loaded onto a MEMS grid specifically adapted for a Protochips Fusion double-tilt heating holder and dried in air overnight. Plasma cleaning was avoided to prevent major changes in the redox state of iron in the sample. After introducing the sample holder into the TEM column, it was preemptively treated at 200 °C for 1 h to remove possible volatile contaminants. The subsequent in situ experiment involved manual heating at 1 °C s⁻¹ to various temperatures between 200 °C and 750 °C, where isothermal dwells of 30-60 s were applied to facilitate nanoscale observation in TEM mode (Supplementary Fig. 6). Sample drift was manually compensated during the heating ramps. After the experiment, the acquired data was manually resampled (3 images for each isothermal dwell) and re-aligned using the software DigitalMicrograph GMS.3 (Gatan). To identify nanocrystalline phases in the silicate glasses, we performed Fast Fourier transform (FFT) on HR-TEM images. The EDS maps were taken in STEM mode with an acquisition time of 30 s using a sub-nanometer-sized electron beam of 1 Å. To accumulate statistically relevant characteristic X-ray counts in a quantitative EDS map, the total acquisition time was approximately 11 min.

Viscosity parametrization

The combination of C-DSC, F-DSC, MP and CC viscosity data enabled the parametrization of the melt viscosity of our samples as a function of temperature $\eta(T)$, via the Mauro-Yue-Ellison-Gupta-Allan (MYEGA) equation (Eq. 5)⁵⁴:

$$log_{10}\eta(T) = log_{10}\eta_{\infty} + \left(12 - log_{10}\eta_{\infty}\right) \frac{T_g}{T} exp\left[\left(\frac{m}{12 - log_{10}\eta_{\infty}} - 1\right)\left(\frac{T_g}{T} - 1\right)\right]$$
 (5)

where $log_{10}\eta_{\infty}=-2.93\pm0.3$ is the logarithmic viscosity at infinite temperature ^{53,54}, T_g is the glass transition temperature (in K) determined by C-DSC (T_{onset} at $q_{h,c}=10$ °C min⁻¹) and m is the melt fragility defined in Eq. 6⁹⁸ as the slope of viscosity curve evaluated at T_g :

$$m = \frac{\partial log_{10}\eta}{\partial T_g/T}\bigg|_{T=T} \tag{6}$$

The melt fragility parameter, m, can be determined by fitting Eq. 5 to our viscosity datasets (Supplementary Table 2) and the measured T_g via C-DSC (Table 1). Additionally, m also can be inferred from BLS measurements using the empirical relationship introduced by Cassetta et al. (Eq. 7),

$$m = 43 \cdot \frac{K}{G} - 31 \tag{7}$$

Small- and -wide angle X-ray scattering (SAXS and WAXS)

The SAXS and WAXS measurements were conducted at the ID02 beamline of the European Synchrotron Radiation Facility (ESRF)⁶⁷ in Grenoble, France. The experiments utilized a monochromatic, highly collimated, and intense X-ray beam in a pinhole configuration, with a sample-to-detector distance of 6 meters. This arrangement enabled the exploration of a scattering vector range from 0.01 nm^{-1} to 2.5 nm^{-1} , where q is the scattering vector, defined as

$$q = |q| = \frac{4\pi \sin(\theta)}{1},\tag{8}$$

with the X-ray wavelength $\lambda=1$ Å and θ is the scattering angle. To eliminate parasitic background around the primary beam, a guard slit before the sample was set to 0.45 mm vertically and 0.5 mm horizontally. Data reduction was performed using PyFAI, which leverages the geometry of ID02.

The analysis of the SAXS data was performed using a custom-developed software package, which has been successfully validated and applied in previous studies 100,101 . Assuming a spherical form factor for the nanoparticles, and based on TEM observations indicating potential close contact among the nanoparticles, the scattering intensity, I(q), was modeled using the decoupling approximation $^{100,102-104}$:

$$I(q) = \Delta(\rho)^2 S(q) P(q) + bck + \frac{K_{porod}}{q^4}$$
(9)

where $\Delta(\rho)^2$ is the difference of electronic density between the nanoparticles and the surroundings, *bck* is the background constant, P(q) is the contribution given by a poly-disperse system of not-interacting homogeneous spheres,

$$P(q) = \int_{a}^{\infty} D(\bar{R}, r) F(r, q, \bar{R})^2 r^6 dr$$
(10)

F(q, r) is the form factor of a sphere of radius r given by Eq. 11

$$F(q,r) = \frac{\sin(qr) - qr\cos(qr)}{qr^3} \tag{11}$$

and $D(r, \bar{R})$ is the Weibull size distribution of particle sizes defined as

$$D(r,\bar{R}) = \left(\frac{r}{\bar{p}}\right)^{(b-1)} \exp\left(\frac{r}{\bar{p}}\right)^b, \tag{12}$$

in which \bar{R} is the average radius of the nanoparticle. The possibility of having a bimodal distribution is also included in the fitting. In this case the distribution function is given by the sum of two Weibull distribution functions centered in R_1 and R_2 . S(q) is the structure factor for interacting spheres with a hard-sphere radius R_{HS} , constituting the effective interaction distance between particles. The η_{HS} is the hard sphere volume fraction. S(q) can be calculated analytically using the PercuseYevick approximation which works well for systems characterized by a short-range interaction potential. Accordingly, S(q) is equal to:

$$S(q, R_{HS}) = [1 + 24\eta_{HS}f(R_{HS}, q)]^{-1}$$
 (13)

and by defining $x = R_{HS}$ q it is possible to arrange f(x) as the following:

$$f(x) = \frac{\alpha(-x\cos x + \sin x)}{x^3} + \frac{\beta(-x^2\cos x + 2x\sin x + 2\cos x - 2)}{x^4}$$

$$+ y[-x^4\cos x + 4x^3\sin x + 12x^2\cos x - 24x\sin x - 24\cos x + 24]$$

$$(14)$$

with,

$$\alpha = \frac{\left(1 + 2\eta_{HS}\right)^2}{\left(1 - \eta_{HS}\right)^4},\tag{15}$$

$$\beta = \frac{-6\eta_{HS} \left(1 + \frac{\eta_{HS}}{2}\right)^2}{\left(1 - \eta_{HS}\right)^4} \tag{16}$$

$$\gamma = \frac{\eta_{HS}\alpha}{2} \tag{17}$$

Finally, by assuming that a particle grows at the expense of the surrounding iron oxide content, R_{HS} is proportional to the actual nanoparticle radius $R_{HS} = 2Rkc^{100,102,103}$, where kc is a constant term ≥ 1 . This parameter considers the possibility that the nanoparticles are not fully in contact. To reproduce the SAXS pattern at very low q a Porod behavior K_{porod}/q^4 has also been added. This inverse fourth power dependence indicates that at high q values, the scattering intensity decreases sharply. The Porod function is instrumental in understanding the surface roughness and the specific surface area of the particles in the sample. It assumes an ideal, smooth interface, leading to a clean power law, but deviations from this behavior can reveal information about surface fractal dimensions and the nature of the interface.

Finally, we calculated d-spacings (d) for the crystalline phases from WAXS experiments using Eq. 18^{105} ,

$$d = \frac{2\pi}{q_{peak}} \tag{18}$$

with q_{peak} corresponding to the WAXS peaks (Fig. 6b).

Data availability

Data supporting the findings of this study are available within the article or in the Supplementary Information. Additional source data for figures are available in the following link: https://zenodo.org/records/15342490.

Received: 2 October 2024; Accepted: 28 May 2025; Published online: 12 June 2025

References

- Loughlin, S. C., Sparks, S., Brown, S. K., Jenkins, S. F. & Vye-Brown, C. Global Volcanic Hazards and Risk. Global Volcanic Hazards and Risk (Cambridge University Press, Cambridge, 2015). https://doi. org/10.1017/CBO9781316276273.
- Papale, P. Strain-induced magma fragmentation in explosive eruptions. *Nature* 397, 425–428 (1999).
- 3. Gonnermann, H. M. Magma Fragmentation. *Annu. Rev. Earth Planet. Sci.* **43**, 431–458 (2015).
- Cashman, K. V. & Scheu, B. Magmatic Fragmentation. The Encyclopedia of Volcanoes. https://doi.org/10.1016/b978-0-12-385938-9.00025-0 (Elsevier Inc., 2015).
- Cassidy, M., Manga, M., Cashman, K. & Bachmann, O. Controls on explosive-effusive volcanic eruption styles. *Nat. Commun.* 9, 2839 (2018).
- Kueppers, U., Scheu, B., Spieler, O. & Dingwell, D. B. Fragmentation efficiency of explosive volcanic eruptions: A study of experimentally generated pyroclasts. *J. Volcanol. Geotherm. Res.* 153, 125–135 (2006).
- Mueller, S., Scheu, B., Spieler, O. & Dingwell, D. B. Permeability control on magma fragmentation. Geology 36, 399–402 (2008).
- Dingwell, D. B. Volcanic dilemma: Flow or blow?. Science 273, 1054–1055 (1996).
- Okumura, S., Nakamura, M., Nakano, T., Uesugi, K. & Tsuchiyama, A. Shear deformation experiments on vesicular rhyolite: implications for brittle fracturing, degassing, and compaction of magmas in volcanic conduits. J. Geophys. Res. Solid Earth 115, 1–10 (2010).
- Arzilli, F. et al. Magma fragmentation in highly explosive basaltic eruptions induced by rapid crystallization. *Nat. Geosci.* 12, 1023–1028 (2019).

- La Spina, G., Burton, M., De'Michieli Vitturi, M. & Arzilli, F. Role of syn-eruptive plagioclase disequilibrium crystallization in basaltic magma ascent dynamics. Nat. Commun. 7. (2016).
- La Spina, G. et al. Explosivity of basaltic lava fountains is controlled by magma rheology, ascent rate and outgassing. *Earth Planet. Sci.* Lett. 553, 116658 (2020).
- Bamber, E. C. et al. Outgassing behaviour during highly explosive basaltic eruptions. Commun. Earth Environ. 5 (2024).
- Sato, H. et al. Viscosity of andesitic lava and its implications for possible drain-back processes in the 2011 eruption of the Shinmoedake volcano, Japan. Earth, Planets Sp. 65, 623–631 (2013).
- Vetere, F., lezzi, G., Perugini, D. & Holtz, F. Rheological changes in melts and magmas induced by crystallization and strain rate. Comptes Rendus. Géoscience 354, 227–248 (2022).
- Yamada, K., Emori, H. & Nakazawa, K. Time-evolution of bubble formation in a viscous liquid. Earth, Planets Sp. 60, 661–679 (2008).
- Bamber, E. C. et al. Pre- and syn-eruptive conditions of a basaltic Plinian eruption at Masaya Volcano, Nicaragua: The Masaya Triple Layer (2.1 ka). J. Volcanol. Geotherm. Res. 392, 106761 (2020).
- Sable, J. E., Houghton, B. F., Del Carlo, P. & Coltelli, M. Changing conditions of magma ascent and fragmentation during the Etna 122 BC basaltic Plinian eruption: Evidence from clast microtextures. *J. Volcanol. Geotherm. Res.* 158, 333–354 (2006).
- Okumura, S. et al. Rheology of nanocrystal-bearing andesite magma and its roles in explosive volcanism. *Commun. Earth Environ.* 3, 241 (2022).
- Valdivia, P. et al. Are volcanic melts less viscous than we thought? The case of Stromboli basalt. Contrib. to Mineral. Petrol. 178, 45 (2023).
- Scarani, A. et al. A chemical threshold controls nanocrystallization and degassing behaviour in basalt magmas. *Commun. Earth Environ.* 3, 284 (2022).
- Liebske, C., Behrens, H., Holtz, F. & Lange, R. A. The influence of pressure and composition on the viscosity of andesitic melts. *Geochim. Cosmochim. Acta* 67, 473–485 (2003).
- Fanesi, E. et al. A review of the differential scanning calorimetry shift–factor approach: Application to Colli Albani melt viscosity and implications for mafic Plinian eruptions. J. Volcanol. Geotherm. Res. 461, 108276 (2025).
- 24. Zellmer, G. F. et al. Inferring the effects of compositional boundary layers on crystal nucleation, growth textures, and mineral chemistry in natural volcanic tephras through submicron-resolution imaging. *Front. Earth Sci.* **4**, 1–7 (2016).
- Di Genova, D. et al. A compositional tipping point governing the mobilization and eruption style of rhyolitic magma. *Nature* 552, 235–238 (2017).
- Eichheimer, P. et al. Combined numerical and experimental study of microstructure and permeability in porous granular media. Solid Earth Discuss. 1–25 https://doi.org/10.5194/se-2019-199 (2020).
- Knafelc, J. et al. Havre 2012 pink pumice is evidence of a short-lived, deep-sea, magnetite nanolite-driven explosive eruption. Commun. Earth Environ. 3, 1–11 (2022).
- Barone, G. et al. Nanoscale surface modification of Mt. Etna volcanic ashes. Geochim. Cosmochim. Acta 174, 70–84 (2016).
- Mujin, M. & Nakamura, M. A nanolite record of eruption style transition. Geology 42, 611–614 (2014).
- Yoshida, K. et al. Oxidation-induced nanolite crystallization triggered the 2021 eruption of Fukutoku-Oka-no-Ba. *Japan. Sci. Rep.* 13, 7117 (2023).
- Sharp, T. G., Stevenson, R. J. & Dingwell, D. B. Microlites and 'nanolites' in rhyolitic glass: Microstructural and chemical characterization. *Bull. Volcanol.* 57, 631–640 (1996).
- Mujin, M. & Nakamura, M. Late-stage groundmass differentiation as a record of magma stagnation, fragmentation, and rewelding. *Bull.* Volcanol. 82 (2020).

- Cáceres, F. et al. Oxide nanolitisation-induced melt iron extraction causes viscosity jumps and enhanced explosivity in silicic magma. Nat. Commun. 15 (2024).
- Pereira, L. et al. The rheological response of magma to nanolitisation. J. Volcanol. Geotherm. Res. 448, 108039 (2024).
- Di Genova, D. et al. In situ observation of nanolite growth in volcanic melt: A driving force for explosive eruptions. Sci. Adv. 6, (2020).
- Cáceres, F. et al. Can nanolites enhance eruption explosivity?.
 Geology 48, 997–1001 (2020).
- Mujin, M., Nakamura, M. & Miyake, A. Eruption style and crystal size distributions: Crystallization of groundmass nanolites in the 2011 Shinmoedake eruption. *Am. Mineral.* 102, 2367–2380 (2017).
- Di Genova, D., Caracciolo, A. & Kolzenburg, S. Measuring the degree of "nanotilization" of volcanic glasses: Understanding syn-eruptive processes recorded in melt inclusions. *Lithos* 318–319, 209–218 (2018).
- 39. Giordano, D., Russell, J. K. & Dingwell, D. B. Viscosity of magmatic liquids: A model. *Earth Planet. Sci. Lett.* **271**, 123–134 (2008).
- Di Genova, D., Zandona, A. & Deubener, J. Unravelling the effect of nano-heterogeneity on the viscosity of silicate melts: Implications for glass manufacturing and volcanic eruptions. *J. Non. Cryst. Solids* 545, 120248 (2020).
- Bondar, D. et al. Nanolite Crystallization in Volcanic Glasses: Insights From High-Temperature Raman Spectroscopy and Low-Temperature Rock-Magnetic Analysis. Geochemistry, Geophys. Geosystems 26 (2025).
- Stabile, P. et al. The effect of iron and alkali on the nanocrystal-free viscosity of volcanic melts: A combined Raman spectroscopy and DSC study. Chem. Geol. 559, 119991 (2021).
- Shebanova, O. N. & Lazor, P. Raman spectroscopic study of magnetite (FeFe2O4): a new assignment for the vibrational spectrum. *J. Solid State Chem.* 174, 424–430 (2003).
- Jubb, A. M. & Allen, H. C. Vibrational Spectroscopic Characterization of Hematite, Maghemite, and Magnetite Thin Films Produced by Vapor Deposition. ACS Appl. Mater. Interfaces 2, 2804–2812 (2010).
- Zandonà, A. et al. Crystallization Mechanism of Gel-Derived SiO2-TiO2 Amorphous Nanobeads Elucidated by High-Temperature In Situ Experiments. Cryst. Growth Des. 23, 4545–4555 (2023).
- Deubener, J. et al. Updated definition of glass-ceramics. J. Non. Cryst. Solids 501, 3–10 (2018).
- Charles, R. J. Metastable Liquid Immiscibility in Alkali Metal Oxide–Silica Systems. J. Am. Ceram. Soc. 49, 55–62 (1966).
- Wechsler, B. A., Lindsley, D. H. & Prewitt, C. T. Crystal structure and cation distribution in titanomagnetites (Fe3-xTixO4). *Am. Mineral.* 69, 754–770 (1984).
- Zinin, P. et al. Raman spectroscopy of titanomagnetites: Calibration of the intensity of Raman peaks as a sensitive indicator for their Ti content. Am. Mineral. 96, 1537–1546 (2011).
- Cormier, L., Galoisy, L., Lelong, G. & Calas, G. From nanoscale heterogeneities to nanolites: cation clustering in glasses. *Comptes Rendus. Phys.* 24, 199–214 (2024).
- Thivet, S. et al. Metastable liquid immiscibility in the 2018–2021 Fani Maoré lavas as a mechanism for volcanic nanolite formation. Commun. Earth Environ. 4 (2023).
- Zandonà, A. et al. Non-stoichiometric crystal nucleation in a spodumene glass containing TiO2 as seed former: Effects on the viscosity of the residual melt. J. Non. Cryst. Solids 619, 122563 (2023).
- Langhammer, D., Di Genova, D. & Steinle-Neumann, G. Modeling the Viscosity of Anhydrous and Hydrous Volcanic Melts. Geochemistry, Geophys. Geosystems 22, 1–26 (2021).
- Mauro, J. C., Yue, Y., Ellison, A. J., Gupta, P. K. & Allan, D. C. Viscosity of glass-forming liquids. *Proc. Natl. Acad. Sci. USA.* 106, 19780–19784 (2009).

- 55. Araya, N. et al. Shallow magma pre-charge during repeated Plinian eruptions at Sakurajima volcano. *Sci. Rep.* **9**, 1–10 (2019).
- Scherrer, M. C., Hess, K., Fehr, K. T. & Dingwell, D. B. Oxidationstate dependence of rheology in peralkaline glasses of phonolitic composition. *Geophys. Res. Abstr.* 14, 5805 (2012).
- 57. Dingwell, D. B. Redox viscometry of some Fe-bearing silicate melts. *Am. Mineral.* **76**, 1560–1562 (1991).
- Okumura, S. et al. Rheology of nanocrystal-bearing andesite magma and its roles in explosive volcanism. *Commun. Earth Environ.* 3, 1–7 (2022).
- Singh, M. et al. Vapour phase approach for iron oxide nanoparticle synthesis from solid precursors. *J. Solid State Chem.* 200, 150–156 (2013).
- Koch, A. Neue Minerale aus dem Andesit des Aranyer Berges in Siebenbürgen. Mineral. und Petrogr. Mitteilungen 1, 331–361 (1878).
- Muthukumar, K. et al. Synthesis and characterization of magnetic copper-iron-titanate and uptake studies of americium from nuclear waste solutions. RSC Adv. 6, 111822–111830 (2016).
- Guo, C. & Zhang, Y. Multicomponent diffusion in silicate melts: SiO2-TiO2-Al2O3-MgO-CaO-Na2O-K2O System. Geochim. Cosmochim. Acta 195, 126-141 (2016).
- 63. Honour, V. C. et al. Compositional boundary layers trigger liquid unmixing in a basaltic crystal mush. *Nat. Commun.* **10** (2019).
- 64. Kleebusch, E., Patzig, C., Höche, T. & Rüssel, C. The evidence of phase separation droplets in the crystallization process of a Li2O-Al2O3-SiO2 glass with TiO2 as nucleating agent – An X-ray diffraction and (S)TEM-study supported by EDX-analysis. Ceram. Int. 44, 2919–2926 (2018).
- Raghuwanshi, V. S., Harizanova, R., Tatchev, D., Hoell, A. & Rüssel, C. Structural analysis of Fe-Mn-O nanoparticles in glass ceramics by small angle scattering. *J. Solid State Chem.* 222, 103–110 (2015).
- Fielitz, P., Helsch, G., Borchardt, G. & Deubener, J. Al-26 and O-18 tracer diffusion in a titania-coated sodium aluminosilicate glass. *J. Non. Cryst. Solids* 614, 122400 (2023).
- Narayanan, T. et al. Performance of the time-resolved ultra-smallangle X-ray scattering beamline with the Extremely Brilliant Source. J. Appl. Crystallogr. 55, 98–111 (2022).
- Cameron, M., Sueno, S., Prewitt, C. T. & Papike, J. J. High-Temperature crystal chemistry of acmite, diopside, hedenbergite, jadeite, spodumene, and Ureyite. *Am. Mineral.* 58, 594–618 (1973).
- Mader, H. M., Llewellin, E. W. & Mueller, S. P. The rheology of twophase magmas: A review and analysis. *J. Volcanol. Geotherm. Res.* 257, 135–158 (2013).
- Hess, P. C. Chapter 6. Thermodynamic Mixing Properties And The Structure Of Silicate Melts. in Structure, Dynamics, and Properties of Silicate Melts (eds. Stebbins, J. F., McMillan, P. F. & Dingwell, D. B.) 145–190. https://doi.org/10.1515/9781501509384-008 (De Gruyter, Berlin, Boston, 1995).
- Bouhifd, M. A., Richet, P., Besson, P., Roskosz, M. & Ingrin, J. Redox state, microstructure and viscosity of a partially crystallized basalt melt. *Earth Planet. Sci. Lett.* 218, 31–44 (2004).
- Chevrel, M. O., Giordano, D., Potuzak, M., Courtial, P. & Dingwell, D. B. Physical properties of CaAl2Si2O8-CaMgSi2O6-FeO-Fe2O3 melts: Analogues for extra-terrestrial basalt. *Chem. Geol.* 346, 93–105 (2013).
- Tuheen, M. I., Wilkins, M. C., McCloy, J. & Du, J. The structures of iron silicate glasses with varying iron redox ratios from molecular dynamics simulations and EXAFS analysis. *J. Non. Cryst. Solids* 624, 122713 (2024).
- Di Genova, D. et al. In situ observation of nanolite growth in volcanic melt:
 A driving force for explosive eruptions. Sci. Adv. 6, eabb0413 (2020).
- Mollo, S. & Hammer, J. E. Dynamic crystallization in magmas. Mineral reaction kinetics: Microstructures, textures, chemical and isotopic signatures vol. 16 0 at https://doi.org/10.1180/EMU-notes. 16.12 (2017).

- Di Fiore, F. et al. Magma titanium and iron contents dictate crystallization timescales and rheological behaviour in basaltic volcanic systems. Commun. Earth Environ. 5. (2024).
- Turner, M. B., Cronin, S. J., Bebbington, M. S., Smith, I. E. M. & Stewart, R. B. Relating magma composition to eruption variability at andesitic volcanoes: A case study from Mount Taranaki, New Zealand. *Bull. Geol. Soc. Am.* 123, 2005–2015 (2011).
- Dubosq, R. et al. Bubbles and atom clusters in rock melts: A chicken and egg problem. J. Volcanol. Geotherm. Res. 428, (2022).
- Kennedy, B. M., Jellinek, A. M., Russell, J. K., Nichols, A. R. L. & Vigouroux, N. Time- and temperature-dependent conduit wall porosity: A key control on degassing and explosivity at Tarawera volcano, New Zealand. *Earth Planet. Sci. Lett.* 299, 126–137 (2010).
- McBirney, A. R. Factors governing the intensity of explosive andesitic eruptions. *Bull. Volcanol.* 37, 443–453 (1973).
- 81. Hornby, A. J. et al. Nanoscale silicate melt textures determine volcanic ash surface chemistry. 1–10 (2024).
- Hughes, E. C. et al. Low analytical totals in EPMA of hydrous silicate glass due to sub-surface charging: obtaining accurate volatiles by difference. Chem. Geol. 505, 48–56 (2019).
- 83. Behrens, H. et al. Structural relaxation mechanisms in hydrous sodium borosilicate glasses. *J. Non. Cryst. Solids* **497**, 30–39 (2018).
- 84. Di Genova, D., Romano, C., Alletti, M., Misiti, V. & Scarlato, P. The effect of CO2 and H2O on Etna and Fondo Riccio (Phlegrean Fields) liquid viscosity, glass transition temperature and heat capacity. *Chem. Geol.* 377, 72–86 (2014).
- 85. Douglas, R. W., Armstrong, W. L., Edward, J. & Hall, D. A penetration viscometer. *Glas. Technol.* **6**, 52–55 (1965).
- Meerlender, G. Viskositäts-Temperaturverhalten des Standardglases I der DGG. Glas. Ber. 47, 1–3 (1974).
- Di Fiore, F. et al. Experimental insights on the shear-induced crystallization of a phonotephrite magma. *Chem. Geol.* 637, 121682 (2023).
- 88. Di Fiore, F., Vona, A., Costa, A., Mollo, S. & Romano, C. Quantifying the influence of cooling and shear rate on the disequilibrium rheology of a trachybasaltic melt from Mt. Etna. *Earth Planet. Sci. Lett.* **594**, 117725 (2022).
- 89. Al-Mukadam, R., Di Genova, D., Bornhöft, H. & Deubener, J. High rate calorimetry derived viscosity of oxide melts prone to crystallization. *J. Non. Cryst. Solids* **536**, 119992 (2020).
- Yue, Y. The iso-structural viscosity, configurational entropy and fragility of oxide liquids. J. Non. Cryst. Solids 355, 737–744 (2009).
- Zheng, Q., Mauro, J. C. & Yue, Y. Reconciling calorimetric and kinetic fragilities of glass-forming liquids. *J. Non. Cryst. Solids* 456, 95–100 (2017).
- Whitfield, C. H., Brody, E. M. & Bassett, W. Elastic moduli of NaCl by Brillouin scattering at high pressure in a diamond anvil cell. Rev. Sci. Instrum. 47, 942–947 (1976).
- Sinogeikin, S. et al. Brillouin spectrometer interfaced with synchrotron radiation for simultaneous x-ray density and acoustic velocity measurements. Rev. Sci. Instrum. 77 (2006).
- Prescher, C., McCammon, C. & Dubrovinsky, L. MossA: a program for analyzing energy-domain Mössbauer spectra from conventional and synchrotron sources. J. Appl. Crystallogr. 45, 329–331 (2012).
- Van Cappellen, E. & Doukhan, J. C. Quantitative transmission X-ray microanalysis of ionic compounds. Ultramicroscopy 53, 343–349 (1994).
- Van Cappellen, E. The parameterless correction method in X-ray microanalysis. *Microsc. Microanal. Microstruct.* 1, 1–22 (1990).
- Berg, S. et al. llastik: interactive machine learning for (Bio)Image analysis. Nat. Methods 16, 1226–1232 (2019).
- Angell, C. A. Formation of glasses from liquids and biopolymers. Science 267, 1924–1935 (1995).
- Cassetta, M. et al. Estimating the viscosity of volcanic melts from the vibrational properties of their parental glasses. Sci. Rep. 11, 1–14 (2021).

- Longo, A. et al. Dynamic role of gold d-orbitals during CO oxidation under aerobic conditions. ACS Catal. 12, 3615–3627 (2022).
- Maurizio, C. et al. Grazing-incidence small-angle X-ray scattering and X-ray diffraction from magnetic clusters obtained by Co + Ni sequential ion implantation in silica. *J. Appl. Crystallogr.* 36, 732–735 (2003).
- Jensen, H. et al. Determination of size distributions in nanosized powders by TEM, XRD, and SAXS. J. Exp. Nanosci. 1, 355–373 (2006).
- Jeffries, C. M. et al. Small-Angle X-Ray and Neutron Scattering. Nature Reviews Methods Primers vol. 1 (Springer US, 2021).
- Förster, S. et al. Scattering curves of ordered mesoscopic materials.
 J. Phys. Chem. B 109, 1347–1360 (2005).
- 105. Gumede, T. P., Luyt, A. S., Pérez-Camargo, R. A., Tercjak, A. & Müller, A. J. Morphology, nucleation, and isothermal crystallization kinetics of Poly(Butylene Succinate) mixed with a polycarbonate/MWCNT masterbatch. *Polymers (Basel)*. 10, 1–22 (2018).
- Arzilli, F. et al. Characterization of nanocrystals in volcanic glass. https://doi.org/10.15151/ESRF-ES-1734554218.
- Prata, G. S. et al. A new parameterization of volcanic ash complex refractive index based on NBO/T and SiO₂ content. *J. Geophys. Res. Atmos.* 124, 1779–1797 (2019).

Acknowledgements

Pedro Valdivia (P.V.) and Danilo Di Genova (D.D.G.) acknowledge the funding by Deutsche Forschungsgemeinschaft (DFG) project DI 2751/2-1. D.D.G. acknowledges the funding from the European Research Council (ERC) under the European Union's Horizon 2020 research and innovation programme (NANOVOLC, ERC Consolidator Grant - No. 101044772). D.D.G. acknowledges funding by MUR-PRIN Project (CRYSTALIKIN, 2022L2APNR). This project has benefited from the expertise and facilities of the Platform MACLE-CVL, which has been co-funded by the European Union and the Centre-Val de Loire Region (FEDER). Joachim Deubener acknowledges DFG for financial support via the grant DE 598/33-1. The Scios FIB and the Titan G2 STEM at Baverisches Geoinstitut were financed by DFG Grants INST 91/315-1 FUGG and INST 91/251-1 FUGG, respectively. Mathieu Allix and Cécile Genevois acknowledge funding from the Agence Nationale de la Recherche (ANR) through project ANR-23-CE08-0013-01. Claudia Romano and Alessandro Vona acknowledge funding by MUR-PRIN Project P20222BP7J. We acknowledge the European Synchrotron Radiation Facility (ESRF) for provision of synchrotron radiation facilities under proposal number ES-1474¹⁰⁶ and we would like to thank Peter Boesecke for assistance and support in using beamline ID02. We thank Alexander Rother and Raphael Njul for sample preparation, Dorothea Wiesner for the FIB lamella preparation and Catherine McCammon for facilitating the Mössbauer facilities at the Bayerisches Geoinstitut. We thank Adrian Hornby and all other reviewers for their constructive feedback and continuous contributions throughout the review process.

Author contributions

Pedro Valdivia (P.V.) drafted the original manuscript, synthesized the starting materials, processed the experimental data, performed the data analyses, derived the viscosity models, conducted Mössbauer experiments and constructed the figures and tables. P.V., Alessio Zandonà (A.Z.) and Danilo Di Genova (D.D.G.) conceptualized the original idea. A.Z. and Cécile Genevois carried out the in situ high-temperature TEM experiments. Dmitry Bondar and Aurélien Canizarès performed the high-temperature Raman measurements. P.V., Jessica Löschmann and D.D.G. conducted micropenetration, room-temperature Raman and calorimetry analyses. P.V. and Nobuyoshi Miyajima executed the room-temperature TEM. P.V. and Fabrizio Di Fiore carried out concentric cylinder measurements. P.V., Alexander Kurnosov and Tiziana Boffa Ballaran performed the Brillouin analyses. Joachim Deubener, Claudia Romano, Alessandro Vona and Mathieu Allix facilitated laboratory access and instrument availability. P.V., A.Z., Emily C. Bamber and D.D.G. revised the manuscript following peer review. D.D.G.

and Alessandro Longo processed SAXS/WAXS data. All co-authors provided feedback and contributed to the final version of the manuscript.

Funding

Open Access funding enabled and organized by Projekt DEAL.

Competing interests

The authors declare no competing interests.

Additional information

Supplementary information The online version contains supplementary material available at https://doi.org/10.1038/s43247-025-02424-9.

Correspondence and requests for materials should be addressed to Pedro Valdivia.

Peer review information Communications Earth & Environment thanks Adrian Hornby and the other, anonymous, reviewer(s) for their contribution to the peer review of this work. Primary Handling Editor: Carolina Ortiz Guerrero. A peer review file is available.

Reprints and permissions information is available at http://www.nature.com/reprints

Publisher's note Springer Nature remains neutral with regard to jurisdictional claims in published maps and institutional affiliations.

Open Access This article is licensed under a Creative Commons Attribution 4.0 International License, which permits use, sharing, adaptation, distribution and reproduction in any medium or format, as long as you give appropriate credit to the original author(s) and the source, provide a link to the Creative Commons licence, and indicate if changes were made. The images or other third party material in this article are included in the article's Creative Commons licence, unless indicated otherwise in a credit line to the material. If material is not included in the article's Creative Commons licence and your intended use is not permitted by statutory regulation or exceeds the permitted use, you will need to obtain permission directly from the copyright holder. To view a copy of this licence, visit http://creativecommons.org/licenses/by/4.0/.

© The Author(s) 2025

Nanoscale chemical heterogeneities control the viscosity of andesitic magmas

Supplementary Information

Pedro Valdivia^{1,2}*, Alessio Zandonà³, Jessica Löschmann³, Dmitry Bondar^{1,2}, Cécile Genevois⁴, Aurélien Canizarès⁴, Mathieu Allix⁴, Nobuyoshi Miyajima¹, Alexander Kurnosov¹, Tiziana Boffa Ballaran¹, Fabrizio Di Fiore⁵, Alessandro Vona⁶, Claudia Romano⁶, Joachim Deubener³, Emily C. Bamber^{2,7}, Alessandro Longo⁸, Danilo Di Genova²

¹Bayerisches Geoinstitut, University of Bayreuth, Universitätsstraße 30, 95447, Bayreuth, Germany ²Institute of Science, Technology and Sustainability for Ceramics (ISSMC) of the National Research Council (CNR), Via Granarolo 64, I-48018, Faenza, RA, Italy

³Institute of Non-Metallic Materials, Clausthal University of Technology, Zehntnerstraße 2a, D-38678 Clausthal-Zellerfeld, Germany

⁴CNRS, CEMHTI UPR3079, Univ. Orléans, France.

⁵Istituto Nazionale di Geofisica e Vulcanologia, Sezione Roma 1, Via di Vigna Murata 605, 00143 Rome, Italy ⁶Dipartimento di Scienze, Università degli Studi Roma Tre, Largo San L. Murialdo 1, 00146 Rome, Italy ⁷Department of Earth Sciences, University of Turin, Via Valperga Caluso, 35, 10125 Turin, Italy ⁸ESRF - The European Synchrotron, 38043 Cedex 9 Grenoble, France

*Corresponding author: pedro.valdivia-munoz@uni-bayreuth.de

Supplementary Preliminary characterization

In Supplementary Table 1, we present microprobe chemical analysis results of our samples, alongside chemistry data from relevant literature^{1–5}, calculated NBO/T for each sample⁶, Brillouin and Mössbauer spectroscopy results. Our chemical analysis results affirm that the composition of AND100 (SiO₂ = 60.38 wt%; NBO/T=0.34) closely aligns, considering experimental uncertainties, with previous andesites reported in the literature^{1,2,5}. We also confirm that samples AND100ox (retrieved after concentric-cylinder viscometry) and AND100red (melted under reductive conditions) are virtually identical to that of AND100. Moreover, we achieved the synthesis of a transition-metal-free analogue (AND0, SiO₂ = 65.91 wt%; NBO/T=0.16), which is meant to represent the complete removal of iron (FeO_{tot}), titanium (TiO₂), and manganese (MnO) from sample AND100. Lastly, we successfully produced an intermediate glass AND65 (SiO₂ = 62.65 wt%; NBO/T=0.27), designed to contain 65% of the total transition metal contained in AND100.

Mössbauer results reveal Fe^{3+}/Fe_{tot} ratios of 0.27, 0.64 and 0.70 for as-synthesized AND100red, AND100 and AND65 glasses, respectively (Supplementary Table 1). The Fe^{3+}/Fe_{tot} ratio of AND100ox ($Fe^{3+}/Fe_{tot} = 0.71$) was slightly higher than AND100, revealing that concentric cylinder (CC) viscometry measurements induced a non-negligible iron oxidation.

0 614	.017		
no materi		0	
ctort	3177		
tore of	5000		
1001 - 1/2	3		
77. 9110			
moho chomictm	111121	•	
0	2		
1010101			
Portron			
1			
0			
	- -	•	
nomonic		•	
2			
•	2		

	SiO_2	TiO ₂	Al ₂ O ₃	FeOtot	MnO	MgO	CaO	Na ₂ O	K ₂ O	P ₂ O5	$Fe^{3+}/\!$	NBO/Tb	K/G°
$AND100^d$	60.38 (0.36)	0.79 (0.04)	16.69 (0.18)	6.77 (0.12)	0.17 (0.03)	3.00 (0.07)	6.62 (0.09)	3.50 (0.15)	1.58 (0.07)	0.18 (0.05)	0.64	0.34	1.56 (0.02)
$AND100red^d$	60.47 (0.40)	0.80 (0.07)	16.83 (0.22)	6.87 (0.12)	0.18 (0.04)	2.94 (0.06)	6.51 (0.11)	3.46 (0.10)	1.65 (0.07)	0.18 (0.05)	0.27	0.34	1.57 (0.02)
$AND100ox^d$	60.56 (0.35)	0.81 (0.06)	16.79 (0.19)	6.76 (0.15)	0.18 (0.03)	2.95 (0.06)	6.49 (0.11)	3.40 (0.10)	1.66 (0.06)	0.18 (0.05)	0.71	0.34	1.58 (0.02)
AND65 ^d	62.52 (0.19)	0.56 (0.04)	17.28 (0.22)	4.40 (0.11)	0.11 (0.03)	3.02 (0.07)	6.76 (0.13)	3.49 (0.11)	1.70 (0.05)	0.16 (0.05)	0.70	0.27	1.53 (0.02)
$AND0^d$	65.91 (0.34)	0.04 (0.03)	18.01 (0.11)	0.04 (0.03)	0.01 (0.01)	3.21 (0.06)	7.26 (0.11)	3.82 (0.14)	1.75 (0.06)	0.04 (0.03)	1	0.16	1.48 (0.02)
And	61.47 (0.26)	0.81 (0.14)	16.25 (0.15)	6.76 (0.19)	0.14 (0.13)	2.78 (0.09)	6.53 (0.09)	3.54 (0.08)	1.61 (0.05)	0.11 (0.08)	1	0.34	ı
$ m MST^{f}$	60.71	0.58	18.29	6.38	0.19	2.58	7.1	3.57	0.85	ı	1	0.29	ı
$AndU^g$	56.65 (0.41)	1.01 (0.04)	17.41 (0.15)	8.16 (0.21)	0.13 (0.04)	4.30 (0.07)	7.38 (0.11)	3.23 (0.15)	1.56 (0.07)	ı	0.33-0.57	0.44	1
iron-free AndU ^g	58.69 (0.33)	0.01 (0.01)	21.57 (0.33)	0.02 (0.03)	0.02 (0.02)	5.38 (0.10)	9.49 (0.18)	3.30 (0.10)	1.57 (0.12)		1	0.23	ı
$ME13IIe^{h}$	59.70	0.52	18.30	7.58	0.20	2.59	7.21	3.44	06.0	0.17		0.33	
Andesite ^h	62.40 (0.69)	0.55 (0.02)	20.01 (0.11)	0.03 (0.03)	0.02 (0.03)	3.22 (0.05)	9.08 (0.14)	3.52 (0.07)	0.93 (0.05)	0.12 (0.03)	1	0.16	1
Andesitei	61.17 (0.15)	0.84 (0.02)	17.29 (0.05)	5.39 (0.19)	1	3.35 (0.05)	5.83 (0.05)	3.85 (0.06)	1.39 (0.02)	1		0.30	,

Parentheses represent $\pm 1\sigma$.

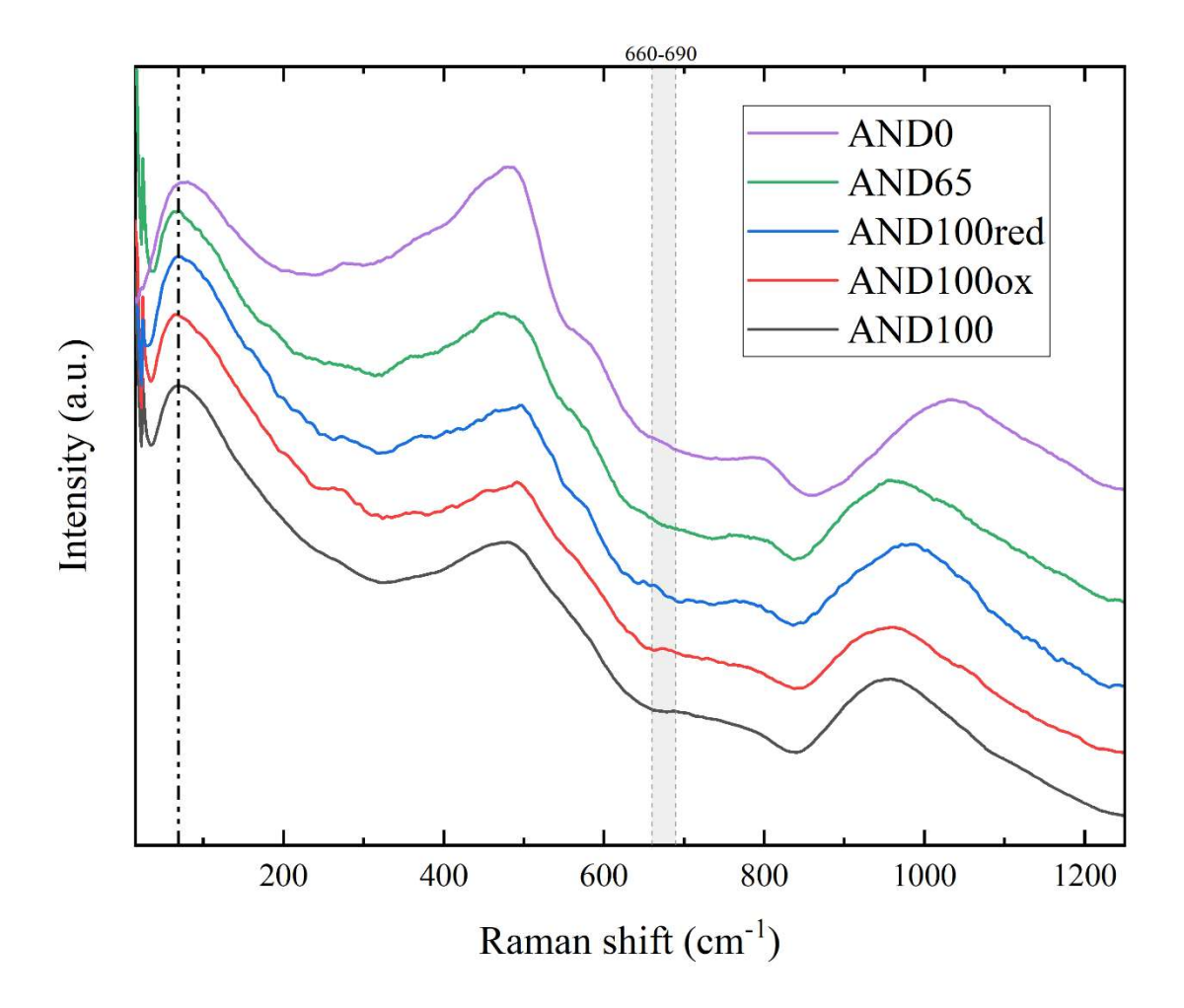
^aRatios derived using Mossa software ⁷.

^bNBO/T values were calculated using a supporting spreadsheet reported by Prata et al. (2019).

^cValues derived using Brillouin spectroscopy data and Eq. 4.

^dThis study. ^eOkumura et al. (2022). ^fGiordano et al. (2006). ^gLiebske et al. (2003). ^hRichet et al. (1996). ⁱNeuville et al. (1993).

To verify the amorphous nature of all these specimens, we combined scanning electron microscopy (SEM) imaging, in backscattered electron (BSE) mode, with Raman spectroscopy analysis. While SEM imaging verified the absence of bubbles and micro-sized crystals, our Raman results (Supplementary Fig. 1) showed that all our starting glasses are amorphous and are in good agreement with previously reported Raman spectra for similar compositions^{8,9}. This conclusion is drawn from the absence of characteristic features in the 660-690 cm⁻¹ range, which were previously linked to the presence of Fe-Ti-oxide nanolites 10-13. However, we acknowledge that this methodology may not fully resolve the nanoscale differences between amorphous nanoheterogeneities (such as minor elemental segregation) and proto-nanolites. For example, we notice a minor (almost negligible) peak for samples AND100red and AND100ox within the 660-690 cm⁻¹ range (Supplementary Fig. 1). Nevertheless, the Boson peak position^{15,21,22} of these samples (70 cm⁻¹) is in good agreement with the Boson peak position of AND100, suggesting that all these starting materials were completely amorphous and crystal-free. The Boson peak, which is located below 100 cm⁻¹, serves as a distinctive marker for the intrinsic disorder within the system and is associated with the collective atomic motions, especially acoustic phonons, arising from the shortto-medium range order of glasses 15,21,22. Our study offers a practical approach, utilizing SEM and Raman spectroscopy as preliminary tools to confirm the absence of nanolites.



Supplementary Figure 1. **Raman spectra of glassy samples before the experiments**. The shaded area in grey (660-690 cm⁻¹) corresponds to the most prominent area commonly affected by the presence of Fe-Ti-oxides^{11,14} and the dashed line (70 cm⁻¹) corresponds to the Boson peak^{15,21,22}.

Additionally, using sound velocities (v_p and v_s) from BLS measurements and Eq. 4, we calculated the K/G ratios for all five starting materials (Supplementary Table 1). The K/G ratios inversely correlate with the SiO₂ wt% of the glasses, in agreement with Cassetta et al.¹⁵. Notably, the measured K/G value of AND65 corresponds to an ideal mixing between its two compositional endmembers (AND100 and AND0).

Supplementary conventional differential scanning calorimetry (C-DSC)

Supplementary Table 2 lists the measured characteristic T_{onset} and T_{peak} , which are defined as characteristic temperatures related to phase transitions or thermal events observed during the heating or cooling of a sample, at various matching heating-cooling rates $(q_h = q_c)$ via C-DSC (10-20 °C min⁻¹) and F-DSC (1000-10000 °C s⁻¹). We observed that both T_{onset} and T_{peak} increase with increasing $q_h = q_c$ values (Supplementary Table 2). AND0 displays the highest T_{onset} (737 °C) and T_{peak} (782 °C) at a heating rate of 10 °C min⁻¹, while sample AND100red exhibits the lowest T_{onset} (645 °C) and T_{peak} (694 °C) under the same conditions. At the same heating rate, the T_{onset} and T_{peak} of AND100, AND100ox, and AND65 fall between AND0 and AND100red.

Supplementary Table 2. C-DSC, F-DSC, MP, and CC result as a function of temperature and post-experimental Mössbauer results.

Sample	Type ^a	<i>T</i> (°C)	$\log \eta \ (\eta \text{ in Pa s})^a$	Fe^{3+}/Fe_{tot}^{b}
AND100	$C\text{-}DSC_{10_on}$	654	11.98	0.12
	C-DSC_{10_pk}	715	10.62	0.12
	$C\text{-}DSC_{10bis_on}$	654	11.98	0.16
	$C\text{-}DSC_{10bis_pk}$	695	10.62	0.16
	C-DSC_{20_on}	675	11.68	0.05
	C-DSC_{20_pk}	724	10.32	0.05
	$F\text{-}DSC_{1000_on}$	796	8.20	-
	$F\text{-}DSC_{1000_pk}$	867	6.84	-
	$F\text{-}DSC_{10000_on_\#1}$	851	7.40	-
	$F\text{-}DSC_{10000_on_\#2}$	858	7.40	-
	$F\text{-}DSC_{10000_on_\#3}$	864	7.40	-
	$F\text{-}DSC_{10000_on_\#4}$	886	7.40	-
	$F\text{-}DSC_{10000_on_\#5}$	890	7.40	-
	MP_{660_0}	657	12.00	-
	MP_{660_90}	660	12.70	0.06
	MP_{723_0}	720	11.04	-
	MP_{723_60}	723	11.90	0.15
	MP_{808_0}	807	9.74	-
	MP_{808_60}	808	10.17	0.19
	CC	1435	2.03	
	CC	1405	2.19	
	CC	1355	2.45	-
	CC	1306	2.75	-
	CC	1255	3.09	-
	CC	1226	3.29	-
	CC	1206	3.44	-
	CC	1182	3.62	-
	CC	1152	3.87	-
AND100ox	C-DSC_{10_on}	662	11.98	0.02
	C-DSC_{10_pk}	702	10.62	0.02
AND100red	C-DSC _{10_on}	645	11.98	0.02
	C-DSC_{10_pk}	694	10.62	0.02

	$C ext{-}DSC_{20_pk}$	652	11.68	0.02
AND65	C-DSC_{10_on}	696	11.98	0.02
	$F\text{-}DSC_{1000_on}$	847	8.20	-
	$F\text{-}DSC_{1000_pk}$	929	6.84	-
	MP_{695}	695	12.13	0.03
	MP_{711}	711	11.66	0.01
	MP ₇₆₁	761	10.23	0.01
AND0	C-DSC_{10_on}	737	11.98	-
	$C ext{-}DSC_{10_pk}$	782	10.62	-
	C-DSC_{20_on}	747	11.68	-
	$C ext{-}DSC_{20_pk}$	792	10.32	-
	MP_{792}	792	10.43	-
	CC	1404	2.82	-
	CC	1355	3.11	-
	CC	1307	3.43	-
	CC	1256	3.79	-
	CC	1205	4.20	-
	CC	1179	4.42	-
	CC	1154	4.65	-
	CC	1130	4.91	-

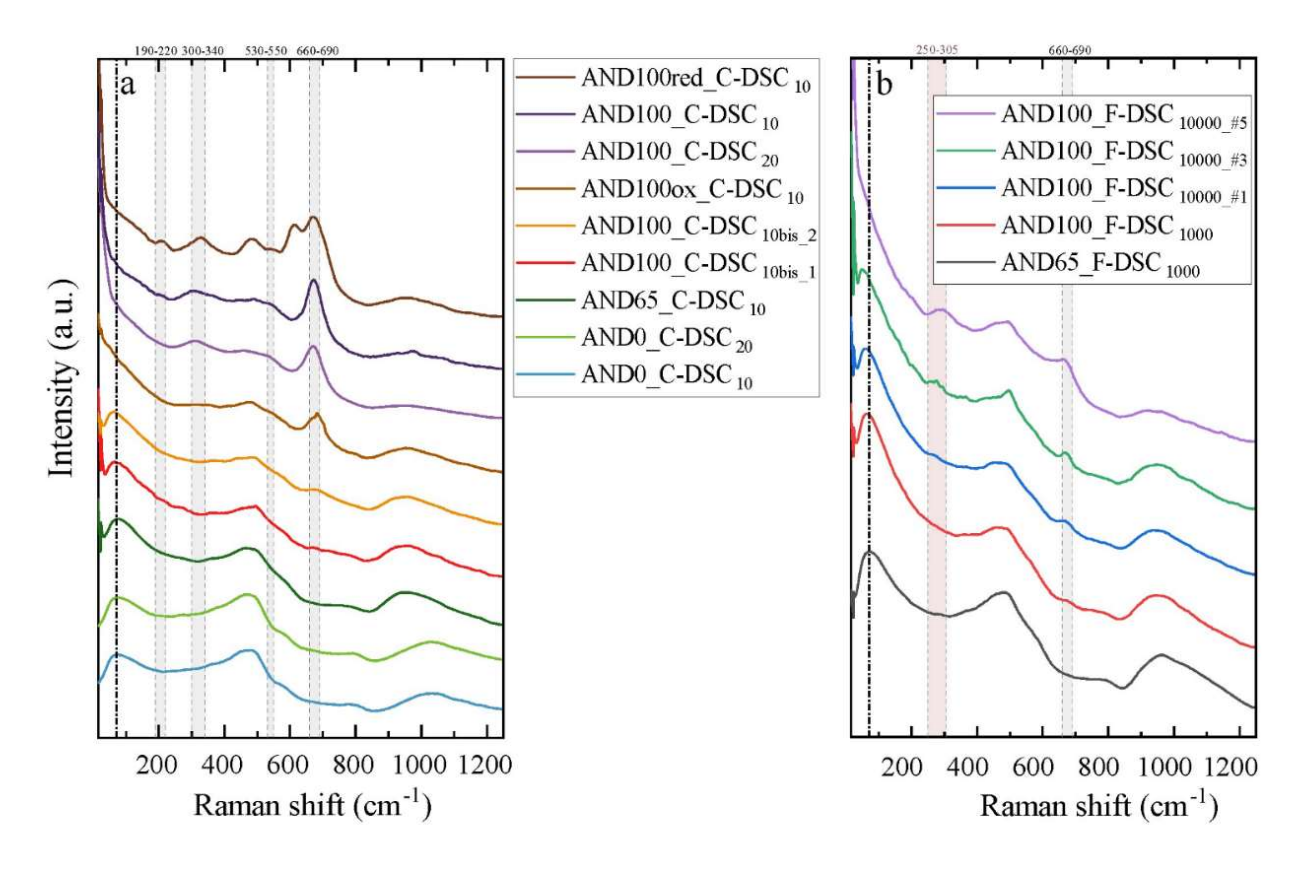
^aC- and F-DSC-type experiments are reported as DSC_{heating-rate thermal-event}, with heating rates expressed in °C min⁻¹ and °C s⁻¹, respectively. C- and F-DSC-derived viscosity values using Eq. 2 (main text). Thermal events are identified as on = T_{onset} and pk = T_{peak} with an error of ±0.5 °C for C-DSC experiments and ±1 °C for F-DSC experiments. F-DSC experiments at 10000 K s⁻¹ are numbered to show their relative positions in the series of measurements. Micropenetration (MP) data is reported as MP_{temperature duration}, with temperature expressed in °C and the duration in minutes. If time is not reported, the measurement remained constant within the experimental time, with an error of ±2 °C. Concentric Cylinder results with an error of ±2 °C.

Our C-DSC data suggest that T_{onset} increases with increasing SiO₂ content and decreasing FeO_{tot} content (Supplementary Table 1 and 2). Moreover, at a heating rate of 10 °C min⁻¹, we observe that T_{onset} of isochemical samples (i.e., AND100red, AND100, and AND100ox) increased with increasing initial Fe³⁺/Fe_{tot}, (Supplementary Table 1). Nevertheless, we did not observe the

^bDifference between Fe³⁺/Fe_{tot} after measurements and initial conditions from Supplementary Table 1. Ratios derived using Mossa software⁷. Mössbauer results have an associated error margin of 3%.

same trend when comparing the T_{peak} values of these three samples, as we obtained T_{peak} values of 694, 715 and 702 °C for AND100red, AND100, and AND100ox, respectively.

To assess potential sample crystallization and/or iron oxidation during the C-DSC heat treatments^{10–12,16–18} we conducted Mössbauer and Raman spectroscopy analyses on the recovered samples. For sample AND100, we observed an increase in ΔFe³⁺/Fe_{tot} by 0.12 and 0.16 following C-DSC measurements at 10 (AND100_C-DSC₁₀) and 20 °C min⁻¹ (AND100_C-DSC₂₀), respectively (Supplementary Table 2). On the other hand, Raman spectra of AND100_C-DSC₁₀ and AND100_C-DSC₂₀ displayed the development of noticeable peaks associated with titanomagnetite crystallization^{19,20} (Supplementary Fig. 2a), suggesting that nanocrystallization of Fe-Ti-oxide occurred during measurements. In addition, we noticed the total disappearance of their respective Boson peaks (Supplementary Fig. 2a).



Supplementary Figure 2. Raman spectra of samples after DSC measurements. a After C-DSC measurements. b Raman spectra of the same AND100 sample after a series of F-DSC measurements. The shaded area in grey corresponds to Raman peaks for titanomagnetite ^{19,20}. The shaded area in red corresponds to one Raman peak for hematite ²⁰.

Consistent with recent literature 10,16,18 , our findings indicate that C-DSC experiments have the potential to induce structural modifications (including nanocrystallization) and alter the iron oxidation state within the sample, particularly when the temperature exceeds T_{onset} at the end of the heating segments. To mitigate temperature overshoot after reaching their respective T_{onset} , and to explore the possible changes during heating, we conducted a conservative C-DSC experiment on sample AND100 (AND100_C-DSC_{10bis}) dividing it into two steps: (1) the first upscan was performed as usual but halted after the matching cooling segment with $q_c = -10$ °C min⁻¹ and (2) using the same sample, we completed the matching C-DSC measurement with $q_h = 10$ °C min⁻¹. Mössbauer and Raman spectroscopy were carried out after steps 1 and 2 to detect potential

modifications in each segment. Mössbauer results show that sample AND100 did not experience iron oxidation after step 1 (C-DSC_{10bis_1}) but showed a slight increase in Fe³⁺/Fe_{tot} after step 2 (C-DSC_{10bis_2}), from 0.64 to 0.69 (Supplementary Table 2). Similarly, Raman spectroscopy results (Supplementary Fig. 2a) suggest no changes after step 1, while the Raman spectrum collected after step 2 shows a new and weak contribution around 660–690 cm⁻¹, and a Boson peak shift from 70 to 63 cm⁻¹ (Supplementary Fig. 2a). After this run, we obtained T_{onset} and T_{peak} values of 654 and 694 °C, respectively (Supplementary Table 2). We notice a significant decrease in the T_{peak} , from 715 (AND100_C-DSC_{10_pk}) to 695 °C (AND100_C-DSC_{10bis_pk}). After this run, we observe only a slight oxidation of iron, in addition to a weak contribution in the 660-690 cm⁻¹ Raman range. Furthermore, we infer that the most accurate C-DSC results for the AND100 composition are those obtained after AND100_DSC10_{bis} which was the sample that displayed the fewest changes after the measurement.

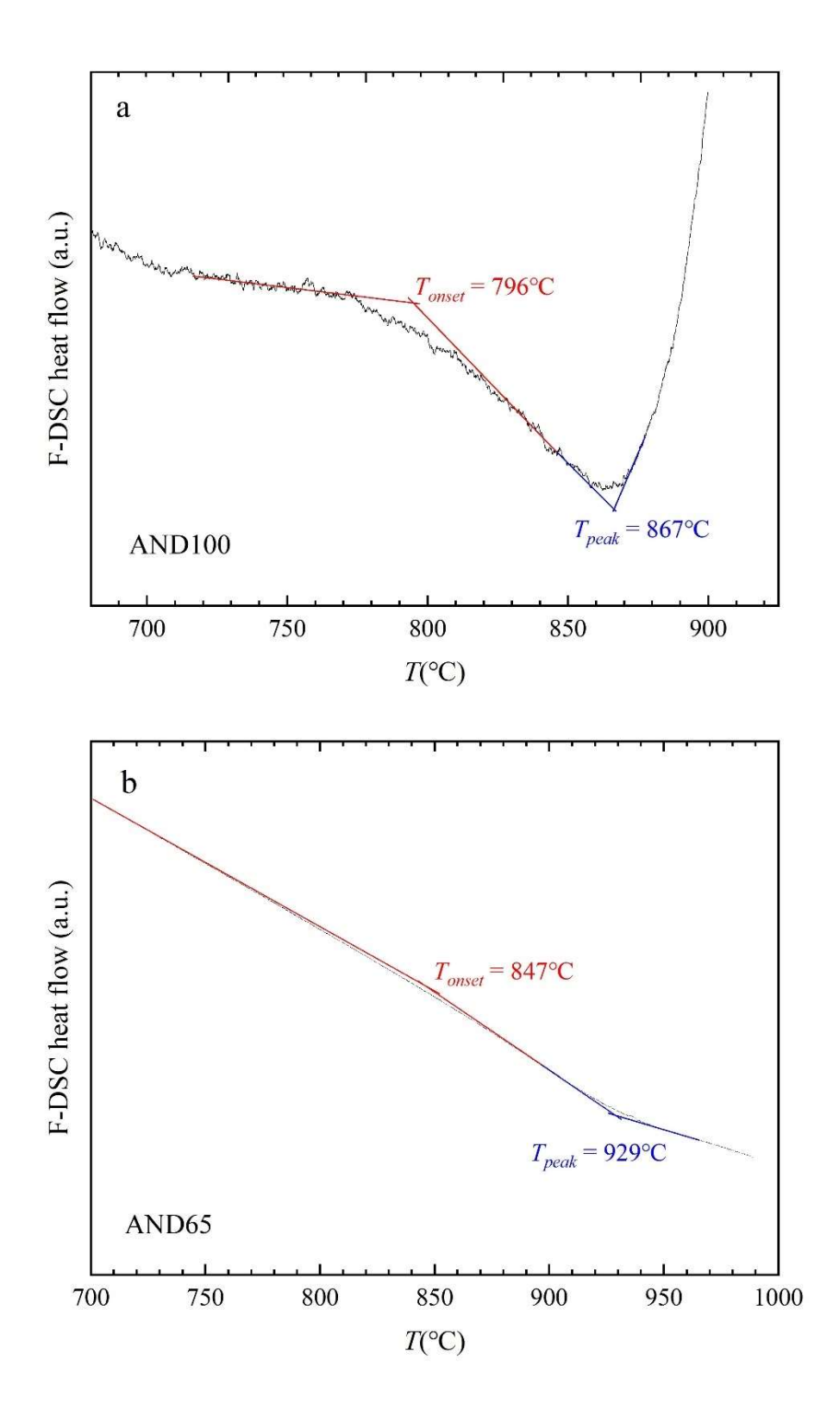
For both samples AND100red and AND100ox, Mössbauer results indicated a minor alteration, within error, in the iron oxidation following C-DSC experiments at 10 °C min⁻¹, with ΔFe³⁺/Fe_{tot} equal to 0.02 (Supplementary Table 2). In contrast, Raman spectroscopy results suggest that both samples developed prominent peaks within the 660–690 cm⁻¹ range after C-DSC measurements, accompanied by the complete shift of the Boson peak under the Rayleigh line (Supplementary Fig. 2a). On the other hand, samples AND65 and AND0 did not display significant changes following C-DSC experiments, as indicated by both Mössbauer and Raman results (Supplementary Table 2 and Supplementary Fig. 2a).

Using our T_{onset} measurements at 10 °C min⁻¹ and Eq. 2 (main text, Materials and Methods), we derived C-DSC-based glass transition temperature T_g ($\eta \sim 10^{12}$ Pa s) values of 645, 654, 662, 696 and 737 °C (±0.5 °C) for samples AND100red, AND100, AND100ox, AND65, and AND0,

respectively. All in all, we argue that C-DSC measurements performed at T_g remained virtually unaffected by potential nanocrystallization and/or iron oxidation, especially when employing a conservative temperature treatment during the first upscan, as evidenced by the congruent T_{onset} values of AND100_C-DSC₁₀ and AND100_C-DSC_{10bis}, in contrast to the considerable different T_{peak} values of 715 vs 695 °C (±0.5 °C), respectively. By applying Eq. 2 (main text, Materials and Methods), we associated our characteristic T_{onset} and T_{peak} from our C-DSC measurements, which are dependent on $q_h = q_c$, to viscosity values (Supplementary Table 2).

Supplementary Flash differential scanning calorimetry (F-DSC)

F-DSC measurements of AND100 and AND65 using a heating rate of 1000 °C s⁻¹ resulted in T_{onset} values of 796±1 and 847±1 °C, and T_{peak} values of 867±1 and 929±1 °C, respectively (Supplementary Fig. 3; Supplementary Table 2). We observe that F-DSC T_{onset} and T_{peak} increased with increasing SiO₂ and decreasing FeO_{tot} content, in good agreement with our previous C-DSC results. Additionally, we performed a subsequent series of measurements on the same sample AND100 used before but increasing the heating rate from 1000 to 10000 °C s⁻¹. Our results evidenced a sustained increase in T_{onset} , from 851±1 (F-DSC_{10000_on_#1}) to 890±1 °C (F-DSC_{10000_on_#5}) (Supplementary Table 2).



Supplementary Figure 3. **F-DSC results**. a AND100 b AND65 using $q_h = q_c = 1000$ °C s⁻¹.

The collected Raman spectra after F-DSC measurement suggested that sample AND100 underwent minimal changes after the first measurement at 1000 °C s⁻¹, manifesting a subtle contribution within the 660–690 cm⁻¹ range and a shift in the Boson peak from 70 to 64 cm⁻¹ (Fig 4b). In contrast, sample AND65 did not show any changes after the F-DSC measurement using the same conditions. Noticeably, the collected Raman spectra of AND100 at 10000 °C s⁻¹ showed a progressive increase in the 660–690 cm⁻¹ range, alongside a continuous shift of the Boson peak towards lower wavenumbers until the complete disappearance after the last run (F-DSC_{1000_#5}; Fig 3b). Moreover, we noted the appearance and gradual strengthening of a new Raman contribution within the 250-305 cm⁻¹ range (highlighted in red in Supplementary Fig. 3b) following the measurement of F-DSC_{10000_on_#1}. This peak is likely associated with the formation of hematite²⁰, possibly arising from the oxidation of previously crystallized titanomagnetite nanolites during the F-DSC experiments. Finally, by applying Eq. 2 (main text, Materials and Methods section), we evaluated viscosity values to our characteristic *T*_{onset} and *T*_{peak} from our F-DSC measurements (Supplementary Table 2).

Supplementary Micropenetration (MP)

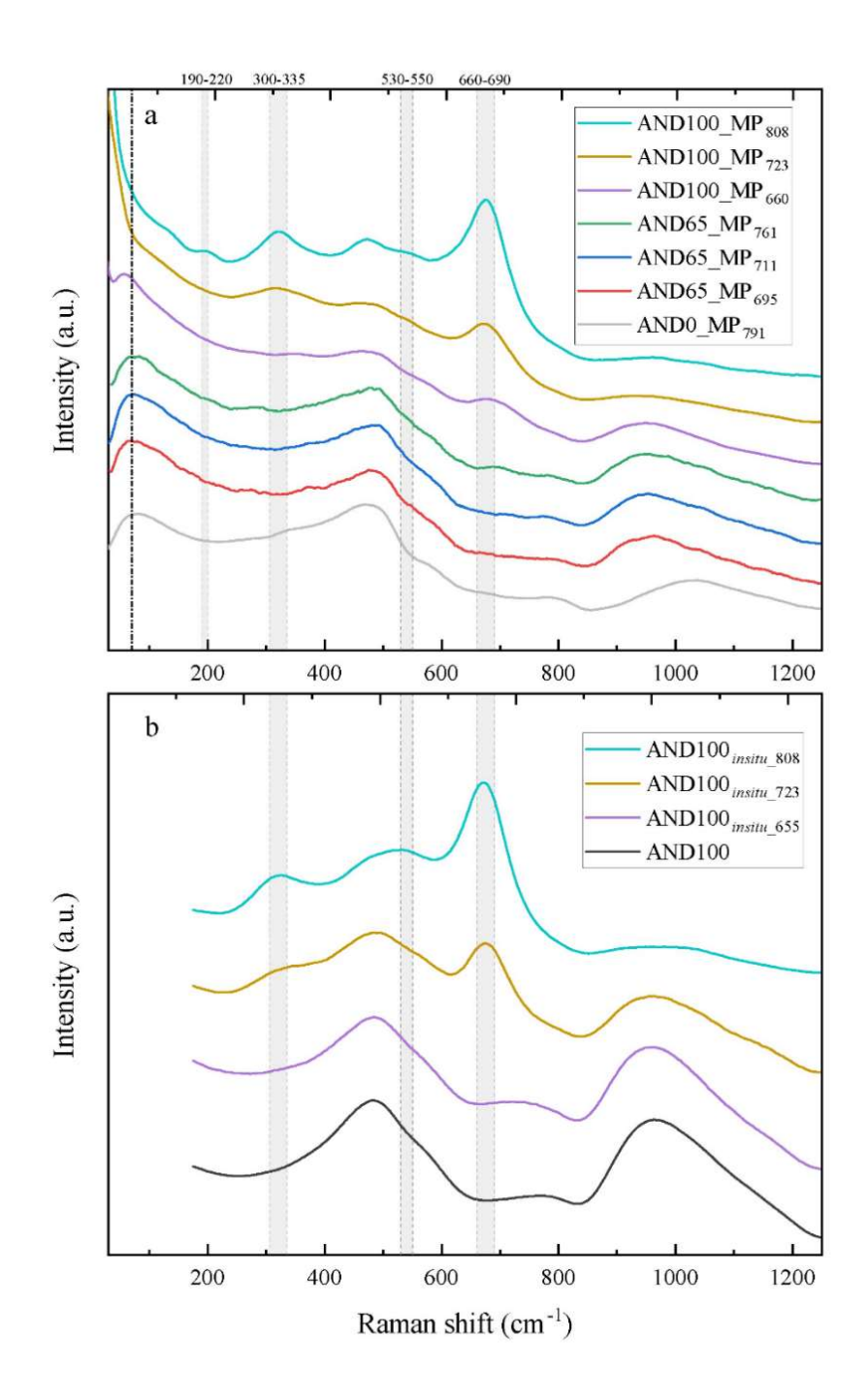
Micropenetration viscometry results are reported in Supplementary Table 2 as a function of temperature and experimental duration. To account for the applicability of the shift factor method (Eq. 1) for our sample compositions, we measured the viscosity of samples AND0, AND65 and AND100 at temperatures relative to our previous C-DSC measurements. For AND0, we explored the highest characteristic temperature derived via C-DSC (792 °C), which corresponds to the C-DSC_{20-pk} temperature. For AND65, we employed the T_g (C-DSC_{10-on}, 696 °C) and two additional temperatures: $T_g + 15$ °C (711 °C) and $T_g + 65$ °C (761 °C). For AND100, we selected

the retrieved T_g (C-DSC_{10_on}, 654 °C) and C-DSC_{20_pk} (724 °C) temperatures. In addition, we measured the viscosity at 808 °C which corresponds to the maximum temperature employed by Okumura et al. ¹ for a similar andesitic melt ("Ande" in Supplementary Table 1).

Micropenetration results (Supplementary Table 2) showed that viscosity decreases with increasing temperature and that sample AND0 is the most viscous composition, followed by AND65 and then AND100, respectively. For AND0, we measured a viscosity of $10^{10.43}$ Pa s at 792 °C. For AND65, we recorded viscosities of $10^{12.13}$, $10^{10.23}$ and $10^{11.66}$ Pa s at 696, 711 and 761 °C, respectively. Notably, for sample AND100, we observed a time-dependent increase in viscosity at fixed temperatures. For instance, the viscosity of AND100 at 658.5 ± 1.5 °C increased from 10^{12} to $10^{12.7}$ Pa s in 60 minutes. At 723 ± 1.5 °C, we observed an increase from $10^{11.04}$ to $10^{11.90}$ Pa over 90 minutes. Finally, at 807 ± 0.5 °C, we recorded an increase from $10^{9.74}$ to $10^{10.17}$ Pa s in 60 minutes, exhibiting a similar viscosity increase as the one reported by Okumura et al. 1 at the same temperature (namely, $\sim 0.5 \log_{10}$ units).

Following Eq. 2, we expected to measure a viscosity of $\sim 10^{12}$ Pa s for measurements performed at the calorimetric T_g (C-DSC_{10-on}) and $\sim 10^{10.3}$ Pa s for measurements close to the C-DSC_{20-peak} temperature. This was found to be the case for samples AND0 and AND65 where viscosity did not increase over time within the experimental timescale. Nonetheless, in the case of AND100, our observations indicate that only the initially recorded viscosity in proximity to the calorimetric T_g corresponds to the anticipated C-DSC-derived viscosity (AND100_MP_{660_0}). It is important to mention that the good agreement between our nanolite-free DSC-derived viscosity data with our nanolite-free micropenetration data confirms that the shift factor approach (Eq. 2) is valid for our compositions.

Following the micropenetration measurements, all our samples underwent subsequent Mössbauer and Raman analyses. Mössbauer and Raman results of post-micropenetration AND65 and AND0 experiments show no evidence of relevant modifications during measurements (Supplementary Table 2, Supplementary Fig. 4). In contrast, Mössbauer results evidence that samples AND100 MP₆₆₀, AND100 MP₇₂₃ and AND100 MP₈₀₈ underwent a significant change in Fe³⁺/Fe_{tot}, namely from Fe³⁺/Fe_{tot} of 0.64 to 0.70, 0.79 and 0.83 respectively (Supplementary Table 2). Likewise, these samples exhibited notable development of Raman peaks within the 660– 690 cm⁻¹ range (Supplementary Fig. 4a), suggesting Fe-Ti-oxide nanocrystallization^{10,11}. Moreover, samples AND100 MP₇₂₃ and AND100 MP₈₀₈ developed two additional Raman peaks in the 305-335 and 530-550 cm⁻¹ ranges (Supplementary Fig. 4a). Additionally, sample AND100 MP₈₀₈ developed a fourth peak in the 190-200 cm⁻¹ range (Supplementary Fig. 4a). We notice that these four peaks perfectly match with four of the five theoretically predicted phonon bands of titanomagnetite^{19,20}. In addition, we noted that the Boson peak position of sample AND100 MP₆₆₀ shifted from 70 to 57 cm⁻¹, while for samples AND100 MP₇₂₃ and AND100 MP₈₀₈, the Boson peaks completely disappeared after micropenetration experiments. Importantly, we observed a direct correlation between the degree of iron oxidation and nanocrystallization and the experimental temperature. Specifically, samples that deviated further from T_g exhibited more pronounced changes during the measurements.



Supplementary Figure 4. Raman spectra after high-temperature experiments. a Post-micropenetration measurements. The numeric suffixes correspond to the experimental temperature. b Raman spectra of AND100 after in situ Raman experiments. The shaded area in grey corresponds to Raman peaks for titanomagnetite 19,20. Sample names are reported in the text according to the scheme SampleName_{experiment_temperature}, with temperature representing the final experimental temperature expressed in °C.

Supplementary Post-insitu Raman

We conducted room-temperature Raman measurements after in-situ high-temperature Raman experiments. Figure 4 shows a comparison between room-temperature Raman spectra after micropenetration measurements and Raman spectra after in situ Raman experiments. At a given temperature, we observe that post-run samples of both methods displayed similar spectroscopic features. In addition, we explored the applicability of Raman spectroscopy to identify the presence of Fe-Ti-oxides and to investigate glass structures at high temperatures. Investigating nano-bearing glass, we observed that the intensity of the peak at 660–690 cm⁻¹ range gradually decreases with increasing temperature from the room temperature until it completely disappears at about 500 °C. While cooling, the mentioned peak reemerges similarly. However, since the concentration of nanolites remains constant below the glass transition, this effect is purely spectroscopic.

Supplementary In-situ high-temperature TEM

Supplementary Table 3 presents the results of the TEM Energy-dispersive X-ray (TEM-EDS) analysis conducted before and after the in situ high-temperature experiments. These results reflect individual TEM measurements at low magnification, which were averaged over a broad field of view. It is important to note that the data are influenced by systematic errors, particularly due to the contribution from the MEMS sample holder used for the heating experiments, as evidenced by the observed increases in SiO₂, P₂O₅ and Na₂O contents. Figure 5a presents the STEM-HAADF and STEM-EDS elemental maps of sample AND100 after in-situ high-temperature experiments. The bright nanocrystals observed in the STEM-HAADF image correspond to iron oxides, while the surrounding matrix is primarily composed of Si. Additionally, Al-enriched domains are visible, which do not coincide with the iron oxide crystals but instead

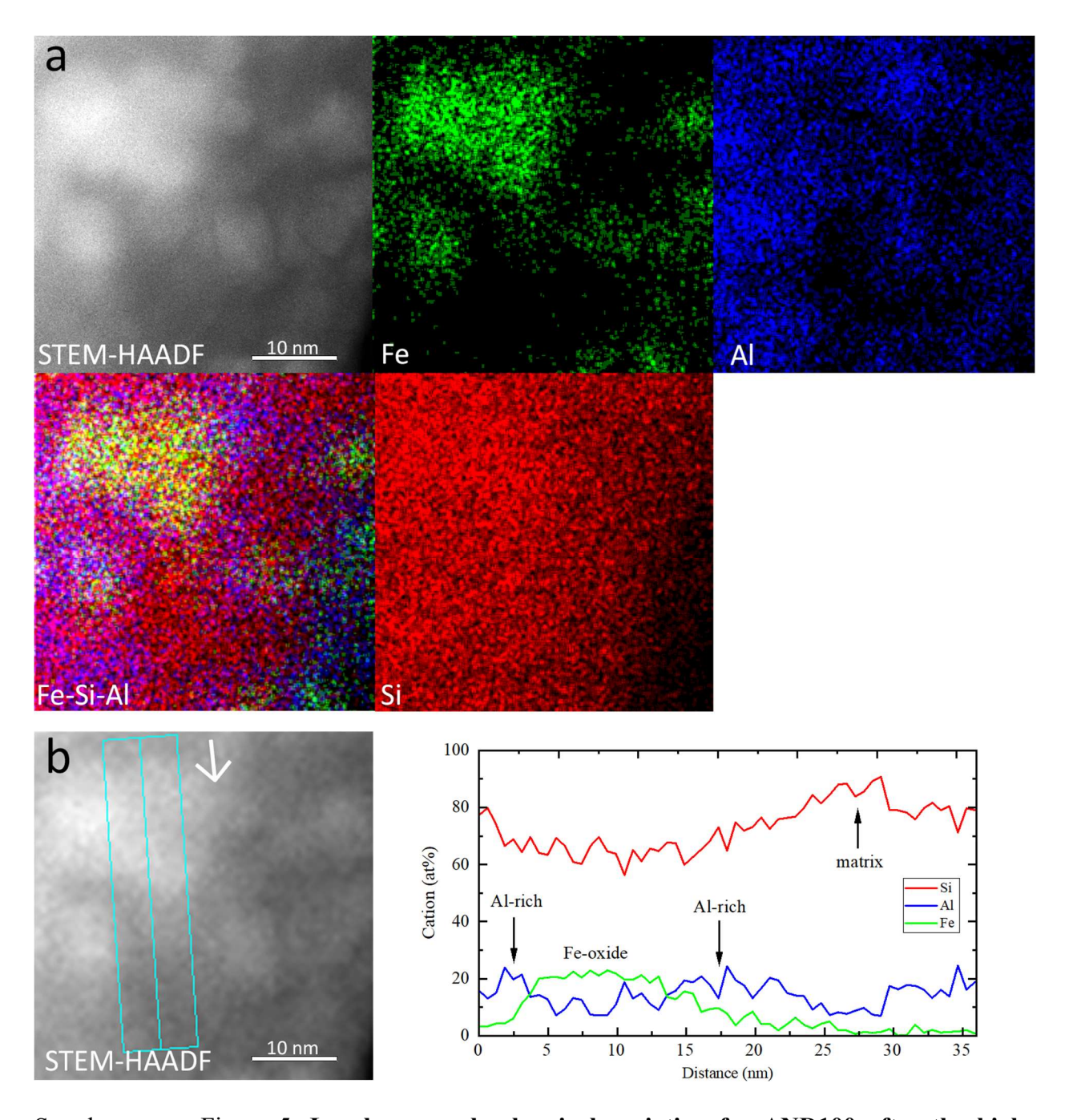
appear as gray regions in the HAADF image. The intensity of the EDS maps (Supplementary Fig. 5a) is directly proportional to the number of counts, reflecting the elemental distribution within the sample. It is important to note that these measurements were performed on a sample with variable thickness, as evident in the HAADF image, where the right-hand side appears significantly thinner. To minimize the influence of thickness variations, we generated a cationic profile (Supplementary Fig. 5b) from a quantitative EDS elemental map, applying spectrum deconvolution to avoid peak overlap, Z-number correction (Cliff-Lorimer k-factor correction), and absorption correction based on the estimated thickness of the beam scanning area. This profile reveals that Al-enriched domains are preferentially distributed around Fe-oxide nanocrystals, while the remaining matrix exhibits a pronounced Si enrichment.

Supplementary Table 3. High-temperature STEM-EDS results.

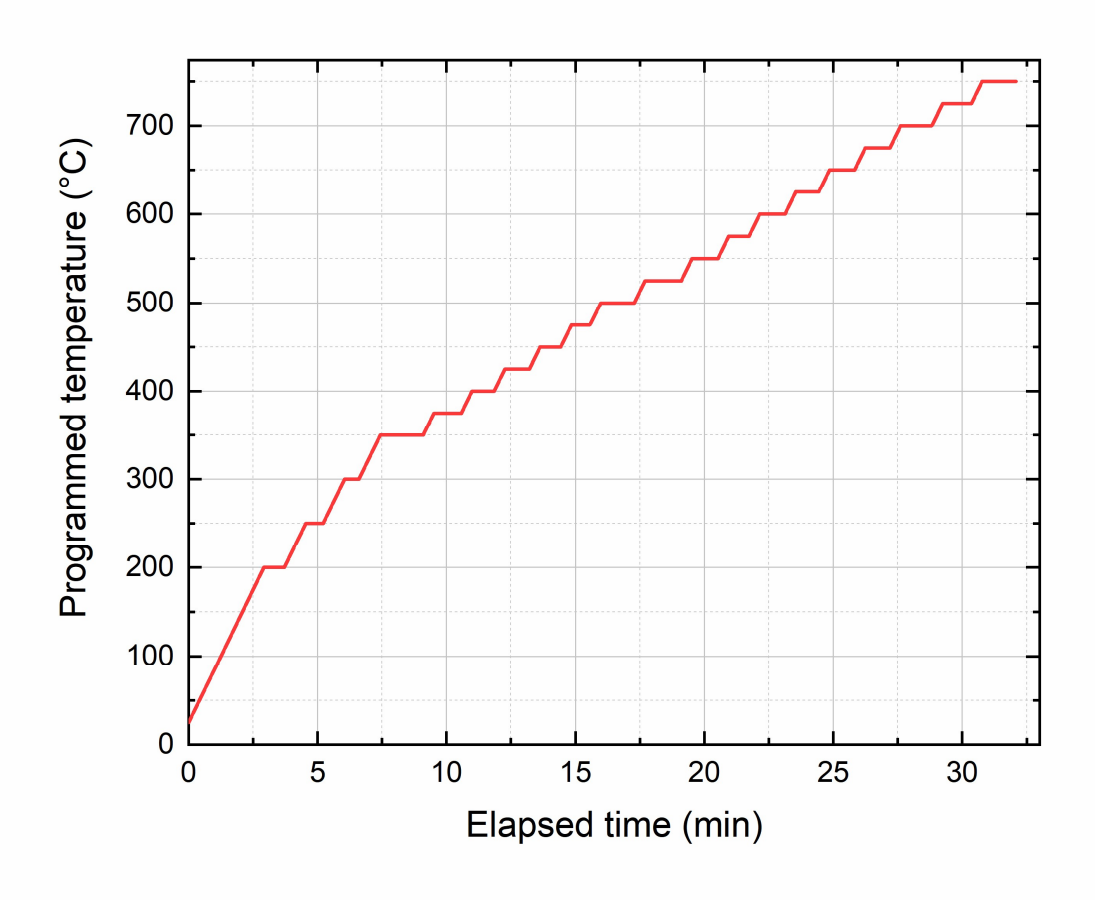
	Bulkbefore ^a	Bulkafter, e-beama	Bulkafter, no-beam ^b	
SiO ₂	61.0	65.9	61.3	
TiO_2	1.0	0.9	0.8	
Al_2O_3	14.1	18	15.7	
FeO_{tot}	7.0	6.7	6.7	
MgO	2.2	2.1	2.7	
CaO	6.2	5	7.2	
Na ₂ O	3.1	0	2.7	
K_2O	1.6	0	1.3	
P_2O_5	3.8	1.4	1.6	

^aSTEM-EDS result of AND100 before and after the in-situ experiment. Recalculated values in wt%. Measurements have an average error of 2 wt%. Every measurement corresponds to one region of interest.

^bTEM-EDS result of an adjacent region that was not directly affected by the electron beam.



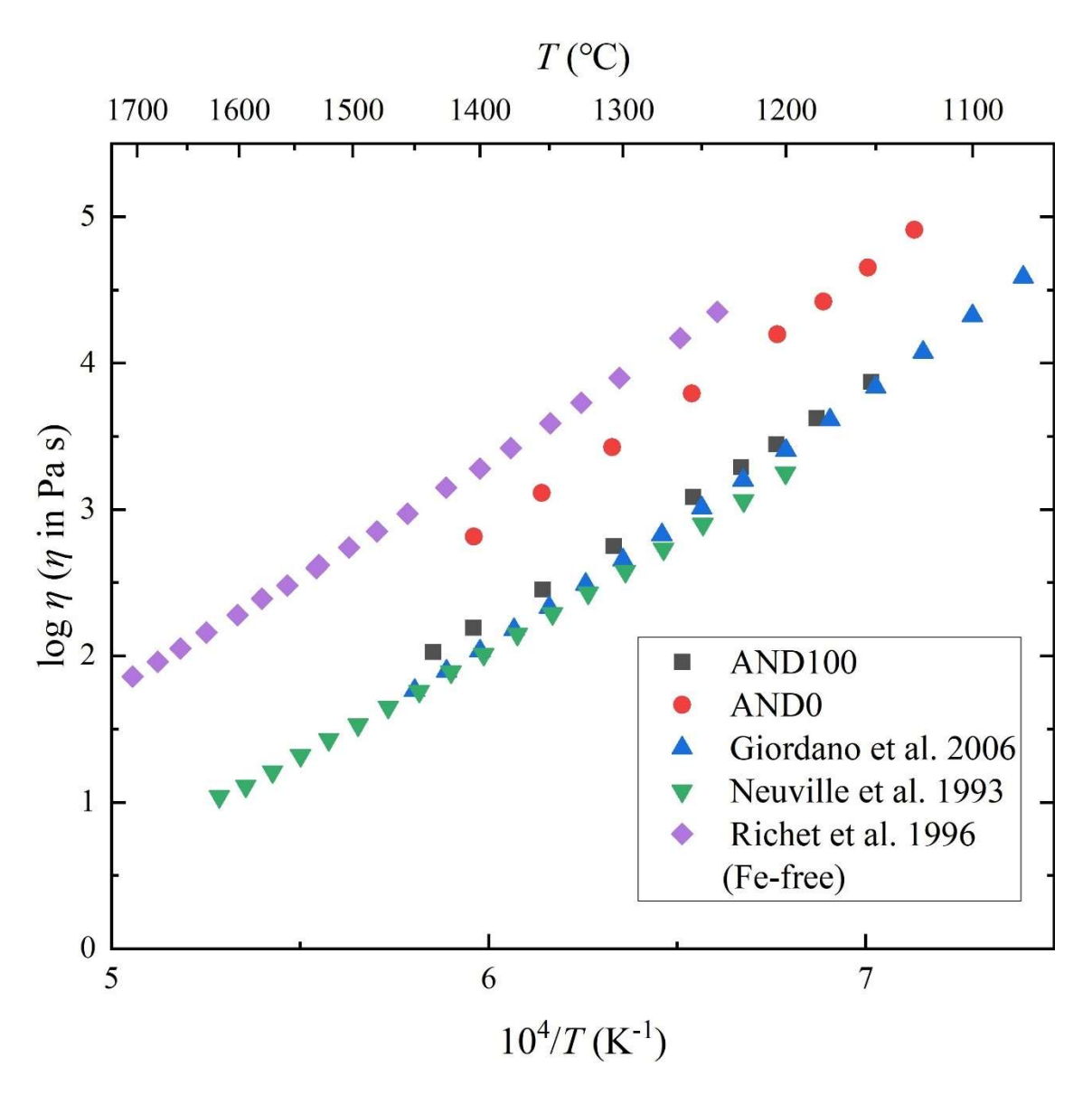
Supplementary Figure 5. Local nanoscale chemical variation for AND100 after the high-temperature in-situ experiment. a STEM-HAADF and STEM-EDS elemental maps showing the distribution of Fe, Si, Al, and their combined signal (Fe+Si+Al). The bright pixels in the STEM-HAADF image represent the crystalline phase. b Cationic profile illustrating the distribution of Fe, Si, and Al across the sample. The white arrow in the STEM-HAADF image marks the relative starting point and direction of the profile shown in light blue.



Supplementary Figure 6. Temperature profile for high-temperature TEM experiment.

Supplementary Concentric cylinder (CC)

The super-liquidus viscosity of AND100 and AND0 melts was determined using a concentric cylinder setup. CC results are reported as a function of temperature in Supplementary Supplementary Table 2 and shown in Supplementary Fig. 7. AND100 melt viscosity increases from $10^{2.0}$ to $10^{3.8}$ Pa s when decreasing the temperature from 1435 to 1150 °C. The AND0 viscosity increased from $10^{2.8}$ to $10^{4.9}$ Pa s when decreasing the temperature from 1404 to 1130 °C. At constant temperature, the viscosity of AND100 is at least $\sim 10^{0.8}$ Pa s lower than AND0 within this temperature range, showing a direct relationship with SiO₂ content and thereby NBO/T (Supplementary Table 1).



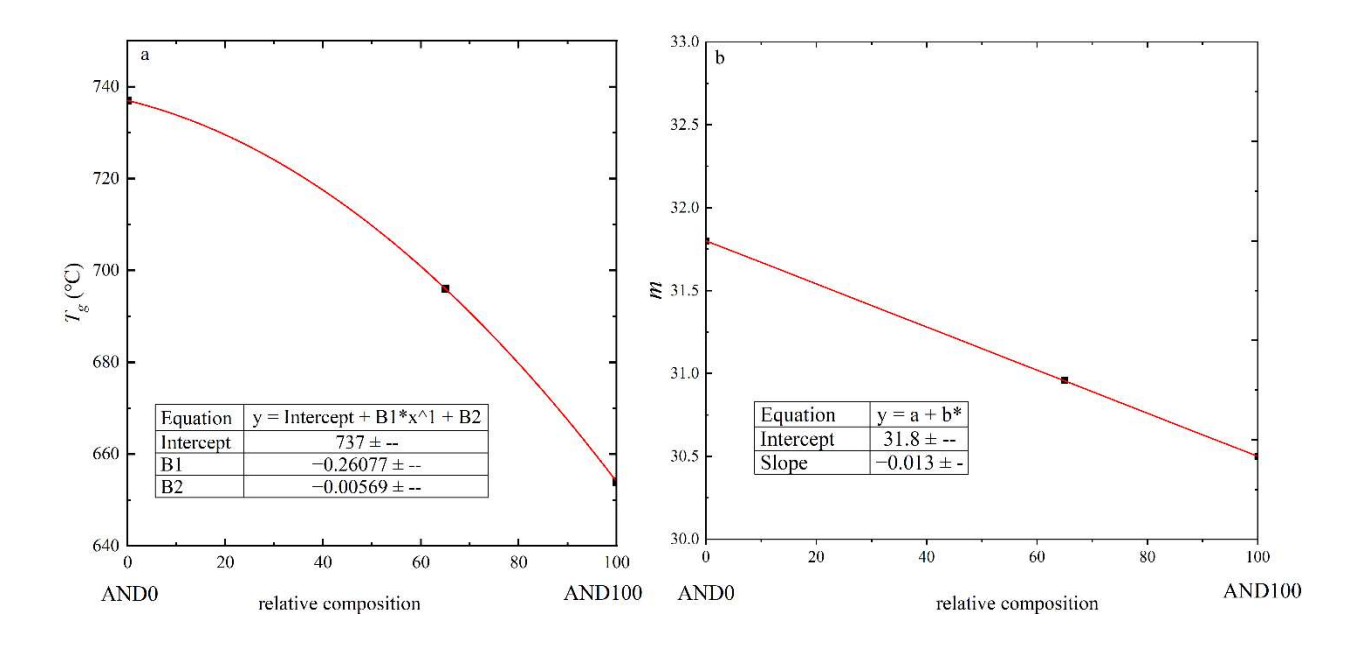
Supplementary Figure 7. Concentric cylinder results and literature viscosity data^{2,4,5}.

Supplementary Viscosity Parametrization

Considering our experimental investigations, we introduce three pure-melt viscosity parameterizations for various andesitic compositions (Supplementary Fig. 8). These curves are obtained by fitting viscosity data from samples free of nanolites, classified by consistent iron oxidation states. Together with our C-DSC-derived T_g (Supplementary Table 2), we utilized the

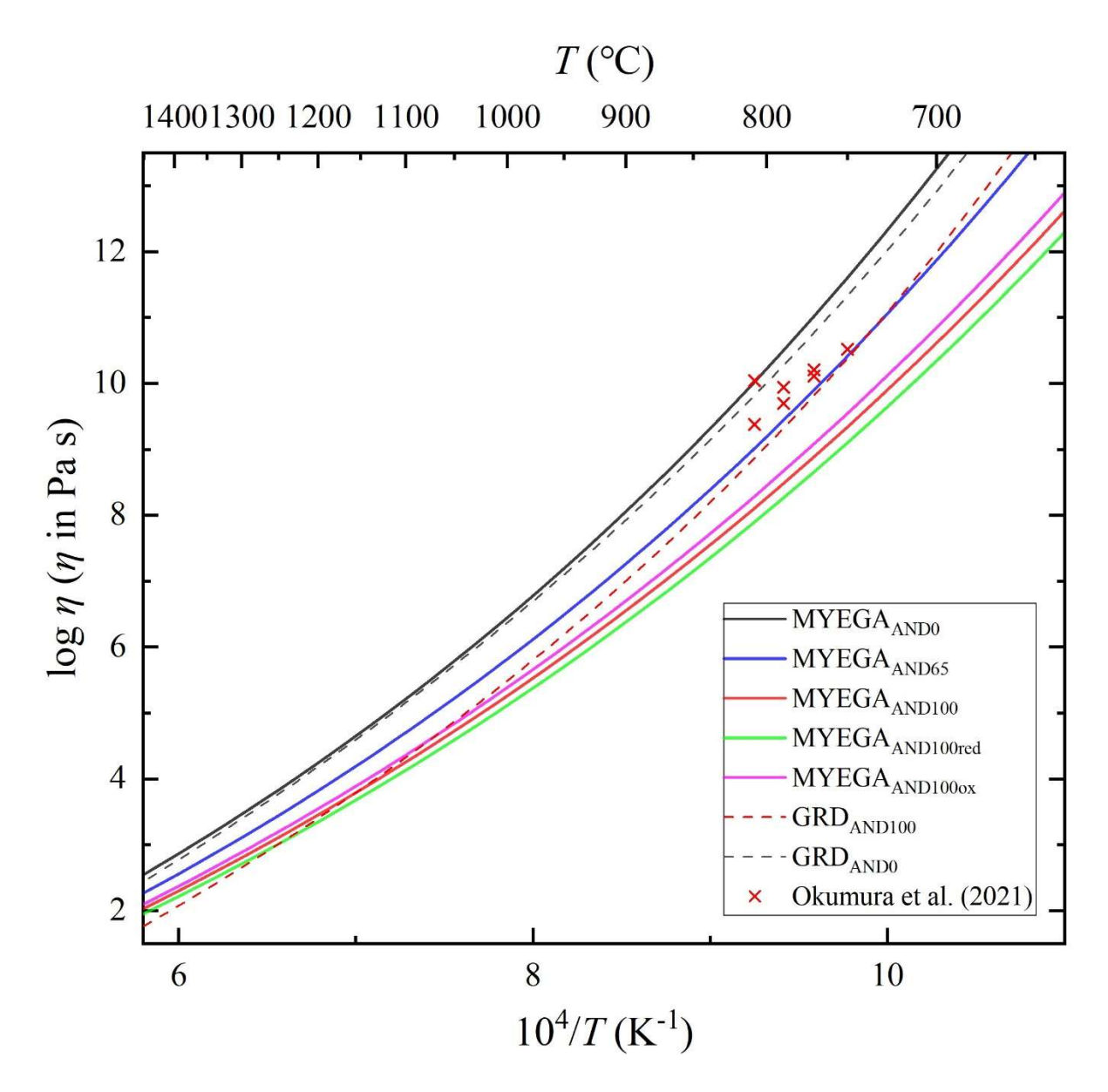
MYEGA parametrization (Eq. 5), with $\log_{10}\eta_{\infty}$ fixed at -2.93^{16,18,23,24} to fit the melt fragility index (m). This approach enables us to characterize melt viscosity over a broad range of temperatures.

For our AND100, we combined our high-temperature concentric cylinder viscosity data along with C- and F-DSC-derived viscosity data (Supplementary Table 2). By fitting T_g AND100 = 654 ± 0.5 °C (from AND100_DSC_{10-matching}), and using Eq. 5, we derived a fragility (m_{AND100}) of 30.5 ± 1 . For the iron-free analogue sample (AND0), by utilizing our C-DSC-derived viscosity data along with micropenetration and concentric cylinder data (Supplementary Table 2), and fitting $T_{\rm g_AND0} = 737 \pm 0.5$ °C, we determined $m_{\rm AND0} = 31.8 \pm 0.2$. For AND65, we combined our micropenetration and F-DSC-derived viscosity values along our C-DSC derived $T_{g_AND65} = 696 \pm$ 0.5 °C, obtaining a $m_{AND65} = 31.3 \pm 0.2$. Notably, we observed that the K/G ratio of AND65 exhibited ideal mixing relative to its two end members in terms of transition metal content, namely AND0 and AND100. Similarly, our fitted fragility m_{AND65} also exhibits ideal mixing relative to its two end members (i.e., $m_{AND65} = 0.65 \times m_{AND100} + 0.35 \times m_{AND0} = 31 \pm 0.6$; Supplementary Fig. 8b). Moreover, to model the viscosity of our andesitic compositions as a function of temperature and transition metal content, we propose a simple parametrization for T_g and m relative to the transition metal content of AND100 as illustrated in Supplementary Fig. 8. Finally, by using the MYEGA parametrization (Eq. 5), we provide a viscosity model for various andesitic compositions between AND100 and AND0 (Supplementary Data).



Supplementary Figure 8. Parametrization of T_g and m relative to AND100 content.

Regarding AND100red and AND100ox, the absence of viscosity data in the high-temperature range via concentric cylinder measurements prevents direct determination of the melt fragility index (m). Nevertheless, we can estimate their fragility values by leveraging our prior fragility estimations (i.e., AND100) along with our Brillouin data. Brillouin results show that the K/G ratios of AND100red, AND100ox and AND100 are identical within experimental uncertainty (Supplementary Table 1). Therefore, assuming a linear correlation between K/G and $m^{15,25}$, we infer that the fragilities of AND100red and AND100ox are comparable to that of AND100 ($m_{AND100red} = m_{AND100ox} = m_{AND100} = 30.5 \pm 1$). Furthermore, by using $T_{g_AND100red} = 645 \pm 0.5$ °C and $T_{g_AND1000ox} = 662 \pm 0.5$ °C (Supplementary Table 1), and Eq. 5, we derive the viscosity parametrization for AND100red and AND100ox (Fig 9). Overall, our viscosity parametrization for AND100red aligns slightly lower than that of AND100, while AND100ox sits slightly above AND100, consistent with their respective lower and higher Fe³⁺/Fe^{tot} content and T_g values.

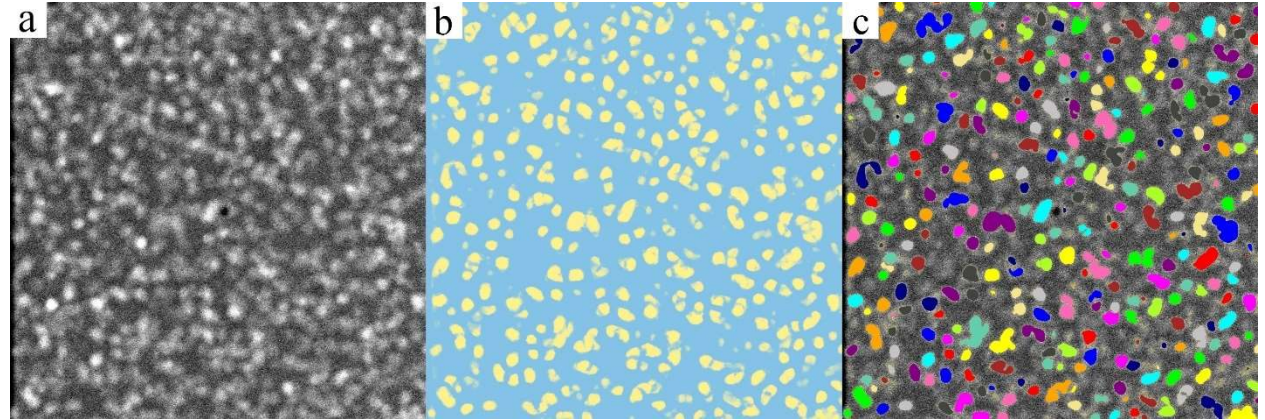


Supplementary Figure 9. MYEGA parametrizations and literature data. Each color represents a distinct chemical composition (Supplementary Table 1). The proposed viscosity models, based on Mauro et al.²⁴, are represented by straight lines. Red crosses depict viscosity from Okumura et al.¹, showing a composition similar to our AND100. The red and black dashed line corresponds to the predicted viscosity from Giordano et al.²⁶, for the AND100 and AND0 compositions, respectively.

Supplementary (Post-micropenetration) STEM-EDS

To account for nanolite geometrical features, STEM-HAADF images were segmented and separated based on hand-picked contrast thresholds software training using the ilastik software²⁷

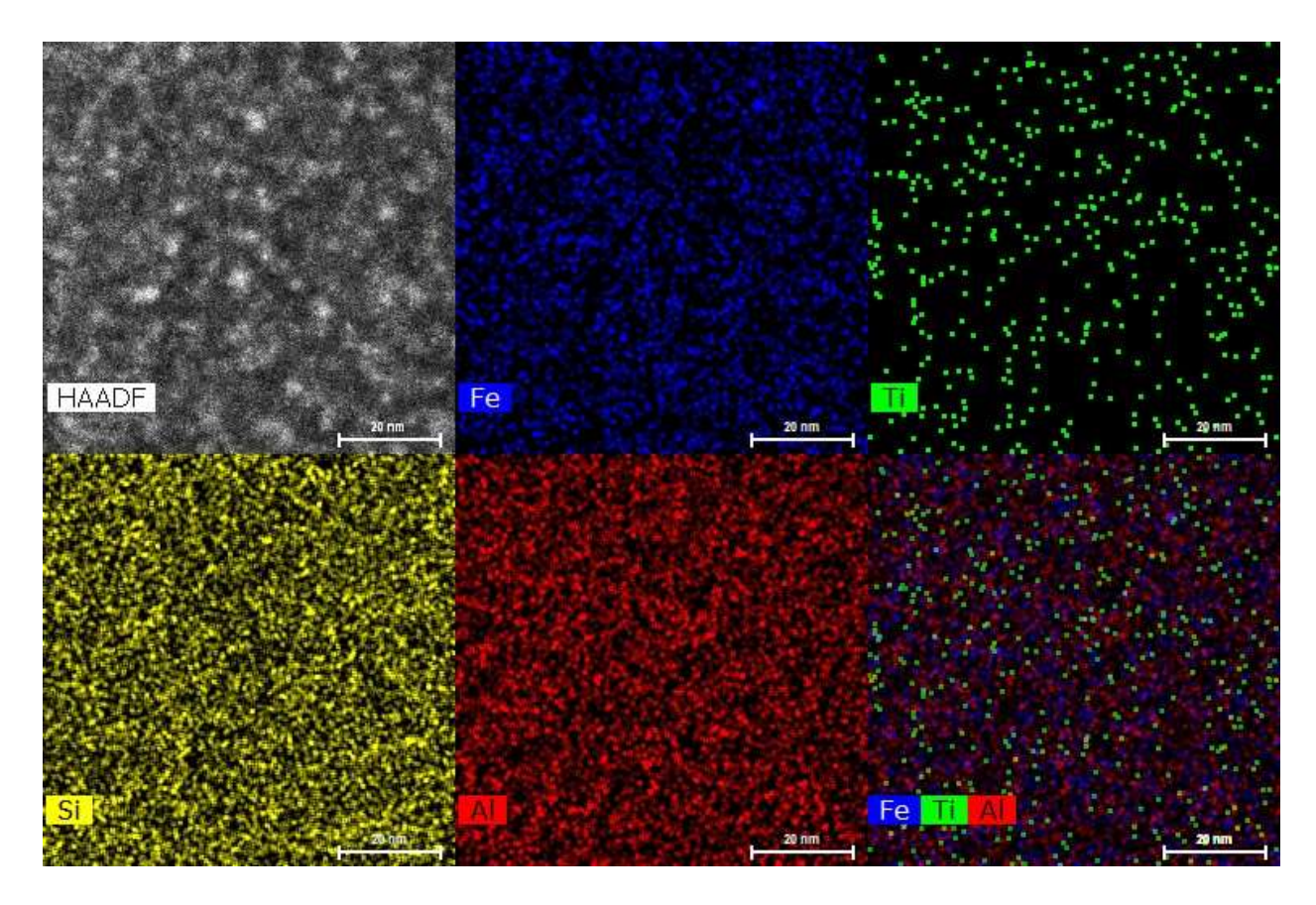
(Supplementary Fig. 11). First, we extracted the minimum (r_{min}) and maximum (r_{max}) radius of isolated nanolites in 2D and calculated their average ellipse radius (r_{avg}). Then, we computed 3D nanolite volumes by generating 3D triaxial ellipsoids of radius r_{min} , r_{avg} and r_{max} . It is important to mention that this method allows us to determine a minimum nanolite content (in vol%) and minimum nanolite number density (NND). This limitation arises because nanolites may overlap along the axis perpendicular to the plane of view, and there are also unavoidable uncertainties associated with pixel segmentation and separation due to the Al-rich zones surrounding the Feoxide nanolites (Supplementary Fig. 5). For this, we trained the ilastik software using probabilistic



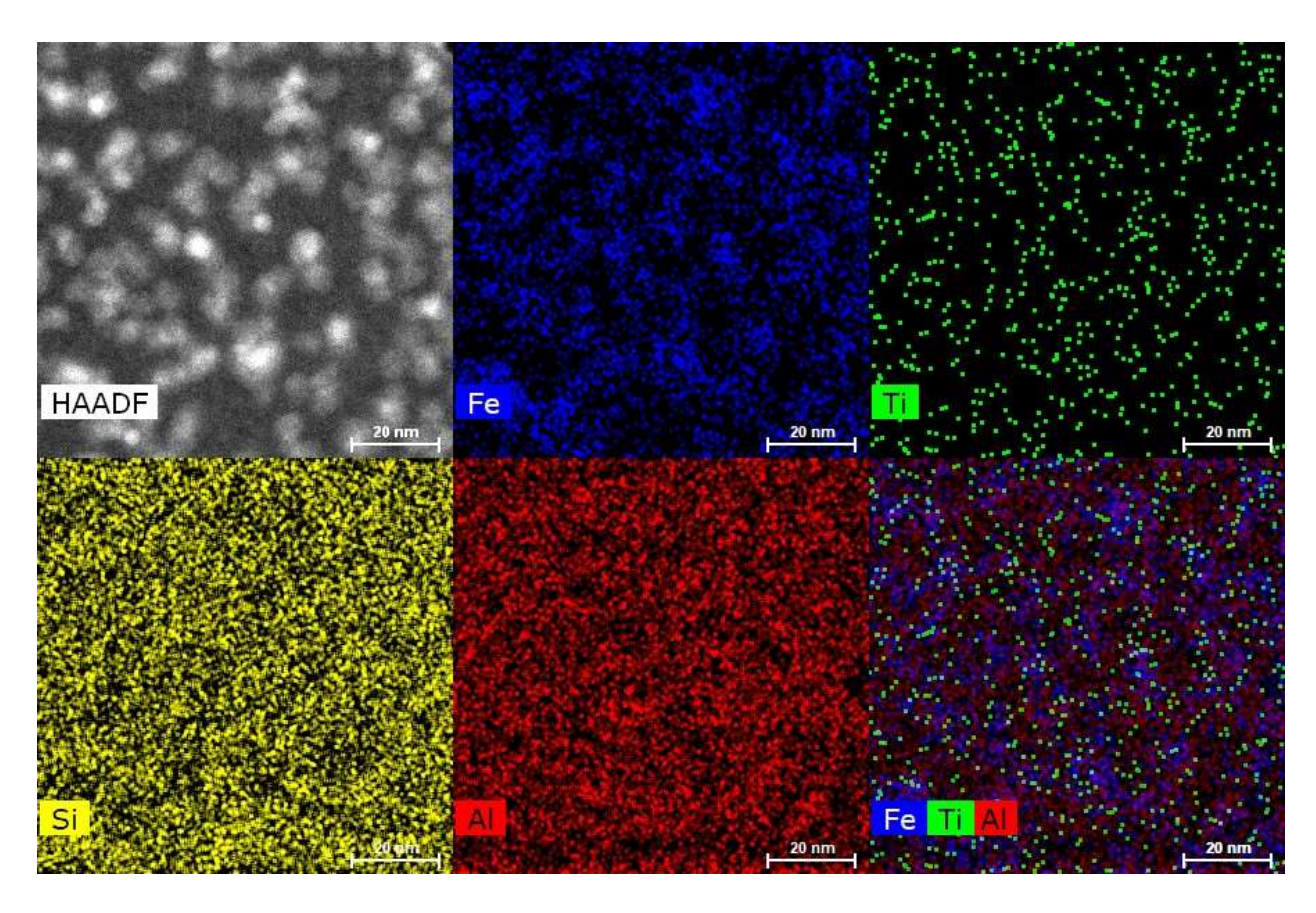
maps (Supplementary Fig. 10b) within the ilastik Object Classification Workflow²⁷.

Supplementary Figure 10. **Pixel segmentation and separation**. **a** STEM-HAADF image of sample AND100_ MP₇₂₃. **b** pixel segmentation of HAADF image c. phase separation of nanolites. Pixel segmentation and separation using the ilastik software, version 1.4.0 ²⁷. The pixel size is 0.2 nm.

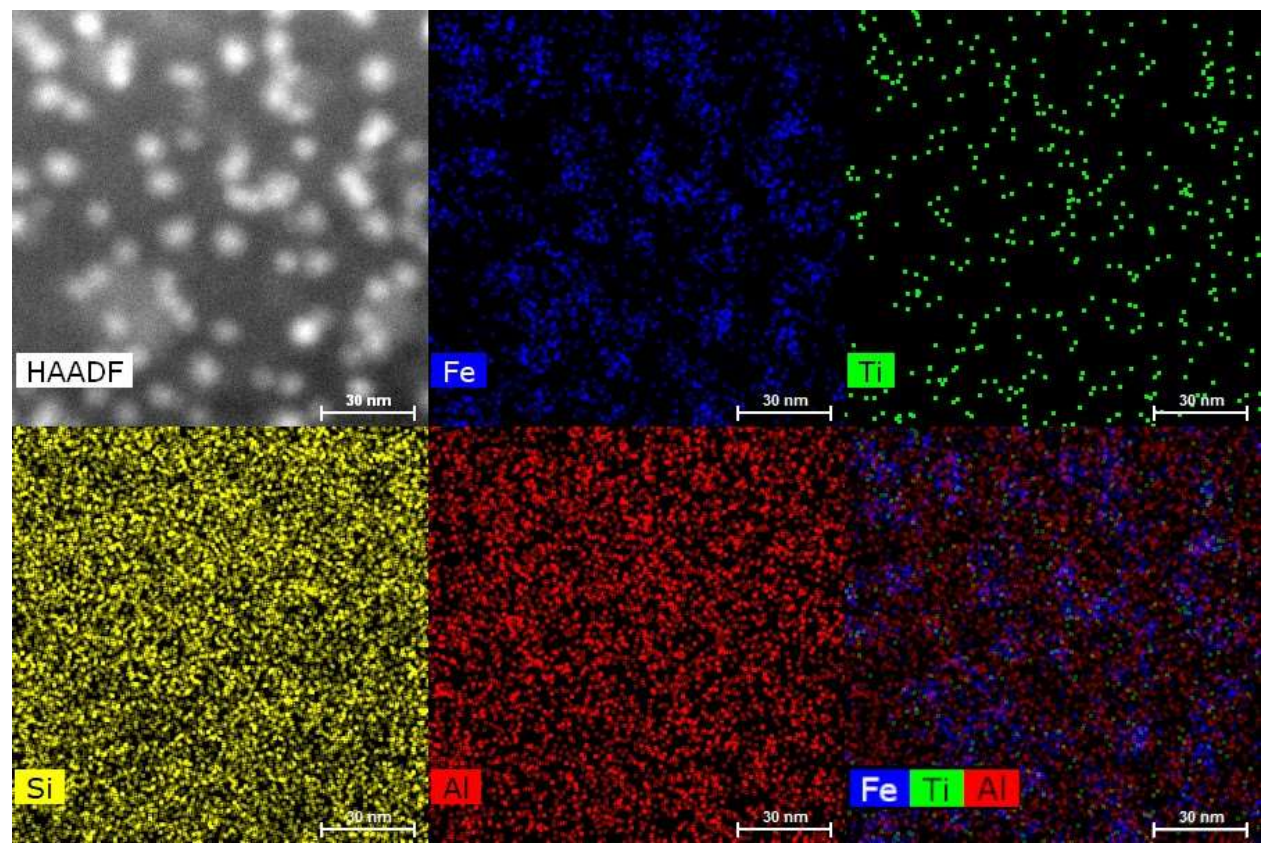
Nanolites are distinguishable in the STEM-HAADF images (Supplementary Fig. 11, Supplementary Fig. 12, and Supplementary Fig. 13) by their bright appearance, indicating a denser phase. Elemental maps (Supplementary Fig. 11, Supplementary Fig. 12, and Fig. Supplementary 13) reveal that these particles are Fe-rich.



Supplementary Figure 11. **HAADF and EDS elemental map of sample AND100_MP**₆₆₀. Each element is represented by one color, showing the Fe, Ti, Si, Al, and Fe+Ti+Al distribution.



Supplementary Figure 12. **HAADF and EDS elemental map of sample AND100_MP723**. Each element is represented by one color, showing the Fe, Ti, Si, Al, and Fe+Ti+Al distribution.



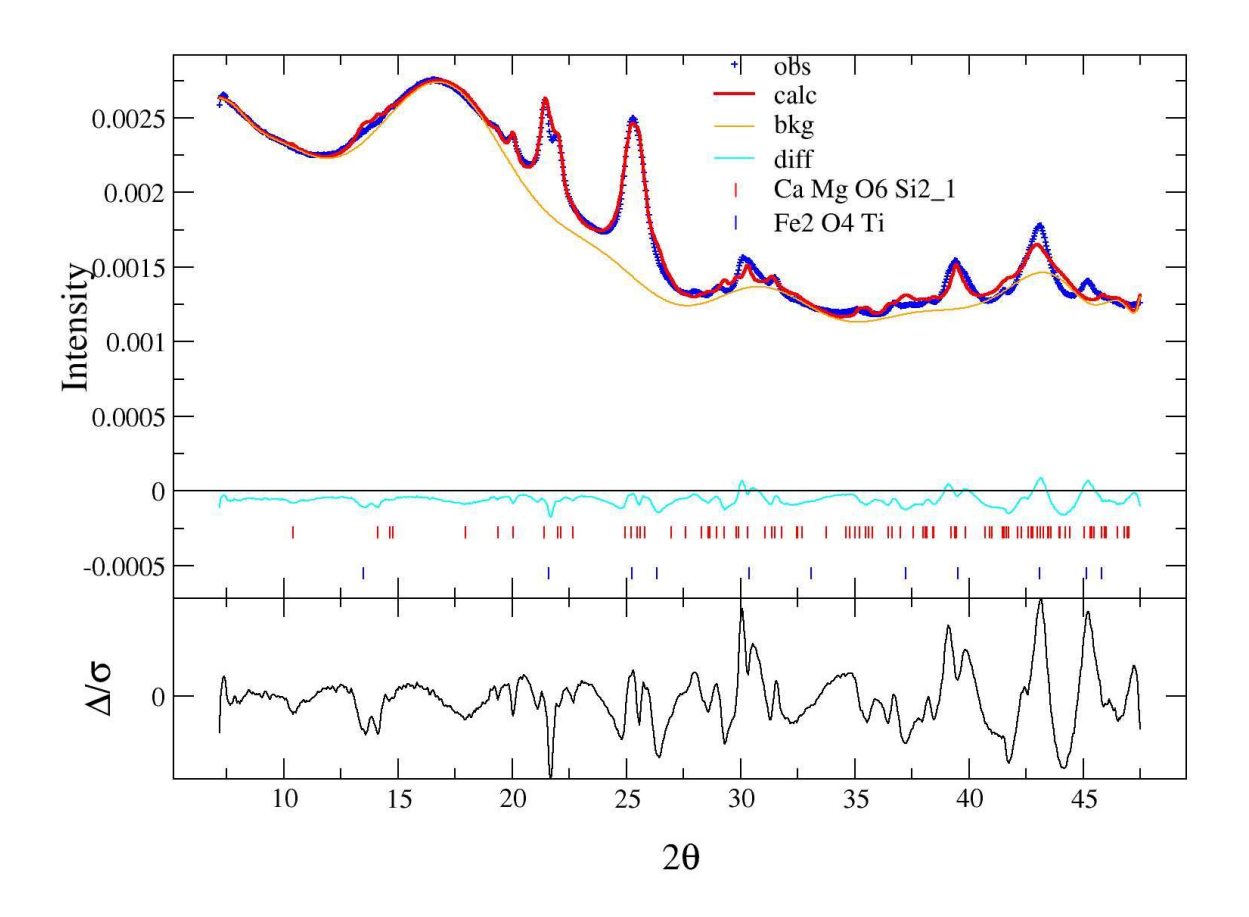
Supplementary Figure 13. **HAADF and EDS elemental map of sample AND100_MP**₈₀₈. Each element is represented by one color, showing the Fe, Ti, Si, Al, and Fe+Ti+Al distribution.

Supplementary SAXS and WAXS results

SAXS fit parameters are shown in Supplementary Table 3 and WAXS-Rietveld results for $AND100_MP_{808}$ are shown in Supplementary Fig. 14.

Supplementary Table 4. SAXS fit parameters for post-micropenetration AND100 samples.

Parameter	AND100_MP660	error	AND100_MP723	error	AND100_MP808	error
b	3.000E+01	5.00E+00	6.30E+00	1.00E-01	3.10E+00	2.00E-01
fscala	2.600E-04	6.00E-06	6.80E-05	6.00E-07	5.00E-05	3.40E-07
η_{HS}	1.160E-01	2.80E-03	1.13E-01	3.00E-03	8.00E-02	4.00E-02
kc	1.140E+00	3.60E-02	1.63E+00	5.00E-02	1.26E+00	1.00E-01
bck	6.500E-03	7.00E-05	5.51E-03	4.60E-05	1.30E-02	2.50E-04
Porod	1.400E-05	1.80E-06	2.40E-07	1.30E-07	1.20E-05	2.50E-06
fract	3.536E+00	5.00E-01	4.00E+00	1.60E-01	3.62E+00	2.10E-02
$R = R_1 (nm)$	1.700E+00	2.00E-02	3.10E+00	1.00E-02	1.40E+01	1.00E+00



Supplementary Figure 14. WAXS Rietveld results for AND100_MP808.

Supplementary References

- 1. Okumura, S. *et al.* Rheology of nanocrystal-bearing andesite magma and its roles in explosive volcanism. *Commun. Earth Environ.* **3**, 241 (2022).
- 2. Giordano, D. *et al.* An expanded non-Arrhenian model for silicate melt viscosity: A treatment for metaluminous, peraluminous and peralkaline liquids. *Chem. Geol.* **229**, 42–56 (2006).
- 3. Liebske, C., Behrens, H., Holtz, F. & Lange, R. A. The influence of pressure and composition on the viscosity of andesitic melts. *Geochim. Cosmochim. Acta* **67**, 473–485 (2003).
- 4. Richet, P., Lejeune, A. M. M., Holtz, F. & Roux, J. Water and the viscosity of andesite melts. *Chem. Geol.* **128**, 185–197 (1996).
- 5. Neuville, D. R., Courtial, P., Dingwell, D. B. & Richet, P. Thermodynamic and rheological properties of rhyolite and andesite melts. *Contrib. to Mineral. Petrol.* **113**, 572–581 (1993).
- 6. Prata, G. S. *et al.* A New Parameterization of Volcanic Ash Complex Refractive Index Based on NBO/T and SiO 2 Content. *J. Geophys. Res. Atmos.* **124**, 1779–1797 (2019).
- 7. Prescher, C., McCammon, C. & Dubrovinsky, L. MossA: a program for analyzing energy-domain Mössbauer spectra from conventional and synchrotron sources. *J. Appl. Crystallogr.* **45**, 329–331 (2012).
- 8. Le Losq, C., Neuville, D. R., Moretti, R. & Roux, J. Determination of water content in silicate glasses using Raman spectrometry: Implications for the study of explosive volcanism. *Am. Mineral.* **97**, 779–790 (2012).
- 9. Giordano, D. *et al.* A calibrated database of Raman spectra for natural silicate glasses: implications for modelling melt physical properties. *J. Raman Spectrosc.* **51**, 1822–1838 (2020).
- 10. Di Genova, D. *et al.* In situ observation of nanolite growth in volcanic melt: A driving force for explosive eruptions. *Sci. Adv.* **6**, (2020).
- 11. Di Genova, D., Zandona, A. & Deubener, J. Unravelling the effect of nano-heterogeneity on the viscosity of silicate melts: Implications for glass manufacturing and volcanic eruptions. *J. Non. Cryst. Solids* **545**, 120248 (2020).
- 12. Di Genova, D. *et al.* Effect of iron and nanolites on Raman spectra of volcanic glasses: A reassessment of existing strategies to estimate the water content. *Chem. Geol.* **475**, 76–86 (2017).
- 13. Schiavi, F. *et al.* Water quantification in silicate glasses by Raman spectroscopy: Correcting for the effects of confocality, density and ferric iron. *Chem. Geol.* **483**, 312–331 (2018).
- 14. Stabile, P. *et al.* The effect of iron and alkali on the nanocrystal-free viscosity of volcanic melts: A combined Raman spectroscopy and DSC study. *Chem. Geol.* **559**, 119991 (2021).
- 15. Cassetta, M. *et al.* Estimating the viscosity of volcanic melts from the vibrational properties of their parental glasses. *Sci. Rep.* **11**, 1–14 (2021).
- 16. Scarani, A. *et al.* A chemical threshold controls nanocrystallization and degassing behaviour in basalt magmas. *Commun. Earth Environ.* **3**, 284 (2022).
- 17. Di Genova, D. *et al.* A compositional tipping point governing the mobilization and eruption style of rhyolitic magma. *Nature* **552**, 235–238 (2017).
- 18. Valdivia, P. *et al.* Are volcanic melts less viscous than we thought? The case of Stromboli basalt. *Contrib. to Mineral. Petrol.* **178**, 45 (2023).
- 19. Shebanova, O. N. & Lazor, P. Raman spectroscopic study of magnetite (FeFe2O4): a new assignment for the vibrational spectrum. *J. Solid State Chem.* **174**, 424–430 (2003).
- 20. Jubb, A. M. & Allen, H. C. Vibrational Spectroscopic Characterization of Hematite, Maghemite, and Magnetite Thin Films Produced by Vapor Deposition. *ACS Appl. Mater. Interfaces* **2**, 2804–2812 (2010).
- 21. Schroeder, J. *et al.* Raman scattering and Boson peaks in glasses: Temperature and pressure effects. *J. Non. Cryst. Solids* **349**, 88–97 (2004).
- 22. Zanatta, M. *et al.* Debye to non-Debye scaling of the Boson peak dynamics: Critical behavior and local disorder in vitreous germania. *J. Chem. Phys.* **135**, (2011).

- 23. Langhammer, D., Di Genova, D. & Steinle-Neumann, G. Modeling the Viscosity of Anhydrous and Hydrous Volcanic Melts. *Geochemistry, Geophys. Geosystems* **22**, 1–26 (2021).
- 24. Mauro, J. C., Yue, Y., Ellison, A. J., Gupta, P. K. & Allan, D. C. Viscosity of glass-forming liquids. *Proc. Natl. Acad. Sci. U. S. A.* **106**, 19780–4 (2009).
- 25. Novikov, V. N., Ding, Y. & Sokolov, A. P. Correlation of fragility of supercooled liquids with elastic properties of glasses. *Phys. Rev. E Stat. Nonlinear, Soft Matter Phys.* **71**, 1–12 (2005).
- 26. Giordano, D., Russell, J. K. & Dingwell, D. B. Viscosity of magmatic liquids: A model. *Earth Planet. Sci. Lett.* **271**, 123–134 (2008).
- 27. Berg, S. *et al.* Ilastik: Interactive Machine Learning for (Bio)Image Analysis. *Nat. Methods* **16**, 1226–1232 (2019).

4.3 A viscosity model for hydrous andesitic magmas

Pedro Valdivia^{1,2}*, Jessica Löschmann³, Alessio Zandonà³, Dmitry Bondar^{1,2}, Alexander Kurnosov¹, Joachim Deubener³, Danilo Di Genova²

¹Bayerisches Geoinstitut, University of Bayreuth, Universitätsstraße 30, 95440, Bayreuth, Germany

²Institute of Science, Technology and Sustainability for Ceramics (ISSMC) of the National Research Council (CNR), Via Granarolo 64, I-48018, Faenza, RA, Italy

³Institute of Non-Metallic Materials, Clausthal University of Technology, Zehntnerstraße 2a, D-38678 Clausthal-Zellerfeld, Germany

*Corresponding author: pedro.valdivia-munoz@uni-bayreuth.de

Status: To be submitted to Earth Planet. Sci. Lett.

A viscosity model for hydrous andesitic magmas

Pedro Valdivia^{1,2*}, Jessica Löschmann³, Alessio Zandonà³, Dmitry Bondar^{1,2}, Alexander Kurnosov¹, Joachim Deubener³, Danilo Di Genova²

¹Bayerisches Geoinstitut, University of Bayreuth, Universitätsstraße 30, 95440, Bayreuth, Germany
²Institute of Science, Technology and Sustainability for Ceramics (ISSMC) of the National Research Council (CNR), Via Granarolo 64, I-48018, Faenza, RA, Italy
³Institute of Non-Metallic Materials, Clausthal University of Technology, Zehntnerstraße 2a, D-38678 Clausthal-Zellerfeld, Germany

*Corresponding author: pedro.valdivia-munoz@uni-bayreuth.de

Abstract

Magma viscosity is a critical parameter governing volcanic processes, including magma transport, deformation, and eruptive behavior. Andesitic magmas, characterized by high viscosity and volatile content, are particularly prone to explosive eruptions. However, existing viscosity models often fail to accurately predict the rheological behavior of hydrous andesitic magmas, especially those affected by nanocrystallization. In this study, we present a new viscosity model for hydrous andesitic melts, based on experimental measurements of iron-bearing and iron-free analog compositions representative of the Sakurajima volcano. Using viscometry, differential scanning calorimetry, Raman and Brillouin spectroscopy, we quantify the dependence of viscosity on temperature, water content, and transition metal concentration. Our results reveal that previous estimates of magma viscosity under pre-eruptive conditions at Sakurajima were overestimated by up to a factor of 45, with similar discrepancies (up to a factor of 380) observed for other andesitic systems. By integrating the effects of water and transition metals on the glass transition temperature and melt fragility, our model offers a more accurate framework for predicting magma ascent rates, eruption dynamics, and associated volcanic hazards.

Keywords: andesite, viscosity, hydrous viscosity, differential scanning calorimetry, Brillouin spectroscopy, Raman spectroscopy.

Introduction

The study of magma viscosity is crucial for understanding volcanic processes, as it controls magma transport (Gonnermann, 2015; Webb and Dingwell, 1990; Zhang, 1999), deformation response (Dingwell, 1996; Okumura et al., 2010; Papale, 1999), and ultimately the eruptive style (Sparks, 2003). This is particularly relevant for andesitic magmas, which are highly viscous (Vetere et al., 2008) and gas-rich (Takeuchi, 2011), making them prone to explosive eruptions (Gonnermann, 2015). Andesitic volcanoes, primarily found along subduction zones such as the Pacific Ring of Fire (Dickinson and Hatherton, 1967), account for a significant proportion of global volcanic activity. Their explosive potential can produce pyroclastic flows, ash clouds, and lahars, posing severe risks to human populations, infrastructure, and the environment. Therefore, given the high concentration of andesitic volcanoes in densely populated regions, understanding the viscosity and behavior of andesitic magmas is essential for improving volcanic hazard assessments, early warning systems, and mitigation strategies.

Melt fragility (m), defined as the steepness of the viscosity-temperature relationship at the glass transition temperature (T_g) in the Angell plot (Angell, 1995), is a key parameter that, when combined with T_g , can describe viscosity variations across a broad temperature range (Langhammer et al., 2022; Mauro et al., 2009). Melt fragility is particularly valuable from a practical standpoint, as it enables the extrapolation of viscosity to eruptive conditions, where direct measurements are challenging due to the rapid degassing and crystallization that volcanic melts experience during standard high-temperature viscosity experiments.

Previous studies suggest that *m* can be determined using sound velocity data (Cassetta et al., 2021; Novikov et al., 2005; Novikov and Sokolov, 2004; Sokolov et al., 2007) and can also be correlated with the number of non-bridging oxygens per tetrahedrally coordinated cation (NBO/T)

(Giordano and Dingwell, 2003; Malfait and Sanchez-Valle, 2013). However, these approaches are fundamentally challenged by recent findings. Studies (Fanesi et al., 2025; Valdivia et al., 2025, 2023) demonstrate that melt fragility derived from these correlations, as well as from widespread viscosity models (Giordano et al., 2008; Langhammer et al., 2022), systematically fails to predict the viscosity of andesitic and basaltic compositions prone to nanocrystallization.

This predictive failure stems from a critical process occurring during viscosity measurements: the nanostructural reorganization within the melt and/or crystallization of Fe-Tioxide nanocrystals, referred as nanolites (Cáceres et al., 2024; Fanesi et al., 2025; Liebske et al., 2003; Okumura et al., 2022; Pereira et al., 2024; Scarani et al., 2022; Valdivia et al., 2025, 2023). These processes substantially increase magma viscosity in both laboratory experiments and natural systems, while simultaneously triggering water exsolution (Cáceres et al., 2020; Di Genova et al., 2020a; Fanesi et al., 2025; Valdivia et al., 2023). Critically, nanolites are not merely laboratory artifacts: their presence in volcanic products from explosive eruptions (Barone et al., 2016; Di Genova et al., 2017; Knafelc et al., 2022; Mujin and Nakamura, 2020, 2014; Sharp et al., 1996; Yoshida et al., 2023; Zellmer et al., 2016) indicates they actively control magma ascent and eruption dynamics in nature. Their crystallization creates a coupled feedback system: rheological stiffening occurs alongside chemical evolution of the melt, altering the physicochemical conditions that govern volcanic processes (Mujin et al., 2017; Mujin and Nakamura, 2020, 2014). However, the quantification of rheological changes driven by chemical variations induced by nanocrystallization in hydrous magmas remains poorly understood and, thereby, it represents a critical limitation in our understanding of volcanic systems and eruption forecasting capabilities.

In this study, we introduce two simplified empirical equations that correlate the melt fragility index (m) with sound velocity data of glasses obtained from Brillouin spectroscopy for

compositions ranging from andesites to basalts. One equation applies to transition metal-bearing samples (i.e., Fe-, Ti-, and Mn-bearing glasses), while the other is tailored for transition metal-free compositions (i.e., Fe-Ti-Mn-free). These relationships enable rapid fragility determination without time-intensive viscosity measurements that can induce nanocrystallization and degassing, thereby avoiding experimental artifacts that compromise the accuracy of volcanic processes modelling.

Building on established laboratory methodologies (Di Genova et al., 2023; Fanesi et al., 2025; Valdivia et al., 2025, 2023), we developed a viscosity model for hydrous andesitic melts, accounting for variations in transition metal content, as a function of temperature and water concentration. This approach directly addresses the systematic failure of existing viscosity models for Fe-Ti-rich compositions prone to nanostructuration and nanocrystallization. We focus on the andesitic composition of Sakurajima volcano, one of the most active and hazardous volcanic systems in Japan (Okumura et al., 2024). Recent studies (Bondar et al., 2025; Valdivia et al., 2025) demonstrated that the anhydrous composition of this volcanic center develops chemical heterogeneities at the nanoscale, leading to a significant increase in viscosity. This experimental behavior mirrors natural observations, as andesitic magmas erupted from Sakurajima carry abundant nanolites (Araya et al., 2019; Mujin and Nakamura, 2020, 2014), confirming their key role in controlling magma rheology and eruptive dynamics.

Our refined viscosity estimates across a range of andesitic compositions provide two key advances: (1) improved tracking of iron depletion during magma ascent, and (2) a more physically robust basis for eruption forecasting within probabilistic frameworks, essential for hazard mitigation at active volcanic systems globally.

Materials and methods

Synthesis of starting glasses

The starting materials consist of synthetic andesitic glasses based on three base compositions with varying water contents. The first composition (AND100) mirrors the natural chemical composition of Sakurajima andesite including all transition metals (Okumura et al., 2022; Valdivia et al., 2025). The other two composition, AND65 and AND0 respectively, are simplified analogs in which 35% and 100% of the total transition metal content (i.e, FeOtot, TiO2, and MnO) were removed (Valdivia et al., 2025). Thus, the number in their nomenclature (i.e., AND100, AND65 and AND0) corresponds to transition metal content relative to the AND100. For example, AND65 denotes an andesite formed by the ideal mixing of 65% AND100 and 35% of AND0.

For each base composition, multiple samples were synthesized with different water concentrations, resulting in six hydrous AND100 samples, seven hydrous AND0 samples, and one hydrous AND65 sample used to verify the model.

AND100 hydrous glasses were synthesized using an internally heated pressure vessel (IHPV) apparatus at the Bayerisches Geoinstitut (BGI) in Bayreuth, Germany. Starting hydrous materials were prepared by grinding the starting anhydrous glasses into a fine powder, which was then sieved into two grain-size fractions (i.e., <100 μm and 100–250 μm). To improve grain packing and minimize porosity, these fractions were combined in a 1:1 weight ratio. Distilled water was added stepwise to the dry glass powder, which was then sealed in Au₈₀Pd₂₀ capsules (4.6 mm inner diameter, 20 mm length) to minimize iron loss during synthesis (Pichavant et al., 2013). After welding and weighing, the capsules were heated overnight at 150°C to check for water loss. IHPV experiments were performed at 5 kbar and 1250°C for 24 h at relatively oxidizing conditions

 $(f_{O_2} = \text{NNO} + 3 \pm 1)$ as determined by Schuessler et al. (2008). Samples were rapidly quenched with a cooling rate of ~150 K s⁻¹ at isobaric pressure.

AND65 and AND0 hydrous glasses were synthesized using a piston-cylinder apparatus at BGI, using Au₈₀Pd₂₀ capsules of 4.6 mm inner diameter and 10-12 mm length. Glass syntheses were carried out at 1250-1,300°C and 5–7 kbar under reduced oxygen fugacity conditions (<NNO+0), with a dwell time of 24 hours to ensure water homogenization within the samples. Rapid quenching (<100 K s⁻¹) was achieved by cutting off the heating power while pressure remained controlled. Samples are labeled according to their measured water content in wt% (e.g., AND100 0 for the anhydrous material and AND100 4.2 for a sample with 4.2 ± 0.01 wt% H₂O).

Additionally, we synthesized an iron-free basaltic composition (BAS0) by mixing powder reagents (SiO₂, Al₂O₃, MgO, CaCO₃, Na₂CO₃, K₂CO₃ and P₂O₅) targeting a basaltic composition of Etna (Scarani et al., 2022) depleted of transition metals following the methodology presented in Valdivia et al. (2025).

To ensure homogeneity and the amorphous nature of these starting materials, the resulting glasses were examined using electron microprobe chemical analysis (EMPA), Raman and Mössbauer spectroscopy.

Electron microprobe analyses (EMPA)

The major elemental composition (Si, Ti, Al, Fe_{tot.}, Mn, Mg, Ca, Na, K, and P) of our samples were determined using a JEOL JXA-8200 electron microprobe at BGI. Glasses were mounted in epoxy, polished, and coated with carbon before analysis. Measurements were conducted at an accelerating voltage of 15 kV, a beam current of 5 nA, and a counting time of 20 seconds using a defocused 10 µm beam. To assess sample homogeneity, 10 points were measured

per sample. Calibration was performed using synthetic standards: wollastonite for Ca and Si, periclase for Mg, hematite for Fe, spinel for Al, orthoclase for K, albite for Na, manganese titanate for Mn and Ti, and apatite for P. To minimize alkali migration, Na and K were analyzed first (Hughes et al., 2019). EMPA analyzes were performed in backscattered electron (BSE) imaging mode to assess the presence or absence of potential micro-sized crystalline phases or vesicles before chemical acquisition.

Raman spectroscopy

Raman spectroscopy was conducted on glass samples both before and after experiments to identify potential alterations at the nano- and microscale, including variations in the iron oxidation state. For this, we used a confocal Raman imaging microscope at the Institute of Non-Metallic Materials, TU Clausthal (alpha300R, WITec GmbH), where spectra were acquired using a 100x objective in the ranges between 10–1,300 cm⁻¹ for the silicate region, and between 2,700-4,000 cm⁻¹ to inspect the water bands. Acquisition parameters included an integration time of 10 seconds, an accumulation count of 5, and a laser power of 10 mW. Spectra were smoothed to enhance the signal-to-noise ratio.

Mössbauer spectroscopy

Mössbauer measurements were conducted at BGI on glass samples approximately 4 mm in diameter and 600 μ m thick, both before and after experiments. The analyses were performed at room temperature (293 K) using a constant acceleration Mössbauer spectrometer with a high-specific-activity ⁵⁷Co point source (370 MBq) embedded in a 12 μ m thick Rh matrix. The velocity scale was calibrated against a 25 μ m thick α -Fe foil, and data were collected over a velocity range

of ± 5 mm s⁻¹, with acquisition times of 2 to 3 days per sample. Spectral fitting was conducted using the full transmission integral approach in the MossA software (Prescher et al., 2012), and Fe³⁺/Fe²⁺ ratios were determined based on the relative area of each iron species.

Water content determination

The water content of our glasses was determined using a Karl-Fischer titration (KFT) device and by Fourier–transform infrared spectroscopy (FTIR) at BGI.

KFT is a coulometric technique based on the quantitative reaction of water with iodine (Eq. 1):

$$I_2 + SO_2 + H_2O \leftrightarrow 2HI + SO_3$$
 (1)

Iodine is generated electrolytically at the anode according to (Eq. 2):

$$2I^- \leftrightarrow I_2 + 2e^- \tag{2}$$

Since one mole of iodine reacts with one mole of water, the water content was directly calculated from the charge required for electrolysis, where 1 mg of H_2O corresponds to 10.71 coulombs. Samples of ~20 mg were finely crushed and heated in an induction coil at $100^{\circ}C$ min⁻¹ under controlled conditions following Behrens et al. (1996). The quantity of water was measured with a coulometer (Mitsubishi CA 05) using pyridine-free reagents (Aquamicron AS, Aquamicron CS). The titration process was initiated after 2 minutes to remove traces of water after we loaded the sample and was terminated when the sample reached 1,300°C. This method results in absolute values of H_2O with uncertainties of ± 0.1 wt%.

For FTIR-based water analysis, we utilized a Bruker IFS 120 spectrometer coupled with a Bruker IR microscope. Spectra were obtained using a tungsten white light source, a silicon-coated calcium fluoride beam-splitter, and a liquid-nitrogen-cooled narrowband mercury cadmium telluride (MCT) detector. Measurements spanned the 1,000 to 10,000 cm⁻¹ range on doubly polished samples with thicknesses between 0.2 and 0.6 mm. Each measurement spot had a diameter of 60 µm, with spectra recorded at a resolution of 4 cm⁻¹. To improve accuracy and account for potential heterogeneity, 200 scans per spectrum were accumulated, and data were collected from three distinct locations per glass sample. The total FTIR-derived water content (H₂O_{total}) was derived from the integrated areas of the hydroxyl (OH⁻) and molecular water (H₂O_{mol}) absorption bands, positioned around 4,500 cm⁻¹ and 5,200 cm⁻¹, respectively. We followed the methodology presented in Ohlhorst et al. (2001), which incorporates glass density and SiO₂ content in wt% into the calculation (Bondar et al., 2023). We used a double gaussian baseline correction for areas and peaks (GG_{area} and GG_{peak}) and determined the density using the buoyancy method. Total water contents were quantified using the normalized SiO₂ wt% content obtained from EMPA measurements.

Micropenetration viscometry

Micropenetration (MP) viscometry was performed on plane-parallel, polished glass chips with a thickness of 2–3 mm. These measurements were conducted using a vertical dilatometer (Bähr VIS 404) at the Institute of Non-Metallic Materials, TU Clausthal. We measured the indentation rate of a sapphire sphere (r = 0.75 mm) during isothermal holding at controlled temperatures. Temperature regulation was achieved using an S-type thermocouple (Pt-PtRh) positioned approximately 1.5 mm from the sample surface, with an estimated error of ± 2 °C due

to thermocouple accuracy and placement (Behrens et al., 2018). Standard procedures (Di Genova et al., 2020b, 2014; Scarani et al., 2022; Valdivia et al., 2023) were followed to ensure proper thermal equilibration at the target temperature. The indentation depth was continuously recorded over time, and viscosity was calculated using Eq. 3 (Douglas et al., 1965):

$$\eta = \frac{3F}{16\sqrt{2rL}\frac{dl}{dt}}\tag{3}$$

where η is the Newtonian viscosity (Pa s), F is the applied force (N), t is the time (s), r is the radius of the sphere (m), L is the cumulative indentation depth (m), and $\frac{dl}{dt}$ is the indentation within a measurement interval. The dilatometer was calibrated with standard glass DGG-1, yielding viscosity values consistent with certified data (Meerlender, 1974) within a deviation of ± 0.1 log units.

Concentric cylinder (CC) viscometry

High-temperature viscosity measurements were conducted using a Haake RV20 Viscometer at the Institute of Non-Metallic Materials, TU Clausthal. The torque measurement of the device was calibrated over strain rates from 0.1 to 96 s⁻¹ using the standard DGG-1 (Deubener et al., 2009), and the error in viscosity was determined to be ± 0.02 log₁₀ units. Temperature monitoring was carried out using a factory-calibrated S-type thermocouple, with a precision of ± 2 °C. To achieve complete thermo-chemical homogenization, the glass materials were placed in a platinum crucible and stirred at a controlled shear rate under high-temperature conditions for

several hours. The temperature was then gradually reduced to lower set points. At each step, viscosity measurements were taken after maintaining stable conditions for a sufficient duration.

Differential scanning calorimetry

Both conventional differential scanning calorimetry (C–DSC) and flash differential scanning calorimetry (F–DSC) were employed to analyze the thermal properties of our hydrous glasses. Conventional differential scanning calorimetry (C–DSC) measurements of AND100 and AND0 hydrous samples were performed at the Institute of Non-Metallic Materials, TU Clausthal. Approximately 15 mg (\pm 5) of glass was placed in a Pt₈₀Rh₂₀ crucible under a constant N₂ (5.0) flow rate of 20 ml min⁻¹. Heat flow measurements were conducted using two conventional differential scanning calorimeters (C–DSC, 404 F3 Pegasus and 404 cell, Netzsch) at heating rates (q_h) of 10 and 20°C min⁻¹. In addition, flash differential scanning calorimetry (F–DSC) was performed on ~50 ng of glass using a Flash DSC 2+ (Mettler Toledo) with UFH 1 sensors, under a constant argon (Ar 5.0) flow of 40 ml min⁻¹. For the hydrous AND65 sample, C–DSC and F–DSC measurements were conducted at the GLASS (Gateway Laboratory of Amorphous and Structured Solids and Melts), CNR–ISSMC in Rome.

In our C–DSC experiments, we followed the methodology described by Stabile et al., 2021. To erase the thermal history of the glass, we applied a two-step thermal treatment. First, the sample underwent an initial upscan at a heating rate of $q_h = 20^{\circ}$ C min⁻¹ until it reached a temperature slightly above T_{peak} , referred to as T_{max} . Then, the melt was cooled to 100° C at rates of $q_c = 10$ or 20° C min⁻¹. The actual C–DSC measurements were carried out using the rate-matching method, which involved an additional upscan at a rate identical to the preceding cooling step (i.e., $q_h = q_c$). From the heat flow data recorded during this matching upscan, we determined the characteristic

temperatures T_{onset} and T_{peak} , both associated with phase transitions or thermal events occurring during the heating or cooling process. For further details see the methodology presented in previous work (Fanesi et al., 2025; Valdivia et al., 2023). For F–DSC experiments, we followed the methodology described above employing a $q_h = q_c = 1,000$ °C s⁻¹ (60,000 °C min⁻¹).

Viscosity values of iron-bearing samples, including an iron-free basalt, were derived from C- and F-DSC data using the relationship between the matching heating rate (q_h) of the measurement and the shift factors K_{onset} and K_{peak} (Al-Mukadam et al., 2020; Di Genova et al., 2020b; Yue, 2009; Zheng et al., 2017) expressed in Eq. 4:

$$log_{10}\eta(T_{onset,peak}) = K_{onset,peak} - log_{10}(q_h)$$
(4)

where $K_{onset} = 11.20 \pm 0.15$ and $K_{peak} = 9.84 \pm 0.20$ (Di Genova et al., 2020b; Stabile et al., 2021). It is important to mention that when q_h is 10 °C min⁻¹, $\eta(T_{onset}) \approx 10^{12}$ Pa s, and therefore, $T_{onset} \approx T_g$. The applicability of the shift factor approach for these compositions has been examined in Valdivia et al. (2025).

C–DSC-derived viscosities for hydrous AND0 used the same shift factors as iron-bearing samples. F–DSC data from the iron-free standard glass DGG-1 (70 wt% SiO₂) showed good agreement using $K_{onset} = 11.20 \pm 0.15$, but K_{peak} was slightly lower (~9.4 ± 0.20). We applied this correction to F–DSC-derived viscosities at peak temperatures for hydrous AND0.

Brillouin spectroscopy

Brillouin spectroscopy (BLS) measurements were performed at BGI. Glass plates with a plane-parallel geometry and a thickness of approximately 50 µm were analyzed using a solid-state

Nd:YVO₄ laser source (532 nm wavelength, 50 mW power). The Brillouin frequency shift was determined with a six-pass Fabry–Perot interferometer (Whitfield et al., 1976) coupled to a single-pixel photon counter detector. A symmetric forward scattering configuration (Cassetta et al., 2021; Whitfield et al., 1976) with a scattering angle of $\theta = 79.8^{\circ}$, was employed, with the angle accuracy verified through calibration against a reference silica glass. The frequency shifts ($\Delta\omega$) were converted into longitudinal (ν_p) and shear (ν_s) sound velocities using Eq. 5:

$$v = \frac{\Delta\omega\lambda}{2\sin(\theta/2)}\tag{5}$$

where λ is the laser wavelength and θ is the angle between the incident and scattered beams (Sinogeikin et al., 2006; Whitfield et al., 1976). Eight spectra were collected for each sample at varying rotation angles ranging from -180° to +180° to account for potential uncertainties. Finally, the K/G factor was determined by Eq. 6:

$$\frac{K}{G} = \left(\frac{v_p}{v_s}\right)^2 - \frac{4}{3} \tag{6}$$

Results and discussion

Characterization of starting materials

We synthesized six AND100 hydrous glasses with water contents ranging from 1.14 ± 0.1 to 5.15 ± 0.07 wt% H₂O, and seven hydrous AND0 glasses coverings 0.59 ± 0.1 to 5.56 ± 0.1 wt% H₂O. SEM-BSE analysis confirmed the absence of microlites or vesicles, indicating that no micrometric crystallization or degassing occurred during synthesis of hydrous glasses. The EMPA

chemical compositions are summarized in Tables 1 and 2, while Raman spectroscopy results of starting materials are presented in Fig. 1.

Raman analysis confirmed the lack of significant nanostruturation (i.e., nanoscale phase separation) and/or the presence of Fe-Ti-oxides crystals, feature in the 660-690 cm⁻¹ range (Bondar et al., 2025; Di Genova et al., 2020b; Jubb and Allen, 2010; Shebanova and Lazor, 2003; Valdivia et al., 2023). A minor, nearly negligible peak was observed in the 660-690 cm⁻¹ range for both AND100 and AND0 samples (Fig. 1). Nevertheless, the Boson peak position (Cassetta et al., 2021; Fanesi et al., 2025; Schroeder et al., 2004; Zanatta et al., 2011) (~70 cm⁻¹) closely matches that of anhydrous AND100 and AND0 samples (Valdivia et al., 2025). The Boson peak, located below 100 cm⁻¹, is a well-established signature of intrinsic structural disorder and is linked to collective atomic motions, particularly acoustic phonons, reflecting the short-to-medium-range order of glasses (Cassetta et al., 2021; Schroeder et al., 2004; Zanatta et al., 2011). Therefore, Raman spectroscopy results suggest that the starting materials were amorphous and virtually crystal-free.

KFT and FTIR total water concentration results are summarized in Table 1 and 2, while FTIR-derived water speciations are shown in Fig. 2.

Table 1. Chemical composition^a (wt%), densitiy^b, water contents (wt%) determined by KFT and FTIR, Brillouin spectroscopy results (K/G), Fe^{3+}/Fe_{tot} ratio^e, and glass transition temperature (T_g) of hydrous starting materials (AND100 and AND65 series).

	AND100_1.14	AND100_1.56	AND100_2.21	AND100_3.21	AND100_3.81	AND100_5.15	AND65_4.2
SiO ₂	58.39 (0.24)	58.22 (0.26)	57.32 (0.32)	57.48 (0.25)	57.28 (0.27)	56.73 (0.29)	58.10 (0.19)
TiO_2	0.80 (0.05)	0.73 (0.03)	0.76 (0.05)	0.71 (0.06)	0.77 (0.05)	0.75 (0.05)	0.48 (0.03)
Al_2O_3	16.13 (0.12)	16.12 (0.09)	15.91 (0.12)	15.92 (0.17)	15.78 (0.12)	15.60 (0.11)	16.19 (0.19)
FeO_{tot}	6.52 (0.15)	6.42 (0.20)	6.51 (0.10)	6.15 (0.07)	6.09 (0.13)	5.88 (0.13)	3.87 (0.05)
MnO	0.15 (0.04)	0.15 (0.03)	0.17 (0.02)	0.15 (0.03)	0.16 (0.04)	0.16 (0.04)	0.09 (0.04)
MgO	2.85 (0.06)	2.82 (0.08)	2.77 (0.05)	2.71 (0.06)	2.70 (0.08)	2.62 (0.09)	2.92 (0.07)
CaO	6.41 (0.12)	6.30 (0.14)	6.38 (0.11)	6.17 (0.12)	6.13 (0.10)	5.99 (0.08)	6.34 (0.12)
Na ₂ O	3.27 (0.07)	3.26 (0.06)	3.31 (0.10)	3.27 (0.07)	3.18 (0.08)	3.14 (0.09)	3.25 (0.10)
K_2O	1.46 (0.06)	1.49 (0.03)	1.50 (0.02)	1.47 (0.05)	1.47 (0.05)	1.47 (0.05)	1.49 (0.05)
P_2O5	0.18 (0.06)	0.20 (0.04)	0.17 (0.05)	0.16 (0.04)	0.19 (0.07)	0.19 (0.07)	0.19 (0.05)
H_2O (KFT)	1.14 (0.1)	1.56 (0.1)	2.21 (0.1)	-	3.85 (0.1)	-	-
H ₂ O ^c (GG _{area})	1.01 (0.02)	1.3 (0.03)	2.2 (0.07)	3.2 (0.01)	-	5.15 (0.07)	4.2 (0.24)
H ₂ O ^c (GG _{peak})	1.15 (0.02)	1.49 (0.03)	2.43 (0.07)	3.47 (0.01)	-	5.49 (0.07)	4.73 (0.14)
ρ (g l ⁻¹)	2578 (2)	2576 (3)	2556 (2)	2510 (2)	-	2506 (2)	2450 (3)
K/G^d	-	1.59 (0.02)	1.60 (0.02)	1.61 (0.02)	1.62 (0.02)	1.64 (0.02)	1.59 (0.02)
$Fe^{3+}\!/F{e_{tot}}^e$	0.22	0.33	0.41	0.42	-	0.35	-
$T_g^f(^{\circ}C)$	545.1 (1)	516.5 (1)	474.6 (1)	437.4 (1)	389.7 (1)	380.3 (1)	411 (1)

^aAverage chemical composition from electron microprobe analysis (n = 10); errors represent $\pm 1\sigma$.

 $^{^{}b}$ Density values obtained using the Archimedes' buoyancy method; errors represent $\pm 1\sigma$

 $^{^{}c}$ Water content determined by FTIR analysis following Ohlhorst et Al. (2001); errors represent $\pm 1\sigma$.

^dElastic moduli derived from Brillouin spectroscopy; errors represent $\pm 1\sigma$.

 $^{{}^{}c}Fe^{3+}/Fe_{tot.}$ ratio estimated using Mossa software (Prescher et al. 2012). ${}^{f}Glass$ transition temperatures determined by C-DSC; experimental errors are reported in parentheses.

Table 2. Chemical composition^a (wt%), densitiy^b, water contents (wt%) determined by KFT and FTIR, Brillouin spectroscopy results (K/G), Fe³⁺/Fe_{tot.} ratio^e, and glass transition temperature (T_g) of hydrous starting materials (AND0 series).

	AND0_0.59	AND0_0.94	AND0_2.00	AND0_2.21	AND0_3.18	AND0_4.76	AND0_5.56
SiO_2	63.73 (0.24)	63.58 (0.27)	63.20 (0.39)	63.04 (0.39)	62.56 (0.32)	61.80 (0.20)	60.50 (0.28)
TiO_2	0.03 (0.03)	0.03 (0.03)	0.03 (0.04)	0.03 (0.03)	0.03 (0.03)	0.03 (0.03)	0.03 (0.02)
Al_2O_3	17.57 (0.13)	17.49 (0.13)	17.27 (0.11)	17.22 (0.11)	17.05 (0.12)	16.77 (0.12)	16.56 (0.17)
FeO_{tot}	0.02 (0.02)	0.01 (0.02)	0.01 (0.01)	0.01 (0.01)	0.01 (0.01)	0.00 (0.00)	0.01 (0.02)
MnO	0.01 (0.01)	0.01 (0.01)	0.01 (0.01)	0.01 (0.01)	0.01 (0.01)	0.01 (0.01)	0.01 (0.01)
MgO	3.05 (0.06)	3.02 (0.06)	2.90 (0.06)	2.90 (0.06)	2.89 (0.06)	2.88 (0.06)	2.85 (0.06)
CaO	7.08 (0.07)	7.05 (0.07)	6.94 (0.11)	6.92 (0.10)	6.88 (0.10)	6.81 (0.11)	6.69 (0.07)
Na_2O	3.67 (0.11)	3.64 (0.11)	3.54 (0.10)	3.52 (0.10)	3.49 (0.10)	3.43 (0.11)	3.26 (0.11)
K_2O	1.69 (0.08)	1.69 (0.08)	1.70 (0.06)	1.69 (0.06)	1.66 (0.06)	1.61 (0.05)	1.57 (0.05)
P_2O5	0.22 (0.04)	0.22 (0.04)	0.21 (0.06)	0.21 (0.06)	0.20 (0.06)	0.19 (0.06)	0.19 (0.07)
H ₂ O (KFT)	0.59 (0.1)	0.94 (0.1)	2.00 (0.1)	2.21 (0.1)	3.18 (0.1)	4.76 (0.1)	5.56 (0.1)
H ₂ O ^c (GG _{area})	0.43 (0.01)	-	2.02 (0.01)	2.12 (0.01)	-	4.42 (0.01)	6.60 (0.03)
H ₂ O ^c (GG _{peak})	0.46 (0.01)	-	2.09 (0.01)	2.24 (0.1)	-	4.52 (0.01)	6.71 (0.03)
ρ (g 1 ⁻¹)	2659 (2)	-	2400 (2)	2484 (3)	-	2363 (2)	2233 (3)
K/G^{d}	1.49 (0.02)	1.51 (0.02)	1.52 (0.02)	1.51 (0.02)	1.53 (0.02)	1.55 (0.02)	1.56 (0.02)
T_g^e (°C)	630.3 (1)	615.4(1)	515.8 (1)	503.3 (1)	450.2 (1)	418.8 (1)	383.4 (1)

^aAverage chemical composition from electron microprobe analysis (n = 10); errors represent $\pm 1\sigma$.

FTIR water speciation trend for AND100 aligns with previous findings for hydrous andesitic glasses reported by Richet et al. (1996), where hydroxyl groups dominate at water concentrations below 3.5 wt%. In contrast, for AND0, hydroxyl dominance extends up to ~4.5 wt%, similar to observations by Ohlhorst et al. (2001). This difference is likely due to variations in quenching rates during synthesis, as AND100 was cooled rapidly (~150 °C s⁻¹) in an IHPV, while AND0 experienced slower cooling (~100 °C s⁻¹) in a piston-cylinder apparatus, leading to greater retention of molecular water and altering final water speciation (Bondar et al., 2023; Dingwell, 1990).

 $^{^{}b}$ Density values obtained using the Archimedes' buoyancy method; errors represent $\pm 1\sigma$

[°]Water content determined by FTIR analysis following Ohlhorst et Al. (2001); errors represent $\pm 1\sigma$.

^dElastic moduli derived from Brillouin spectroscopy; errors represent $\pm 1\sigma$.

 $^{^{}e}Fe^{3+}/Fe_{tot.}$ ratio estimated using Mossa software (Prescher et al. 2012).

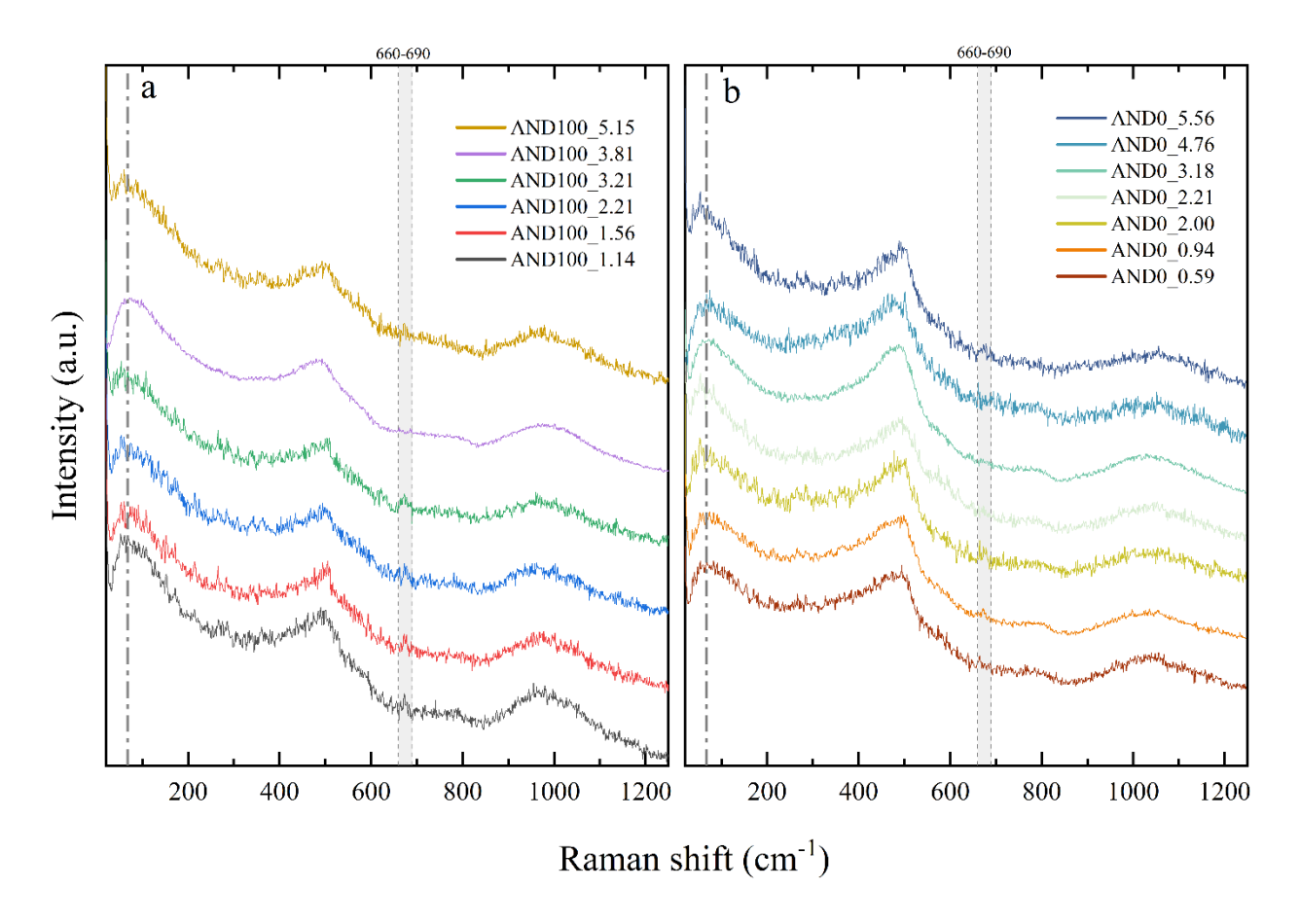


Figure 1. **Raman spectra of starting materials**. The shaded area in grey (660-690 cm⁻¹) corresponds to the most prominent area commonly affected by nanostruturation and/or the presence of Fe-Ti-bearing crystals (Di Genova et al., 2020b; Valdivia et al., 2023) and the dashed line corresponds to the Boson peak (Cassetta et al., 2021; Schroeder et al., 2004; Zanatta et al., 2011). a) AND100 hydrous starting samples. b) AND0 hydrous starting samples.

The close agreement between FTIR and KFT results (Fig. 3, Tables 1 and 2) confirms the reliability of both methods for measuring water content in andesitic glasses. However, at H₂O_{total} concentrations exceeding ~5 wt%, FTIR measurements tend to overestimate water content relative to KFT. Notably, GG_{area}-based water estimations align more closely with KFT values in the 2-6 wt% H₂O_{total} range (Fig. 3). Given these observations, KFT measurements are adopted as the reference for water content in this study, providing a reliable basis for evaluating the influence of water and transition metal content on andesitic melt viscosity.

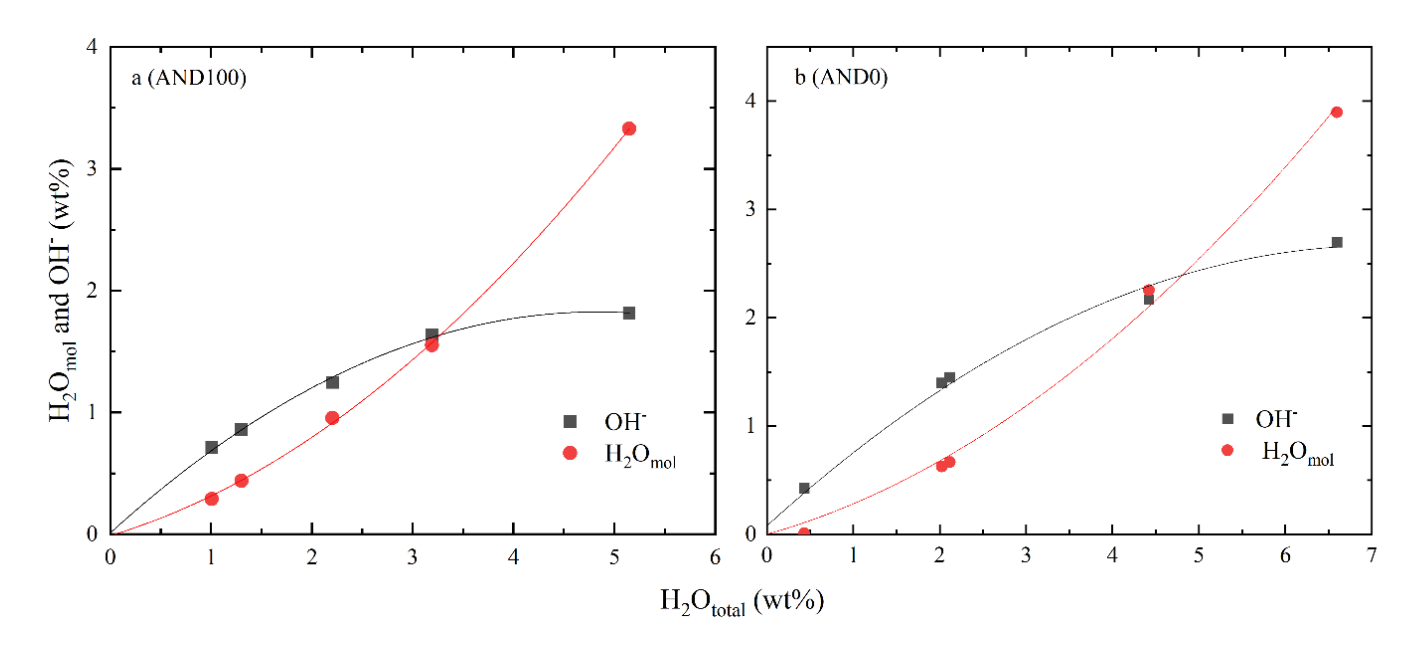


Figure 2. FTIR-derived concentrations of molecular water (H_2O_{mol}) and hydroxyl groups (OH^-) plotted against total water content (H_2O_{total}) . Standard deviations of measurements are smaller than the symbol size. a) AND100 b) AND0.

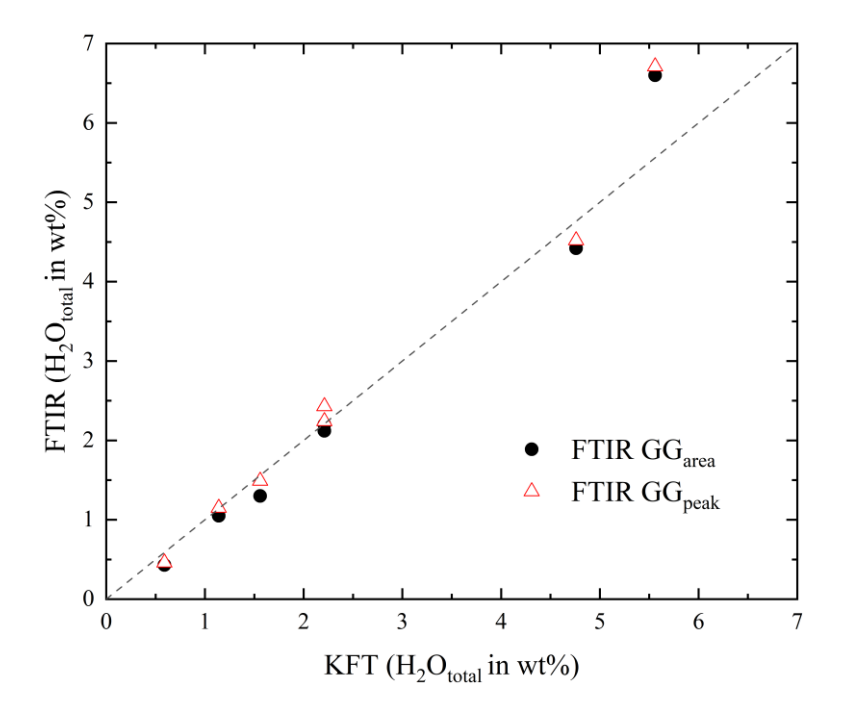


Figure 3. FTIR-derived concentrations of molecular water (H_2O_{mol}) and hydroxyl groups (OH^-) of AND100 and AND0 samples plotted against total water content (H_2O_{total}) . Standard deviations of measurements are smaller than the symbol size.

Mössbauer spectroscopy results for the AND100 starting materials (Table 1) indicate a general increase in $Fe^{3+}/Fe_{tot.}$ with increasing water content, followed by a slight decline at 5.15 ± 0.07 wt% H_2O . This pattern align with findings by Fanesi et al. (2025) for tephri-phonolitic compositions and further highlights the influence of water on iron redox dynamics in hydrous silicate glasses.

Viscosity results

Viscosity measurements of hydrous andesitic melts were conducted using micropenetration (MP) viscometry, complemented by data obtained from C-DSC and F-DSC (Al-Mukadam et al., 2020; Stabile et al., 2021). To evaluate potential alterations in melt properties during experiments, such as amorphous phase separation (e.g., Valdivia et al. 2025), nanocrystallization (e.g., Di Genova et al., 2017), water loss (e.g., Valdivia et al., 2023), or iron oxidation (e.g., Di Genova et al., 2016), post-run characterizations were performed using Raman spectroscopy, FTIR, and Mössbauer spectroscopy.

The resulting viscosity values, with post-experimental Mössbauer analyses, are summarized in Table 3. Mössbauer spectroscopy confirms that the AND100 hydrous samples experienced minimal iron oxidation during C-DSC and MP analyses, with variations in Fe³⁺/Fe_{tot}. (Δ Fe³⁺/Fe_{tot}) ranging between 0.01 to 0.05, well within the analytical uncertainty. The glass transition temperature (T_g), defined as the temperature at which viscosity is equal to 10^{12} Pa s, was determined using the T_{onset} values obtained via C-DSC experiments with at a heating rate of 10 °C min⁻¹ (i.e., C-DSC_{10_on} in Table 3). T_g values for the AND100 and AND0 series are reported in Table 1 and Table 2, respectively. In both series, T_g decreases systematically with increasing water content. Considering the T_g values reported in Valdivia et al. (2025), the AND100 T_g drops from

654± 1 °C to 380±1 °C (ΔT_g = 274°C) as total water content increases from anhydrous conditions up to 5.15 wt.% (Fig. 2). In contrast, AND0 exhibits a more pronounced decrease, with T_g declining from 737±1 °C to 383.4±1 °C (ΔT_g = 353°C) over a similar water content range up to 5.56 wt.%. Thus, while both compositions show a negative correlation between T_g and water content, the magnitude of ΔT_g is significantly larger for the AND0 series compared to AND100, suggesting a stronger depolymerizing effect of water in the Fe-free system.

When comparing our T_g results for hydrous AND100 with predictions from the Giordano et al. (2008) model (GRD), we observe a good correlation for water contents between 1.4 and 1.56 wt.%. However, at water contents exceeding 2 wt.%, the GRD model does not account for the effect of transition metals, predicting almost the same T_g values for AND100 and AND0 compositions. In contrast, the GRD model aligns better with our measurements for AND0, showing a smaller discrepancy across the entire water content range. This behavior aligns with the findings of Valdivia et al. (2023), suggesting that the GRD model may overestimate viscosities of transition-metals-bearing melts.

Following C-DSC measurements, MP experiments were conducted at the C-DSC_{10_pk} temperatures (Table 3). Post-MP Raman spectroscopic analyses (Fig. 5) revealed that all AND100 hydrous glasses, with the exception of AND100_1.14, experienced nanocrystallization of Fe-Ti oxides during MP experiments (Fig. 5a). This is evidenced by the emergence of Raman peaks between 660-690 cm⁻¹, characteristic of Fe-Ti-nanolites (Bondar et al., 2025; Di Genova et al., 2017; Fanesi et al., 2025; Valdivia et al., 2023), along with a shift of the Boson peak toward lower frequencies (Fanesi et al., 2025).

Table 3. C-DSC, F-DSC, MP, and CC result as a function of temperature and post-experimental Mössbauer results.

ANDIOQ_L14	Sample	Type ^a	T (°C)	$\log \eta \ (\eta \ \text{in Pa s})$	$\Delta Fe^{3+}/Fe_{tot}^{b}$	Sample	Type ^a	T (°C)	$\log \eta \; (\eta \; \text{in Pa s})$
C-DSC _{01 in} 548 11.68 - C-DSC _{01 in} 644 11.68 10.32 C-DSC _{01 in} 687 10.32 10.32 C-DSC _{01 in} 687 10.32 C-DSC _{01 in} 688 10.32 C-DSC _{01 in} 688 688 C-DSC _{01 in} 689 C-DSC _{01 in} 689	AND100_1.14	C-DSC _{10 on}	545	11.98	-	AND0_0.59	$C\text{-}DSC_{10}$ on	630	11.98
C-DSC _{29 1k} 590 10.32 0.03 C-DSC _{29 1k} 687 10.32 P-DSC _{100 co} 661 8.20 - F-DSC _{100 co} 769 8.20 P-DSC _{100 co} 769 8.20 P-DSC _{100 co} 789 8.20 P-DSC _{100 co} 7		$\text{C-DSC}_{10\ pk}$	580	10.62	0.05		$\text{C-DSC}_{10\ pk}$	675	10.62
F-DSC-1000 as 661 8.20 - F-DSC-1000 as 871 6.84 F-DSC-1000 as 738 6.84 - F-DSC-1000 as 871 6.84 MP-311 581 10.77 0.05 MP-82 675 11.02 AND100_1.56 C-DSC-10 as 517 11.98		C-DSC _{20 on}	548	11.68	-		C-DSC _{20 on}	644	11.68
F-DSC _{1000 pt} 738 6.84 - F-DSC _{1000 pt} 871 6.84		$C\text{-}DSC_{20\ pk}$	590	10.32	0.03		$\text{C-DSC}_{20\ pk}$	687	10.32
AND100_1.56		$F\text{-}DSC_{1000\ on}$	661	8.20	-		$F\text{-}DSC_{1000\ on}$	769	8.20
AND100_1.56 C-DSC _{10 ak} 556 10.62 0.01 C-DSC _{10 ak} 652 10.6		$F\text{-}DSC_{1000\ pk}$	738	6.84	-		$F\text{-}DSC_{1000\ pk}$	871	6.84
C-DSC _{10 pk} 556 10.62 0.01 C-DSC _{10 pk} 652 10.62 10.62 C-DSC _{20 pk} 652 10.62 11.68 - MP _{cut} 648 10.87 C-DSC _{20 pk} 569 10.32 - AND0_2.00 C-DSC _{10 pk} 559 10.62 11.98 F-DSC _{1000 pk} 559 10.62 11.98 P-DSC _{1000 pk} 559 10.62 11.98 P-DSC _{1000 pk} 555 10.88 - C-DSC _{20 pk} 559 10.62 P-DSC _{20 pk} 555 11.03 0.01 F-DSC _{100 pk} 555 11.03 0.01 F-DSC _{100 pk} 563 10.32 P-DSC _{20 pk} 514 11.68 P-DSC _{20 pk} 515 11.03 0.01 P-DSC _{20 pk} 510 11.68 P-DSC _{20 pk} 515 10.32 0.02 P-DSC _{20 pk} 553 10.32 P-DSC _{20 pk} 515 10.32 0.02 P-DSC _{20 pk} 553 10.32 P-DSC _{20 pk} 515 10.92 P-DSC _{20 pk} 515 10.32 P-DSC _{20 pk} 515 10.32 P-DSC _{20 pk} 515 10.92 P-DSC _{20 pk} 516 11.98 P-DSC _{20 pk} 516 11.98 P-DSC _{20 pk} 516 11.98 P-DSC _{20 pk} 515 10.92 P-DSC _{20 pk} 515 10.92 P-DSC _{20 pk} 515 10.92 P-DSC _{20 pk} 516 11.98 P-DSC _{20 p}		MP_{581}	581	10.77	0.05		MP ₆₇₅	675	11.02
C-DSC _{20 gas} 525	AND100_1.56	$C ext{-}DSC_{10 \ on}$	517	11.98	-	AND0_0.94	$C\text{-}DSC_{10\ on}$	615	11.98
C-DSC _{20 pk} 569 10.32 - AND0_2.00 C-DSC _{10 m} 516 11.98		C-DSC _{10 pk}	556	10.62	0.01		$\text{C-DSC}_{10\ pk}$	652	10.62
F-DSC 1000 cm 630 8.20 - C-DSC 20 cm 514 11.68 F-DSC 1000 μk 703 6.84 - C-DSC 20 cm 514 11.68 MP 255 0 555 10.85 - C-DSC 20 cm 514 11.68 MP 255 100 555 11.03 0.01 F-DSC 1000 cm 631 8.20 AND100 2.21 C-DSC 20 cm 475 11.98 - F-DSC 1000 cm 503 11.98 C-DSC 20 cm 475 11.68 - C-DSC 20 cm 503 11.98 C-DSC 20 cm 481 11.68 - C-DSC 20 cm 510 11.68 C-DSC 20 cm 481 11.68 - C-DSC 20 cm 510 11.68 F-DSC 1000 cm 580 8.20 - C-DSC 20 cm 510 11.68 F-DSC 1000 cm 515 10.92 - F-DSC 1000 cm 621 8.20 MP 315 0 515 10.92 - F-DSC 1000 cm 621 8.20 MP 315 0 515 11.01 - MP 346 546 10.65 AND100 3.21 C-DSC 20 cm 437 11.98 - AND0 3.18 C-DSC 20 cm 450 11.98 C-DSC 20 cm 440 11.68 - C-DSC 20 cm 450 11.68 C-DSC 20 cm 440 11.68 - C-DSC 20 cm 462 11.68 C-DSC 20 cm 440 11.68 - C-DSC 20 cm 462 11.68 C-DSC 20 cm 440 11.68 - C-DSC 20 cm 462 11.68 C-DSC 20 cm 440 11.68 - C-DSC 20 cm 462 11.68 C-DSC 20 cm 440 11.68 - C-DSC 20 cm 462 11.68 C-DSC 20 cm 440 11.68 - C-DSC 20 cm 462 11.68 C-DSC 20 cm 440 11.68 - C-DSC 20 cm 442 11.68 C-DSC 20 cm 443 10.62 - AND0 4.76 C-DSC 20 cm 442 11.68 C-DSC 20 cm 438 10.62 - C-DSC 20 cm 428 11.68 C-DSC 20 cm 438 10.62 - C-DSC 20 cm 428 11.68 C-DSC 20 cm 438 10.62 - C-DSC 20 cm 428 11.68 C-DSC 20 cm 445 11.68 - C-DSC 20 cm 428 11.68 C-DSC 20 cm 445 11.68 - C-DSC 20 cm 428 11.68 C-DSC 20 cm 445 11.68 - C-DSC 20 cm 428 11.68 C-DSC 20 cm 445 11.68 - C-DSC 20 cm 428 11.68 C-DSC 20 cm		C-DSC _{20 on}	525	11.68	-		MP_{648}	648	10.87
F-DSC _{1000 pk} 703 6.84 - C-DSC _{20 m} 514 11.68 MP _{355 100} 555 10.85 - C-DSC _{20 mk} 563 10.32 MP _{555 100} 555 11.03 0.01 F-DSC _{100 cm} 631 8.20 AND100_2.21 C-DSC _{10 cm} 475 11.98 - F-DSC _{100 cm} 503 11.98 C-DSC _{20 cm} 481 11.68 - C-DSC _{10 cm} 503 11.98 C-DSC _{20 cm} 527 10.32 0.02 C-DSC _{10 cm} 510 11.68 F-DSC _{100 cm} 580 8.20 - C-DSC _{20 cm} 510 11.68 F-DSC _{100 cm} 655 6.84 - F-DSC _{100 cm} 621 8.20 MP _{315 100} 515 10.92 - F-DSC _{100 cm} 621 8.20 MP _{315 100} 515 11.01 - F-DSC _{100 cm} 621 8.20 AND100_3.21 C-DSC _{10 cm} 437 11.98 - AND0_3.18 C-DSC _{10 cm} 503 11.98 C-DSC _{20 cm} 440 11.68 - C-DSC _{20 cm} 465 11.68 C-DSC _{20 cm} 440 11.68 - C-DSC _{20 cm} 465 11.68 C-DSC _{20 cm} 440 11.68 - C-DSC _{20 cm} 462 11.68 C-DSC _{20 cm} 440 11.68 - C-DSC _{20 cm} 462 11.68 C-DSC _{20 cm} 440 11.68 - C-DSC _{20 cm} 462 11.68 C-DSC _{20 cm} 440 11.68 - C-DSC _{20 cm} 462 11.68 C-DSC _{20 cm} 433 10.32 - C-DSC _{20 cm} 462 11.68 C-DSC _{20 cm} 440 11.68 - C-DSC _{20 cm} 462 11.68 C-DSC _{20 cm} 440 11.68 - C-DSC _{20 cm} 462 11.68 C-DSC _{20 cm} 440 11.68 - C-DSC _{20 cm} 462 11.68 C-DSC _{20 cm} 440 11.68 - C-DSC _{20 cm} 462 11.68 C-DSC _{20 cm} 440 11.68 - C-DSC _{20 cm} 462 11.68 C-DSC _{20 cm} 440 11.68 - C-DSC _{20 cm} 462 11.68 C-DSC _{20 cm} 440 11.68 - C-DSC _{20 cm} 462 11.68 C-DSC _{20 cm} 440 11.68 - C-DSC _{20 cm} 462 11.68 C-DSC _{20 cm} 440 11.68 - C-DSC _{20 cm} 462 11.68 C-DSC _{20 cm} 440 11.68 - C-DSC _{20 cm} 462 11.68 C-DSC _{20 cm} 440 11.68 - C-DSC _{20 cm} 462 11.68 C-DSC _{20 cm} 440 11.68 - C-DSC _{20 cm} 462 11.68 C-DSC _{20 cm} 453 10.32 - C-DSC _{20 cm} 428 11.68 C-DSC _{20 cm} 411 11.68 - C-DSC _{20 cm} 428 11.68 C-DSC _{20 cm} 453 10.32 - C-DSC _{20 cm} 428 11.68 C-DSC _{20 cm} 453 10.32 - C-DSC _{20 cm} 465 10.69 C-DSC _{20 cm} 453 10.32 - C-DSC _{20 cm} 465 10.69 C-DSC _{20 cm} 453 10.32 - C-DSC _{20 cm} 465 10.69 C-DSC _{20 cm} 453 10.32 - C-DSC _{20 cm} 465 10.69 C-DSC _{20 cm} 453 10.32 - C-DSC _{20 cm} 465 10.69 C-DSC _{20 cm} 453 10.62 - AND0_5.56 C-DSC _{20 cm} 383 11.98		C-DSC _{20 pk}	569	10.32	-	AND0_2.00	$C\text{-}DSC_{10\ on}$	516	11.98
MP _{355 100} 555 10.85 - C-DSC _{20 pik} 563 10.32 AND100_2.21 C-DSC _{10 pik} 516 11.98 - F-DSC _{1000 pik} 722 6.84 C-DSC _{20 pik} 516 10.62 0.01 AND0_2.21 C-DSC _{10 pik} 546 10.62 C-DSC _{20 pik} 527 10.32 0.02 C-DSC _{20 pik} 546 10.62 F-DSC _{1000 pik} 655 6.84 - C-DSC _{20 pik} 553 10.32 F-DSC _{1000 pik} 655 6.84 - F-DSC _{1000 pik} 515 11.01 - F-DSC _{1000 pik} 546 10.75 AND100_3.21 C-DSC _{10 pik} 482 10.62 0.01 AND0_3.18 C-DSC _{10 pik} 546 10.75 AND100_3.21 C-DSC _{20 pik} 493 10.32 - AND0_3.18 C-DSC _{20 pik} 500 10.62 C-DSC _{20 pik} 493 10.32 - C-DSC _{20 pik} 500 10.62 C-DSC _{20 pik} 493 10.32 - C-DSC _{20 pik} 500 10.62 AND100_3.81 C-DSC _{10 pik} 485 10.62 0.01 C-DSC _{20 pik} 500 10.62 C-DSC _{20 pik} 493 10.32 - C-DSC _{20 pik} 500 10.62 C-DSC _{20 pik} 493 10.32 - C-DSC _{20 pik} 500 10.62 C-DSC _{20 pik} 493 10.32 - C-DSC _{20 pik} 500 10.62 C-DSC _{20 pik} 493 10.32 - C-DSC _{20 pik} 500 10.62 C-DSC _{20 pik} 493 10.32 - C-DSC _{20 pik} 507 10.32 F-DSC _{1000 pik} 616 6.84 - C-DSC _{20 pik} 465 10.62 AND100_3.81 C-DSC _{10 pik} 438 10.62 - AND0_4.76 C-DSC _{20 pik} 465 10.62 C-DSC _{20 pik} 438 10.62 - C-DSC _{20 pik} 472 10.32 C-DSC _{20 pik} 438 10.62 - C-DSC _{20 pik} 465 10.62 C-DSC _{20 pik} 453 10.32 - C-DSC _{10 pik} 605 6.84 AND100_5.15 C-DSC _{10 pik} 453 10.32 - C-DSC _{10 pik} 605 6.84 AND100_5.15 C-DSC _{10 pik} 453 10.32 - C-DSC _{10 pik} 605 6.84 AND100_5.15 C-DSC _{10 pik} 423 10.62 - AND0_5.56 C-DSC _{10 pik} 605 6.84		$F\text{-}DSC_{1000~on}$	630	8.20	-		$\text{C-DSC}_{10\ pk}$	559	10.62
ANDIOQ_2.21 C-DSC _{10 on} 555 11.03 0.01 F-DSC _{1000 on} 631 8.20 ANDIOQ_2.21 C-DSC _{10 on} 475 11.98 - F-DSC _{1000 on} 722 6.84 C-DSC _{10 on} 516 10.62 0.01 ANDO_2.21 C-DSC _{10 on} 503 11.98 C-DSC _{20 on} 481 11.68 - C-DSC _{20 on} 510 11.68 F-DSC _{1000 on} 527 10.32 0.02 C-DSC _{20 on} 510 11.68 F-DSC _{1000 on} 580 8.20 - C-DSC _{20 on} 553 10.32 F-DSC _{1000 on} 655 6.84 - F-DSC _{1000 on} 621 8.20 MP _{515 o} 515 10.92 - F-DSC _{1000 on} 621 8.20 MP _{515 o} 515 11.01 - MP ₅₄₆ 546 10.75 ANDIOQ_3.21 C-DSC _{20 on} 440 11.68 - ANDO_3.18 C-DSC _{10 on} 450 11.98 C-DSC _{20 on} 440 11.68 - C-DSC _{20 on} 462 11.68 C-DSC _{20 on} 539 8.20 - ANDO_4.76 C-DSC _{20 on} 462 11.68 F-DSC _{1000 on} 539 8.20 - ANDO_4.76 C-DSC _{10 on} 419 11.98 F-DSC _{1000 on} 539 8.20 - ANDO_4.76 C-DSC _{10 on} 419 11.98 F-DSC _{1000 on} 539 8.20 - ANDO_4.76 C-DSC _{20 on} 442 11.68 C-DSC _{20 on} 443 11.98 F-DSC _{1000 on} 539 8.20 - ANDO_4.76 C-DSC _{20 on} 428 11.68 C-DSC _{20 on} 428 11.68 C-DSC _{20 on} 443 11.98 F-DSC _{1000 on} 539 8.20 - ANDO_4.76 C-DSC _{10 on} 419 11.98 F-DSC _{1000 on} 539 8.20 - ANDO_4.76 C-DSC _{20 on} 428 11.68 C-DSC _{20 on} 428 11.68 C-DSC _{20 on} 441 11.68 - C-DSC _{20 on} 428 11.68 C-DSC _{20 on} 428 11.68 C-DSC _{20 on} 441 11.68 - C-DSC _{20 on} 428 11.68 C-DSC _{20 on} 442 11.68 C-DSC _{20 on} 443 11.98 - C-DSC _{20 on} 442 10.32 C-DSC _{20 on} 441 11.68 C-DSC _{20 on} 442 11.68 C-DSC _{20 on} 442 11.68 C-DSC _{20 on} 443 11.68 C-DSC _{20 on} 442 11.68 C-DS		$F\text{-}DSC_{1000\ pk}$	703	6.84	-		C-DSC _{20 on}	514	11.68
AND100_2.21 C-DSC _{10 on} 475 11.98		$MP_{555\ 0}$	555	10.85	-		$\text{C-DSC}_{20\ pk}$	563	10.32
C-DSC _{10 pk} 516 10.62 0.01 ANDO_2.21 C-DSC _{10 on} 503 11.98 C-DSC _{20 on} 481 11.68 - C-DSC _{20 pk} 546 10.62 C-DSC _{20 pk} 527 10.32 0.02 C-DSC _{20 pk} 546 10.62 F-DSC _{1000 on} 580 8.20 - C-DSC _{20 pk} 553 10.32 F-DSC _{1000 pk} 655 6.84 - F-DSC _{1000 pk} 655 6.84 - F-DSC _{1000 pk} 717 6.84 MP _{315 0} 515 11.01 - MP ₃₄₆ 546 10.75 ANDIOO_3.21 C-DSC _{10 pk} 482 10.62 0.01 C-DSC _{10 pk} 482 10.62 0.01 C-DSC _{20 pk} 500 10.62 C-DSC _{20 pk} 493 10.32 - C-DSC _{20 pk} 507 10.32 F-DSC _{1000 on} 539 8.20 - ANDO_4.76 C-DSC _{20 pk} 507 10.32 F-DSC _{1000 on} 438 10.62 - C-DSC _{20 pk} 465 10.62 ANDIOO_3.81 C-DSC _{10 pk} 438 10.62 - C-DSC _{20 pk} 472 10.32 C-DSC _{20 on} 411 11.68 - C-DSC _{20 on} 428 11.68 C-DSC _{20 on} 411 11.68 - F-DSC _{1000 on} 430 11.98 C-DSC _{20 on} 428 11.68 C-DSC _{20 on} 411 11.68 - C-DSC _{20 on} 428 11.68 C-DSC _{20 on} 411 11.68 - C-DSC _{20 on} 428 11.68 C-DSC _{20 on} 428 11.68 C-DSC _{20 on} 438 10.62 - C-DSC _{20 on} 428 11.68 C-DSC _{20 on} 411 11.68 - C-DSC _{20 on} 428 11.68 C-DSC _{20 on} 438 10.32 - C-DSC _{20 on} 428 11.68 C-DSC _{20 on} 411 11.68 - C-DSC _{20 on} 428 11.68 C-DSC _{20 on} 438 10.62 - C-DSC _{20 on} 428 11.68 C-DSC _{20 on} 438 10.32 - C-DSC _{20 on} 428 11.68 C-DSC _{20 on} 438 10.32 - C-DSC _{20 on} 455 10.69 C-DSC _{20 on} 452 10.69 C-DSC _{20 on} 453 10.32 C-DSC _{20 on} 455 10.69 C-DSC _{20 on} 455 10.69 C-DSC _{20 on} 452 10.69 C-DSC ₂₀		MP _{555 100}	555	11.03	0.01		F-DSC _{1000 on}	631	8.20
C-DSC _{20 on} 481 11.68 - C-DSC _{10 pk} 546 10.62 C-DSC _{20 pk} 527 10.32 0.02 C-DSC _{20 on} 510 11.68 F-DSC _{1000 on} 580 8.20 - C-DSC _{20 pk} 553 10.32 F-DSC _{1000 pk} 655 6.84 - F-DSC _{1000 en} 621 8.20 MP _{515 0} 515 10.92 - F-DSC _{1000 pk} 717 6.84 MP _{515 100} 515 11.01 - MP ₅₄₆ 546 10.75 AND100_3.21 C-DSC _{10 pk} 482 10.62 0.01 C-DSC _{10 pk} 500 11.68 C-DSC _{20 pk} 493 10.32 - C-DSC _{20 pk} 507 10.32 F-DSC _{1000 pk} 616 6.84 - C-DSC _{20 pk} 507 10.32 F-DSC _{1000 pk} 616 6.84 - C-DSC _{20 pk} 465 10.62 AND100_3.81 C-DSC _{10 pk} 438 10.62 - C-DSC _{20 on} 428 11.68 C-DSC _{20 on} 411 11.68 - C-DSC _{20 on} 428 11.68 C-DSC _{20 on} 411 11.68 - F-DSC _{1000 pk} 465 10.62 AND100_5.15 C-DSC _{20 on} 411 11.68 - F-DSC _{1000 pk} 465 10.62 C-DSC _{20 pk} 438 10.62 - F-DSC _{1000 pk} 465 10.62 C-DSC _{20 pk} 438 10.62 - F-DSC _{1000 pk} 465 10.62 C-DSC _{20 pk} 453 10.32 - F-DSC _{1000 pk} 465 10.62 C-DSC _{20 pk} 453 10.32 - F-DSC _{1000 pk} 465 10.62 C-DSC _{20 pk} 453 10.32 - F-DSC _{1000 pk} 465 10.69 C-DSC _{20 pk} 453 10.32 - F-DSC _{1000 pk} 465 10.69 C-DSC _{20 pk} 453 10.32 - F-DSC _{1000 pk} 465 10.69 C-DSC _{20 pk} 453 10.32 - F-DSC _{1000 pk} 465 10.69 C-DSC _{20 pk} 453 10.32 - MND ₄₆₅ 465 10.69 C-DSC _{20 pk} 453 10.62 - AND ₄₆₅ C-DSC _{10 on} 383 11.98	AND100_2.21	C-DSC _{10 on}	475	11.98	-		F-DSC _{1000 pk}	722	6.84
C-DSC _{20 pk} 527 10.32 0.02 C-DSC _{20 cm} 510 11.68 F-DSC _{1000 cm} 580 8.20 - C-DSC _{20 pk} 553 10.32 F-DSC _{1000 pk} 655 6.84 - F-DSC _{1000 cm} 621 8.20 MP _{515 0} 515 10.92 - F-DSC _{1000 pk} 717 6.84 MP _{515 10} 515 11.01 - MP ₅₄₆ 546 10.75 AND100_3.21 C-DSC _{10 cm} 437 11.98 - AND0_3.18 C-DSC _{10 cm} 450 11.98 C-DSC _{10 pk} 482 10.62 0.01 C-DSC _{10 pk} 500 10.62 C-DSC _{20 pk} 493 10.32 - C-DSC _{20 cm} 462 11.68 C-DSC _{20 pk} 493 10.32 - C-DSC _{20 pk} 507 10.32 F-DSC _{1000 pk} 616 6.84 - C-DSC _{10 cm} 419 11.98 F-DSC _{1000 pk} 616 6.84 - C-DSC _{10 pk} 465 10.62 AND100_3.81 C-DSC _{10 cm} 438 10.62 - C-DSC _{20 cm} 428 11.68 C-DSC _{20 cm} 411 11.68 - C-DSC _{20 cm} 428 11.68 C-DSC _{20 cm} 411 11.68 - C-DSC _{20 cm} 428 11.68 C-DSC _{20 cm} 411 11.68 - C-DSC _{20 cm} 526 8.20 C-DSC _{20 pk} 453 10.32 - F-DSC _{1000 cm} 526 8.20 C-DSC _{20 pk} 453 10.32 - F-DSC _{1000 pk} 605 6.84 AND100_5.15 C-DSC _{10 cm} 380 11.98 - MP ₄₆₅ 465 10.69 C-DSC _{10 cm} 380 11.98 - MP ₄₆₅ 465 10.69 C-DSC _{10 cm} 380 11.98 - MP ₄₆₅ 465 10.69 C-DSC _{10 cm} 381 11.98 - MP ₄₆₅ 465 10.69 C-DSC _{10 cm} 381 11.98 - MP ₄₆₅ 465 10.69 C-DSC _{10 cm} 381 11.98 - MP ₄₆₅ 465 10.69 C-DSC _{10 cm} 383 11.98 - MP ₄₆₅ 465 10.69 C-DSC _{10 cm} 383 11.98 - MP ₄₆₅ 465 10.69 C-DSC _{10 cm} 383 11.98 - MP ₄₆₅ 465 10.69 C-DSC _{10 cm} 383 11.98 - MP ₄₆₅ 465 10.69 C-DSC _{10 cm} 383 11.98 - MP ₄₆₅ 465 10.69 C-DSC _{10 cm} 383 11.98 - MP ₄₆₅ 465 10.69 C-DSC _{10 cm} 383 11.98 - MP ₄₆₅ 465 10.69 C-DSC _{10 cm} 383 11.98 - MP ₄₆₅ 465 10.69 C-DSC _{10 cm} 383 11.98 - MP ₄₆₅		C-DSC _{10 pk}	516	10.62	0.01	AND0_2.21	C-DSC _{10 on}	503	11.98
F-DSC _{1000 cn} 580 8.20 - C-DSC _{20 pk} 553 10.32 F-DSC _{1000 pk} 655 6.84 - F-DSC _{1000 cn} 621 8.20 MP _{515 0} 515 10.92 - F-DSC _{1000 pk} 717 6.84 MP _{515 100} 515 11.01 - MP ₅₄₆ 546 10.75 AND100_3.21 C-DSC _{10 cn} 437 11.98 - AND0_3.18 C-DSC _{10 cn} 450 11.98 C-DSC _{10 pk} 482 10.62 0.01 C-DSC _{10 cn} 462 11.68 C-DSC _{20 cn} 440 11.68 - C-DSC _{20 cn} 462 11.68 C-DSC _{20 pk} 493 10.32 - C-DSC _{20 cn} 462 11.68 C-DSC _{10 pk} 507 10.32 F-DSC _{1000 cn} 539 8.20 - AND0_4.76 C-DSC _{10 cn} 419 11.98 F-DSC _{1000 pk} 616 6.84 - C-DSC _{10 cn} 465 10.62 AND100_3.81 C-DSC _{10 cn} 390 11.98 - C-DSC _{20 cn} 428 11.68 C-DSC _{20 cn} 411 11.68 - C-DSC _{20 cn} 428 11.68 C-DSC _{20 cn} 411 11.68 - F-DSC _{1000 cn} 526 8.20 C-DSC _{20 cn} 411 11.68 - F-DSC _{1000 cn} 526 8.20 C-DSC _{20 cn} 423 10.32 - F-DSC _{1000 cn} 526 8.20 C-DSC _{20 cn} 453 10.32 - F-DSC _{1000 cn} 526 8.20 C-DSC _{20 cn} 453 10.32 - AND10_5.56 C-DSC _{10 cn} 383 11.98		C-DSC _{20 on}	481	11.68	-		C-DSC _{10 pk}	546	10.62
F-DSC _{1000 pk} 655 6.84 - F-DSC _{1000 on} 621 8.20 MP _{515 0} 515 10.92 - F-DSC _{1000 pk} 717 6.84 MP _{515 100} 515 11.01 - MP ₅₄₆ 546 10.75 AND100_3.21 C-DSC _{10 on} 437 11.98 - AND0_3.18 C-DSC _{10 on} 450 11.98 C-DSC _{10 pk} 482 10.62 0.01 C-DSC _{10 pk} 500 10.62 C-DSC _{20 on} 440 11.68 - C-DSC _{20 pk} 507 10.32 F-DSC _{1000 pk} 493 10.32 - C-DSC _{20 pk} 507 10.32 F-DSC _{1000 pk} 616 6.84 - C-DSC _{10 pk} 465 10.62 AND100_3.81 C-DSC _{10 on} 390 11.98 - C-DSC _{20 on} 428 11.68 C-DSC _{20 pk} 438 10.62 - C-DSC _{20 pk} 472 10.32 C-DSC _{20 pk} 453 10.32 - F-DSC _{1000 on} 526 8.20 C-DSC _{20 pk} 453 10.32 - F-DSC _{1000 on} 526 8.20 C-DSC _{20 pk} 453 10.32 - MP ₄₆₅ 465 10.69 C-DSC _{10 pk} 453 10.32 - AND1 ₀ _5.56 C-DSC _{10 on} 383 11.98		C-DSC _{20 pk}	527	10.32	0.02		C-DSC _{20 on}	510	11.68
$\begin{array}{c ccccccccccccccccccccccccccccccccccc$		$F\text{-}DSC_{1000\ on}$	580	8.20	-		C-DSC _{20 pk}	553	10.32
MP _{515 100} 515 11.01 - MP ₅₄₆ 546 10.75 AND100_3.21 C-DSC _{10 on} 437 11.98 - AND0_3.18 C-DSC _{10 on} 450 11.98 C-DSC _{10 pk} 482 10.62 0.01 C-DSC _{10 pk} 500 10.62 C-DSC _{20 on} 440 11.68 - C-DSC _{20 on} 462 11.68 C-DSC _{20 pk} 493 10.32 - C-DSC _{20 pk} 507 10.32 F-DSC _{1000 on} 539 8.20 - AND0_4.76 C-DSC _{10 on} 419 11.98 F-DSC _{1000 pk} 616 6.84 - C-DSC _{10 pk} 465 10.62 AND100_3.81 C-DSC _{10 on} 390 11.98 - C-DSC _{20 on} 428 11.68 C-DSC _{20 on} 411 11.68 - C-DSC _{20 on} 428 11.68 C-DSC _{20 on} 411 11.68 - F-DSC _{1000 on} 526 8.20 C-DSC _{20 pk} 453 10.32 - F-DSC _{1000 on} 526 8.20 C-DSC _{20 pk} 453 10.32 - F-DSC _{1000 on} 526 8.20 C-DSC _{10 pk} 453 10.32 - AND1 ₀ _5.56 C-DSC _{10 on} 383 11.98		F-DSC _{1000 pk}	655	6.84	-		$F\text{-}DSC_{1000\ on}$	621	8.20
AND100_3.21		$MP_{515\ 0}$	515	10.92	-		$F\text{-DSC}_{1000\ pk}$	717	6.84
C-DSC _{10 pk} 482 10.62 0.01 C-DSC _{10 pk} 500 10.62 C-DSC _{20 on} 440 11.68 - C-DSC _{20 on} 462 11.68 C-DSC _{20 pk} 493 10.32 - C-DSC _{20 pk} 507 10.32 F-DSC _{1000 on} 539 8.20 - ANDO_4.76 C-DSC _{10 on} 419 11.98 F-DSC _{1000 pk} 616 6.84 - C-DSC _{10 pk} 465 10.62 AND100_3.81 C-DSC _{10 on} 390 11.98 - C-DSC _{20 on} 428 11.68 C-DSC _{10 pk} 438 10.62 - C-DSC _{20 pk} 472 10.32 C-DSC _{20 on} 411 11.68 - F-DSC _{1000 on} 526 8.20 C-DSC _{20 pk} 453 10.32 - F-DSC _{1000 pk} 605 6.84 AND100_5.15 C-DSC _{10 on} 380 11.98 - MP ₄₆₅ 465 10.69 C-DSC _{10 pk} 423 10.62 - ANDO_5.56 C-DSC _{10 on} 383 11.98		$MP_{515\ 100}$	515	11.01	-		MP ₅₄₆	546	10.75
C-DSC _{20 on} 440 11.68 - C-DSC _{20 on} 462 11.68 C-DSC _{20 pk} 493 10.32 - C-DSC _{20 pk} 507 10.32 F-DSC _{1000 on} 539 8.20 - ANDO_4.76 C-DSC _{10 on} 419 11.98 F-DSC _{1000 pk} 616 6.84 - C-DSC _{10 pk} 465 10.62 AND100_3.81 C-DSC _{10 on} 390 11.98 - C-DSC _{20 pk} 472 10.32 C-DSC _{20 on} 411 11.68 - F-DSC _{1000 pk} 453 10.32 - F-DSC _{1000 pk} 605 6.84 AND100_5.15 C-DSC _{10 on} 380 11.98 - MP ₄₆₅ 465 10.69 C-DSC _{10 pk} 423 10.62 - AND0_5.56 C-DSC _{10 on} 383 11.98	AND100_3.21	$C\text{-}DSC_{10\ on}$	437	11.98	-	AND0_3.18	C-DSC _{10 on}	450	11.98
C-DSC _{20 pk} 493 10.32 - C-DSC _{20 pk} 507 10.32 F-DSC _{1000 on} 539 8.20 - ANDO_4.76 C-DSC _{10 on} 419 11.98 F-DSC _{1000 pk} 616 6.84 - C-DSC _{10 pk} 465 10.62 AND100_3.81 C-DSC _{10 on} 390 11.98 - C-DSC _{20 on} 428 11.68 C-DSC _{10 pk} 438 10.62 - C-DSC _{20 pk} 472 10.32 C-DSC _{20 on} 411 11.68 - F-DSC _{1000 on} 526 8.20 C-DSC _{20 pk} 453 10.32 - F-DSC _{1000 pk} 605 6.84 AND100_5.15 C-DSC _{10 on} 380 11.98 - MP ₄₆₅ 465 10.69 C-DSC _{10 pk} 423 10.62 - ANDO_5.56 C-DSC _{10 on} 383 11.98		$\text{C-DSC}_{10\ pk}$	482	10.62	0.01		C-DSC _{10 pk}	500	10.62
F-DSC _{1000 on} 539 8.20 - ANDO_4.76 C-DSC _{10 on} 419 11.98 F-DSC _{1000 pk} 616 6.84 - C-DSC _{10 pk} 465 10.62 AND100_3.81 C-DSC _{10 on} 390 11.98 - C-DSC _{20 pk} 472 10.32 C-DSC _{20 on} 411 11.68 - F-DSC _{1000 on} 526 8.20 C-DSC _{20 pk} 453 10.32 - F-DSC _{1000 pk} 605 6.84 AND100_5.15 C-DSC _{10 pk} 423 10.62 - ANDO_5.56 C-DSC _{10 on} 383 11.98		C-DSC _{20 on}	440	11.68	-		C-DSC _{20 on}	462	11.68
F-DSC _{1000 pk} 616 6.84 - C-DSC _{10 pk} 465 10.62 AND100_3.81 C-DSC _{10 on} 390 11.98 - C-DSC _{20 on} 428 11.68 C-DSC _{10 pk} 438 10.62 - C-DSC _{20 pk} 472 10.32 C-DSC _{20 on} 411 11.68 - F-DSC _{1000 on} 526 8.20 C-DSC _{20 pk} 453 10.32 - F-DSC _{1000 pk} 605 6.84 AND100_5.15 C-DSC _{10 on} 380 11.98 - MP ₄₆₅ 465 10.69 C-DSC _{10 pk} 423 10.62 - AND0_5.56 C-DSC _{10 on} 383 11.98		C-DSC _{20 pk}	493	10.32	-		C-DSC _{20 pk}	507	10.32
AND100_3.81		$F\text{-}DSC_{1000\ on}$	539	8.20	-	AND0_4.76	C-DSC _{10 on}	419	11.98
$ \begin{array}{cccccccccccccccccccccccccccccccccccc$		$F\text{-}DSC_{1000\ pk}$	616	6.84	-		C-DSC _{10 pk}	465	10.62
C-DSC _{20 on} 411 11.68 - F-DSC _{1000 on} 526 8.20 C-DSC _{20 pk} 453 10.32 - F-DSC _{1000 pk} 605 6.84 AND100_5.15 C-DSC _{10 on} 380 11.98 - MP ₄₆₅ 465 10.69 C-DSC _{10 pk} 423 10.62 - AND0_5.56 C-DSC _{10 on} 383 11.98	AND100_3.81	$C\text{-}DSC_{10\ on}$	390	11.98	-		C-DSC _{20 on}	428	11.68
C-DSC _{20 pk} 453 10.32 - F-DSC _{1000 pk} 605 6.84 AND100_5.15 C-DSC _{10 on} 380 11.98 - MP ₄₆₅ 465 10.69 C-DSC _{10 pk} 423 10.62 - AND0_5.56 C-DSC _{10 on} 383 11.98		$\text{C-DSC}_{10\ pk}$	438	10.62	-		C-DSC _{20 pk}	472	10.32
AND100_5.15 C-DSC _{10 on} 380 11.98 - MP ₄₆₅ 465 10.69 C-DSC _{10 pk} 423 10.62 - AND0_5.56 C-DSC _{10 on} 383 11.98		C-DSC _{20 on}	411	11.68	-		$F\text{-}DSC_{1000\ on}$	526	8.20
C-DSC _{10 pk} 423 10.62 - AND0_5.56 C-DSC _{10 on} 383 11.98		C-DSC _{20 pk}	453	10.32	-		F-DSC _{1000 pk}	605	6.84
	AND100_5.15	$C\text{-DSC}_{10 \text{ on}}$	380	11.98	-		MP_{465}	465	10.69
C-DSC _{20_on} 390 11.68 - C-DSC _{10_pk} 420 10.62		C-DSC _{10 pk}	423	10.62	-	AND0_5.56	$C\text{-DSC}_{10 \ on}$	383	11.98
		C-DSC_{20_on}	390	11.68	-		$C\text{-}DSC_{10_pk}$	420	10.62

	$\text{C-DSC}_{20\ pk}$	429	10.32	-		$\text{C-DSC}_{20\ on}$	390	11.68
	$F\text{-}DSC_{1000\ on}$	474	8.20	-		$C ext{-}DSC_{20\ pk}$	430	10.32
	$F\text{-}DSC_{1000\ pk}$	541	6.84	-		$F\text{-}DSC_{1000\ on}$	471	8.20
	$MP_{423\ 0}$	423	10.72	-		$F\text{-}DSC_{1000\ pk}$	545	6.84
	$MP_{423\ 100}$	423	11.88	0.02		MP_{386}	386	12.00
AND65_4.3	C-DSC _{10 on}	410	11.98	-	BAS0	CC	1426	1.85
	C-DSC _{10 pk}	448	10.62	-		CC	1370	2.14
	$F\text{-}DSC_{1000\ on}$	505	8.20	-		CC	1322	2.42
						CC	1274	2.74
						CC	1225	3.09
						CC	1439	1.78
						$C ext{-}DSC_{10\ on}$	712	11.98
						$C ext{-}DSC_{10\ pk}$	751	10.62
						C-DSC _{20 on}	724	11.68
						$C ext{-}DSC_{20\ pk}$	764	10.32
						MP ₇₆₃	763	10.42
						$F\text{-}DSC_{1000\ on}$	852	8.2
						$F\text{-}DSC_{1000\ pk}$	909	6.84
						$F\text{-}DSC_{5000\ on}$	893	7.50
						F-DSC _{5000 pk}	963	6.14

 $^{^{}a}$ C- and F-DSC-type experiments are reported as DSC_{heating-rate thermal-event}, with heating rates expressed in o C min⁻¹ and o C s⁻¹, respectively. Thermal events are identified as on = T_{onset} and pk = T_{peak} . F-DSC experiments at 10000 K s⁻¹ are numbered to show their relative possitions in the series of measurements. MP data is reported as MP_{temperature duration}, with temperature expressed in o C and the duration in minutes.

Notably, post-experiment FTIR spectra of AND100_5.15 (Fig. 5b) shows the development of a new absorption feature around 4300 cm⁻¹ (Fig. 4b), coupled with a decrease in the intensity of bands related to OH⁻ and molecular water. These changes suggest that water exsolution and crystallization occurred during the experiment. Concurrently, a marked increase in viscosity was observed for the same sample, rising from 10^{10.72} to 10^{11.88} Pa s over 100 minutes at 423 °C. The appearance of the 4300 cm⁻¹ FTIR feature may be associated with the formation of free hydroxyl species, potentially linked alkaline earth cations such as Ca and Mg, as suggested by Bondar et al. (2023).

^bDifference between Fe³⁺/Fe_{tot} after measurements and innitial conditions from Table 1. All Ratios derived using Mossa software (Prescher et al. 2012).

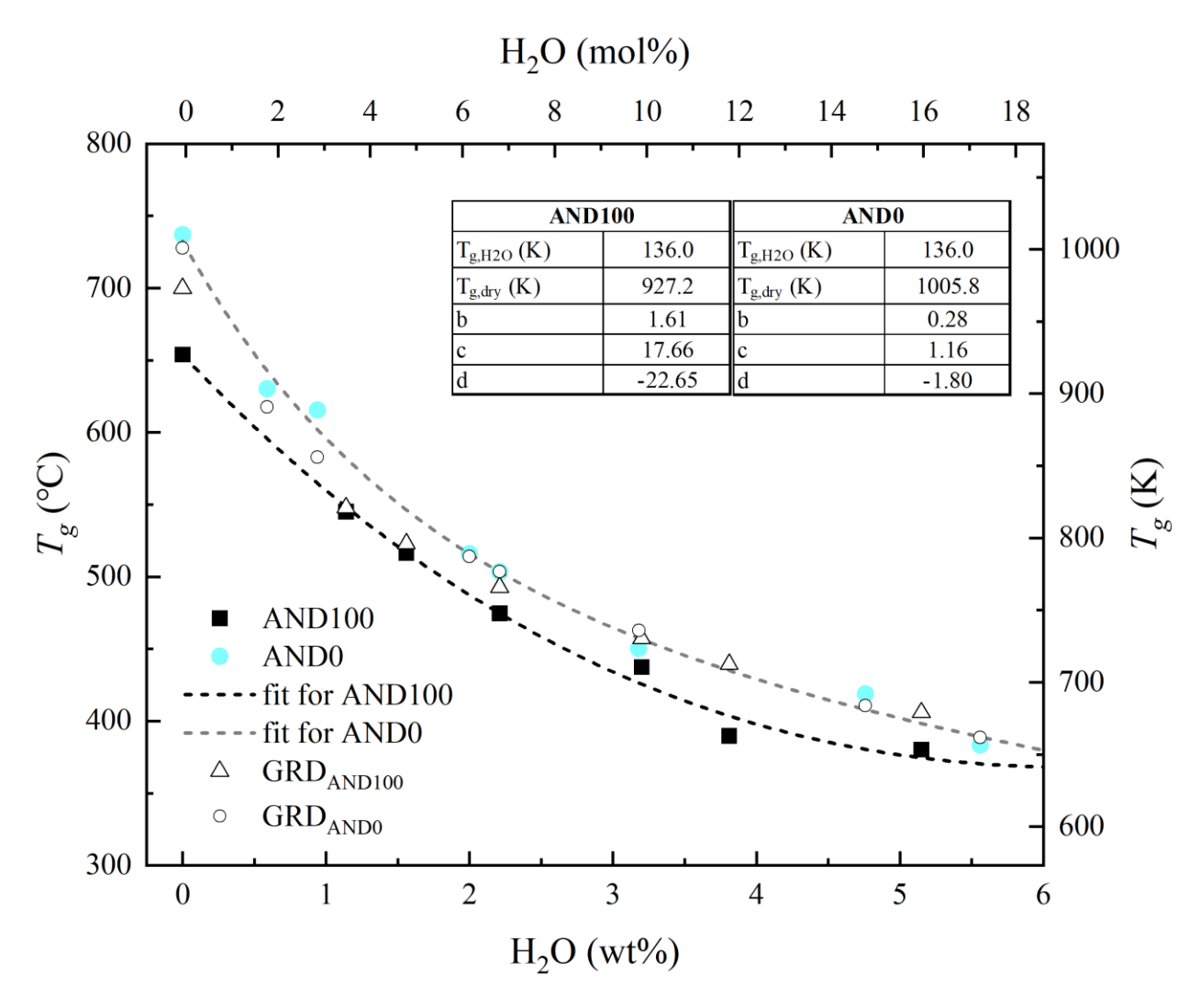


Figure 4. Glass transition temperature (T_g) as a function of water content (wt%). The dashed line corresponds to the best fit solutions using the Schneider et al. (1997) equation. Fit parameters are summarized in the tables in the plot. Upper axis (H_2O in mol%) is tailored for the AND100 composition. Open symbols correspond to the T_g values derived from Giordano et al. (2008), for AND100 (GRD_{AND100}) and AND0 (GRD_{AND00}) compositions.

This interpretation aligns with findings by Valdivia et al. (2023) for hydrous Stromboli basaltic melt. The viscosity increase in AND100_5.15 during the MP experiments at 423 °C is thus attributed to the formation of new crystalline phase, altering the residual melt composition and promoting water extraction as the experimental temperature crossed T_g (Valdivia et al., 2025, 2023).

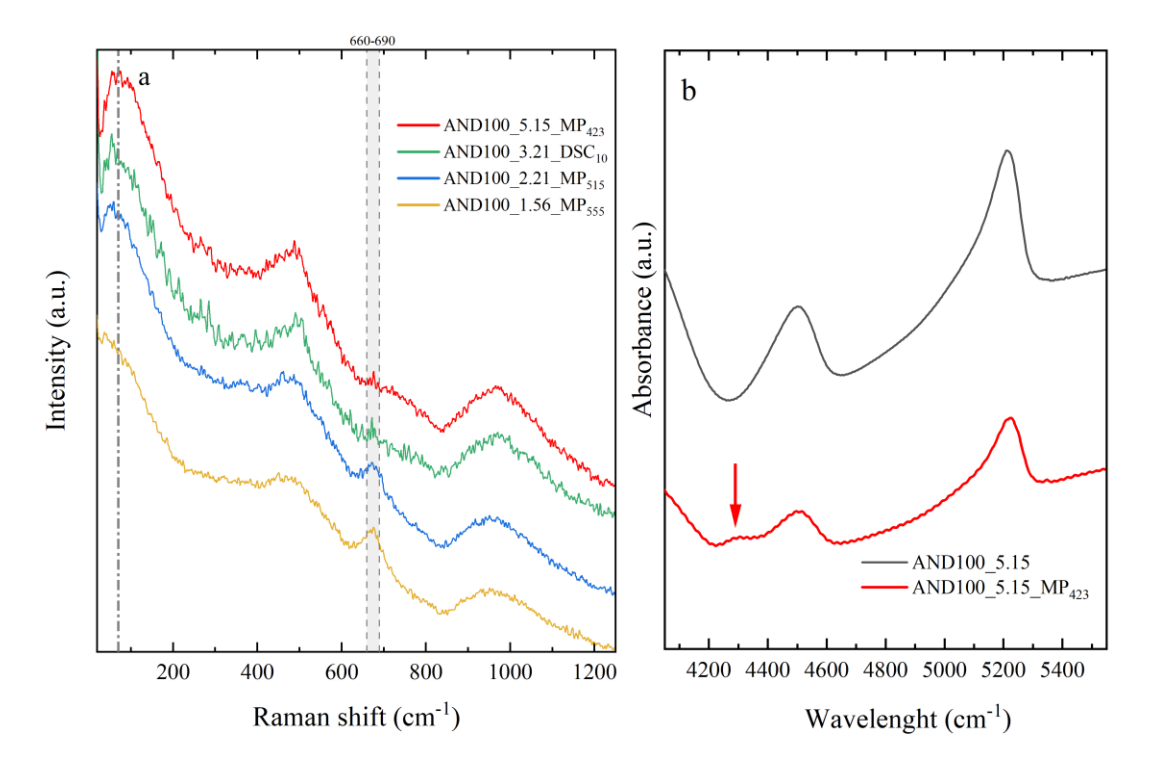


Figure 5. Raman and FTIR measurements of samples affected by crystallization and/or water exsolution during measurement. a) Raman spectra of hydrous glasses after C-DSC and micropenetration measurements. The spectral range (660–690 cm⁻¹) shaded in gray indicates the presence of Fe-Ti-oxides (Bondar et al., 2025; Di Genova et al., 2020b; Fanesi et al., 2025; Valdivia et al., 2023). b) FTIR water bands for AND100_5.15 sample. Red arrow shows the formation of a new peak at ~4300 cm⁻¹ after micropenetration measurement, possibly attributed to the apparition of free hydroxyl groups (Bondar et al., 2022; Larre et al., 2020; Valdivia et al., 2023).

In contrast, FTIR analyses of AND0 samples show that water maintained mostly unchanged after treatment, indicating a lower tendency for crystallization and water loss compared to the AND100 series. These findings further support the idea that volcanic melts and their analogues, such as AND100, are more susceptible to nanostructuration, nanocrystallization and/or water exsolution during experiments above T_g in the supercooled liquid state. Consequently, special care must be taken during viscosity measurements to avoid misinterpretations caused by these processes.

Viscosity parametrization

Previous work (Di Genova et al., 2023; Fanesi et al., 2025; Langhammer et al., 2022; Valdivia et al., 2023) shows that the viscosity of hydrous melts can be described using the Mauro–Yue–Ellison–Gupta–Allan (MYEGA) equation (Eq. 7) (Mauro et al., 2009):

$$log_{10}\eta(T) = log_{10}\eta_{\infty} + (12 - log_{10}\eta_{\infty}) \frac{T_g}{T} exp\left[\left(\frac{m}{12 - log_{10}\eta_{\infty}} - 1\right)\left(\frac{T_g}{T} - 1\right)\right]$$
(7)

where $log_{10}\eta_{\infty} = -2.93 \pm 0.3$ is the logarithmic viscosity at infinite temperature (Langhammer et al., 2022; Mauro et al., 2009), T_g is the glass transition temperature determined by C-DSC (T_{onset} at $q_{h,c} = 10$ °C min⁻¹) and m is the melt fragility defined in Eq. 6 (Angell, 1995) as the steepness of viscosity-temperature curve evaluated at T_g :

$$m = \frac{\partial \log_{10} \eta}{\partial T_g / T} \bigg|_{T = T_g} \tag{8}$$

The effect of water on melt viscosity is incorporated through the water dependence of both T_g and m parameters.

To describe the dependence of T_g on water content, we used the model by Schneider et al. (1997), as later adopted by Langhammer et al. (2021):

$$T_g(x_{H_2O}) = w_1 T_{g,H_2O} + w_2 T_{g,d} + c w_1 w_2 (T_{g,d} - T_{g,H_2O}) + d w_1 w_2^2 (T_{g,d} - T_{g,H_2O})$$
(9)

with

$$w_1 = \frac{x_{H_2O}}{b(100 - x_{H_2O}) + x_{H_2O}}$$
 and $w_2 = \frac{b(100 - x_{H_2O})}{b(100 - x_{H_2O}) + x_{H_2O}}$, (10)

where X_{H_2O} is the mol% of dissolved water, $T_{g,d}$ is the glass transition temperature of the anhydrous composition and T_{g,H_2O} is the glass transition of pure water equal to 136 K (Kohl et al., 2005). The $T_g(x_{H_2O})$ parametrization for hydrous AND100 and AND100 compositions, along with the fitting parameters b, c, and d are shown in Fig. 4.

Determining the water dependence of melt fragility presents a significant challenge. Direct fragility calculation requires high-temperature viscosity data that are difficult to obtain for hydrous melts due to degassing and syn-experimental alterations. To overcome this constraint, we employed an alternative approach using Brillouin spectroscopy. Previous research (Cassetta et al., 2021; Novikov et al., 2005; Novikov and Sokolov, 2004; Sokolov et al., 2007) has established linear relationships between K/G and melt fragility across a wide range of compositions. Building on this, we employed Brillouin spectroscopy to determine the K/G

values of our hydrous glasses using Eq. 6. Our calculated K/G results are summarized in Tables 1 and 2 and illustrated in Fig. 6.

We observe a linear increase in K/G data with increasing water content for both AND100 and AND0 compositions (Fig. 6). Specifically, for AND100, K/G increases from 1.59 \pm 0.02 to 1.64 \pm 0.02 as total water content increases from 1.59 to 5.15 wt% (Table 1). A similar trend is observed for AND0, where K/G increases from 1.49 \pm 0.02 to 1.56 \pm 0.02 as water content increases from 0.59 to 5.56 wt% (Table 2). By incorporating anhydrous K/G data of AND100 and AND0 from Valdivia et al. (2025) (Table 4), we derived two linear equations describing K/G as a function of composition and water concentrations (Fig. 6).

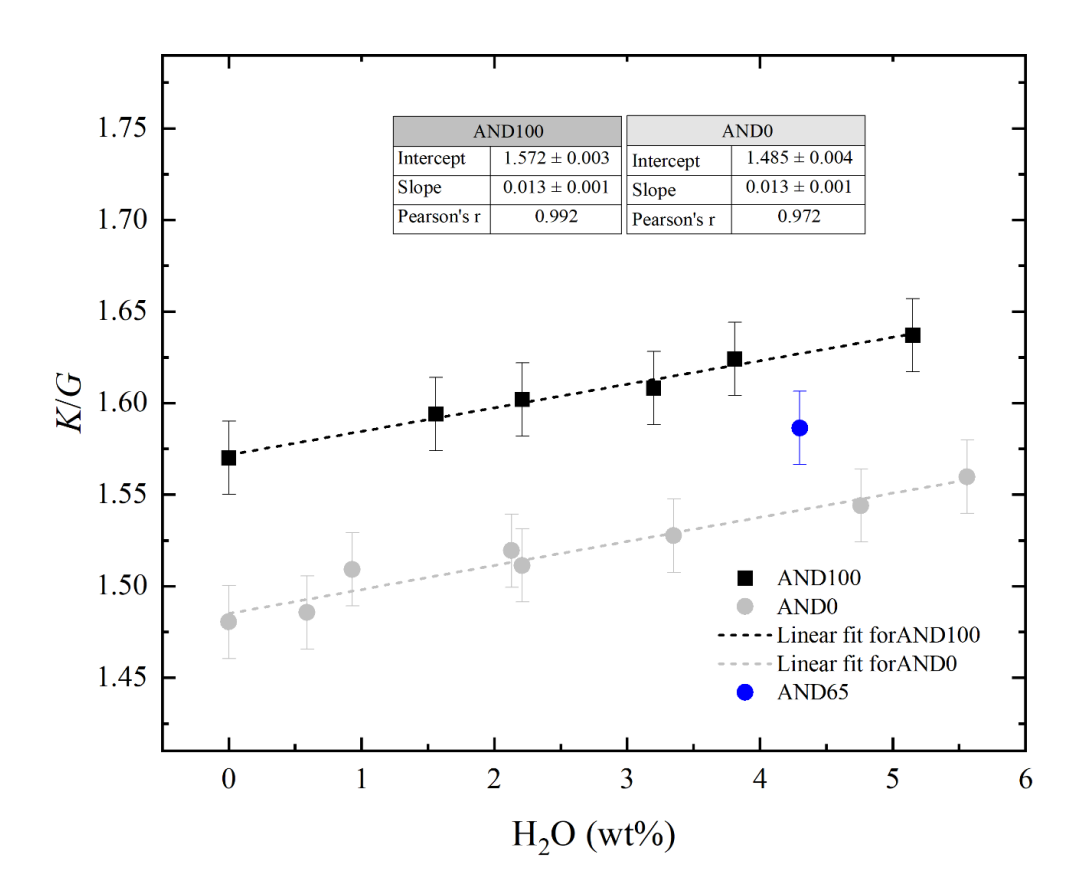


Figure 6. *K/G* and melt fragility as a function of water content for AND100 and AND0 samples. The dashed lines correspond to the linear regression of the AND100 and AND0 data. Fit values are shown in the figure.

While the model proposed by Cassetta et al. (2021) represents an important step forward in understanding how melt fragility varies with chemical composition and water content, effectively describing general trends of increasing or decreasing fragility, it still requires refinement when applied to a broader range of compositions. Recent studies on melts prone to nanocrystallization, such as andesitic, basaltic, and tephri-phonolitic compositions (Fanesi et al., 2025; Valdivia et al., 2025, 2023), have demonstrated that the Cassetta et al. (2021) relationships between K/G and m do not accurately predict fragility values across these complex systems.

Building on this foundation, and using new, well-characterized datasets from this study, we propose two revised empirical equations that correlate the melt fragility index (m) with sound velocity data obtained from Brillouin spectroscopy. These updated relationships are specifically tailored for compositions ranging from andesites to basalts: one equation applies to transition metal-bearing melts, while the other addresses transition metal-free systems. This distinction explicitly accounts for the influence of transition metals on the silicate network structure and their impact on melt fragility (Malfait and Sanchez-Valle, 2013). We selected representative end members within each compositional range. For the iron-bearing system, we chose an anhydrous andesite (AND100) from Valdivia et al. (2024) and an anhydrous basalt (i.e., Stromboli melt) from Valdivia et al. (2023). These compositions span K/G values from 1.58 ± 0.02 to 1.73 ± 0.02 (Table 4), encompassing the K/G range observed in our hydrous AND100 samples. Importantly, both studies carefully assessed and excluded the influence of nanolite formation, ensuring that the derived fragility (m) values are reliable for this analysis.

For the transition metal-free system, we relied on the anhydrous AND0 data reported by Valdivia et al. (2024), which has a $K/G = 1.48 \pm 0.02$. To further extend coverage across the

compositional range of transition metal-free melts, we additionally investigated an anhydrous, iron-free basaltic composition (BAS0; Tab. 4).

To fully constrain the melt fragility index for BAS0, viscosity was measured over a wide temperature range using a combination of C-DSC, F-DSC, MP, and CC viscometry. The resulting viscosity data (Tab. 3; Fig. 7), were fitted with the MYEGA equation (Eq. 6), yielding a fragility index of $m = 35.9 \pm 0.3$ (Table 4; Fig. 7).

Table 4. Chemical compositions, Brillouin results and MYEGA parameters of anhydrous basalts and andesites.

	BAS0 ^a	BAS100b	AND0°	AND100°
SiO ₂	55.98 (0.65)	49.74 (0.77)	65.91 (0.34)	60.38 (0.36)
TiO_2	0.02 (0.02)	0.9 (0.08)	0.04 (0.03)	0.79 (0.04)
Al_2O_3	20.96 (0.29)	17.46 (0.04)	18.01 (0.11)	16.69 (0.18)
FeO_{tot}	0.03 (0.02)	7.58 (0.05)	0.04 (0.03)	6.77 (0.12)
MnO	0.01 (0.01)	0.14 (0.1)	0.01 (0.01)	0.17 (0.03)
MgO	3.1 (0.10)	6.06 (0.14)	3.21 (0.06)	3.00 (0.07)
CaO	11.61 (0.28)	11.22 (0.10)	7.26 (0.11)	6.62 (0.09)
Na ₂ O	4.99 (0.13)	2.58 (0.24)	3.82 (0.14)	3.50 (0.15)
K_2O	1.83 (0.13)	2.04 (0.07)	1.75 (0.06)	1.58 (0.07)
P_2O5	0.54 (0.09)	0.53 (0.03)	0.04 (0.03)	0.18 (0.05)
K/G^d	1.58 (0.02)	1.73 (0.02)	1.48 (0.02)	1.57 (0.02)
T_g^{e} (°C)	713 (1.4)	666.9 (0.8)	737 (1)	654 (1)
m^f	35.9 (0.3)	40.7 (0.7)	31.8 (0.2)	30.5 (1)

aThis work

^bValdivia et al. (2023).

^cValdivia et al. (2025).

^dValues derived using Brillouin spectroscopy.

^eDSC-derived values.

^fFitted fragility using the Mauro-Yue-Elli- son-Gupta-Allan (MYEGA) parametrization.

Our measurements show that the viscosity of BAS0 is 1-1.5 \log_{10} unites higher than BAS100, consistent with previous observations (Cáceres et al., 2024; Valdivia et al., 2025) indicating that the melt viscosity of silicates increases with the extraction of transition metal content. Brillouin spectroscopy provided K/G ratio for BAS0 of $K/G = 1.58 \pm 0.02$, effectively bridging the range of K/G values obtained for the hydrous AND0 compositions ($K/G = 1.49 - 1.56 \pm 0.02$). Altogether, the selected endmembers ensure a continuous and well-characterized reference framework across both transition metal-bearing and transition metal-free systems.

Although the transition metal—free compositions (BAS0 and AND0) are not representative of natural terrestrial magmas, they were deliberately selected to isolate the effect of transition metals on melt viscosity and fragility. Despite exhibiting similar K/G ratios, BAS0 and AND100 display markedly different melt fragility values derived from viscosity data (Table 4; Fig. 8). This discrepancy indicates that melt fragility does not depend solely on the K/G ratio but is instead strongly influenced by compositional factors. In particular, variations in transition metal content, which affect the degree of polymerization and the nature of network-modifying cations, appear to exert a key control on melt relaxation behavior. The higher fragility observed in BAS0 compared to AND100 suggests that the relationship between K/G and melt fragility is composition-dependent, with transition metal content serving as a primary controlling factor. These results align with the linear trends reported by Cassetta et al. (2021) but also highlight the need for further investigation across a broader compositional range to refine the link between structural parameters and melt fragility.

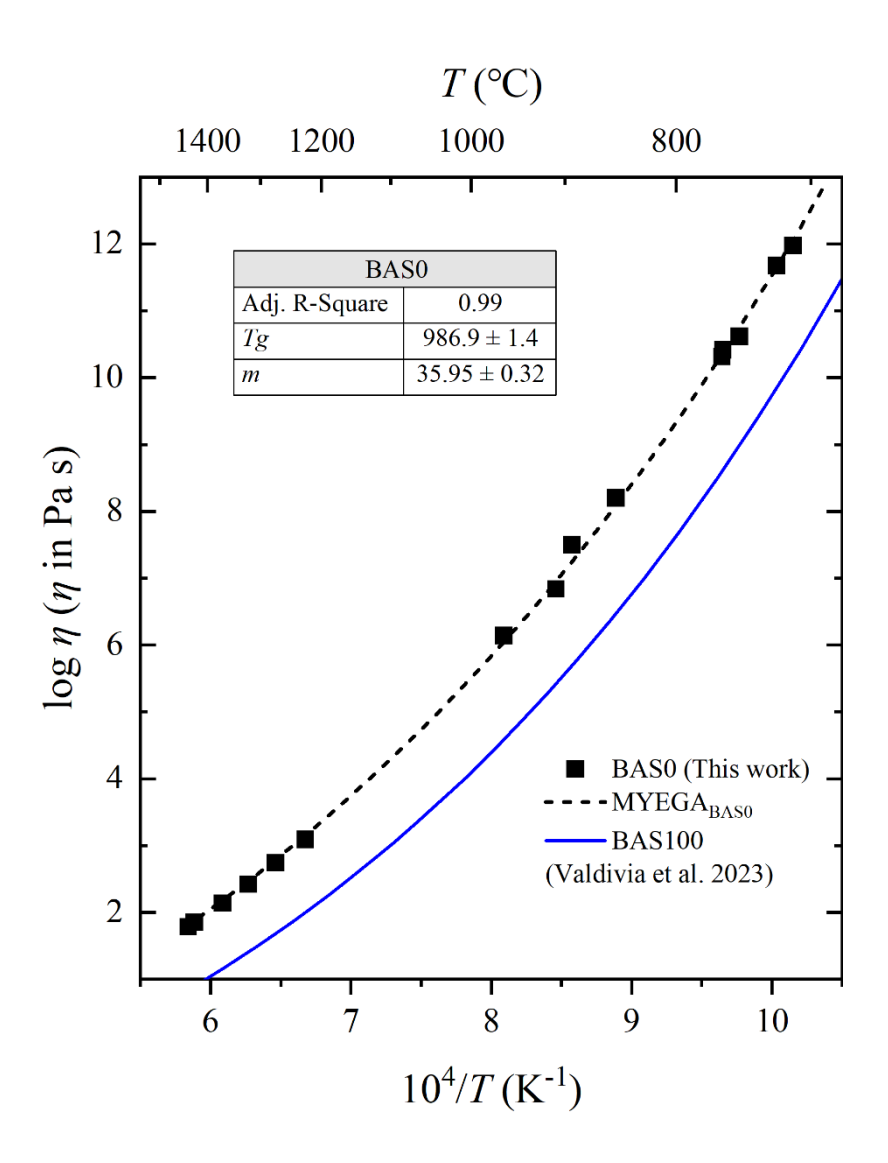


Figure 7. Viscosity data for the transition metal-free composition BAS0. The dashed line represents the best-fit curve obtained using the MYEGA equation. For comparison, the viscosity parameterization of the transition metal-bearing BAS100 composition from Valdivia et al. (2023) is also shown.

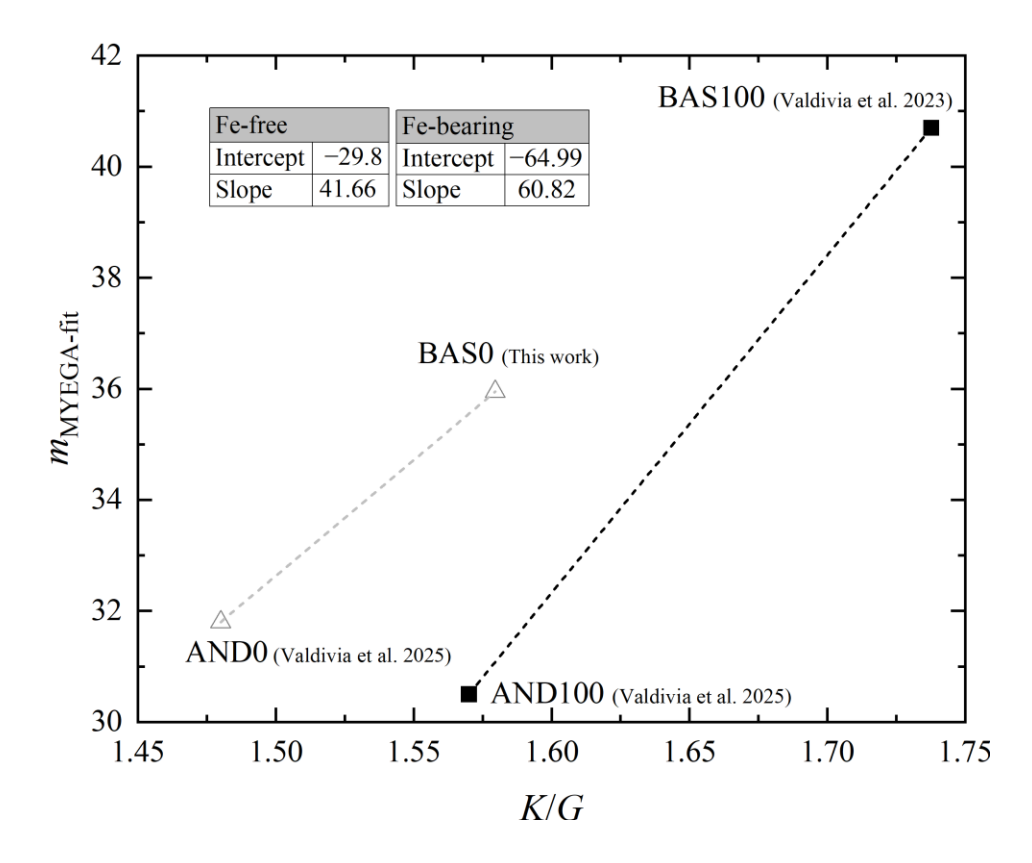


Figure 8. Viscosity-derived melt fragility ($m_{\text{MYEGA-fit}}$) as a function of K/G ratio. White open triangles are Fe-free samples and black filled squares are Fe-bearing compositions. Dashed lines represent the linear regressions, corresponding to Equations 11 and 12. Symbol sizes exceed error bars.

To account for this compositional effect, we used the melt fragility derived from viscosity measurements via the MYEGA Eq. 6 for four anhydrous endmember compositions (AND0, AND100, BAS0, and BAS100) to establish two distinct empirical relationships. These linear relationships relate melt fragility to K/G and are specific to transition metals-free (Eq. 11) and transition metals-bearing systems (Eq. 12), respectively, as illustrated in Fig. 8:

$$m_{metal-free} = 41.66 \cdot \frac{K}{G} - 29.8 \tag{11}$$

$$m_{metal-bearing} = 60.82 \cdot \frac{K}{G} - 64.99 \tag{12}$$

Using Eq. 11 and Eq. 12, we calculated the melt fragility (*m*) for the hydrous AND100 and AND0 samples. The results are summarized in Tables 1 and 2 and illustrated in Fig. 9. A linear regression applied to these data reveals a clear and positive correlation between melt fragility and water content for both compositional series.

Importantly, our melt fragility estimates diverge significantly from those predicted by the Giordano et al. (2008) model, which predicts a dramatic decrease in melt fragility with increasing water content (Fig. 9). This discrepancy is consistent with observations from previous studies (Fanesi et al., 2025; Valdivia et al., 2023), which highlight that nanocrystallization, often unavoidable during viscosity measurements of hydrous samples, can lead to anomalously high viscosity. As a result, the derived melt fragilities may deviate from the true behavior of fully amorphous, crystal-free melts. Finally, by integrating the water dependence on T_g and m and applying the MYEGA parametrization (Eq. 6), we present two viscosity models for these compositions (Fig. 10).

Our two models were validated using viscosity data derived from C-DSC and F-DSC, which were not used to train the models except for T_g values. Fig. 11 compares our viscosity measurements (Table 3) with model predictions for the AND100 and AND0 composition (Fig. 10). We find that hydrous viscosity data from melts that did not experience significant nanocrystallization or water exsolution closely match the model predictions. The strong predictive performance of our models highlights the importance of incorporating both the water dependence of T_g and m into the MYEGA parametrization. This approach provides an accurate and reliable description of viscosity across a wide range of water contents.

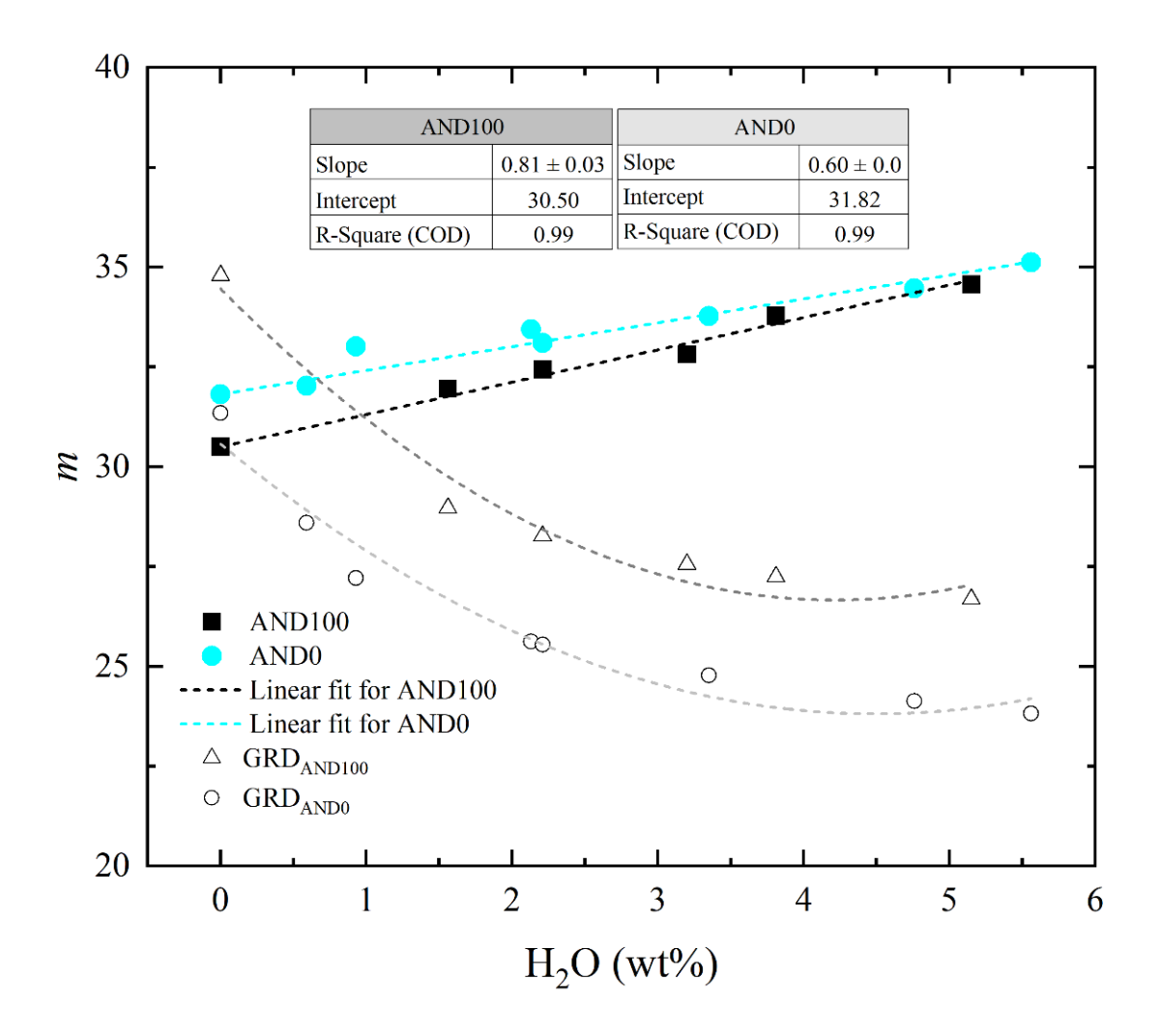


Fig. 9. Melt fragility (m), derived from K/G ratios, plotted as a function of water content (wt%) for hydrous andesite melts. Fragility values were calculated using the empirical relationship from Eq. 11 and 12 (Fig. 8). Black and blue dashed lines represent the linear regressions of the AND100 and AND0 data sets, respectively. Grey lines indicate the predicted fragility trends from the Giordano et al. (2008) model for the both compositions.

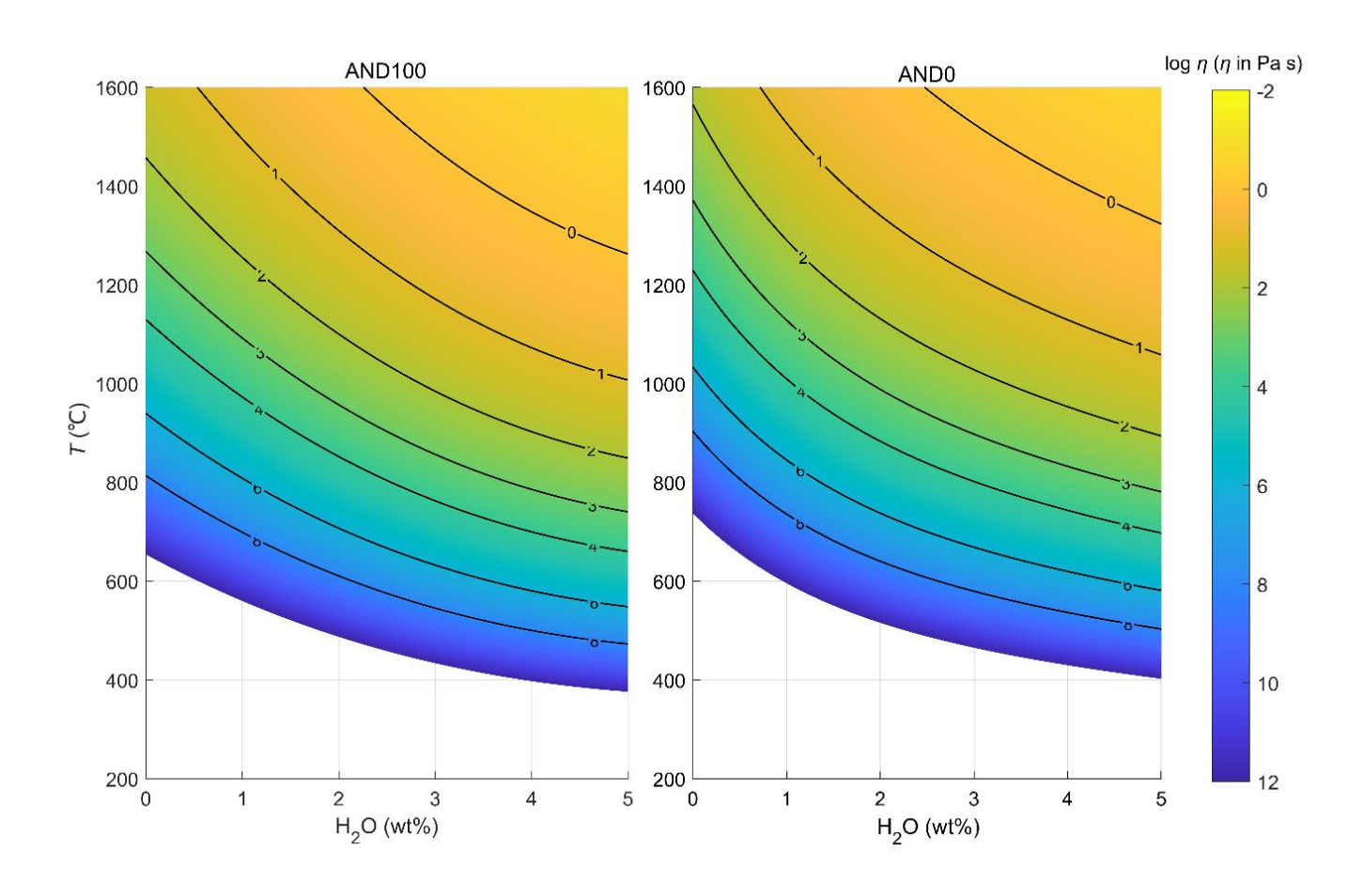


Figure 10. Viscosity of AND100 and AND0 as a function of water content (wt%) and temperature (°C).

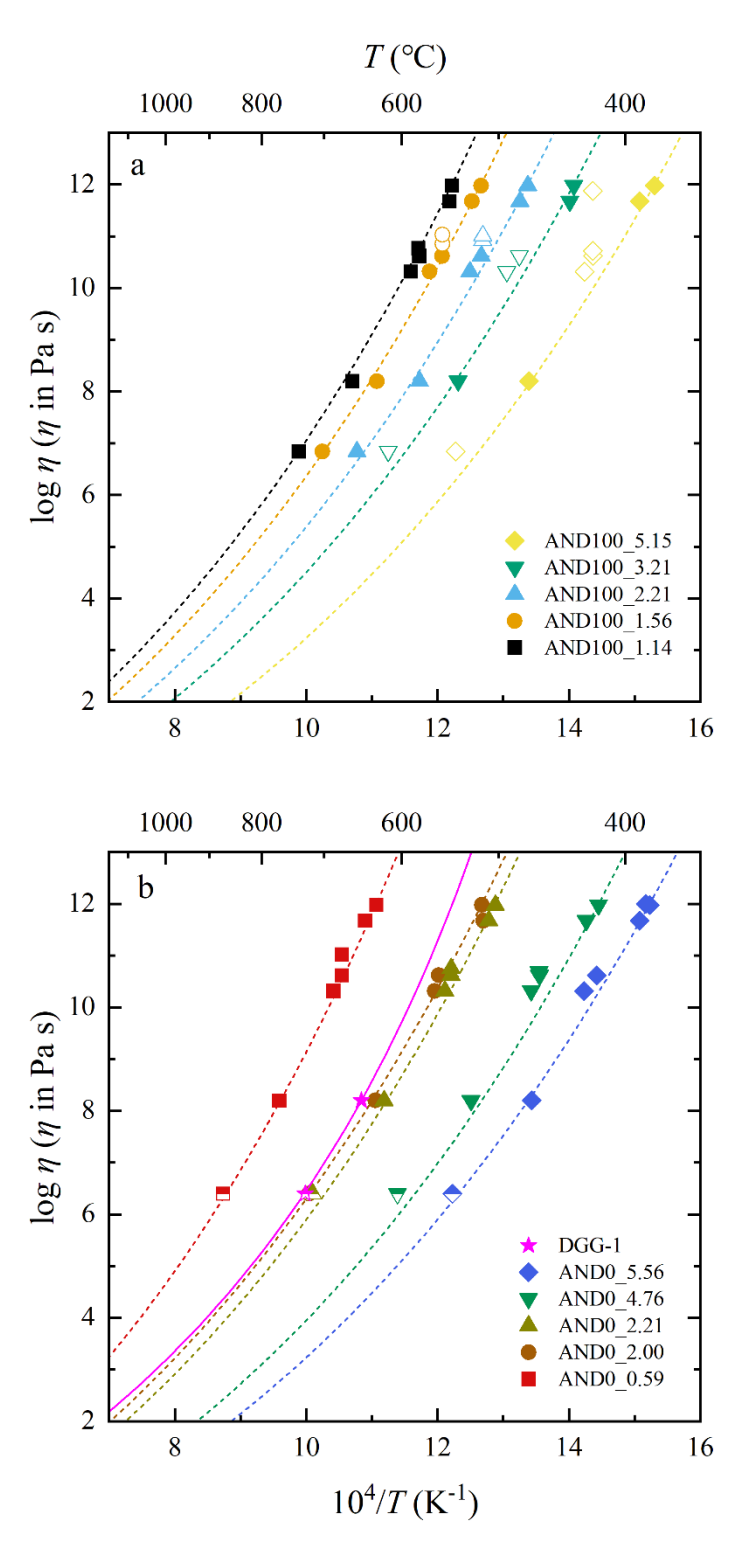


Figure 11. Hydrous viscosity results. a) AND100. b) AND0. Colored symbols represent nanolite-free viscosity data. Open symbols represent viscosity data affected by degassing and/or nanocrystallization. Half-filled symbols represent corrected F-DSC-derived viscosity data by using $K_{peak} = 9.4$ Pa K (see Methods for details). Dashed lines correspond to the prediction of our viscosity models. Every color represents one water content in wt%.

A general viscosity model for andesitic melts

To develop a general viscosity model for andesitic compositions, we parametrized T_g as a function of water and transition metals concentration. This relationship follows a parabolic relationship between the two compositional endmembers, as shown in Fig. 12 and expressed in Eq. 13:

$$T_g(ANDX, H_2O) = T_g(AND0, H_2O) - \left| \frac{T_g(AND0, H_2O) - \left(T_g(AND100, H_2O)\right)}{10000} \right| \bullet X^2 - A(H_2O) \bullet e^{-\frac{(x-50)^2}{1200}} (13)$$

where

$$A(H_20) = 5.4 - 0.82 \cdot H_20 \tag{14}$$

Here, X represents the relative proportion of the AND100 endmember in a binary AND100-AND0 system, with H₂O expressed in wt%. For example, a composition labeled AND65 corresponds to a mixture of 65% AND100 and 35% AND0.

By assuming an ideal mixing behavior of melt fragility relative to its two end members (Valdivia et al., 2025), and using the T_g parametrization from Eq. 13 and 14, we constructed a general viscosity model based on the MYEGA parametrization (Eq. 7) that accounts for variations in water content, temperature, and transition metal concentration. A viscosity calculator implementing this model is provided as Supplementary Material.

To validate our viscosity model, we synthesized an AND65 glass with 4.2 wt% H₂O, referred to as AND65_4.2. EMPA results (Table 1) indicate that AND65_4.2 composition is in good agreement with the theoretical composition expected from ideal mixing in this binary system. Additionally, we performed Brillouin, C-DSC, and F-DSC measurements following the same methodology used for hydrous AND100 samples.

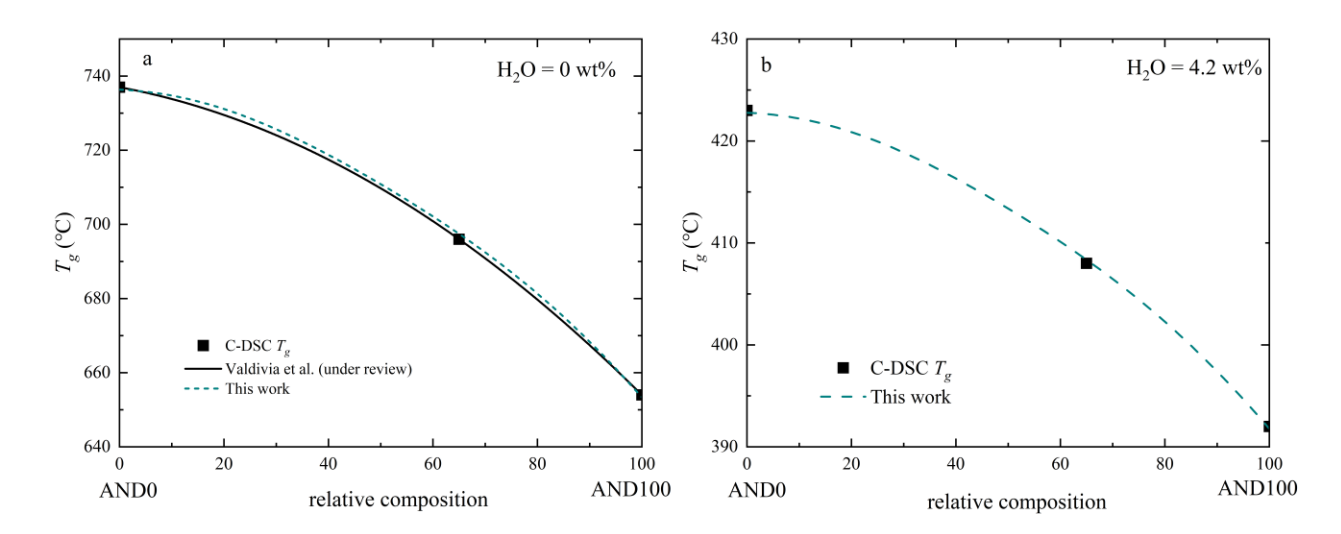


Fig. 12. Parametrization of T_g as a function of AND100 content in the AND0–AND100 binary compositional system. The black line represents the polynomial fit used in Valdivia et al. (2024), while the green line shows the parabolic fit proposed in this study.

Brillouin results show that the K/G ratio of AND65_4.2 follows a linear mixing trend between hydrous AND100 and AND0 compositions (Fig. 6), consistent with findings reported by Valdivia et al. (2024) for the anhydrous endmembers. Furthermore, C-DSC measurements yielded a T_g value of 410 \pm 1 °C, in excellence agreement with the predicted T_g of 408.6 °C by our model.

Notably, at the measured F-DSC_{1000_on} temperature (505 °C, Table 3), our viscosity model predicts a viscosity of 10^{8.23} Pa s, which is in excellent agreement with the F-DSC-derived value of 10^{8.2} Pa s obtained using the shift factor approach. A minor discrepancy is observed at the C-DSC_{10_pk} temperature (448 °C, Table 3), where our model predicts a viscosity of 10^{10.23} Pa s in contrast to the expected 10^{10.62} Pa s from the shift factor approach. Overall, the results from sample AND65_4.2 confirm the applicability of our general model for compositions between AND100 and AND0 across water contents typical of natural andesitic volcanoes (Takeuchi, 2011; Wallace, 2005).

Applying our model to the pre-eruptive conditions of Sakurajima volcano (T = 1030°C and $H_2O = 3.00$) (Yamanoi et al., 2008), we obtained a pre-eruptive viscosity of $10^{1.74}$ Pa s. This value

is approximately 48 times lower than the prediction reported by Takeuchi (2011) (Table 5), which is based on the Giordano et al (2008) viscosity model. This discrepancy aligns with previous studies (Fanesi et al., 2025; Giuliani et al., 2024; Valdivia et al., 2025, 2023), which highlight that the Giordano et al. (2008) model systematically predicts an increase in melt fragility with increasing water content, contrary to our findings, and those of recent works, which show that water actually decreases melt fragility, especially in compositions prone to nanocrystallization.

Using our general model, we estimated pre-eruptive viscosities for several explosive andesitic volcanic centers using compositions from Takeuchi (2011) (Table 3). We selected the best anhydrous analogs within our binary system (AND100–AND0) by matching the degree of polymerization (NBO/T), using the spreadsheet provided by Prata et al. (2019).

Within our compositional range, we successfully approximated the compositions of the andesitic magmas from Mt. Pinatubo, Mt. Rainer, and the trachyandesite from Cerro Hudson, assigning them compositions of AND40, AND40, and AND45, respectively. Incorporating the pre-eruptive temperature and water content (Table 5), we calculated pre-eruptive melt viscosities of $10^{2.62}$, $10^{2.69}$, and $10^{3.11}$ Pa s, respectively. These viscosity estimations are approximately 380, 100 and 4 times lower than previous viscosity predictions (Table 5).

Additionally, we extended our model to slightly less evolved andesitic compositions by ensuring that Gram Formula Weight (GFW) remained within the compositional range of our studied range (Giordano et al., 2008). We matched the compositions of Agnung, Hokaido Komagatake, and Aniakchak volcanoes (Takeuchi, 2011, and references therein), assigning compositions of AND110, AND120 and AND125, respectively. Using their reported pre-eruptive conditions (Table 5), we obtained viscosities of 10^{1.45}, 10^{1.55}, and 10^{1.46} Pa s, respectively, which are approximately 9, 56 and 14 times lower than previous estimates, respectively (Table 5).

While our model is constrained by the compositional range between AND100-AND0, the results strongly suggest that previous viscosity models have systematically overestimated the melt viscosity of natural magmas prone to nanocrystallization, particularly in explosive volcanic systems like Sakurajima, Mt. Pinatubo, Mt. Rainer and Cerro Hudson. For Agnung, Hokaido Komagatake and Aniakchak, further experimental validation is required to confirm these findings.

Overall, our model can be extended to other volcanic centers to enhance the estimation of melt viscosity for numerical modeling of volcanic processes involving andesitic magmas. Andesitic compositions are particularly widespread in active volcanic systems worldwide, making accurate viscosity predictions critical for hazard assessment. Given that our results show 1-2 orders of magnitude viscosity reductions compared to widely-used models, the implications extend beyond individual volcanic systems to the fundamental understanding of explosive volcanism globally. In particular, they provide new insights into caldera-forming and highly explosive systems, as illustrated by the andesitic magmas investigated in this study, including those from Pinatubo, Mount Rainier, Cerro Hudson, Agung, Hokkaido Komagatake, and Aniakchak, and Sakurajima. By correcting systematic viscosity overestimations that have persisted for over a decade, our framework can now be implemented in volcanic conduit modeling. Ultimately, by refining viscosity estimations, our model improves predictions of magma ascent rates, explosivity, and lava flow behavior, providing a more accurate framework for volcanic hazard assessment.

Table 5. Chemical compositions (in wt%), literature viscosity data and viscosity calculations for different andesitic volcanoes.

	Sakurajima andesite ^a	Pinatubo andesite ^b	Rainer Andesite ^b	Cerro Hudson trachyandesite ^b	Agnungb	Hokaido Komagatake ^b	Aniakchak ^b
SiO ₂	60.41	64.8	64.7	62.80	59.10	57.9	58.6
TiO ₂	0.82	0.7	0	1.20	1.10	0.7	1.5
Al_2O_3	17.41	16.3	16.2	16.10	16.70	18.2	16.1
FeO_{tot}	7.31	6.0	5.0	4.70	8.70	8.5	8.1
MnO	0.15	0.1	0.1	0.20	0.20	0.2	0
MgO	2.81	1.3	1.9	1.50	3.30	3.1	2.8
CaO	6.89	4.4	4.4	3.20	6.40	7.7	6.1
Na ₂ O	3.38	4.7	4.5	6.70	1.60	3.2	4.5
K_2O	1.52	2.1	2.2	2.60	1.90	0.5	1.6
P_2O5	0.18	0	0	0.00	0.40	0	0
NBO/T ^c	0.33	0.22	0.22	0.23	0.35	0.37	0.38
AND_X	AND100	AND40	AND40	AND45	AND110	AND120	AND125
NBO/T _{ANDX} ^c	0.33	0.22	0.22	0.23	0.35	0.37	0.38
H_2O_{melt}	3.00	6.30	3.00	2.00	3.00	3.00	3.50
<i>T</i> (°C)	1030	760	930	972	1070	1040	1000
GRD ₂₀₀₈ (log Pa s) ^b	3.40	5.20	4.70	3.70	2.40	3.30	2.60
This work melt viscosity (log Pa s)	1.74	2.61	2.66	3.07	1.45	1.55	1.45

^afrom Yamanoi et al. (2008).

Conclusions

Our findings demonstrate that transition metal-bearing and esitic melts are highly susceptible to nanostructuration, nanocrystallization, and water loss above the glass transition temperature (T_g), processes that significantly compromise the accuracy of viscosity measurements. This experimental bias has propagated through decades of melt viscosity research, skewing our understanding of magma rheology. In particular, the bias affects the derivation of key physical properties, including the glass transition temperature and melt fragility; these properties are critical for interpreting the rheological behavior of volcanic melts.

We show that the relationship between K/G of the parental glass and melt fragility is composition-dependent, particularly influenced by the transition metal content. Building on this,

^bfrom Takeuchi (2011).

[°]NBO/T calculated after Prata et al. (2019).

we present two empirical relationships linking the melt fragility to K/G for both transition metal-free and metal-bearing melts.

Leveraging these insights, we present a new viscosity model for andesitic melts that accounts for water content, temperature, and transition metal content. Application of this model to pre-eruptive conditions of Sakurajima volcano reveals that previous viscosity estimates were overestimated by a factor of more than 45 times. When extended to other andesitic volcanic systems worldwide, we observe systematic overestimations ranging from 3 to 380 times.

Our results represent a shift in magma rheology modelling, revealing that widely used viscosity models have systematically overestimated melt viscosity for over decades. Furthermore, by refining viscosity calculations, our model improves predictions of magma ascent rates, eruptive explosivity, and lava flow dynamics, thereby enhancing the reliability of conduit flow models and volcanic hazard assessments in andesitic settings and providing a more accurate foundation for understanding explosive volcanism.

Acknowledgements

PV and DDG acknowledge the funding by Deutsche Forschungsgemeinschaft (DFG) project DI 2751/2–1. DDG acknowledges the funding from the European Research Council (ERC) under the European Union's Horizon 2020 research and innovation programme (NANOVOLC, ERC Consolidator Grant – No. 101044772). DDG acknowledges funding by MUR-PRIN Project (CRYSTALIKIN, 2022L2APNR). This project has benefited from the expertise and facilities of the Platform MACLE-CVL, which has been co-funded by the European Union and the Centre-Val de Loire Region (FEDER). JD acknowledges DFG for financial support via the grant DE 598/33-1. We thank Alexander Rother and Raphael Njul for sample preparation, Catherine McCammon

for facilitating the Mössbauer facilities, Tiziana Boffa Ballaran for providing the BLS laboratory, and Hansjörg Bornhöft for performing concentric cylinder measurements.

All authors declare that they have no conflicts of interest.

Author contributions

P.V. drafted the original manuscript, processed the experimental data, performed the Raman analyses, derived the viscosity models, conducted Mössbauer experiments, conducted KFT measurements, and constructed the figures and tables. P.V and D.B synthesized starting materials and conducted FTIR measurements. P.V. and D.D.G. conceptualized the original idea. P.V. and J.L. conducted micropenetration and calorimetry experiments. P.V. and A.K. performed the Brillouin analyses. P.V., A.Z., and D.D.G. revised the manuscript following peer review. All coauthors provided feedback and contributed to the final version of the manuscript.

Data availability

Data supporting the findings of this study are available within the article or as Supplementary Material. Additional source data for figures is available under request.

References

- Al-Mukadam, R., Di Genova, D., Bornhöft, H., Deubener, J., 2020. High rate calorimetry derived viscosity of oxide melts prone to crystallization. J. Non. Cryst. Solids 536, 119992. https://doi.org/10.1016/j.jnoncrysol.2020.119992
- Angell, C.A., 1995. Formation of Glasses from Liquids and Biopolymers. Science. 267, 1924–1935. https://doi.org/10.1126/science.267.5206.1924
- Araya, N., Nakamura, M., Yasuda, A., Okumura, S., Sato, T., Iguchi, M., Miki, D., Geshi, N., 2019. Shallow magma pre-charge during repeated Plinian eruptions at Sakurajima volcano. Sci. Rep. 9, 1–10. https://doi.org/10.1038/s41598-019-38494-x
- Barone, G., Mazzoleni, P., Corsaro, R.A., Costagliola, P., Di Benedetto, F., Ciliberto, E., Gimeno, D., Bongiorno, C., Spinella, C., 2016. Nanoscale surface modification of Mt. Etna volcanic ashes. Geochim. Cosmochim. Acta 174, 70–84. https://doi.org/10.1016/j.gca.2015.11.011
- Behrens, H., Bauer, U., Reinsch, S., Kiefer, P., Müller, R., Deubener, J., 2018. Structural relaxation mechanisms in hydrous sodium borosilicate glasses. J. Non. Cryst. Solids 497, 30–39. https://doi.org/10.1016/j.jnoncrysol.2018.05.025

- Behrens, H., Romano, C., Nowak, M., Holtz, F., Dingwell, D.B., 1996. Near-infrared spectroscopic determination of water species in glasses of the system MAlSi3O8 (M = Li, Na, K): an interlaboratory study. Chem. Geol. 128, 41–63. https://doi.org/10.1016/0009-2541(95)00162-X
- Bondar, D., Canizarès, A., Bilardello, D., Valdivia, P., Zandonà, A., Romano, C., Allix, M., Di Genova, D., 2025. Nanolite crystallization in volcanic Glasses: Insights from high-temperature Raman spectroscopy and low-temperature rock-magnetic analysis. Geochemistry, Geophys. Geosystems 26. https://doi.org/10.1029/2024GC011846
- Bondar, D., Withers, A.C., Whittington, A.G., Fei, H., Katsura, T., 2023. Dissolution mechanisms of water in depolymerized silicate (peridotitic) glasses based on infrared spectroscopy. Geochim. Cosmochim. Acta 342, 45–61. https://doi.org/https://doi.org/10.1016/j.gca.2022.11.029
- Bondar, D., Zandona, A., Withers, A.C., Fei, H., Genova, Danilo Di, Miyajima, N., Katsura, T., Di Genova, D., 2022. Rapid-quenching of high-pressure depolymerized hydrous silicate (peridotitic) glasses. J. Non. Cryst. Solids 578. https://doi.org/10.1016/j.jnoncrysol.2021.121347
- Cáceres, F., Hess, K.U., Eitel, M., Döblinger, M., McCartney, K.N., Colombier, M., Gilder, S.A., Scheu, B., Kaliwoda, M., Dingwell, D.B., 2024. Oxide nanolitisation-induced melt iron extraction causes viscosity jumps and enhanced explosivity in silicic magma. Nat. Commun. 15. https://doi.org/10.1038/s41467-024-44850-x
- Cáceres, F., Wadsworth, F.B., Scheu, B., Colombier, M., Madonna, C., Cimarelli, C., Hess, K.U., Kaliwoda, M., Ruthensteiner, B., Dingwell, D.B., 2020. Can nanolites enhance eruption explosivity? Geology 48, 997–1001. https://doi.org/10.1130/G47317.1
- Calvache V., M.L., Williams, S.N., 1997. Geochemistry and petrology of the Galeras Volcanic Complex, Colombia. J. Volcanol. Geotherm. Res. 77, 21–38. https://doi.org/10.1016/S0377-0273(96)00084-4
- Cassetta, M., Di Genova, D., Zanatta, M., Ballaran, T.B., Kurnosov, A., Giarola, M., Mariotto, G., Boffa Ballaran, T., 2021. Estimating the viscosity of volcanic melts from the vibrational properties of their parental glasses. Sci. Rep. 11, 1–14. https://doi.org/10.1038/s41598-021-92407-5
- Deubener, J., Bornhöft, H., Reinsch, S., Müller, R., Lumeau, J., Glebova, L.N., Glebov, L.B., 2009. Viscosity, relaxation and elastic properties of photo-thermo-refractive glass. J. Non. Cryst. Solids 355, 126–131. https://doi.org/10.1016/j.jnoncrysol.2008.10.002
- Di Genova, D., Bondar, D., Zandonà, A., Valdivia, P., Al-Mukadam, R., Fei, H., Withers, A.C., Boffa Ballaran, T., Kurnosov, A., McCammon, C., Deubener, J., Katsura, T., 2023. Viscosity of anhydrous and hydrous peridotite melts. Chem. Geol. 625. https://doi.org/10.1016/j.chemgeo.2023.121440
- Di Genova, D., Brooker, R.A., Mader, H.M., Drewitt, J.W.E., Longo, A., Deubener, J., Neuville, D.R., Fanara, S., Shebanova, O., Anzellini, S., Arzilli, F., Bamber, E.C., Hennet, L., La Spina, G., Miyajima, N., 2020a. In situ observation of nanolite growth in volcanic melt: A driving force for explosive eruptions. Sci. Adv. 6. https://doi.org/10.1126/sciadv.abb0413
- Di Genova, D., Hess, K.U., Chevrel, M.O., Dingwell, D.B., 2016. Models for the estimation of Fe3+/Fetot. ratio in terrestrial and extra- terrestrial alkali- and iron-rich silicate glasses using Raman spectroscopy. Am. Mineral. 101, 943–952.
- Di Genova, D., Kolzenburg, S., Wiesmaier, S., Dallanave, E., Neuville, D.R., Hess, K.U., Dingwell, D.B., 2017. A compositional tipping point governing the mobilization and eruption

- style of rhyolitic magma. Nature 552, 235-238. https://doi.org/10.1038/nature24488
- Di Genova, D., Romano, C., Alletti, M., Misiti, V., Scarlato, P., 2014. The effect of CO2 and H2O on Etna and Fondo Riccio (Phlegrean Fields) liquid viscosity, glass transition temperature and heat capacity. Chem. Geol. 377, 72–86. https://doi.org/10.1016/j.chemgeo.2014.04.001
- Di Genova, D., Zandona, A., Deubener, J., 2020b. Unravelling the effect of nano-heterogeneity on the viscosity of silicate melts: Implications for glass manufacturing and volcanic eruptions. J. Non. Cryst. Solids 545, 120248. https://doi.org/10.1016/j.jnoncrysol.2020.120248
- Dickinson, W.R., Hatherton, T., 1967. Andesitic Volcanism and Seismicity around the Pacific. Science (80-.). 157, 801–803. https://doi.org/10.1126/science.157.3790.801
- Dingwell, D.B., 1996. Volcanic dilemma flow or blow? Science. 273, 1054–1055. https://doi.org/10.1126/science.273.5278.1054
- Dingwell, D.B., 1990. Relaxation in silicate melts: Some applications. Struct. Dyn. Prop. Silic. Melts 32, 21–66.
- Douglas, R.W., Armstrong, W.L., Edward, J., Hall, D., 1965. A penetration viscometer. Glas. Technol. 6, 52–55.
- Eichheimer, P., Thielmann, M., Fujita, W., Golabek, G., Nakamura, M., Okumura, S., Nakatani, T., Kottwitz, M., 2020. Combined numerical and experimental study of microstructure and permeability in porous granular media. Solid Earth Discuss. 1–25. https://doi.org/10.5194/se-2019-199
- Fanesi, E., Di Genova, D., Valdivia, P., Bondar, D., Dominijanni, S., Abeykoon, S., Giuliani, G., Kurnosov, A., Giordano, G., Cassetta, M., Vona, A., Romano, C., Arzilli, F., 2025. A review of the differential scanning calorimetry shift–factor approach: Application to Colli Albani melt viscosity and implications for mafic Plinian eruptions. J. Volcanol. Geotherm. Res. 461, 108276. https://doi.org/10.1016/j.jvolgeores.2025.108276
- Giordano, D., Dingwell, D.B., 2003. The kinetic fragility of natural silicate melts. J. Phys. Condens. Matter 15, S945–S954. https://doi.org/10.1088/0953-8984/15/11/318
- Giordano, D., Russell, J.K., Dingwell, D.B., 2008. Viscosity of magmatic liquids: A model. Earth Planet. Sci. Lett. 271, 123–134. https://doi.org/10.1016/j.epsl.2008.03.038
- Giuliani, G., Di Genova, D., Di Fiore, F., Valdivia, P., Mollo, S., Romano, C., Ballaran, T.B., Kurnosov, A., Vona, A., 2024. The effect of carbonate assimilation and nanoheterogeneities on the viscosity of phonotephritic melt from Vesuvius. Chem. Geol. 670, 122408. https://doi.org/10.1016/j.chemgeo.2024.122408
- Gonnermann, H.M., 2015. Magma Fragmentation. Annu. Rev. Earth Planet. Sci. 43, 431–458. https://doi.org/10.1146/annurev-earth-060614-105206
- Hughes, E.C., Buse, B., Kearns, S.L., Blundy, J.D., Kilgour, G., Mader, H.M., 2019. Low analytical totals in EPMA of hydrous silicate glass due to sub-surface charging: Obtaining accurate volatiles by difference. Chem. Geol. 505, 48–56. https://doi.org/10.1016/j.chemgeo.2018.11.015
- Jubb, A.M., Allen, H.C., 2010. Vibrational Spectroscopic Characterization of Hematite, Maghemite, and Magnetite Thin Films Produced by Vapor Deposition. ACS Appl. Mater. Interfaces 2, 2804–2812. https://doi.org/10.1021/am1004943
- Knafelc, J., Bryan, S.E., Jones, M.W.M., Gust, D., Mallmann, G., Cathey, H.E., Berry, A.J., Ferré, E.C., Howard, D.L., 2022. Havre 2012 pink pumice is evidence of a short-lived, deep-sea, magnetite nanolite-driven explosive eruption. Commun. Earth Environ. 3, 1–11. https://doi.org/10.1038/s43247-022-00355-3
- Kohl, I., Bachmann, L., Mayer, E., Hallbrucker, A., Loerting, T., 2005. Glass transition in

- hyperquenched water? Nature 435, E1-E1. https://doi.org/10.1038/nature03707
- Koyaguchi, T., Mitani, N.K., 2005. A theoretical model for fragmentation of viscous bubbly magmas in shock tubes. J. Geophys. Res. 110, B10202. https://doi.org/10.1029/2004JB003513
- Langhammer, D., Di Genova, D., Steinle-Neumann, G., 2022. Modeling viscosity of volcanic melts with artificial neural networks. Geochemistry Geophys. Geosystems 23. https://doi.org/10.1029/2022GC010673
- Langhammer, D., Di Genova, D., Steinle-Neumann, G., 2021. Modelling the viscosity of anhydrous and hydrous volcanic melt. Geochemistry Geophys. Geosystems n/a, e2021GC009918. https://doi.org/doi.org/10.1029/2021GC009918
- Larre, C., Morizet, Y., Bézos, A., Guivel, C., La, C., Mangold, N., 2020. Particular H2O dissolution mechanism in iron-rich melt: Application to martian basaltic melt genesis. J. Raman Spectrosc. 51, 493–507. https://doi.org/10.1002/jrs.5787
- Lautze, N.C., Houghton, B.F., 2007. Linking variable explosion style and magma textures during 2002 at Stromboli volcano, Italy. Bull. Volcanol. 69, 445–460. https://doi.org/10.1007/s00445-006-0086-1
- Liebske, C., Behrens, H., Holtz, F., Lange, R.A., 2003. The influence pf pressure and composition on the viscocity of andesitic melts. Geochim. Cosmochim. Acta 67, 473–485. https://doi.org/10.1016/S0016-7037(02)01139-0
- Loughlin, S.C., Sparks, S., Brown, S.K., Jenkins, S.F., Vye-Brown, C., 2015. Global volcanic hazards and risk, Global Volcanic Hazards and Risk. Cambridge University Press, Cambridge. https://doi.org/10.1017/CBO9781316276273
- Luhr, J.F., Carmichael, I.S.E., 1980. The Colima Volcanic complex, Mexico. Contrib. to Mineral. Petrol. 71, 343–372. https://doi.org/10.1007/bf00374707
- Malfait, W.J., Sanchez-Valle, C., 2013. Effect of water and network connectivity on glass elasticity and melt fragility. Chem. Geol. 346, 72–80. https://doi.org/10.1016/j.chemgeo.2012.04.034
- Massaro, S., Sulpizio, R., Costa, A., Capra, L., Lucchi, F., 2018. Understanding eruptive style variations at calc-alkaline volcanoes: the 1913 eruption of Fuego de Colima volcano (Mexico). Bull. Volcanol. 80, 62. https://doi.org/10.1007/s00445-018-1235-z
- Mauro, J.C., Yue, Y., Ellison, A.J., Gupta, P.K., Allan, D.C., 2009. Viscosity of glass-forming liquids. Proc. Natl. Acad. Sci. U. S. A. 106, 19780–4. https://doi.org/10.1073/pnas.0911705106
- Meerlender, G., 1974. VISKOSITAETS-TEMPERATUR-VERHALTEN DES STANDARDGLASES I DER DGG. Glas. Ber 47, 1–3.
- Mujin, M., Nakamura, M., 2020. Late-stage groundmass differentiation as a record of magma stagnation, fragmentation, and rewelding. Bull. Volcanol. 82, 48. https://doi.org/10.1007/s00445-020-01389-1
- Mujin, M., Nakamura, M., 2014. A nanolite record of eruption style transition. Geology 42, 611–614. https://doi.org/10.1130/G35553.1
- Mujin, M., Nakamura, M., Miyake, A., 2017. Eruption style and crystal size distributions: Crystallization of groundmass nanolites in the 2011 Shinmoedake eruption. Am. Mineral. 102, 2367–2380. https://doi.org/10.2138/am-2017-6052CCBYNCND
- Novikov, V.N., Ding, Y., Sokolov, A.P., 2005. Correlation of fragility of supercooled liquids with elastic properties of glasses. Phys. Rev. E Stat. Nonlinear, Soft Matter Phys. 71, 1–12. https://doi.org/10.1103/PhysRevE.71.061501
- Novikov, V.N., Sokolov, A.P., 2004. Poisson's ratio and the fragility of glass-forming liquids.

- Nature 431, 961–963. https://doi.org/10.1038/nature02947
- Ohlhorst, S., Behrens, H., Holtz, F., 2001. Compositional dependence of molar absorptivities of near-infrared OH-and H2O bands in rhyolitic to basaltic glasses. Chem. Geol. 174, 5–20. https://doi.org/10.1016/S0009-2541(00)00303-X
- Okumura, S., Nakamura, M., Nakano, T., Uesugi, K., Tsuchiyama, A., 2010. Shear deformation experiments on vesicular rhyolite: Implications for brittle fracturing, degassing, and compaction of magmas in volcanic conduits. J. Geophys. Res. Solid Earth 115, 1–10. https://doi.org/10.1029/2009JB006904
- Okumura, S., Uesugi, K., Goto, A., Sakamaki, T., Matsumoto, K., Takeuchi, A., Miyake, A., 2022. Rheology of nanocrystal-bearing andesite magma and its roles in explosive volcanism. Commun. Earth Environ. 3, 241. https://doi.org/10.1038/s43247-022-00573-9
- Okumura, S.H., Mujin, M., Tsuchiyama, A., Miyake, A., 2024. Crystal habit (tracht) of groundmass pyroxene crystals recorded magma ascent paths during the 2011 Shinmoedake eruption. Am. Mineral. 109, 325–338. https://doi.org/10.2138/am-2022-8765
- Papale, P., 1999. Strain-induced magma fragmentation in explosive eruptions. Nature 397, 425–428. https://doi.org/10.1038/17109
- Pereira, L., Linard, Y., Wadsworth, F.B., Vasseur, J., Hess, K.U., Moretti, R., Dingwell, D.B., Neuville, D.R., 2024. The rheological response of magma to nanolitisation. J. Volcanol. Geotherm. Res. 448, 108039. https://doi.org/10.1016/j.jvolgeores.2024.108039
- Pichavant, M., Di Carlo, I., Rotolo, S.G., Scaillet, B., Burgisser, A., Le Gall, N., Martel, C., 2013. Generation of CO2-rich melts during basalt magma ascent and degassing. Contrib. to Mineral. Petrol. 166, 545–561. https://doi.org/10.1007/s00410-013-0890-5
- Prata, G.S., Ventress, L.J., Carboni, E., Mather, T.A., Grainger, R.G., Pyle, D.M., 2019. A New Parameterization of Volcanic Ash Complex Refractive Index Based on NBO/T and SiO 2 Content. J. Geophys. Res. Atmos. 124, 1779–1797. https://doi.org/10.1029/2018JD028679
- Prescher, C., McCammon, C., Dubrovinsky, L., 2012. MossA: a program for analyzing energy-domain Mössbauer spectra from conventional and synchrotron sources. J. Appl. Crystallogr. 45, 329–331. https://doi.org/10.1107/S0021889812004979
- Richet, P., Lejeune, A.M.M., Holtz, F., Roux, J., 1996. Water and the viscosity of andesite melts. Chem. Geol. 128, 185–197. https://doi.org/10.1016/0009-2541(95)00172-7
- Savov, I.P., Luhr, J.F., Navarro-Ochoa, C., 2008. Petrology and geochemistry of lava and ash erupted from Volcán Colima, Mexico, during 1998-2005. J. Volcanol. Geotherm. Res. 174, 241–256. https://doi.org/10.1016/j.jvolgeores.2008.02.007
- Scarani, A., Zandonà, A., Di Fiore, F., Valdivia, P., Putra, R., Miyajima, N., Bornhöft, H., Vona, A., Deubener, J., Romano, C., Di Genova, D., Zandona, A., 2022. A chemical threshold controls nanocrystallization and degassing behaviour in basalt magmas. Commun. Earth Environ. 3, 284. https://doi.org/10.1038/s43247-022-00615-2
- Schneider, H.A., Rieger, J., Penzel, E., 1997. The glass transition temperature of random copolymers: 2. Extension of the Gordon Taylor equation for asymmetric Tg vs composition curves. Polymer (Guildf). 38, 1323–1337. https://doi.org/10.1016/S0032-3861(96)00652-0
- Schroeder, J., Wu, W., Apkarian, J.L., Lee, M., Hwa, L.-G.G., Moynihan, C.T., 2004. Raman scattering and Boson peaks in glasses: Temperature and pressure effects. J. Non. Cryst. Solids 349, 88–97. https://doi.org/10.1016/j.jnoncrysol.2004.08.265
- Schuessler, J.A., Botcharnikov, R.E., Behrens, H., Misiti, V., Freda, C., 2008. Amorphous materials: Properties, structure, and durability: Oxidation state of iron in hydrous phonotephritic melts. Am. Mineral. 93, 1493–1504. https://doi.org/10.2138/am.2008.2795

- Sharp, T.G., Stevenson, R.J., Dingwell, D.B., 1996. Microlites and "nanolites" in rhyolitic glass: Microstructural and chemical characterization. Bull. Volcanol. 57, 631–640. https://doi.org/10.1007/s004450050116
- Shebanova, O.N., Lazor, P., 2003. Raman spectroscopic study of magnetite (FeFe2O4): a new assignment for the vibrational spectrum. J. Solid State Chem. 174, 424–430. https://doi.org/10.1016/S0022-4596(03)00294-9
- Sinogeikin, S., Bass, J., Prakapenka, V., Lakshtanov, D., Shen, G., Sanchez-Valle, C., Rivers, M., 2006. Brillouin spectrometer interfaced with synchrotron radiation for simultaneous x-ray density and acoustic velocity measurements. Rev. Sci. Instrum. 77, 103905. https://doi.org/10.1063/1.2360884
- Sokolov, A.P., Novikov, V.N., Kisliuk, A., 2007. Fragility and mechanical moduli: Do they really correlate? Philos. Mag. 87, 613–621. https://doi.org/10.1080/14786430600880769
- Sparks, R.S.J., 2003. Dynamics of magma degassing. Geol. Soc. London, Spec. Publ. 213, 5–22. https://doi.org/10.1144/GSL.SP.2003.213.01.02
- Stabile, P., Sicola, S., Giuli, G., Paris, E., Carroll, M.R., Deubener, J., Di Genova, D., 2021. The effect of iron and alkali on the nanocrystal-free viscosity of volcanic melts: A combined Raman spectroscopy and DSC study. Chem. Geol. 559, 119991. https://doi.org/10.1016/j.chemgeo.2020.119991
- Takeuchi, S., 2011. Preeruptive magma viscosity: An important measure of magma eruptibility. J. Geophys. Res. Solid Earth 116. https://doi.org/10.1029/2011JB008243
- Torres-Orozco, R., Capra, L., Márquez-Ramírez, V.H., Sosa-Ceballos, G., De Plaen, R.S.M., Cid, H.E., Sulpizio, R., Arámbula-Mendoza, R., 2024. Andesite magma genesis, conduit dynamics and variable decompression from shallow reservoirs drive contrasting PDC events at Volcán de Colima, Mexico. J. Volcanol. Geotherm. Res. 453. https://doi.org/10.1016/j.jvolgeores.2024.108143
- Torres-Orozco, R., Cronin, S.J., Pardo, N., Palmer, A.S., 2018. Volcanic hazard scenarios for multiphase andesitic Plinian eruptions from lithostratigraphy: Insights into pyroclastic density current diversity at Mount Taranaki, New Zealand. Bull. Geol. Soc. Am. 130, 1645–1663. https://doi.org/10.1130/B31850.1
- Valdivia, P., Zandonà, A., Kurnosov, A., Ballaran, T.B., Deubener, J., Di Genova, D., 2023. Are volcanic melts less viscous than we thought? The case of Stromboli basalt. Contrib. to Mineral. Petrol. 178, 45. https://doi.org/10.1007/s00410-023-02024-w
- Valdivia, P., Zandonà, A., Löschmann, J., Bondar, D., Genevois, C., Canizarès, A., Allix, M., Miyajima, N., Kurnosov, A., Ballaran, T.B., Di Fiore, F., Vona, A., Romano, C., Deubener, J., Bamber, E.C., Longo, A., Di Genova, D., 2025. Nanoscale chemical heterogeneities control the viscosity of andesitic magmas. Commun. Earth Environ. 6, 455. https://doi.org/10.1038/s43247-025-02424-9
- Vetere, F., Behrens, H., Schuessler, J.A., Holtz, F., Misiti, V., Borchers, L., 2008. Viscosity of andesite melts and its implication for magma mixing prior to Unzen 1991-1995 eruption. J. Volcanol. Geotherm. Res. 175, 208–217. https://doi.org/10.1016/j.jvolgeores.2008.03.028
- Vona, A., Romano, C., Dingwell, D.B., Giordano, D., 2011. The rheology of crystal-bearing basaltic magmas from Stromboli and Etna. Geochim. Cosmochim. Acta 75, 3214–3236.

- https://doi.org/10.1016/j.gca.2011.03.031
- Wallace, P.J., 2005. Volatiles in subduction zone magmas: concentrations and fluxes based on melt inclusion and volcanic gas data. J. Volcanol. Geotherm. Res. 140, 217–240. https://doi.org/10.1016/j.jvolgeores.2004.07.023
- Webb, S.L., Dingwell, D.B., 1990. Non-Newtonian rheology of igneous melts at high stresses and strain rates: experimental results for rhyolite, andesite, basalt, and nephelinite. J. Geophys. Res. 95, 15695–15701. https://doi.org/10.1029/jb095ib10p15695
- Whitfield, C.H., Brody, E.M., Bassett, W., 1976. Elastic moduli of NaCl by Brillouin scattering at high pressure in a diamond anvil cell. Rev. Sci. Instrum. 47, 942–947.
- Yamanoi, Y., Takeuchi, S., Okumura, S., Nakashima, S., Yokoyama, T., 2008. Color measurements of volcanic ash deposits from three different styles of summit activity at Sakurajima volcano, Japan: Conduit processes recorded in color of volcanic ash. J. Volcanol. Geotherm. Res. 178, 81–93. https://doi.org/10.1016/j.jvolgeores.2007.11.013
- Yoshida, K., Miyake, A., Okumura, S.H., Ishibashi, H., Okumura, S., Okamoto, A., Niwa, Y., Kimura, M., Sato, T., Tamura, Y., Ono, S., 2023. Oxidation-induced nanolite crystallization triggered the 2021 eruption of Fukutoku-Oka-no-Ba, Japan. Sci. Rep. 13, 7117. https://doi.org/10.1038/s41598-023-34301-w
- Yue, Y., 2009. The iso-structural viscosity, configurational entropy and fragility of oxide liquids. J. Non. Cryst. Solids 355, 737–744. https://doi.org/10.1016/j.jnoncrysol.2009.01.032
- Zanatta, M., Baldi, G., Caponi, S., Fontana, A., Petrillo, C., Rossi, F., Sacchetti, F., 2011. Debye to non-Debye scaling of the Boson peak dynamics: Critical behavior and local disorder in vitreous germania. J. Chem. Phys. 135. https://doi.org/10.1063/1.3656697
- Zellmer, G.F., Sakamoto, N., Hwang, S.L., Matsuda, N., Iizuka, Y., Moebis, A., Yurimoto, H., 2016. Inferring the effects of compositional boundary layers on crystal nucleation, growth textures, and mineral chemistry in natural volcanic tephras through submicron-resolution imaging. Front. Earth Sci. 4, 1–7. https://doi.org/10.3389/feart.2016.00088
- Zhang, Y., 1999. A criterion for the fragmentation of bubbly magma based on brittle failure theory. Nature 402, 648–650. https://doi.org/10.1038/45210
- Zheng, Q., Mauro, J.C., Yue, Y., 2017. Reconciling calorimetric and kinetic fragilities of glass-forming liquids. J. Non. Cryst. Solids 456, 95–100. https://doi.org/10.1016/j.jnoncrysol.2016.11.014

List of publications

As a first author (chronological order):

- 1) Valdivia, P., Löschmann, J., Zandonà, A., Bondar, D., Kurnosov, A., Deubener, J., Di Genova, D. A viscosity model for hydrous andesitic magmas. To be submitted to Earth Planet. Sci. Lett.
- 2) **Valdivia**, **P**., Zandonà, A., Löschmann, J., Bondar, D., Genevois, C., Canizarès, A., Allix, M., Miyajima, N., Kurnosov, A., Ballaran, T.B., Di Fiore, F., Vona, A., Romano, C., Deubener, J., Bamber, E.C., Longo, A., Di Genova, D., 2025. Nanoscale chemical heterogeneities control the viscosity of andesitic magmas. *Commun. Earth. Environ.* 6, 455. DOI: https://doi.org/10.1038/s43247-025-02424-9
- 3) Valdivia, P., Zandonà, A., Kurnosov, A., Ballaran, T.B., Deubener, J., Di Genova, D., 2023. Are volcanic melts less viscous than we thought? The case of Stromboli basalt. *Contrib. Mineral. Petrol.* 178, 45.

DOI: https://doi.org/10.1007/s00410-023-02024-w

4) Valdivia, P., Marshall, A.A., Brand, B.D., Manga, M., Huber, C., 2022. Mafic explosive volcanism at Llaima Volcano: 3D x-ray microtomography reconstruction of pyroclasts to constrain shallow conduit processes. *Bull. Volcanol.* 84, 2.

DOI: https://doi.org/10.1007/s00445-021-01514-8

Others (chronological order):

- 5) Dominijanni S., Calabrò L, Bamber E. C., Giuliani G., Bondar D., Valdivia P., Arzilli F., La Spina G., Kurnosov A., Vona A., Longo A., Di Genova D. Modelling magma viscosity and ascent dynamics of the 472 AD sub-Plinian eruption of Somma-Vesuvius (Italy). To be submitted to *Geochim. Cosmochim. Acta*.
- 6) Colombier M, Cáceres F, Birnbaum J, deGraffenried R, Lavallée Y, Kendrick JE, Scheu B, Thivet S, Valdivia P, Ruhekenya RM, Schlepütz C, Castro J, Hess KU, Dingwell DB. Inherent duality of vesiculation kinematics revealed through 4D imaging. submitted to *J. Volcanol. Geotherm. Res. (under review)*.
- 7) Bamber E.C., Arzilli F., Cipiccia S., Batey D. J., La Spina G., Polacci M., Gholinia A., Bagshaw H., Di Genova D., Brooker R., Giordano D., Valdivia P., Burton M. R. 2025. 3D visualisation of nanolite aggregates in basaltic magmas using X-ray ptychography: Implications for magma rheology. *Nat. Commun.* 16, 7083. DOI: https://doi.org/10.1038/s41467-025-62444-z
- 8) Bondar, D., Canizarès, A., Bilardello, D., Valdivia, P., Zandonà, A., Romano, C., Allix, M., Di Genova, D., 2025. Nanolite Crystallization in Volcanic Glasses: Insights From High-Temperature Raman Spectroscopy and Low-Temperature Rock-Magnetic Analysis. *Geochemistry, Geophys. Geosystems* 26.

DOI https://doi.org/10.1029/2024GC011846

9) Fanesi, E., Di Genova, D., Valdivia, P., Bondar, D., Dominijanni, S., Abeykoon, S., Giuliani, G., Kurnosov, A., Giordano, G., Cassetta, M., Vona, A., Romano, C., Arzilli, F., 2025. A review of the differential scanning calorimetry shift–factor approach: Application to Colli Albani melt viscosity and implications for mafic Plinian eruptions. *J. Volcanol. Geotherm. Res.* 461, 108276.

DOI: https://doi.org/10.1016/j.jvolgeores.2025.108276

10) Giuliani, G., Di Genova, D., Di Fiore, F., **Valdivia**, **P**., Mollo, S., Romano, C., Ballaran, T.B., Kurnosov, A., Vona, A., 2024. The effect of carbonate assimilation and nanoheterogeneities on the viscosity of phonotephritic melt from Vesuvius. *Chem. Geol.* 670, 122408.

DOI: https://doi.org/10.1016/j.chemgeo.2024.122408

11) Di Genova, D., Bondar, D., Zandonà, A., **Valdivia, P**., Al-Mukadam, R., Fei, H., Withers, A.C., Boffa Ballaran, T., Kurnosov, A., McCammon, C., Deubener, J., Katsura, T., 2023. Viscosity of anhydrous and hydrous peridotite melts. *Chem. Geol.* 625.

DOI: https://doi.org/10.1016/j.chemgeo.2023.121440

12) Scarani, A., Zandonà, A., Di Fiore, F., **Valdivia**, **P**., Putra, R., Miyajima, N., Bornhöft, H., Vona, A., Deubener, J., Romano, C., Di Genova, D., Zandona, A., 2022. A chemical threshold controls nano-crystallization and degassing behaviour in basalt magmas. *Commun. Earth Environ.* 3, 284.

DOI: https://doi.org/10.1038/s43247-022-00615-2

13) Marshall, A.A., Brand, B.D., Martínez, V., Bowers, J.M., Walker, M., Wanless, V.D., Andrews, B.J., Manga, M., **Valdivia**, **P**., Giordano, G., 2022. The mafic Curacautín ignimbrite of Llaima volcano, Chile. *J. Volcanol. Geotherm. Res.* 421, 107418.

DOI: https://doi.org/10.1016/j.jvolgeores.2021.107418

14) McGee, L.E., Brahm, R., Rowe, M.C., Handley, H.K., Morgado, E., Lara, L.E., Turner, M.B., Vinet, N., Parada, M.A., Valdivia, P., 2017. A geochemical approach to distinguishing competing tectono-magmatic processes preserved in small eruptive centres. *Contrib. Mineral. Petrol.* 172.

DOI: https://doi.org/10.1007/s00410-017-1360-2

Eidesstattliche) Versicherungen und Erklärungen

(§ 9 Satz 2 Nr. 3 PromO BayNAT)

Hiermit versichere ich eidesstattlich, dass ich die Arbeit selbstständig verfasst und keine anderen als die von mir angegebenen Quellen und Hilfsmittel benutzt habe (vgl. Art. 97 Abs. 1 Satz 8 BayHIG).

(§ 9 Satz 2 Nr. 3 PromO BayNAT)

Hiermit erkläre ich, dass ich die Dissertation nicht bereits zur Erlangung eines akademischen Grades eingereicht habe und dass ich nicht bereits diese oder eine gleichartige Doktorprüfung endgültig nicht bestanden habe.

(§ 9 Satz 2 Nr. 4 PromO BayNAT)

Hiermit erkläre ich, dass ich Hilfe von gewerblichen Promotionsberatern bzw. - vermittlern oder ähnlichen Dienstleistern weder bisher in Anspruch genommen habe noch künftig in Anspruch nehmen werde.

(§ 9 Satz 2 Nr. 7 PromO BayNAT)

Hiermit erkläre ich mein Einverständnis, dass die elektronische Fassung meiner Dissertation unter Wahrung meiner Urheberrechte und des Datenschutzes einer gesonderten Überprüfung unterzogen werden kann.

(§ 9 Satz 2 Nr. 8 PromO BayNAT)

Hiermit erkläre ich mein Einverständnis, dass bei Verdacht wissenschaftlichen Fehlverhaltens Ermittlungen durch universitätsinterne Organe der wissenschaftlichen Selbstkontrolle stattfinden können.

Ort, Datum, Unterschrift		